



MONASH University

**Novel Design of Multicomponent
Materials Using Severe Plastic
Deformation Methods**

by

Yuanshen Qi

BE (Hon.)

A Thesis Submitted for the Degree of Doctor of
Philosophy at Monash University in 2016

Copyright notice

© The author (2016). Except as provided in the Copyright Act 1968, this thesis may not be reproduced in any form without the written permission of the author.

Yuanshen Qi

February 2016

I certify that I have made all reasonable efforts to secure copyright permissions for third-party content included in this thesis and have not knowingly added copyright content to my without the owner's permission.

Copyright Notice

Abstract

Using severe plastic deformation (SPD) methods to design and fabricate multicomponent materials has been drawing increasing attention in recent years [1, 2]. In the present study, equal-channel angular pressing (ECAP), as the most highly developed SPD technique, is investigated to design and fabricate multicomponent materials for three applications. They are (i) high strength and low density materials for structural application, (ii) high strength, low stiffness and good biocompatibility materials for biomedical implant application, and (iii) high strength and high conductivity materials for electrical transmission line application. Accordingly, this project is divided into three sub-projects, which have the same processing principle of ECAP but different constituents in terms of material selection, shape, and scale of the constituents and the processing parameters.

In the first sub-project, multicomponent materials having high strength and low density are aimed to be fabricated using ECAP. Aluminium and magnesium machining chips are used as raw materials. By blending them and consolidating the mixture using ECAP with back pressure of 175MPa, full dense metallic composite is fabricated. Testing results show that substantial improvement of mechanical properties, such as an increase of strength, strain-hardening capability and ductility, can be obtained. This is achieved by changing the strain path, processing temperature and post-ECAP thermal treatment, as well as by optimising the weight fraction of the constituent metals. Microstructure characterisation shows that the strain path can be optimised to achieve profuse breakage of oxide layer along interfaces. Moreover, processing or annealing at 300°C can cause intermetallic phase formation at the interface resulted from enhanced interdiffusivity.

In the second sub-project, multicomponent materials having high strength, low stiffness and good biocompatibility for biomedical implant application are targeted. Three components including titanium, magnesium and silicon powders are used as raw materials. They are blended and consolidated by ECAP with back pressure of 175MPa at 400°C. By leaching out Si and Mg constituents, porous Ti/Mg and porous Ti having bone-like cancellous architecture are successfully fabricated. It is the first successful fabrication of porous Ti/Mg composite with 100% interconnectivity and high mechanical performance. After Mg constituents are leached away, porous Ti possesses excellent mechanical properties and good biocompatibility.

Abstract

Electron microscopy results show that the outstanding mechanical performance of the material is caused by the low processing temperature, elimination of post high temperature annealing and redistribution of constituents during processing. Moreover, biocompatibility is improved by the unique surface morphology resulting from etching of oxide-free surface and ultrafine-grained structure of the Ti substrate.

The objective with the multicomponent material studied in the third sub-project is high strength and high electrical conductivity. The concentric jacket-core architecture is studied on bimetallic rods having an aluminium alloy 6201 out jacket layer and an austenitic steel 316L core, which has the potential application of overhead transmission line. Bimetallic rods with different geometry of constituents are deformed through ECAP with back pressure of 15MPa at 175°C. Compared with as-received bimetallic rods, the deformed ones possess significantly higher strength due to grain refinement. More importantly, for one kind of geometry, the electrical conductivity is not sacrificed by the enhancement of strength. Microstructure characterisation results show that the co-deformation between core and jacket layer is critical in causing extensive dynamic ageing and microstructural refinement in Al component, which contributes to conductivity not being diminished when strength is raised.

Declaration

I hereby declare that this thesis contains no material which has been accepted for the award of any other degree or diploma at any university or equivalent institution and that, to the best of my knowledge and belief, this thesis contains no material previously published or written by another person, except where due reference is made in the text of the thesis.

This thesis includes two original papers published in peer reviewed journals and one unpublished publication. The core theme of the thesis is novel design of multicomponent materials using severe plastic deformation methods. The ideas, development and writing up of all the papers in the thesis were the principal responsibility of myself, the candidate, working within the department of materials science and engineering at Monash University under the supervision of Prof. Yuri Estrin and A/Prof. Rimma Lapovok.

The inclusion of co-authors reflects the fact that the work came from active collaboration between researchers and acknowledges input into team-based research. In the case of Chapters 4, 5, and 6, my contribution to the work involved the following:

Thesis chapter	Publication title	Publication status	Nature and extent (%) of students contribution
4	Multicomponent materials from machining chips compacted by equal-channel angular pressing	Published	80% of the work was done by the candidate; including 90% of the experiments and writing of the paper draft.
5	Ultrafine-grained porous titanium and porous titanium/magnesium composites fabricated by space holder-enabled severe plastic deformation	Published	85% of the work was done by the candidate; including 90% of the experiments and writing of the paper draft.
6	Microstructure and electrical conductivity of aluminium/steel bimetallic rods processed by severe plastic deformation	Submitted	90% of the work was done by the candidate; including 95% of the experiments and writing of the paper draft

Declaration

I have renumbered sections of submitted or published papers in order to generate a consistent presentation within the thesis

Student signature:



Date: 09/02/2016

The undersigned hereby certify that the above declaration correctly reflects the nature and extent of the student and co-authors' contributions to this work.

Main Supervisor signature:



Date: 09/02/2016

Publications

Y. Qi, K. Contreras, H. Jung, E. Kim, R. Lapovok, Y. Estrin. Ultrafine-grained porous titanium and porous titanium/magnesium composites fabricated by space holder-enabled severe plastic deformation. *Materials Science and Engineering C*. 59(2016). 754-765

Y. Qi, R. Lapovok, Y. Estrin. Microstructure and electrical conductivity of aluminium/steel bimetallic rods processed by severe plastic deformation. Submitted.

R. Lapovok, **Y. Qi**, H. P. Ng, V. Maier, Y. Estrin. Multicomponent materials from machining chips compacted by equal-channel angular pressing. *Journal of Materials Science*. 49(2014). 1193-1204.

Publications

Acknowledgements

I would like to express my deepest gratitude to my advisors, Prof. Yuri Estrin and A/Prof. Rimma Lapovok, for their guidance and inspiration. Their enthusiasm for this project, dedication to academic research and rigorous attitude toward presentation shaped my understanding of scientists. Their always humble, patient and considerate manners towards others also hugely influence me.

Beside my advisors, I would like to thank Prof. George Simon who encouraged and supported me to do this PhD project in the beginning. Also many thanks to Prof. Yibing Chen who established the “2+2” project and provided me the opportunity to study in Australia in the past six years.

My sincere thanks also go to Dr. Andrey Molotnikov and Dr. Hoi Pang Ng for their great help in modelling and electron microscopy works and their continuous encouragement.

I am indebted to all the staff of Monash Centre for Electron Microscopy (MCEM). Thanks to Dr. Russell King, Mr. Renji Pan, Dr. Tim Williams, Dr. Xiya Fang, Dr. Yu Chen, Dr. Amelia Liu, Dr. Jisheng Ma, Dr. Annalena Wolff and Dr. Flame Burgmann, who trained me from the very beginning of sample preparation techniques to operation and interpretation of electron microscopes.

I would also like to thank Mr. Daniel Curtis, Mr. Silvio Mattievich and Mr. Eraldo Pulcina for their technical support. Without their help and valuable advice the experiments had not been possible to be conducted.

I gratefully acknowledge Dr. Verena Maier for conducting nanoindentation, Ms. Karla Contreras for carrying out cell assays, Ms. Joan Clark for assistance of cell imaging, Dr. Hyun-Do Jung and Prof. Hyoun-Ee Kim for providing the micro-CT data.

I would also like to thank Dr. Xiaobo Chen and Dr. Enrico Bruder. Without their kind and valuable suggestions, the 2nd and 3rd sub-projects had not been possible to be carried out.

I am very fortunate to work and spend most of my time with my group mates: Dr. Alexander Medvedev, Ms. Yali Wang, Mr. Lee Djumas, Dr. Ehsan Bafekrpour, Ms. Zhen

Acknowledgements

Wang, Mr. Alex Bevacqua, Mr. Marten Jurg and Dr. Anibal Mendes. I would also like to thank the fellow PhD students and postdocs in our department for their help and supports.

Finally, I want to thank my family for their love and support. Particularly my cousin, without whom I might have finished the thesis a quarter earlier, but without whose company this journey would not have been so much fun.

Table of Contents

Copyright notice.....	I
Abstract.....	III
Declaration.....	V
Publications	VII
Acknowledgements	IX
Table of Contents	XI
List of Figures.....	XV
List of Tables	XX
List of Symbols	XXI
Latin symbols	XXI
Greek Symbols.....	XXI
Chapter 1 Introduction	1
1.1 Background and motivation.....	3
1.2 Objectives of research	4
1.3 Structure of the thesis	5
Chapter 2 Literature Review	7
2.1 Outline of the chapter	9
2.2 Metallic hybrid	9
2.2.1 Solid-state bonding	10
2.2.2 Solid-state interdiffusion	15
2.3 Metal based composites.....	17
2.3.1 Metal matrix composite	17
2.3.2 Metallic composite	20
2.4 Multicomponent material.....	21
2.5 New trends of advanced multicomponent materials.....	24
2.6.1 Nanostructured multicomponent materials.....	24

Table of Contents

2.6.2 Architected multicomponent materials	25
2.6 Severe plastic deformation techniques used on multicomponent materials	26
2.6.1 Equal-channel angular pressing	29
2.6.2 High pressure torsion	31
2.6.3 Accumulative roll bonding	32
2.7 Summary of literature review	33
Chapter 3 Experimental Methods	35
3.1 Outline of the chapter	37
3.2 Equal-channel angular pressing apparatus	37
3.3 Materials' performance characterisation	40
3.3.1 Mechanical properties characterisation	40
3.3.2 Functional properties characterisation	41
3.4 Microstructural imaging and characterisation	41
3.4.1 Optical microscopy	42
3.4.2 X-ray diffraction	42
3.4.3 Electron microscopy	43
3.4.4 Energy dispersive X-ray spectroscopy	45
3.4.5 Sample preparation for electron microscopy	46
Chapter 4 Multicomponent materials from aluminium and magnesium machining chips compacted by ECAP with Back pressure	49
4.1. Outline of this chapter	51
4.2. Introduction	51
4.3 Experimental procedures and characterisation	54
4.3.1 Raw materials characterisation and ECAP compaction	54
4.3.2 Mechanical properties measurement	56
4.3.3 Microstructure characterisation	56
4.4 Results and Discussion	57
4.4.1 Density of compacts	57
4.4.2 Grain size evolution	58

Table of Contents

4.4.3 Mechanical properties.....	60
4.4.4 Phase identification.....	62
4.4.5 Electron microscopy characterisation.....	63
4.4.5 Nanoindentation characterisation	68
4.5 Summary of this chapter	70
Chapter 5 Ultrafine-grained porous titanium and porous titanium/magnesium composites fabricated by space holder-enabled Equal-Channel Angular Pressing	73
5.1 Outline of this chapter	75
5.2 Introduction	75
5.3 Specific experimental procedures and characterisation.....	80
5.3.1 Preparation of Ti/Mg/Si composites by ECAP compaction.....	80
5.3.2 Synthesis of porous Ti/Mg and porous Ti	81
5.3.3 Characterisation of porous Ti/Mg and porous Ti	82
5.3.4 Measurement of mechanical properties.....	83
5.3.5 Characterisation of microstructure of pore walls	84
5.3.6 Cell culture and cell viability.....	85
5.4 Results.....	85
5.4.1 Machinability.....	85
5.4.2 Porosity and interconnectivity	86
5.4.3 Mechanical properties.....	88
5.4.4 Microstructure of the Ti struts in the porous structures	90
5.4.5 Characterisation of morphology of pore walls	91
5.4.6 Cell viability	93
5.5 Discussion	95
5.5.1 Redistribution of the constituents during ECAP	95
5.5.2 ECAP-assisted bonding between the constituents.....	96
5.6 Summary of this chapter	99
Chapter 6 Bimetallic rod of aluminium alloy 6201 and austenitic steel 316L manufactured by Equal-Channel Angular Pressing	101

Table of Contents

6.1 Outline of this chapter.....	103
6.2 Introduction	103
6.3 Experimental procedures and characterisation	107
6.3.1 Materials selection and ECAP processing	107
6.3.2 Electrical conductivity measurement	109
6.3.3 Measurement of mechanical properties	109
6.3.4 Microstructure characterisation.....	110
6.4 Results.....	111
6.4.1 Optical microscopic observation after ECAP	111
6.4.2 Mechanical properties measurements	111
6.4.3 Electrical conductivity measurement	112
6.4.4 XRD characterisation	115
6.4.5 TEM characterisation	118
6.5 Discussion	125
6.6 Summary of this chapter.....	126
Chapter 7 Conclusion and Recommendations for Future Work	127
7.1 Outline of this chapter.....	129
7.2 Al/Mg machining chips compacts	129
7.2.1 Maximising interface density and minimising interface space.....	131
7.2.2 Using different kinds of materials.....	131
7.3 Porous Ti and porous Ti/Mg	132
7.3.1 Biological test of porous Ti/Mg composite.....	133
7.3.2 Fabrication of ultrafine-grained porous Mg.....	133
7.4 Al/Steel bimetallic rod	134
7.4.1 Test of more geometries.....	135
7.4.2 Development of finite elements tool	135
References:	137

List of Figures

Figure. 1. 1 Concept of “hybrid materials” after Ashby [7].....	3
Figure. 2. 1 Schematic illustration of explosive bonding [52]	11
Figure. 2. 2 Schematic illustration of bimetal rolling process [60]	12
Figure. 2. 3 Schematic illustration of diffusion bonding set-up [70]	13
Figure. 2. 4 Schematic illustration of stir friction joining between Al alloy and high strength steel [84]	13
Figure. 2. 5 Schematic illustration of ultrasonic bonding between two foils [93]	14
Figure. 2. 6 Schematic illustration of high-diffusivity paths in a solid [98]	17
Figure. 2. 7 Schematic illustration of ultrasonic solidification processing [112].....	19
Figure. 2. 8 Schematic illustration of typical powder metallurgy processing scheme [119]	20
Figure. 2. 9 Designing of architecture and microstructure in multicomponent materials [9].....	24
Figure. 2. 10 Schematic illustration of the formation process of fine grains under SPD condition [177-180]	27
Figure. 2. 11 Schematic illustration of two scenarios of diffusion regimes with increasing time in a coarse-grained substrate with few grain boundaries (top) and in a ultrafine-grained substrate with several grain boundaries (bottom) [99].....	28
Figure. 2. 12 Schematic of equal channel angular pressing process [11].....	29
Figure. 2. 13 Schematic illustration of particle consolidation in conventional sintering (left) and ECAP compaction (right) [195].....	31
Figure. 2. 14 Schematic illustration of HPT processing of one half disc of Al and one half disc of Cu [209].....	32
Figure. 2. 15 Schematic illustration of accumulative roll bonding processing [125].....	33
Figure. 3. 1 ECAP rig with heating element	37
Figure. 3. 2 ECAP die and punches	38
Figure. 3. 3 Four ECAP routes based on rotation of billet between passes [226]	39
Figure. 3. 4 Schematic illustration of ECAP showing the three orthogonal planes x, y and z and the shear planes associated with four processing routes [233].	40
Figure. 3. 5 Schematic illustration of the Bragg diffraction at a set of two lattice planes [235].....	42
Figure. 3. 6 Illustration of signals generated from interaction between incident electron beam and a thin sample [241].....	44
Figure. 3. 7 The schematic illustration of generation of characteristic X-rays [242]	45
Figure. 3. 8 Schematic illustration of the ion beam sputtering process [243]	46
Figure. 4. 1 Recycling process of Mg scrap by remelting and subsequent refinement [246]	52

List of Figures

Figure. 4. 2 Comparison of recycling yield between (a) conventional melting route and (b) direct solid state route [250].....	52
Figure. 4. 3 SEM images of the microstructure of as-received Al and Mg chips	54
Figure. 4. 4 The schematic diagram of the processing chain to fabrication machining chips compacts	55
Figure. 4. 5 Relative densities for all compositions after two passes of ECAP	57
Figure. 4. 6 OM images of compacts processed by RA: (a) Al80Mg20 processed by two ECAP passes at RT; (b) Al20Mg80 processed by two ECAP passes at RT (inset shows cracks in Mg chip); and (c) Al80Mg20 processed by two ECAP passes at 300°C.....	58
Figure. 4. 7 SEM images for Al and Mg grains in Al80Mg20 compact after different processing conditions.....	59
Figure. 4. 8 Average grain size vs. annealing temperature for Al and Mg in Al80Mg20 compacts produced by ECAP at RT using RA (compared to the grain size of compacts produced by ECAP at 300°C, dashed line)	60
Figure. 4. 9 Compression strength (solid lines) and ductility (dashed lines) vs. processing conditions for three compact compositions	61
Figure. 4. 10 XRD spectrum of Al50Mg50 produced by ECAP (RA) under different conditions.....	62
Figure. 4. 11 EDX line scan across an Al/Mg interface (counts per second) for a oxide-free interface and b oxide-containing interface	63
Figure. 4. 12 Interdiffusion zone width (from EDX line scan) vs. the annealing temperature after ECAP at RT (solid lines) compared to the width of interdiffusion zone in samples produced by ECAP at 300°C (dashed lines) for two different processing routes (RA and RBC)	64
Figure. 4. 13 EDX line scan across an Al/Mg interface (counts per second) for samples produced by: a ECAP at RT (RA) followed by annealing at 200°C; b ECAP at 300°C....	65
Figure. 4. 14 Microcracks in the Mg constituents of a compact after ECAP at RT.....	66
Figure. 4. 15 Al/Mg interdiffusion zone in Al80Mg20 sample processed by ECAP at 300°C. a BF-TEM image showing the overview of the interdiffusion zone; b, c zone-axis SAED patterns recorded for the grains labelled b and in the Al ₁₂ Mg ₁₇ layer; and d, e zone-axis SAED patterns recorded for the grains labelled s and e in the Al ₁₃ Mg ₂ layer. (All patterns correspond to the same scale)	67
Figure. 4. 16 Results of nanoindentation testing in the case of ECAP RB _C at 300°C with 50nm indentation size	68
Figure. 4. 17 The width of the interdiffusion zone vs. annealing temperature after compaction by RT ECAP (solid lines) and compaction by ECAP at 300°C (dashed line). An asterisk indicates samples produced at a higher back pressure of 150MPa	70
Figure. 5. 1 Schematic illustration of the plasma spraying process [149].....	76
Figure. 5. 2 Schematic illustration of selective laser melting process [301]	77
Figure. 5. 3 Schematic illustration of fabrication of porous Ti using space holder method [307].....	78
Figure. 5. 4 Scanning electron microscopy of the initial powder materials (a): titanium powder; (b) magnesium powder and (c) silicon powder	81

List of Figures

Figure. 5. 5 Optical micrographs of (a) the initial Ti/Mg/Si compact after compaction by a single ECAP pass, (b) porous Ti/Mg composite after Si particles were leached out, and (c) porous Ti after Mg granules were removed	82
Figure. 5. 6 Schematic illustration of the working principle of micro-CT [327]	83
Figure. 5. 7 Schematic illustration of wedge polishing [329]	84
Figure. 5. 8 SEM images of (a) external thread fabricated by turning and (b) internal hollow core produced by drilling. Inserts (c) and (d) are the corresponding enlarged images	86
Figure. 5. 9 Micro-CT images for the porous Ti/Mg and porous Ti produced by ECAP compaction after (a,d) 1 pass, (b,e) 2 passes and (c,f) 4 passes.....	87
Figure. 5. 10 Average pore size and average wall thickness of porous Ti/Mg and porous Ti produced by ECAP compaction of Ti, Mg and Si particles with subsequent removal of sacrificial material.....	87
Figure. 5. 11 Engineering stress-strain curves for porous Ti/Mg and porous Ti for different numbers of ECAP passes.....	89
Figure. 5. 12 Compressive strength and Young's modulus of porous Ti/Mg and porous Ti produced by ECAP compaction of Ti, Mg and Si particles with subsequent removal of sacrificial material.....	89
Figure. 5. 13 EBSD grain orientation maps for Ti struts after ECAP processing of (a) 1 pass, (b) 2 passes, and (c) 4 passes. The white area in Fig. 12 (b) corresponds to non-indexed pixels. Black lines denote high angle grain boundaries (HAGBs).	90
Figure. 5. 14 Evolution of average grain size in Ti struts with increasing number of ECAP passes.	90
Figure. 5. 15 TEM images of cell wall Ti subjected to 4 ECAP passes with (a) bright field image, (b) tilted dark field image, and inset (c) showing the corresponding SAD pattern using the aperture diameter of 0.75 μm	91
Figure. 5. 16 Three conditions of pore surfaces in porous Ti: (a) completely smooth surface, (b) partially smooth and partially rough surfaces, and (c) completely rough portions of a surface. The inset in (c) shows surface features at high magnification	92
Figure. 5. 17 Representative SEM images of surfaces of pore walls in Ti (a-c) after removal of Si particles by 5M NaOH, (d-f) after subsequent removal of Mg particles by 100 mM HCl. Note the evolution of the surface features with increasing number of ECAP passes	93
Figure. 5. 18 Cell viability measured by MTS assay after culturing for 3 and 7 days on the porous Ti scaffolds from 1, 2,4 ECAP processes.	94
Figure. 5. 19 SEM images of preosteoblast MC3T3-E1 cells cultured for 3 days on porous Ti 1p, 2p and 4p at the magnification of 2500 \times (a-c) and the magnification of 10000 \times with details of filopodia (d-f).....	94
Figure. 5. 20 SEM-BSE images (a-c) and SEM-EDX mappings (d-l) of Ti/Mg/Si compacts after 1, 2 and 4 ECAP passes.....	96
Figure. 5. 21 Interface between Ti particles in a compact obtained by 4 ECAP passes: (a) STEM-BF image and (b) STEM-HAADF image of interface between two Ti particles 'fused' together. Cross-sections (c) and (d) show an oxide fragment embedded in Ti; (e)	

List of Figures

<i>and (f) are the corresponding STEM-EDX mappings showing the distribution of titanium and oxygen, respectively.</i>	<i>97</i>
Figure. 5. 22 <i>Interfaces between Ti and Mg particles in a compact after 4 ECAP passes: (a) STEM-BF and (b) STEM-HAADF image of interfaces between Ti and Mg; (c) and (d) present the corresponding STEM-EDX mappings</i>	<i>98</i>
Figure. 6. 1 <i>Schematic illustration of bimetal rod co-extrusion [358].</i>	<i>105</i>
Figure. 6. 2 <i>Schematic illustration rotary swaging of bimetallic rod [359]</i>	<i>106</i>
Figure. 6. 3 <i>Schematic illustration of ECAP-Conform process [365]</i>	<i>107</i>
Figure. 6. 4 <i>Secondary electron images showing the process chain for fabrication of TEM lamella using FIB: (a) deposited Pt layer and a milled surface; (b) a j-cut is used to allow an easy lift-out; (c) lamella is attached to Kleindiek probe and lifted out; (d) lamella is mounted on a V-shaped Cu grid and Kleindiek is cut and detached from lamella; (e) lamella is ready to be thinned and polished; (f) lamella with thickness less than 100nm.</i>	<i>110</i>
Figure. 6. 5 <i>Optical microscopy images of the cross-sections showing the shape transformation of the steel cores after one and four ECAP passes: (a-c) initial shapes of samples with three different core diameters (before ECAP, denoted 0p), (d-e) after one ECAP pass (denoted 1p), (g-i) after four ECAP passes (denoted 4p).</i>	<i>111</i>
Figure. 6. 6 <i>Electrical conductivity and yield strength of as-received Ø10 AA6201 and steel rods and bimetallic rods with three different geometries (Ø3, Ø4, and Ø5 steel core) after 0, 1, and 4 ECAP passes.</i>	<i>115</i>
Figure. 6. 7 <i>X-ray diffraction patterns of bimetallic rods with Ø5 steel core after 0, 1, and 4 ECAP passes</i>	<i>116</i>
Figure. 6. 8 <i>X-ray diffraction patterns of stand-alone AA6201 and bimetallic rods with three different geometries (Ø3, Ø4, and Ø5 steel core) after 0, 1, and 4 ECAP passes. Note the well annealed commercially pure Al was used as a reference material.</i>	<i>117</i>
Figure. 6. 10 <i>TEM-BF images of (a) the interface between AA6201 (left) and steel (right) from bimetallic rod with Ø3 steel core after one ECAP pass, (b) AA6201, (c) interface, and (d) steel with high magnification. Insets are enlarged views of the areas indicated by arrows.</i>	<i>120</i>
Figure. 6. 11 <i>TEM-BF images of the steel component at the interface with nanostructured grains and (b) the corresponding SADP shows the present of austenite - γ and martensite - α phases. SADP was taken using aperture diameter of 180nm</i>	<i>120</i>
Figure. 6. 12 <i>TEM-BF images of (a) the interface between Al(left)/steel(right) from bimetallic rod with steel core Ø3 after 4 ECAP passes, (b) Al, (c) interface and (d) steel with high magnification. Insets are enlarged view of the areas pointed by arrows</i>	<i>121</i>
Figure. 6. 13 <i>TEM-BF images of (a) the interface between AA6201 (left) and steel (right) from bimetallic rod with Ø5 steel core after four ECAP passes, (b) AA6201, (c) interface, and (d) steel with high magnification. A pair of dashed lines delineate a shear band (SB).</i>	<i>122</i>

List of Figures

Figure. 6. 14 TEM images of steel core Ø5 subjected to 4 ECAP passes with (a) BF image, (b) DF images and (c) the corresponding SADP using aperture diameter of 0.75 µm	123
Figure. 6. 15 TEM-BF images showing AA6201 grain(s) from (a) as-received Al alloy with needle-shaped β'' precipitates clearly visible on (001) plane, (b, c) stand-alone Al after one and four ECAP passes, (d, e) AA6201 component in bimetallic rod with Ø3 steel core after one and four ECAP passes, (f) AA6201 component in bimetallic rod with Ø5 steel core after four ECAP passes. Note that (a, b) were taken normally to <001> zone axis, whereas, due to the strong diffraction contrast, (c-f) were not taken on zone axis. The occurrence of strain contours in some of the images should be noted.	124
Figure. 7. 1 Schematic illustration of the processing chain of the first sub-project – using ECAP to fabricate metal-metal composites and intermetallic-metal composites from machining chips	129
Figure. 7. 2 The unique morphology and length scale of machining chips among other raw materials for fabricating multicomponent materials	130
Figure. 7. 3 Optical micrographs showing the evolution of multi-layered Cu/Nb with increasing number of ARB processes [390]	132
Figure. 7. 4 Schematic illustration of the processing chain of the second sub-project – using space holder enabled ECAP to fabricate a porous scaffold	132
Figure. 7. 5 Schematic illustration of the processing chain of the third sub-project – using ECAP to fabricate bimetallic rod with concentric jacket/core architecture	134

List of Tables

Table. 1.1 Materials selection, architecture and processing of three sub-projects	5
Table. 2.1 Possible classifications and variety of multicomponent materials.....	23
Table. 4. 1 Compositions and Processing conditions	55
Table. 4. 2 Mechanical properties of samples under various processing conditions.....	61
Table. 4. 3 Hardness, Young's modulus and width of the interdiffusion zone determined by nanoindentation	69
Table. 6. 1 Chemical compositions of stainless steel 316L and AA6201 in wt.%	109
Table. 6. 2 Compressive yield strength at 0.2% offset of AA6201 rod and bimetallic rods with three geometries after 0, 1, and 4 ECAP passes (in MPa)	112
Table. 6. 3 Electrical conductivity of AA6201 rod, steel rod and bimetallic rod with three geometries after 0, 1, and 4 ECAP passes (in IACS %)	113
Table. 6. 4 Microstructural characteristics of AA6201 rod and the AA6201 constituents of bimetallic rods after one and four ECAP passes	118

List of Symbols

Latin symbols

<i>Symbol</i>	Description
A	Initial cross-sectional area
b	Magnitude of the Burgers vector
B	Peak broadening
d	Average grain size or dislocation cell size
d_{hkl}	Lattice plane spacing
D	Diffusion coefficient
D_0	Pre-exponential factor for diffusion coefficient
E	Apparent Young's modulus
E^*	True Young's modulus of the tested specimen
f	Volume fraction
k_0	Coefficient in dislocation evolution equation
k_2	Coefficient in dislocation evolution equation
K^*	Compliance of the testing machine
K_{HP}	Constant of yielding
l	Height of the specimen
L	Length of dislocation cell structure
Q	Activation enthalpy for diffusion
R	Molar gas constant
T	Absolute temperature
x	Diffusion distance
Z	Zener-Hollomon parameter

Greek Symbols

<i>Symbol</i>	Description
ε	Equivalent strain

List of Symbols

$\dot{\epsilon}$	Strain rate
ϵ_p	Plastic strain
θ	Scattering angle
λ	Wavelength of incident beam
ρ	Density of dislocation
ρ_w	Density of dislocation in cell walls
ρ_c	Density of dislocation in cell interiors
σ	True stress
σ_0	Lattice friction stress
σ_y	Yield stress
ϕ	Cross-section intersecting angle
ψ	Curvature angle

Chapter 1 Introduction

1.1 Background and motivation	3
1.2 Objectives of research	4
1.3 Structure of the thesis	5

Chapter 1 Introduction

1.1 Background and motivation

The technical progress in the new applications and processing methods as well as the competition of metal manufacturers for markets in the aerospace, automotive, construction, sports equipment, life science and other industries set increasingly high targets for costs and mechanical and physical properties of materials. In many cases, the set of properties required (mechanical, thermal, electromagnetic and biocompatible) is practically impossible to be achieved with individual conventional materials. A new conceptual approach to address this problem was developed by Ashby and his group and published in several papers [3-6]. The most general of them, [5], introduces the concept of “hybrid materials” and the idea of “expanding material-properties space” by combination of materials, as shown in Fig. 1.1. The definition of “hybrid material” is given as follows: “combination of two or more materials in predetermined geometry and scale, optimally serving a specific engineering purpose”.

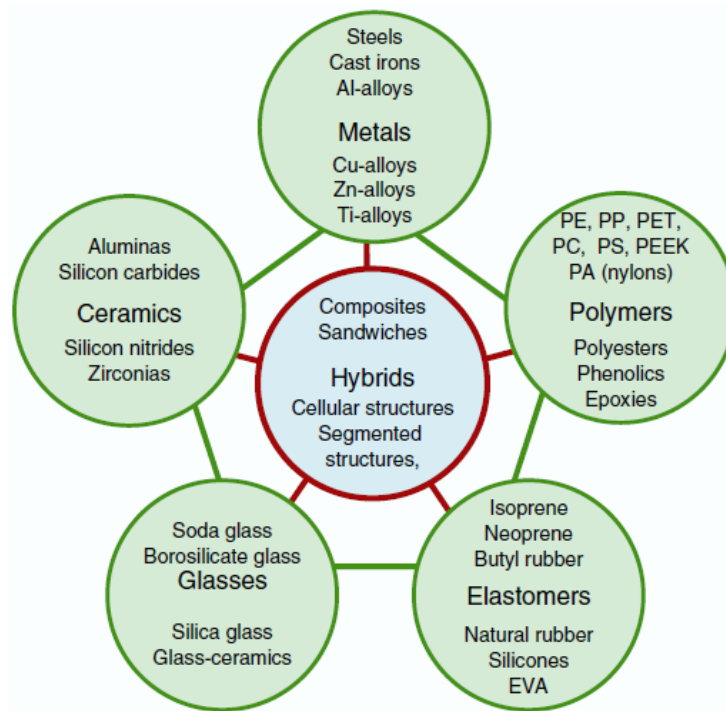


Figure. 1. 1 Concept of “hybrid materials” after Ashby [7]

From Fig. 1.1 it can be seen that the general order of the properties that the hybrid or composite materials will display hugely depends on the intrinsic properties of constituents. In another word, selection of constituents for the hybrid or composite materials with a set of required properties is based on the choice of each component having the best property in one of the categories from this set [6]. Apart from the materials selection, the “shape and scale”

Chapter 1 Introduction

factor was also indicated by Ashby and Brechet [5]. The “shape and scale” factor includes the shape and size of the individual constituents, their structural arrangement and distribution and the relative amount of each of them. In recent publication, this “shape and scale” factor was referred to the architecture of the combined constituents [6, 8, 9]. For targeted specific properties or applications, the optimized material selection and architecture can be obtained by means of simulation and modelling. However, developing a technique to combine the physically or chemically distinct phases and process such “heterogeneous architected materials” to obtain their desired performances is very challenging [8].

Severe plastic deformation (SPD) techniques as one of the most potent ways of producing ultrafine-grained and nano-grained bulk metallic materials have been under extensive investigation in the past three decades [10-13]. In recent years, a number of SPD techniques including equal-channel angular pressing (ECAP) [14], accumulative roll bonding (ARB) [15], high pressure torsion (HPT) [16], high-pressure tube twisting (HPTT) [17] and twist extrusion (TE) [18] etc. were applied in manufacturing of architected multicomponent materials. Though multiple pressing, rolling, rotation and extrusion etc. procedures, high strains is accumulated into and between each constituent. Consequently, solid state bonding by interdiffusion and interlocking and simultaneous microstructure refinement are expected [1, 2, 19, 20]. Despite the considerable progress that has been achieved in this area, there is still vast immense space worthy to be explored in terms of engineering opportunities and scientific problems, also a huge gap between the state of art and industry-scale application.

1.2 Objectives of research

In view of these opportunities and challenges, this PhD project will investigate three kinds of multicomponent materials for three corresponding areas of applications. The scientific hypothesis is that ECAP is an effective and special technique of designing and manufacturing multicomponent materials with optimization of macro-scaled architecture and refinement of microstructure in individual components. What all three sub-projects have in common is that they employ ECAP as the processing techniques. As shown in Table.1.1, beside the design of materials selection and architecture, ECAP processing parameters is another variable. On one hand, we intend to investigate the “shape and scale” effects of constituents on resulting properties. On the other hand, we want to study the effectiveness of ECAP for synthesising and architecturing multicomponent materials with broad application spectrum.

Chapter 1 Introduction

Table. 1.1 *Materials selection, architecture and processing of three sub-projects*

Materials selection	Architecture	Processing	Application
Al machining chips + Mg machining chips	Random mixture by dry mixing	ECAP at RT/300°C	Structural application
Ti powder + Mg powder + Silicon powder	Interactive mixture by wet mixing	ECAP at 400°C	Porous biomedical devices
Al jacket + Steel core	Concentric rod by shrink fit	ECAP at 175°C	Electrical transmission conductor

Specifically, in the first sub-project, multicomponent materials having tangled architecture will be made from machining chips which on one hand, are taken as waste and cheap raw materials, on the other hand can be regarded as unique raw materials having helical shape and fine microstructure. This study could provide a potent approach to solve this environmental concern by reusing the wastes for superior structural application. The establishment of bonding and interdiffusion between dissimilar chips will be studied. In the second sub-project, porous materials having bone-like cancellous architecture for biomedical implants as a high-end product will be investigated. The redistribution and shape evolution of constituents during ECAP processing and the breakage and displacement of oxide layers are studied in depth. In the third sub-project, multicomponent materials with concentric jacket/core architecture are studied for application of electrical transmission line. Severe plastic co-deformation mechanism in this process will be investigated. It can be seen that this project will potentially contribute to both multicomponent materials area and SPD area.

1.3 Structure of the thesis

The body of this thesis begins with a review of current development of multicomponent materials and the use of SPD on this application. Details of the processing method, mechanical measurements and microstructure characterisation techniques are provided in Chapter 3. My original contribution starts from Chapter 4, where ECAP compaction was investigated to manufacture multicomponent materials from Al and Mg machining chips. In Chapter 5, the application is extended to biomedical implant materials. Space holder-enabled ECAP was used to synthesise ultrafine-grained porous Ti/Mg composite and porous Ti. In

Chapter 1 Introduction

Chapter 6, ECAP is employed to manufacture bimetallic rod with Al alloy jacket layer and steel core for conductor application. Conclusions and recommendations for the future work are presented in the final chapter of the thesis, Chapter 7.

Chapter 2 Literature Review

2.1 Outline of the chapter	9
2.2 Metallic hybrid.....	9
2.2.1 Solid-state bonding.....	10
2.2.2 Solid-state interdiffusion	15
2.3 Metal based composites.....	17
2.3.1Metal matrix composite.....	17
2.3.2Metallic composite	20
2.4 Multicomponent material	21
2.5 New trends of advanced multicomponent materials.....	24
2.6.1 Nanostructured multicomponent materials	24
2.6.2 Architected multicomponent materials.....	25
2.6 Severe plastic deformation techniques used on multicomponent materials	26
2.6.1 Equal-channel angular pressing	29
2.6.2 High pressure torsion	31
2.6.3 Accumulative roll bonding.....	32
2.7 Summary of literature review	33

Chapter 2 Literature Review

2.1 Outline of the chapter

Multicomponent material is a broad concept which is on the contrary to monolithic material. Strictly speaking, in metal based multicomponent materials, there should be regions having localised elemental concentrations that are highly non-equilibrium and not achievable in the molten state. These foreign and highly non-equilibrium phases can be termed as another component or constituent and distinguish multicomponent materials from alloys having in-situ precipitates as a foreign phase. There is vast number of literatures regarding to this research area. Some of them call this non-monolithic materials as hybrid materials whereas use the term – composite materials. In Oxford Dictionary, hybrid as an adjective is defined as “*Anything derived from heterogeneous sources, or composed of different or incongruous elements*”. Composite as an adjective is defined as “*Made up of various parts or elements; compound; not simple in structure*”, which are quite similar to the definition of hybrid.

In this section, the difference between these two concepts is analysed in the aspects of microstructural and spatial configurations, applications and synthesis methods. Followed by this, the criteria to fabricate desired multicomponent materials are summarized and analysed. The emphasis is placed on the processing techniques, as it plays the most critical role in determining whether the idea can be successfully implemented and realized. Following the concise summary of traditional processing methods and their corresponding applications, developing trend of multicomponent materials in academic society will be presented. It will be found that the implementing of innovative designs is based on novel processing methods. Then severe plastic deformation (SPD) techniques will be introduced, as they are novel methods that have been extensively investigated to explore their possibilities for the application of multicomponent material in recent five years. Equal channel angular pressing (ECAP), as the most highly developed SPD processing technique is emphatically studied since it is the method investigated through this PhD project.

2.2 Metallic hybrid materials

Metallic hybrid materials as one class of engineering material have been implemented in a number of applications. One component can be jointed to another component to form a layered arrangement such as a cladding layer with a substrate layer or a jacket out layer with a core material. For example, one of the most widely used combinations includes a thin layer

Chapter 2 Literature Review

of expensive and corrosion resistant alloy which provides excellent corrosion protection while a much less costly substrate material, which is usually high-strength carbon steel, ensures adequate structural strength. They are extensively used in various fields of applications such as refinery, petrochemical and chemical industry, oil and gas production, power plants and flue gas desulphurisation plants as well as cooking utensils [21-26]. Besides the combination of high corrosion resistance and mechanical strength, applications with more combinations of functionalities can be obtained by replacing the high strength solid substrate metal with light weight metallic foam core in a sandwich panel architecture [27]. By cladding thick and strong face layers on a foam core using adhesives, high specific strength and stiffness sandwich panels can be fabricated to withstand high-impact loads without skin failure [28-30]. Alternatively, panels can also be produced using thin and soft cladding face layers for the applications such as noise and vibration reduction [27, 31-33]. Furthermore, the concentric jacket/core architecture can be found in the bimetallic concentric wires such as aluminium clad steel core wire, which is employed in transmission line. In this product, the Al jacket improves the corrosion resistance of the steel core and increases the electrical conductivity of it. Overall, comparing with monolithic steel wire, the durability and electrical conductivity of this hybrid wire is better. Equally important, compared with single-phase Al alloy, this hybrid material provides a more cost-effective approach to solve engineering problems.

2.2.1 Solid-state bonding

When it comes to joining of hybrid materials, conventional fusion welding methods, such as arc and laser welding for which both materials melt are not suitable. This is because the melting temperatures for each constituents are different and at high temperature intermetallic reaction layers could form and result in poor mechanical properties [34, 35]. Besides, due to the severe mismatch of coefficients of thermal expansion, thermal distortion, residual stress and thermal shock could occur and damage the interface [36]. Instead, solid-state bonding operating at relatively low temperature is more applicable and suitable for this application. Several solid-state bonding techniques including explosive bonding, roll bonding, diffusion bonding, stir friction joining and ultrasonic bonding have been invented and started to generate interests from various industries.

Explosive bonding, also referred to explosive welding is one of the most widely used techniques in industry [22, 23]. As the process shown in Fig. 2.1, explosive is used to

Chapter 2 Literature Review

generate a massive load and a high velocity jet by detonation, which removes away the impurities on the metal surfaces and results in a metallurgical bonding at the interface of metals [37, 38]. Bimetallic plates and tubes such as Al/steel [39], Cu/steel [40], Ti/steel [41], Al/Cu [42], Mg/Al [43], Cu/Ti [44] and Ti/Ni [45] have been successfully bonded using this method. The interface between two phases is characterised with wave morphology. In some cases intermetallic and amorphous phases are formed at the crests or within the vortex of the waves [46-48]. Even it has been applied in manufacturing of cladding of large areas of planar metal or alloy laminates, more complex architecture such as multi-layered and cylindrical configurations have been studied in recent years [47, 49-51].

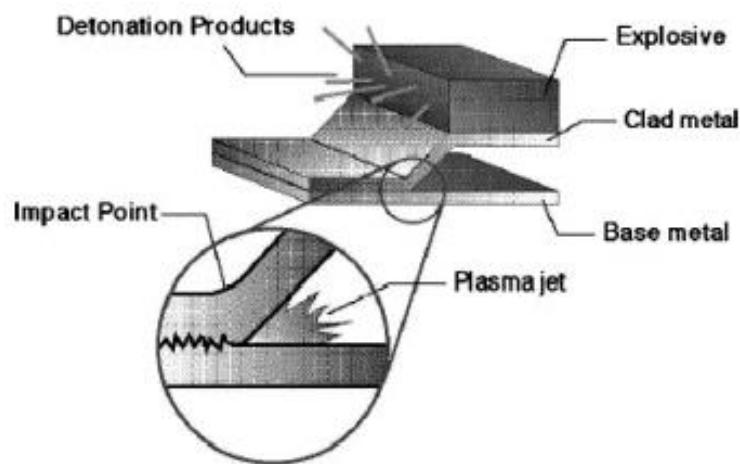


Figure. 2. 1 Schematic illustration of explosive bonding [52]

Roll bonding is another commercially available way for fabrication of large layered bimetallic sheets and foils. The processing is illustrated in Fig. 2.2. Surface preparation such as scratch brushing is critical since high strength bonding can only be formed if there is an intimate contact between metals, which allows an interatomic attractive force to operate [25, 53]. It is believed that the mechanical bonding between mating surfaces is first developed during rolling before the metallurgical bonding in the following processing or heat treatment [25]. Increasing thickness reduction above the strain threshold and pre-heat treatment temperature facilitates surface cracks, extrusion of virgin metals and good bonding [53, 54]. Due to the facile processing procedure, a wide range of bimetallics have been fabricated using this method, such as Al/steel [54], Ti/steel [55], Al/Ti [56], Al/Zn [57], Al/Mg [58] and Al/Cu [59].

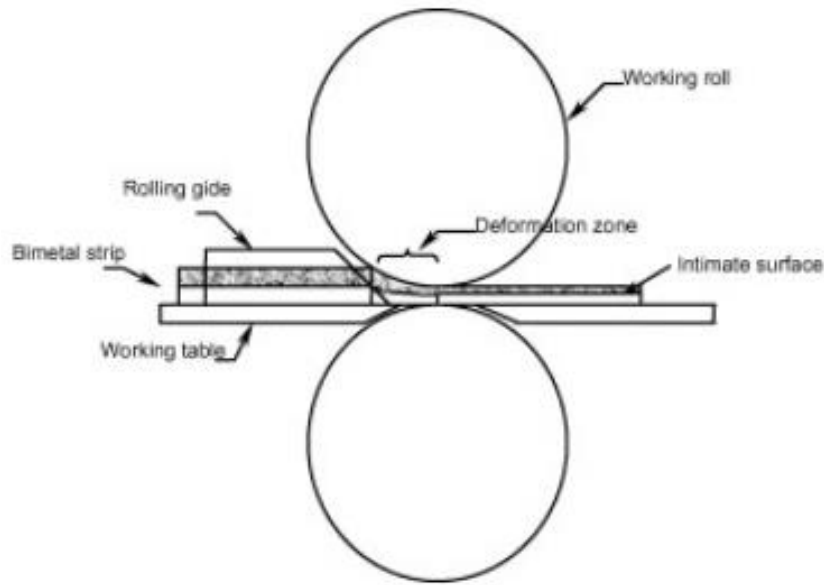


Figure. 2. 2 Schematic illustration of bimetal rolling process [60]

Diffusion bonding is another solid-state bonding technique that allows dissimilar contacting surfaces to be joined under low pressure and at elevated temperature [61]. The typical processing setup is shown in Fig. 2.3. Because there is generally limited macroscopic deformation or relative motion involved, this technique can be implemented on joining complex structures [62]. However, due to this inadequate deformation, high temperature is needed to enhance diffusivity of both elements and oxygen atoms in the oxide layer thus achieving sufficient bonding at interfaces [63]. Consequently, it attributes to formation of intermetallic phases, residual stress and creation of micro-voids and micro-crack in the interface, which have detrimental effects on the bonding performance [64]. Therefore, an intermediate material such as nickel and silver that possesses substantial solid solubility in diffusion couple is usually used as an interlayer and diffusion barrier to tackle these problems [65]. This technique has been used on a wide spectrum of diffusion couples such as Ti/steel [66, 67], Al/Mg [68], Cu/steel [64], Cu/Al [61], Mo/Cu [65] and W/Ta [69].

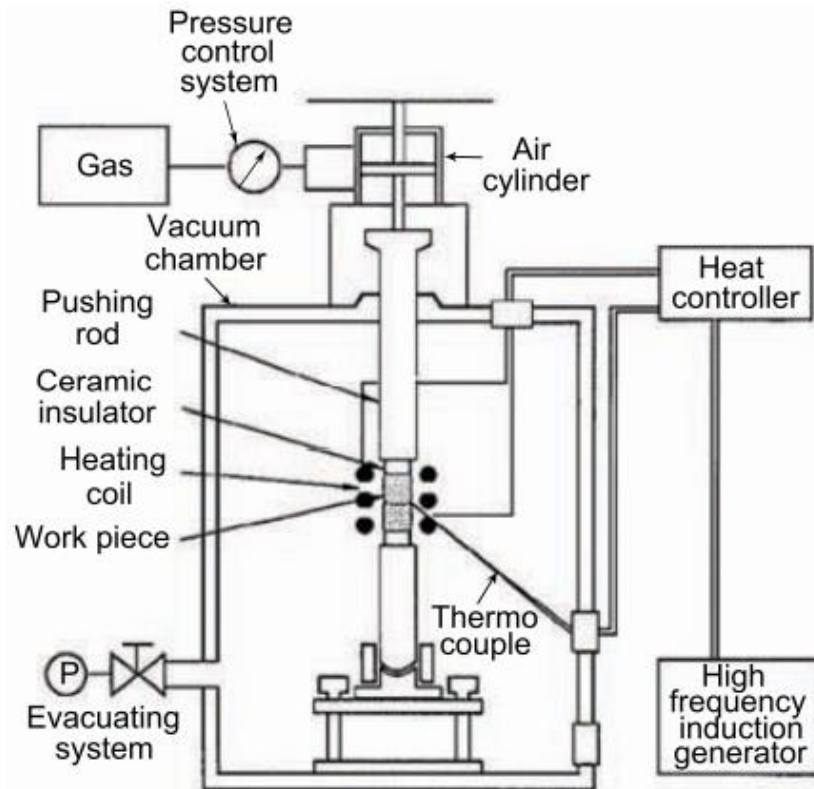


Figure. 2. 3 Schematic illustration of diffusion bonding set-up [70]

Stir friction bonding is one processing method that has been under extensively laboratory research in recent years. This technique shows its ability to joint two dissimilar sheet metals by butt, lap and fillet joints [71, 72]. As it is illustrated in Fig. 2.4, during friction stir processing, the rotating tool induces the mass transfer phenomena between the base metals by the mechanical stirring action [73]. The bonding is caused by a combination of cold pressure welding, diffusion bonding and mechanical alloying at the same time [74]. This technique has been investigated in a number of combinations of materials such as steel/Mg [75], Al/Mg [76, 77], steel/Al [78, 79], Ti/Al [71, 80], steel/Ti [81] and Al/Cu [82, 83].



Figure. 2. 4 Schematic illustration of stir friction joining between Al alloy and high strength steel [84]

Chapter 2 Literature Review

Ultrasonic bonding also refers to ultrasonic welding is a joining process where high frequency vibrations are produced and converted into energy. This energy is applied on work pieces that are held together under pressure, as it is shown in Fig. 2.5 [85]. Deformation and oxide layer breakage at the interface are caused by the combination of static normal clamping force and a high-frequency oscillating shear force [86]. As a result, fresh metal surfaces come in contact with each other and create metallurgical bonding as well as interdiffusion across the interface [87]. A number of dissimilar metals have been investigated using this technique including Al/Cu [88, 89], Al/steel [90], Al/Ti [91] and Al/Mg [92].

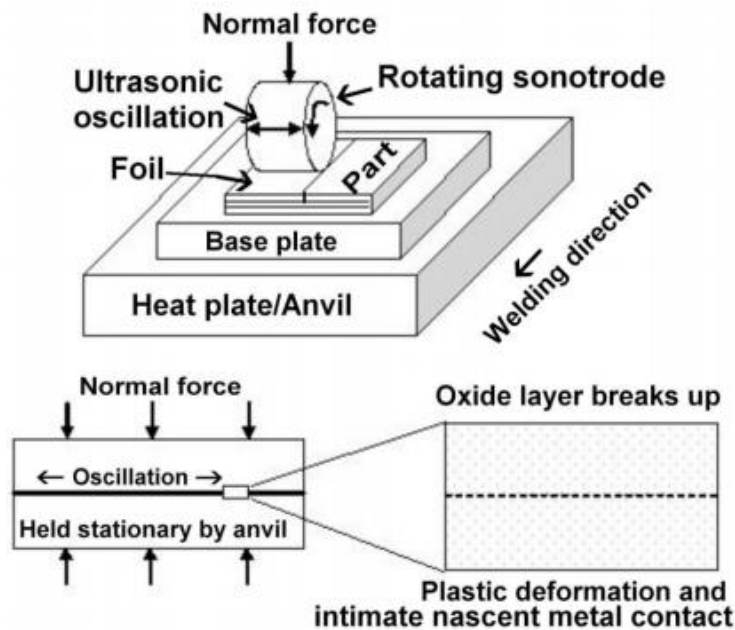


Figure. 2. 5 Schematic illustration of ultrasonic bonding between two foils [93]

As it can be summarised from above mentioned five techniques, pressure and heat are employed in common. At the heterophase interface, element intermixing is governed by interdiffusion and it can only occur when two mating surfaces are in interatomic distance and at elevated temperature. High pressure and plastic deformation on substrate materials benefits this process because it helps disrupt the oxide layers, expose fresh metal surfaces and brings them to atomic distance. In the case of explosion and stir friction bonding which are conducted at ambient temperature, the amount of deformation localized at interfaces is so large that extra heat treatment is not employed. The heat generated at the interfaces during the process is sufficient to cause coalescence and metallurgical bonding between mating surfaces [36]. In contrast, regarding to diffusion and ultrasonic bonding, due to relatively low pressure, heat is essential to trigger the diffusion. Roll bonding involves moderate bulk deformation (in

Chapter 2 Literature Review

contrast to deformation localized at interface regions), which can cause the generation of virgin metal surface contact, but not high enough for the generation of heat and atom intermixing at heterophase interfaces. Thus, processing at warm temperature, post-deformation heat treatment after cold working or even electrical assistance is used in roll bonding [94, 95].

2.2.2 Solid-state interdiffusion

As it was stated by R. Messler, “The key to all welding is atomic-level interdiffusion between the materials being jointed, whether that diffusion occurs in liquid, solid or mixed state. Nothing contributes to jointing better than actual interchanges of atoms, ions or molecules.” [96]. To quantify the extent of interchanges of atoms, the concept of penetration depth or also referred as diffusion distance x is employed here. Its value can be measured from the counts per second vs. relative distance curve from energy-dispersive X-ray line scan. x is defined as the distance between the position of the diffusion front and the Matano plane at time t . The diffusion front is defined by the position of a constant concentration $c(x, t)=k_R$. By fixing k_R a finite value, x can be found [97]. Here we arbitrarily set k_R with a magnitude of 1%. In this condition, we obtain

$$x = \sqrt{Dt} \quad (2.1)$$

where t is the processing time and D is the diffusion coefficient which usually follows an Arrhenius type of temperature dependence:

$$D = D_0 \cdot \exp(-Q/RT) \quad (2.2)$$

where Q is the activation enthalpy for diffusion (J/mol), often referred to as the activation energy, D_0 is the pre-exponential factor and R is the molar gas constant (8.314J/mol•K). The activation energy Q is influenced by the elementary process of atomic motion which generally depends on the foreign substitutional element and the crystal structure and microstructural features of solvent material.

After rearranging equations (2.1) and (2.2) one has

$$\ln x = \ln \sqrt{D_0 t} - \left(\frac{Q}{2R} \right) \frac{1}{T} \quad (2.3)$$

Chapter 2 Literature Review

It can be found that the penetration depth is determined by the activation energy for diffusion and processing temperature. With lower activation energy, higher temperature and longer time, boarder penetration depth is expected. However, to avoid the detrimental effects from elevated processing temperature and expanded time such as coarse microstructures and brittle phase formation, reduction of activation enthalpy for diffusion by microstructure modification is a much more preferred route for achieving high level of interchanges of atoms.

There are several solid-state diffusion paths in polycrystalline metals. Lattice diffusion is the basic diffusion mechanism which has largest activation enthalpy [98]. Since the vacancy mechanism is the dominant mechanism in lattice diffusion, it is believed that high concentration of atomic defects such as vacancies can aid diffusion [98]. Besides, there are high-diffusivity paths such as free surfaces, grain boundaries and dislocations where the jump rates of atoms are much higher than in the lattice (see Fig. 2.6) [98]. For example, grain boundary diffusion is typically four to six orders of magnitude higher than lattice diffusion. Moreover, dislocations also provide more rapid atomic migration path than the regular lattice [98]. It is worth noting here that, the surface diffusion is conducted on oxide free, new, clean and virgin metal surface which is covered by electric cloud due to the broken metallic bonding between the surface atoms and oxide layer. At this statue, the free surface has very high energy and provides fastest diffusion path. Similarly, in the interior of the metal, defects containing distorted or broken metallic bonds will have high energy and promote diffusion and segregation of foreign atoms [98, 99].

Therefore, fast diffusion and board diffusion distance shall be achieved at relatively low temperature within metals containing high concentration of point defects, high volume fraction of grain boundaries and high density of dislocations, which are typical microstructural features produced after heavily cold or warm plastic deformation. Furthermore, recent studies show that further enhancement of diffusion coefficient could be achieved after extreme deformation, wherein long-rang network of interconnected nano- and micropores located predominantly at non-equilibrium grain boundaries and triple junctions act as ultra-fast diffusion paths [100, 101].

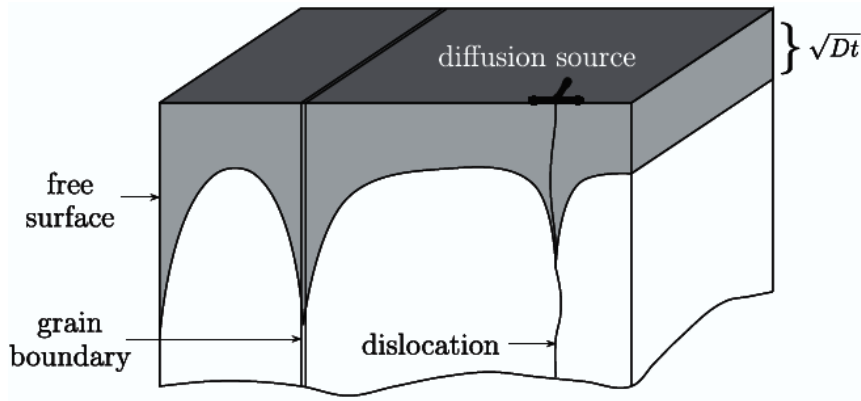


Figure. 2. 6 Schematic illustration of high-diffusivity paths in a solid [98]

2.3 Metal based composites

From both chemical and microstructural perspectives, metal based composite materials can be classified as metal matrix composite having ceramic reinforcement phase and metallic composite or metal-metal composite that contain several metallic phases.

2.3.1 Metal matrix composite

The development of metal matrix composites (MMCs) was initially driven by the high-performance needs of the aerospace industry. Continuous boron fibres having 60 vol.% reinforced aluminium alloy used in the space shuttle orbiter was the first successful MMC product [102]. With more attention drawn in this class of material, the application of MMCs is expanded to the areas of automotive and ground transportation industries and sport equipment industries, where discontinuous reinforcement are used as their manufacture cost is lower than continuous reinforcements [103]. The metal matrix phase is strengthened using ceramic or metal oxide in the form of fibres, whiskers or particles. The influences of different combination of matrix alloy and type, size, shape and volume fraction of reinforcement on properties such as wear behaviour and fatigue performance have been extensively investigated.

The matrix selection largely determines the application. Aluminium based composites have been used in automotive and aerospace applications [102, 104]. The good combination of high specific strength, specific stiffness and wear resistance make them very competitive candidature for brake rotors, brake drums and fins on aircraft comparing with alloys [102, 104]. For example, ventral fins made using Al alloy 6092 having 17.5 vol.% of SiC particles

Chapter 2 Literature Review

has been used on F-16 to replace the Al alloy 2024-T4 made fin. Due to the higher specific stiffness of the composite than its counterpart, the tip deflections is reduced and fatigue problem is alleviated [102]. In ground vehicles, magnesium matrix composites have been applied in high-end cars for its higher specific strength than monolithic Mg alloys [105]. Moreover, laboratory studies have showed that titanium matrix composite has the potential to replace heavier nickel-based superalloys in high-pressure turbine blades and compressor discs for jet engines [102]. Overall, MMCs have been used on high-end products due to its high cost and high performances.

The material selection of reinforcement phase is also important. There are a range of high hardness and elastic modulus particles can be chosen, for instance, silicon carbide (SiC), alumina (Al_2O_3) and boron carbide (B_4C) etc. [102]. However, recent studies show that these ceramic particles can actually increase the wear rate of the mating counterface, due to their abrasive action and reduction of the overall wear resistance of the tribo-system. To tackle this problem, nickel aluminides can be used which can provide high wear resistance while reduce counterface wear rate [106, 107]. Regarding to the shape factor, it has been found that the greatest improvement in longitudinal stiffness and strength is achieved using continuous fibres, followed by whiskers and then particles [102]. Moreover, it has been demonstrated that better dispersion and smaller size of the particles in metal matrix can enhance the mechanical properties [108]. The optimum volume fraction of the reinforcement particles is also critical for the performance. For example, higher volume fraction of reinforcement phase can increase the stiffness of the composite but at the same time deteriorate the damage-tolerance and processability [109]. It is also worth noting that in MMCs interface plays a critical role. The properties of the interface are influenced by those of both constituents as well as by their chemical affinity, atom diffusivity and change of the crystal lattice in the composite [110]. Chemical interactions and reactions between constituents determine the interface adhesion, modify the characteristics of the interface and affect the mechanical characteristics significantly [110]. For example, the SiC fibres in Ti matrix used today have an amorphous C coating on them to minimise the extent of fibre/matrix interaction that forms TiC. This will provide compliance during thermal cycling to minimize interface damage [111].

The principle way of preparing metal matrix composite is via liquid and powder metallurgy [1, 110]. Liquid metallurgy is the most cost effective way among them and can be produced in a wide variety of shapes using methods already developed in the casting industry [110].

Chapter 2 Literature Review

However, uniform distribution of the reinforcement phase is difficult and it is limited to metals with relatively low melting points such as Al and Mg [110]. To tackle this problem, *ultrasonic solidification* (seen in Fig. 2.7) has been investigated by several groups [112-114]. High-intensity ultrasonic waves provides transient cavitation and acoustic streaming in the liquid which is believed to lead to refining microstructures, degassing of liquid and homogenizing the distribution of reinforcement particles [112].

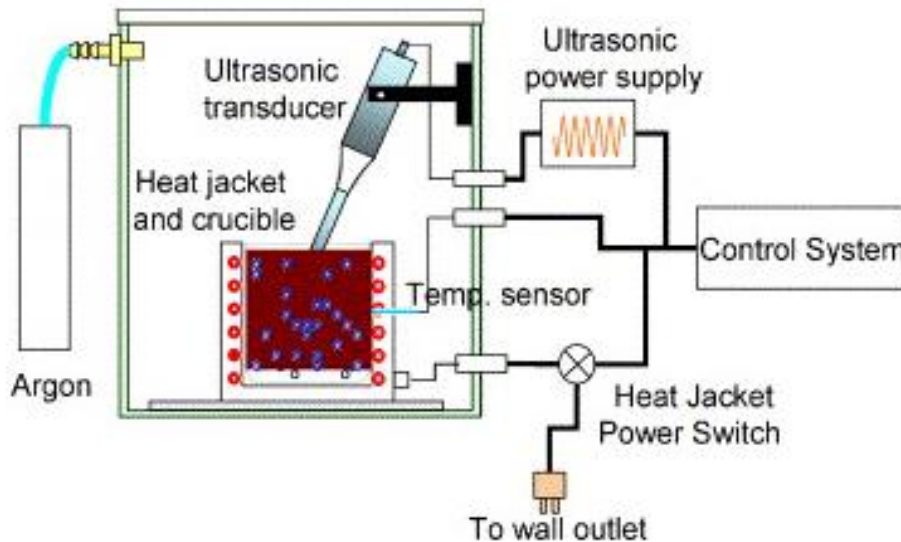


Figure. 2. 7 Schematic illustration of ultrasonic solidification processing [112]

In recent years, more research is focused on solid-state produced MMCs for high-end products which generally have higher mechanical performance than liquid-state process. This is primarily due to the minimization of segregation effects and brittle reaction between matrix and reinforcements at melting temperature [110, 115]. The typical solid-state route is shown in Fig. 2.8. It starts from elemental blends of matrix and reinforcement powders, in which wet mixing and dry mixing can be chosen. Then the mixture goes through consolidation by cold isostatic pressing to form a green compact. Followed by that, a degassing procedure may be used before the hot pressing or sintering to create inter-particle bonding and elimination of porosities in the compact. For this process, *spark plasma sintering* has been investigated as a novel way comparing with conventional hot pressing. In spark plasma sintering processing, the heat is generated by a pulsed DC current, which leads to very high heating and cooling rate thus a very short time sintering [116, 117]. This short processing time allows limited grain growth and reaction at interfaces [118].

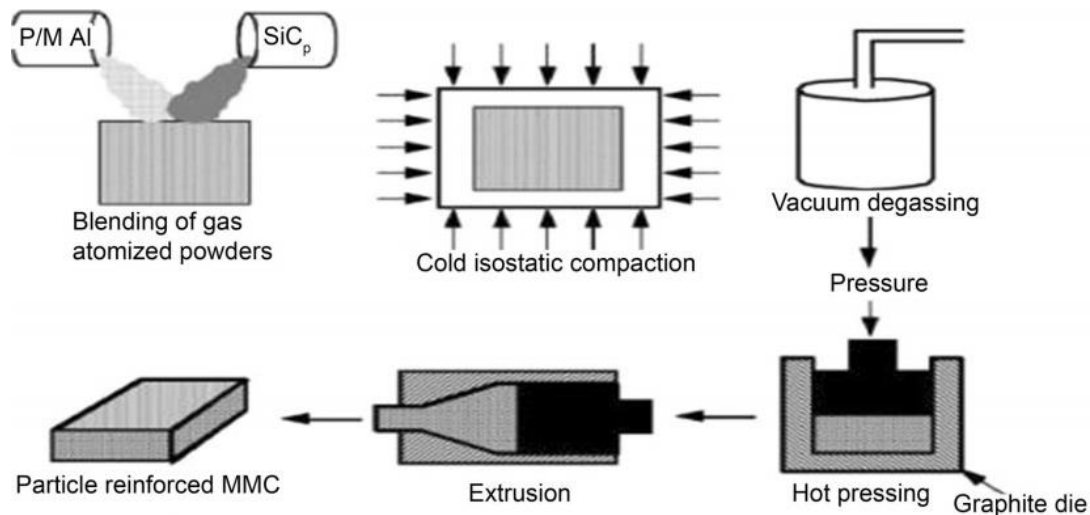


Figure. 2. 8 Schematic illustration of typical powder metallurgy processing scheme [119]

In both liquid and powder metallurgy routes, it can be found in literatures that the secondary processing of the MMCs such as rolling, extrusion and forging is necessary. The induced deformation can further break up agglomeration of reinforcement particles, remove or eliminate cavitation and porosity, trigger dynamic recrystallization and grain refinement of matrix and improve the interface bonding between constituents [119-123].

2.3.2 Metallic composites

In contrast to MMCs having non-deformable reinforcement phases, metallic composite comprise two or more base metals which are all deformable. Under externally imposed strain, the shape reduction and arrangement redistribution of all constituents could occur, although less deformation is expected from the relatively hard phase. This class of composite become of interest when the spacing between phases is reduced within a few microns or even nano-scale via deformation processing and strengthening exceeds the prediction of the rule of mixture [124-128]. This is because the interphase distance and the phase thickness determine the mean free path of the lattice dislocation. At nanoscale interface spacing, dislocation-dislocation interactions and Hall-Petch effect become subsidiary. Instead, interaction between interface and dislocation become dominant [1]. In this case, strengthening is caused by less dislocation activation sources, impediment of dislocation motion and multiplication and Orowan expansion of dislocations [1, 129, 130].

Nanofilament and nanomultilayer metallic composites are two main architectures that have been investigated in this area. Nanofilament Cu/Ag and Cu/Nb composites are usually

Chapter 2 Literature Review

fabricated by accumulative drawing and bundling after extreme total strain that is typically higher than 20 [131-134]. These materials show good combination of high strength and high electrical conductivity, which make them very promising candidatures for advanced electrical applications [135, 136]. Nanomultilayer composites are generally synthesised by accumulative roll bonding from either foils of individual metals or eutectic alloys and by physical vapor deposition [110, 124, 125, 137-139]. They are featured by high shock resistance, thermal stability and radiation resistance [139, 140].

Furthermore, multiphase alloys such as dual phase steels and intermetallic-metal-matrix composite can also be regarded as metallic composite [1, 2]. This is not only due to the coexistence of two distinct phases such as ferrite/martensite [141] and $\text{Al}_3\text{Ni}_2/\text{Ni}$ [142], but also the shape and volume fraction effect and scale effect of them on the overall mechanical properties [141, 143].

2.4 Multicomponent materials

As it can be seen from above two sections, metallic hybrid materials are featured of their variable architectures such as bimetallic plates, tubes and rods and low volume fraction of interfaces. To further conclude them, from a microstructural perspective, they all have one or two layers in the shape of either plate or tube to clad a substrate or core material. By bonding a cladding layer, various functionalities such as corrosion resistance, electrical conductivity and thermal conductivity can be added to the substrate material. The base materials usually provide the mechanical strength. The microstructures in each constituent and interface bonding properties influence the performance of the hybrid. Strong chemical bonding caused by interdiffusion is essential.

The generally accepted metal based composite material including metal matrix composite and metallic composite materials is featured by the configuration of reinforcement phase embedded in matrix phase and high interface density. The size, shape, volume fraction and distribution of reinforcement phases can significantly affect the integral properties. The functionality of the secondary phases is to enhance one specific aspect of the matrix phase, such as wear resistance, shock resistance and radiation resistance. Heterophase interfaces play a very important role in composites due to their high volume fraction and interaction with defects.

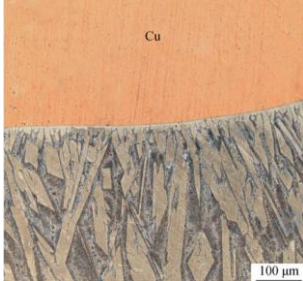
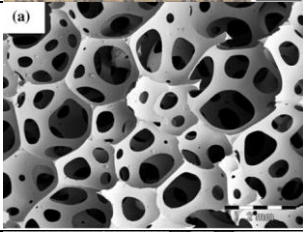
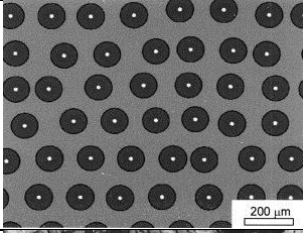
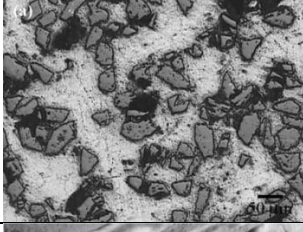
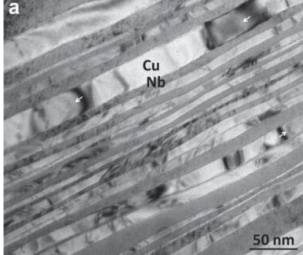
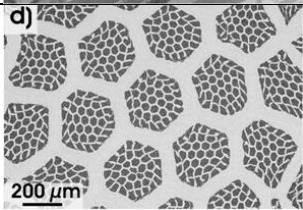
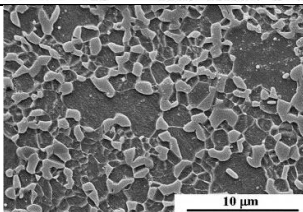
Chapter 2 Literature Review

It is also worth noting here that, metal foams and porous or cellular metals are another special category of hybrid material. Metal foams are characterised by the closed porosity which is created by decomposition of a blowing agent, precipitation of dissolved gas or injection of external gas source in a molten metal [144, 145]. They have a broad range of structural and load-bearing applications due to the high specific stiffness, crush energy absorption capacity, vibration damping and noise reduction properties [30, 145, 146]. In contrast, cellular metals with open porosity are usually fabricated by solid state processing, where the formation of closed pores caused by liquid state surface tension is eliminated [147]. Open porosity hybrid has been extensively investigated for the application in biomedical implants [148-150], which will be described in details in Chapter 5.

A possible classification and variety of multicomponent materials is shown in Table. 2.1. From aspect of “processing-microstructure-properties” relation, the processing methods, typical microstructure and arrangement between constituents and applications of composite and hybrid materials are different. In this study, metallic composite, discontinuous metal matrix composite, porous hybrid and metallic hybrid will be investigated. The term – “multicomponent materials” is used here to cover this broad range of composite and hybrid materials.

Chapter 2 Literature Review

Table. 2.1 Possible classifications and variety of multicomponent materials

Multicomponent materials	Architecture	Typical microstructure	Refs
Metallic hybrids	Layered hybrid (Al/Cu)		[151]
	Porous hybrid (porous Al)		[152]
	Continuous reinforced metal matrix composite (Ti64/SiC monofilaments)		[153]
Metal based composite	Discontinuous reinforced metal matrix composite (Al/SiC)		[154]
	Nanomultilayer metallic composite (Cu/Nb)		[140]
	Nanofilament metallic composite (Al/Ti)		[155]
	Multiphase alloy (Ferrite/Martensite)		[141]

2.5 New trends in advanced multicomponent materials

As stated above, multicomponent materials are very attractive to existing applications as they provide a cost-effective way for tackling engineering problems. Also, they are very promising for emerging markets for high-end products. The imagination of material scientists and engineers is boundless and attempts to develop advanced multicomponent materials for better performances continue. Driven by the enormous engineering opportunities, effort has been consistently put into the optimization of the existing forming routes to reduce the cost and improve the degree of control. On top of that, in recent five years, a more exciting research direction has been developed by implementing novel metal working methods in this area, which are fabrication of advanced nanostructured and architected multicomponent materials. As this principle presented in Fig. 2.9, concurrent optimization of microstructure and architecture in the multicomponent materials is essential to achieve the multifunctional requirements.

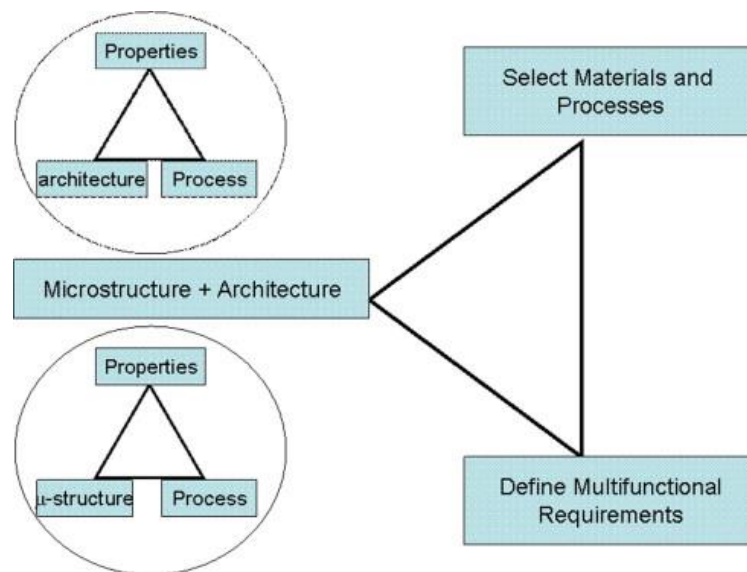


Figure. 2. 9 Designing of architecture and microstructure in multicomponent materials [9]

2.6.1 Nanostructured multicomponent materials

The microstructure in the constituents should be refined to ultrafine or even nanoscale. It has been proved numerously since this century that, in polycrystalline metals, superior properties can be achieved from ultrafine-grained or nano-grained microstructure as well as from the high volume fraction of high angle grain boundaries [11-13, 156-158]. The multicomponent materials manufactured using traditional techniques are characterised of coarse-grained

Chapter 2 Literature Review

microstructure and do not enjoy the merits provided by reduced grain sizes. Recently, efforts have been put into nanostructuring the constituents on top of sound interface bonding in multicomponent materials [1, 2]. It has been found that implementing ultrafine-grained and nano-grained microstructure into each constituent can dramatically improve the combined properties beyond role of mixture [1, 2]. Nanostructuring in multicomponent materials is not limited to traditional concept of grain refinement; it also means refinement of interphase spacing or increase of heterophase interface density. In the case of a metallic composite, under extreme plastic strains, distance between two heterophase interfaces can be reduced to tens of nanometres, which offers attractive functional features for trapping point defects and rare gas atoms under irradiation [159, 160].

2.6.2 Architected multicomponent materials

In addition to the microstructural refinement, smart design of the inner architecture of multicomponent materials is another hot topic [8]. Learning from natural materials which are structured at multiple length-scale [161], architecturing of multicomponent materials should also vary from microstructure within atomic scale to structure at a centimetre scale [8]. The microscopic scale architecture here refers to interface engineering [140]. At this length scale, the architecturing means evolution of interface type [162, 163]. Bulk nanolayered Cu/Nb composite fabricated by accumulative roll bonding contains a narrow distribution of special interface type, which are atomically faceted and differ from the atomically flat interface synthesized by physical vapour deposition [164]. These architected inner interfaces by rolling at extreme plastic strain contributes to better radiation resistance, mechanical strength and thermal stability than its counterpart due to different habit plane orientations [134, 140, 165]. Furthermore, architecturing of inner structure at larger scale is another promising research route. For example, recent study shows that an inclined straight Al fibre embedded in a Cu solid can transfer to spiral shaped fibre after twist extrusion [18, 166]. By architecturing the shape of reinforcement phase, the effective strain hardening of the material is improved [167].

To conclude this section, it can be found that, besides strong bonding at interfaces, the requirements for advanced multicomponent materials include smart and multiple-scale architecture with ultrafine or nanoscale microstructure. This can only be achieved by deforming the heterogeneous architected material to extreme plastic strains using novel metal forming methods, which are severe plastic deformation techniques [1, 2, 19, 20].

2.6 Severe plastic deformation techniques used on multicomponent materials

Severe plastic deformation (SPD) is a range of metalworking techniques which is currently defined as “any method of metal forming under an extensive hydrostatic pressure that may be used to impose a very high strain on a bulk solid without the introduction of any significant change in the overall dimensions of the sample and having the ability to produce exceptional grain refinement” [11]. The microstructure achieved after SPD processing is characterised of ultrafine-grained (UFG) with the size of 100–1000 nm or even nano-grained (NG) with the size less than 100 nm. This grain refinement can influence nearly all aspects of the physical and mechanical behaviour of polycrystalline metals [12]. For example, in polycrystalline materials, average grain size reduction leads to increase in yield stress, which can be mathematically presented by the well-known Hall-Petch equation given by [168, 169]

$$\sigma_y = \sigma_0 + K_{HP}/\sqrt{d} \quad (2.4)$$

where σ_y is the yield stress, σ_0 is the lattice friction stress, K_{HP} is the constant of yielding and d is the average grain size. However, it is worth nothing here that this relation is not valid when grain sizes are less than ~100nm due to the change of dominant deformation mechanism from dislocation-grain boundary interactions such as nucleation, pass-through, absorption and emission [170] to partial dislocation emission from grain boundaries, deformation twinning, perfect dislocation slip, grain boundary sliding and grain rotation [171-173].

Despite the striking properties achieved from grain refinement, the underlying mechanism of this continuous dynamic recrystallization process is still not fully understood. The most widely accepted theory (schematically shown in Fig. 2.10) is based on the notion of dislocation cell structure which forms with imposed plastic strain and transforms to fine grain structure with simultaneous increase of misorientation between neighboring cell structures [12]. In this mode, the total dislocation density ρ is the only internal variable to describe the deformation [174].

$$d\rho/d\varepsilon_p = k_0/bL - k_2\rho \quad (2.5)$$

Chapter 2 Literature Review

where b is the magnitude of the Burgers vector, L is the length of cell structure that determines the dislocation mean free path, k_0 is a constant and k_2 is a mechanism-dependent phenomenological parameter sensitive to strain rate and temperature. Further assumption is made that the average size of dislocation cells d scales inversely with the square root of dislocation density ρ [175, 176].

$$d = K/\sqrt{\rho} \quad (2.6)$$

where K is a proportionality constant. As shown in Fig. 2.10, at low strain, high density of dislocation cells occupy the coarse grain and dislocations are located in both cell walls (ρ_w) and cell interiors as (ρ_c). If the volume fraction of ρ_w is represented by f , the total dislocation density is given [12],

$$\rho = f\rho_w + (1 - f)\rho_c \quad (2.7)$$

With increasing amount of strain, “geometrically unnecessary” dislocations which do not contribute to misorientation between neighbouring cells will recover with strain and resulting in thinning of cell walls, as shown in the middle graph in Fig. 2.10 [12]. Continuously imposing strain leads to gradual transformation of dislocation cell boundaries through low-angle grain boundaries (with misorientation smaller than 15°) to high-angle grain boundaries (with misorientation larger than 15°) [12]. In this process, dislocations with Burgers vectors lying in the boundary plan contribute to the cell boundary sliding and shearing, while other dislocations are responsible for accumulation of misorientation in accordance with their combined Burgers vectors [177].

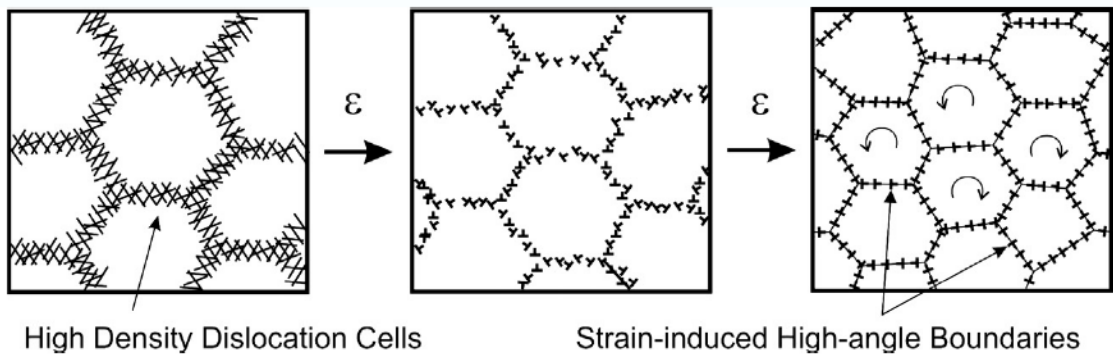


Figure. 2. 10 Schematic illustration of the formation process of fine grains under SPD condition [177-180]

Chapter 2 Literature Review

The ultrafine grains produced by SPD techniques are featured by prevalence of HAGBs in a non-equilibrium or energetically metastable state, which is commonly believed to be a signature that distinguishes them from conventional metal working wherein most of the sub-boundaries are low angle [12].

By refining grain size, the volume fraction of grain boundaries increases simultaneously. Because grain boundaries are sources and sinks of defects, barriers to points and line defects and storage sites for defects, they play a fundamental role in materials properties in various aspects [181, 182]. Most importantly, for the application of multicomponent materials, grain boundaries act as fast diffusion paths to transport foreign atoms and contribute to strong interdiffusion caused chemical bonds at interfaces. As shown in Fig. 2.11, comparing with coarse-grained substrate, ultrafine-grained substrate with more grain boundaries presents a faster and deeper diffusion mechanism [98].

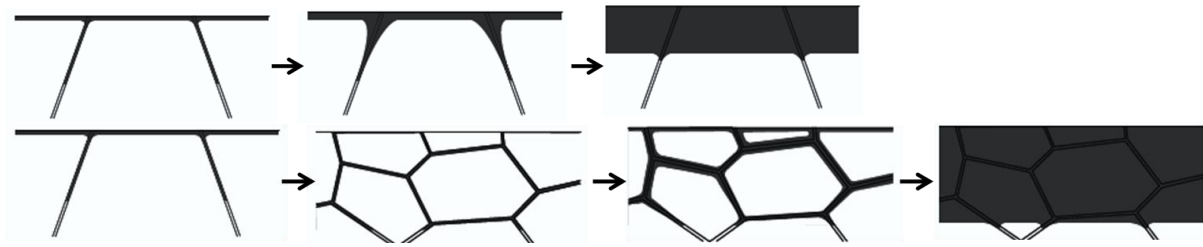


Figure. 2. 11 Schematic illustration of two scenarios of diffusion regimes with increasing time in a coarse-grained substrate with few grain boundaries (top) and in a ultrafine-grained substrate with several grain boundaries (bottom) [99]

Beside the contribution from high volume fraction of GBs, in SPD processed metals, diffusion coefficient can be further improved by ultra-fast diffusion paths. Non-equilibrium HAGBs produced by SPD possesses higher interfacial energy and larger excess free volume than conventional equilibrium HAGBs, which is believed to lead to higher diffusivities [12, 158]. Moreover, together with triple junctions, these non-equilibrium HAGBs also act as long-range network for interconnecting nano- and micropores produced by SPD to provide “ultra-fast” short circuit paths [100, 101].

Overall, from the respective of interface bonding, SPD techniques possess unique advantages in synthesising multicomponent materials. The imposed hydrostatic pressure can cause severe plastic deformation in substrate metals and breakage of brittle oxide layers. Meanwhile, the exposed fresh metal surfaces can be brought in interatomic distance contact and form

physical adhesive bonding. On top of this, chemical interdiffusion bonds are established between two substrates which have superior diffusion-friendly microstructures.

Nowadays many SPD techniques are developed and readily available for fabrication of multicomponent materials. Three “classic” SPD techniques, which have the generic feature of imposed high hydrostatic pressure, are described below.

2.6.1 Equal-channel angular pressing

Equal-channel angular pressing (ECAP) was first introduced by Segal et al. in 1980s [183-185]. During the process, intense plastic strain as a form of simple shear is introduced without changing the cross-section of the billet [11]. Since the early 1990s, ECAP has been further investigated and developed as a SPD method to fabricate ultrafine-grained metals and alloys. It has been demonstrated that ECAP is capable of providing bulk metallic materials with fairly homogeneous and nearly equiaxed microstructures with ultrafine grains in submicrometer range and a large proportion of HAGBs [186, 187].

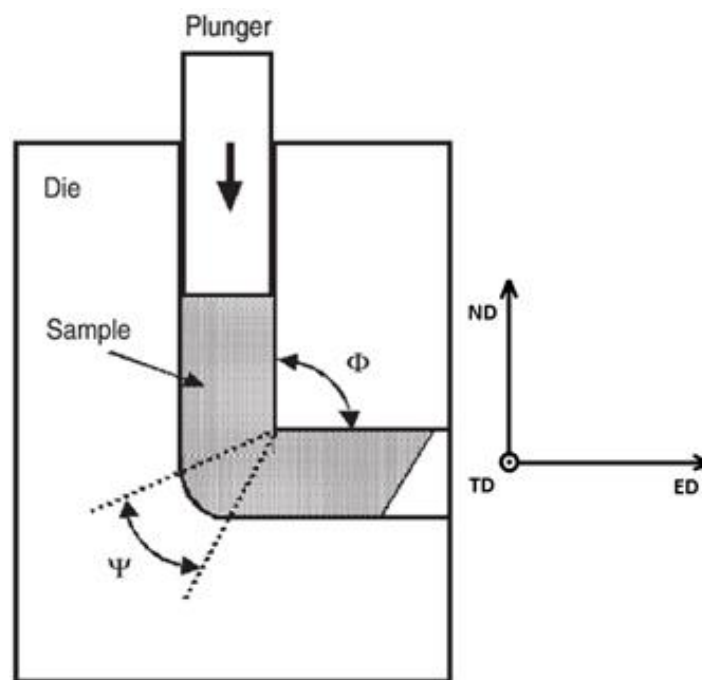


Figure. 2. 12 Schematic of equal channel angular pressing process [11]

The general principle of ECAP is exhibited in Fig. 2.12. The tool consists of a die with two channels of the same cross-section intersecting at an angle ϕ and a curvature angle ψ . A billet of almost the same cross-section is placed in the entrance channel and pushed by the punch

Chapter 2 Literature Review

through the exit channel. The magnitude of these angles along with the number of passes determines the shear strain induced into the sample as the relationship is given by [188]:

$$\varepsilon = \frac{N}{3} \left[2 \cot \left(\frac{\phi}{2} + \frac{\psi}{2} \right) + \phi \csc \left(\frac{\phi}{2} + \frac{\psi}{2} \right) \right] \quad (2.8)$$

where N is the number of passes. The commonly used parameters are $\phi=90^\circ$ and $\psi=0^\circ$, which provide an equivalent strain of 1.15. The shear strain is accumulated in the billet during repetitive processing and by rotating the billet about its longitudinal axis between the passes, so that different slip systems may be activated [184]. For instance, by rotating the billet around the longitudinal axis at angles of 0° and 90° , namely Route A (RA) and Route Bc (RBc), different microstructures emerge. To further improve the properties of materials by ECAP, back pressure can be applied in the exit channel to provide uniform distribution of stress-strain and provide good finished surface in the case of brittle materials [189]. It is worthwhile to point here that back pressure is essential for compacting powders using ECAP.

In addition to refining the microstructure of bulk materials, it has been demonstrated that the simple shear strain combined with the superimposed hydrostatic pressure improves the densification and bonding formation between metallic particles. Ti-6Al-4V powders were successfully compacted using ECAP with back pressure [190-194]. It was showed that due to superior contact between particles and enhanced interdiffusion, which is caused by additional diffusion paths, such as ordered shear band networks and local lattice distortions, ECAP is a powerful method of compaction of metallic particulates. As shown in Fig. 2.13, comparing with conventional powder consolidation methods that involve sintering to cause inter-particle bonding and elimination of porosity, ECAP compaction can achieve better densification and bonding within short time by imposing extreme strain on particles [195]. In addition, studies also showed that it is critical that particulates are shear deformed rather than slide over each other to achieve good bonding between them with high density of the compact [194-199].

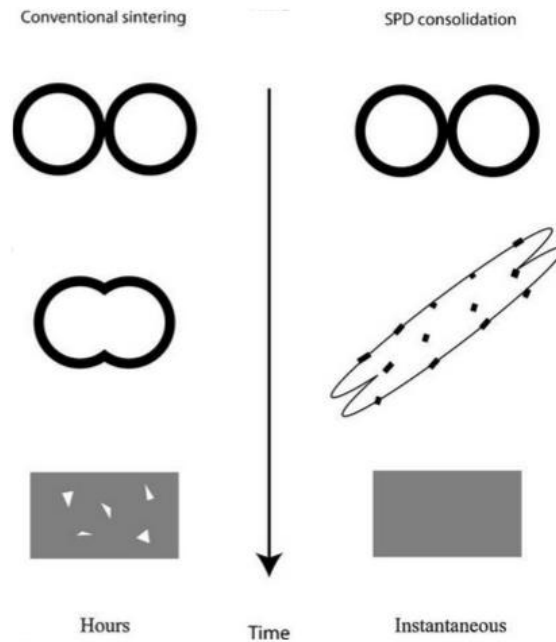


Figure. 2. 13 Schematic illustration of particle consolidation in conventional sintering (left) and ECAP compaction (right) [195].

With this outstanding strength of powder compaction, ECAP has been investigated to fabricate MMCs such as Al/Al₂O₃ composite [198, 200-202] , Cu/carbon nanotube [203], Al/B₄C [204], Mg/Mg₂Si [205] and Cu/TiB₂ [206] to achieve improved mechanical properties and thermal properties.

2.6.2 High pressure torsion

High pressure torsion (HPT) refers to the processing technique wherein samples are subjected under a combination of high compressive pressure with concurrent torsional strain, as the process is illustrated in Fig. 2.14 [12, 207]. This technique allows the most efficient grain refinement among all SPD techniques, however due to restriction of sample size it is used primarily for research purpose [12]. With regarding to multicomponent material, using HPT to gain deeper understanding of atomic interaction between immiscible phases is a very hot topic in the past five years. It has been used on a number of multicomponent metallic systems such as Cu/Nb [159], Cu/Zr [208], Cu/Ag [208], Cu/Ni [208], Al/Cu [209], Ti/Ni [210], Al/Ni [142], Cu/Fe [211] and Al/Ti [212]. Rich scientific discoveries are revealed at heterophase interfaces including atomic-scale structural transition – amorphization and intermetallic formation and chemical intermixing – supersaturated solid solution far beyond equilibrium thermodynamics [1, 142, 210, 211, 213]. Based on these exciting findings,

researchers have been trying to get deep understanding about the mechanism of the deformation-induced interdiffusion and intermixing on the atomic level, amorphization and solid solubility extension in multicomponent systems [214]. Beside the accelerated diffusion and short diffusion paths achieved by imposing intense shear strain, pure mechanical mixing by shuffling of atoms induced by shear of atomic planes and thermodynamic destabilization is another possible driving force [211].

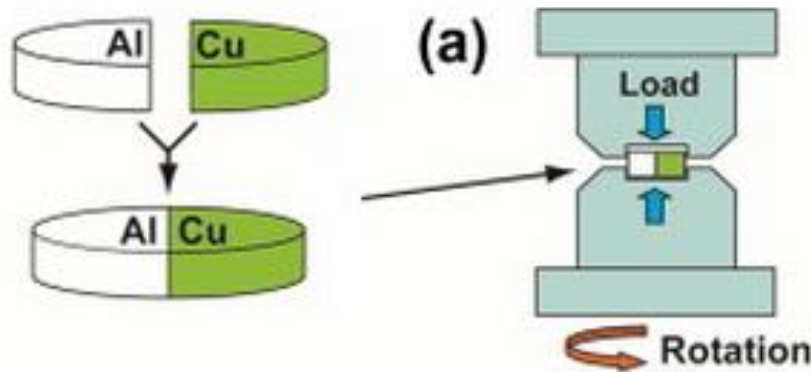


Figure. 2. 14 Schematic illustration of HPT processing of one half disc of Al and one half disc of Cu [209]

2.6.3 Accumulative roll bonding

Accumulative roll bonding (ARB) is another SPD technique where much higher amount of strain can be stored than conventional rolling. As the processing shown in Fig. 2.15, multicomponent sheets are stacked and rolled to over 50% thickness reduction. Then the rolled sheet is cut in two and stacked together for next rolling [12, 215, 216]. In such way, a large strain is accumulated in the bimetallic sheet without any geometrical changing and dissimilar metals are roll bonded [216]. The development of this technique on multicomponent materials is motivated by the exciting performance such as high radiation tolerance and shock resistance of Cu/Nb multilayered nanocomposites, where physical vapor deposition such as magnetron sputtering is used as the fabrication method [160, 162, 217]. ARB provided a way to manufacture bulk multilayered nanocomposites with tunable texture for structural application [162, 163]. Except the extensive investigation on Cu/Nb [139, 162], other combinations including Cu/Al [218], Al/Zn [219], Zr/Nb [220], Ti/Nb [221], Al/steel [222], Al/Mg[163], Cu/Ni[223] and Al/Ni [224] have also been studied. .

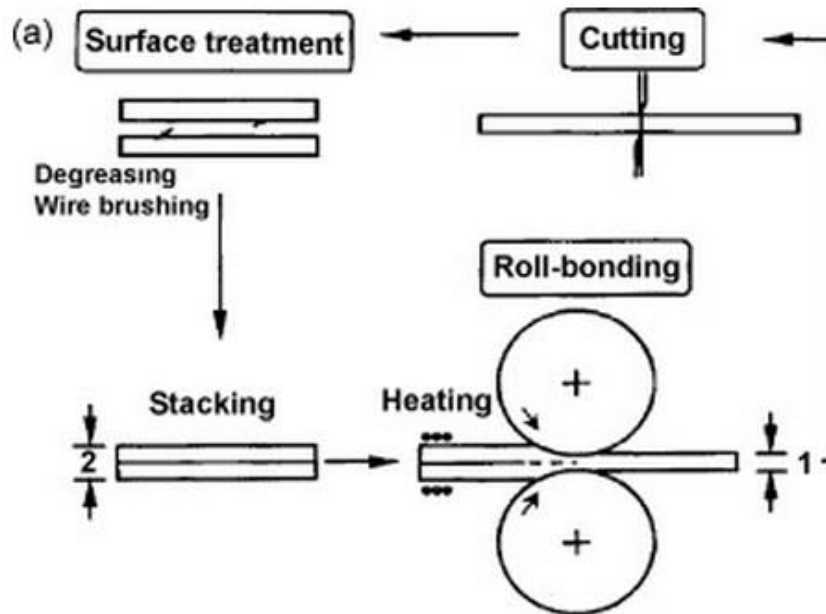


Figure. 2. 15 Schematic illustration of accumulative roll bonding processing [125]

To conclude this section, it can be found that even it has been ten years since ECAP was first studied to produce multicomponent materials [202], the development of this technique is rather slow comparing with other two methods. On one hand, this could be due to the less strain induced by ECAP comparing with HPT thus less scientific discoveries can be achieved at this extent. On the other hand, comparing with the promising engineering applications provided by ARB, the potential of using ECAP on manufacturing multicomponent materials for high-end applications has not been explored.

2.7 Summary of literature review

From the literature review, it can be summarised that multicomponent materials is a very valuable and promising class of materials. In the past, they were used as smart materials to save cost on some of the existing applications by replacing traditional monolithic metals. In the future, nanostructured and architected multicomponent materials are expected to have multifunctionality for high-end applications.

To achieve this goal, development of new processing routes is the most challenging part. Based on the research in the past decade, SPD techniques as a range of novel metal working methods are believed to be one possible avenue for synthesising advanced multicomponent materials. It has been found that the superimposed hydrostatic pressure and extreme plastic deformation from SPD processing facilitate and enable diffusion enhancement,

Chapter 2 Literature Review

microstructure refinement and architecture modification in constituents in multicomponent materials. Fantastic applications can be derived from these novel designs.

However, most of the findings are based on investigation of HPT and ARB. ECAP as the one the most mature SPD technique has relative slow space in this exciting developing area. One of the primary reasons is the lack of functional aspects of design. Since ECAP costs more than traditional metal working processes, more value in either engineering or scientific aspect needs to be added to the ECAP processed multicomponent materials.

Chapter 3 Experimental Methods

3.1 Outline of the chapter	37
3.2 Equal-channel angular pressing apparatus	37
3.3 Materials' performance characterisation	40
3.3.1 Mechanical properties characterisation.....	40
3.3.2 Functional properties characterisation	41
3.4 Microstructural imaging and characterisation	41
3.4.1 Optical microscopy	42
3.4.2 X-ray diffraction.....	42
3.4.3 Electron microscopy.....	43
3.4.4 Energy dispersive X-ray spectroscopy.....	45
3.4.5 Sample preparation for electron microscopy	46

3.1 Outline of the chapter

In this chapter, equipment and techniques that have been used in this project are introduced and described. On one hand, the general experimental procedures and microstructure characterisation techniques sheared in three sub-projects such as ECAP and electron microscopies are described in details. On the other hand, specific tests used to evaluate the functional properties such as biocompatibility and electrical conductivity will be presented in the corresponding chapters.

3.2 Equal-channel angular pressing apparatus

As it was mentioned previously, ECAP is the processing technique investigated in this project. The ECAP rig is shown in Fig. 3.1. The forward pressure is provided by a hydraulic press which has a capacity of 100 tons. The back pressure is provided by a hydraulic cylinder. The heating element is located around the die, which can be heated up to 500°C. During heating a thermal couple is attached to the die through a side hole on the heating element to monitor the temperature.

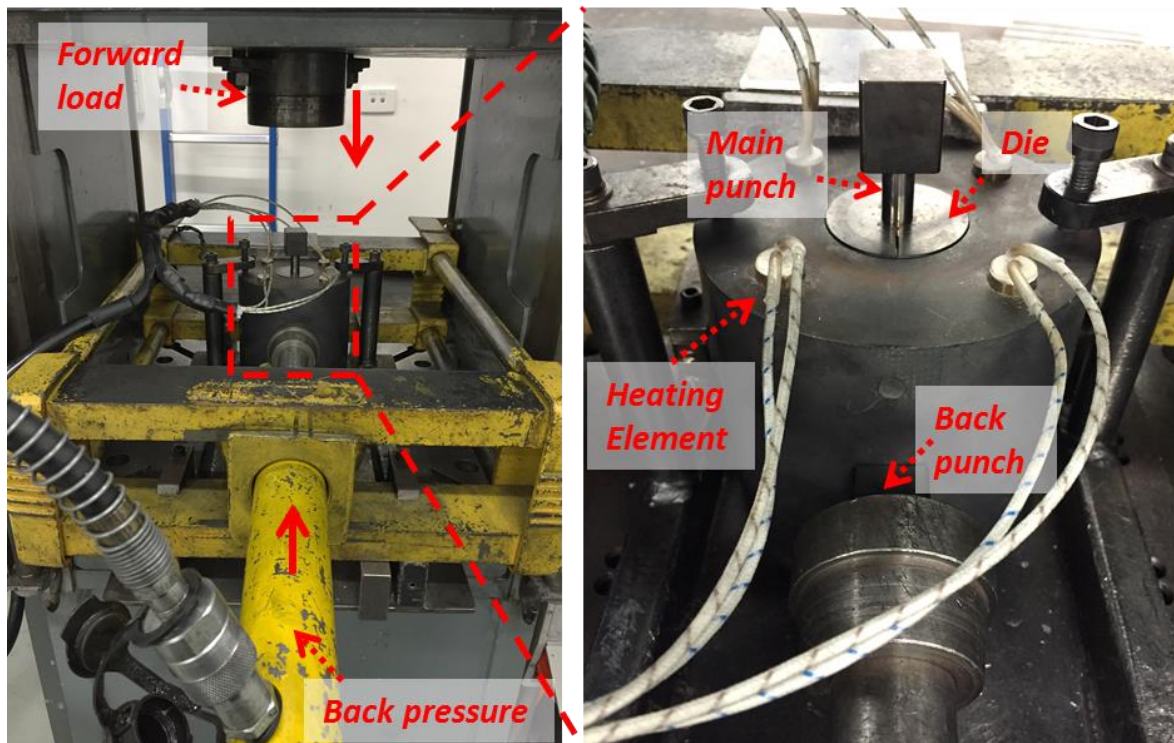


Figure. 3. 1 ECAP rig with heating element

Chapter 3 Experimental Methods

The set of die and punches are shown in Fig. 3.2. Main punch and back punch are made of tungsten carbide and their diameter is slightly smaller than the channel. There are two dies which have 10mm and 12mm diameter of channels used in this project. They are made of H13 tool steel which exhibits high strength at elevated temperature, high hot wear and hot cracking resistance, while good toughness and thermal conductivity. After the machining, they are hardened by austenitizing heat treatment and quenching to achieve the hardness up to 52-54 HRC. As it can be seen from the inset, the channel angle is 90° and the corner arc is very sharp and nearly 0° . With this geometry, the equivalent strain of 1.15 after one ECAP pass can be calculated based on Equation (2.8). Besides, the use of sharp corner angle contributes to narrowly spread plastic zone and homogeneous strain [225]. It is also worth nothing here that graphite lubricant was sprayed on channels and punches before loading and processing the sample, to reduce the friction between the sample and the die walls.

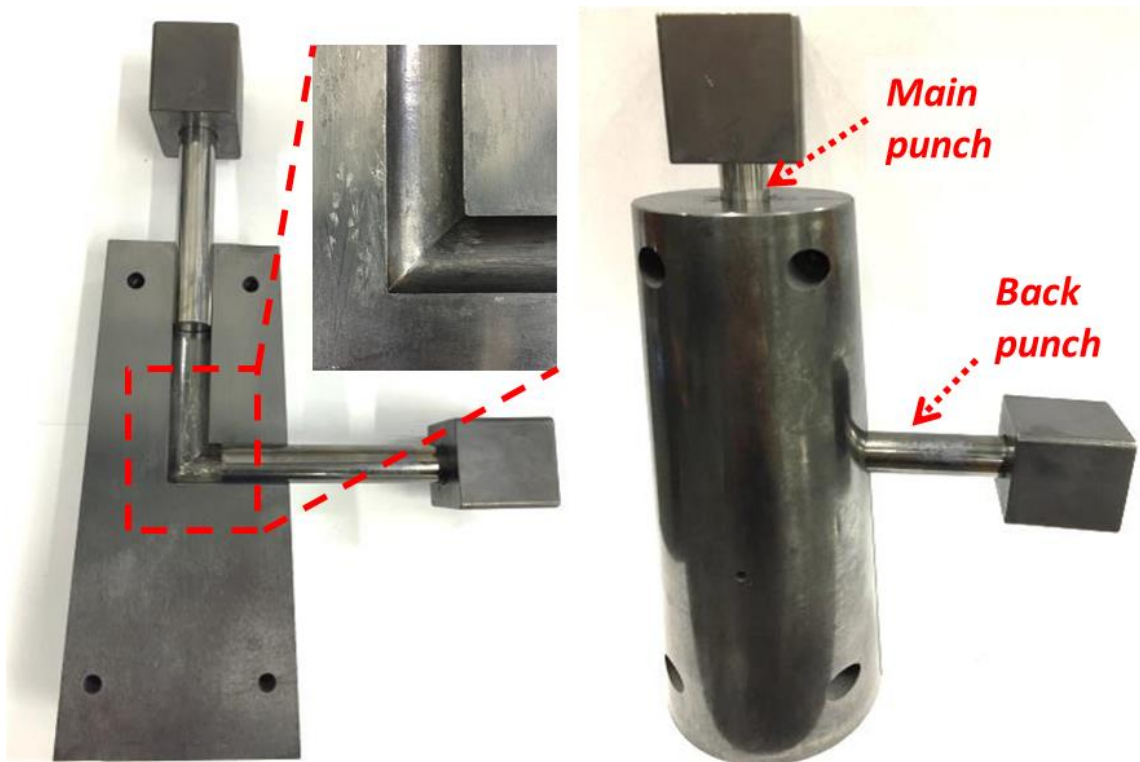


Figure. 3. 2 ECAP die and punches

Because the ECAPed samples do not experience any change in the cross-sectional dimensions, they can be processed repetitively and permit accumulation of strains. Accordingly, the strain path which also refers to processing route can be manipulated by rotating the sample about the processing axis between the passes. There are many possible ways of rotation but generally speaking four representative routes have been studied, as

Chapter 3 Experimental Methods

shown in Fig. 3.3. In route A, the billet does not rotate between two passes; route B_C allows a rotation of 90° in the same sense; in route B_A, the billet is rotated by 90° alternatively between clockwise and counter clockwise; in route C, the billet is rotated by 180° in the same sense.

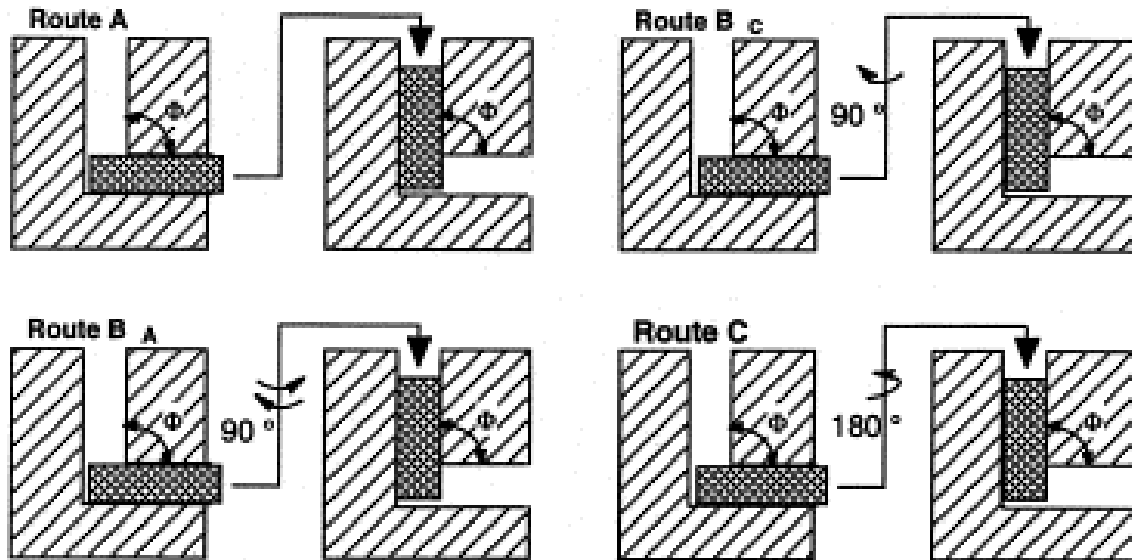


Figure. 3. 3 Four ECAP routes based on rotation of billet between passes [226]

This rotation between passes is in fact an important parameter in ECAP process since it determines the simple shear plane imposed on the billet, as shown in Fig. 3.4. For instance, comparing with other three routes, route B_C provides shearing over large angular ranges on the three orthogonal planes while a regular and periodic restoration of an exquiauxed structure during successive pressing [227]. This makes it the most studied one because it is widely believed to be the most effective route in grain refinement, yielding exquiauxed grains and HAGBs [226, 228]. However, recent studies showed that using the same processing condition and material, route A produced slightly higher fraction of HAGBs than route B_C, which made the most effective processing route quite debatable [229]. Despite the research on existing routes, new ECAP routes have been under development using cylindrical billet, where the rotation angle can be arbitrary. Recent investigation showed that by activating new slip systems at pass-to-pass transitions using new routes, more efficient grain refinement and higher fraction of exquiauxed grains can be achieved in face centre cubic metals than traditional routes [230-232].

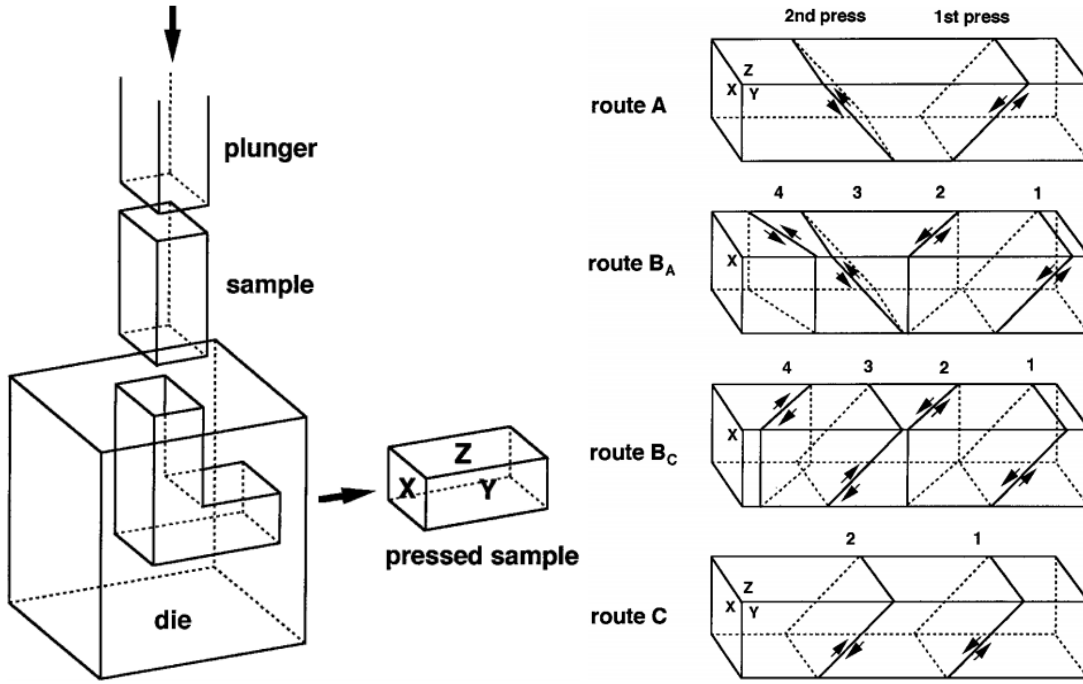


Figure. 3. 4 Schematic illustration of ECAP showing the three orthogonal planes x , y and z and the shear planes associated with four processing routes [233].

Processing temperature and strain rate also affect the grain refinement process, which can be captured in the magnitude of the Zener-Hollomon parameter Z :

$$Z = \dot{\epsilon} \cdot \exp(Q/RT) \quad (3.1)$$

where $\dot{\epsilon}$ is the strain rate, Q is an effective activation energy, R is the gas constant and T is the absolute temperature. Generally speaking, large Z -values benefit the continuous dynamic recrystallization and hinder dynamic recovery, which leads to promotion of the formation of fine grains [234].

Sample preparation before ECAP is another aspect and it will be described in each sub-project.

3.3 Materials' performance characterisation

3.3.1 Mechanical properties characterisation

Uniaxial compression test was used as the primary method to evaluate the mechanical properties of the produced multicomponent materials. A screw-driven universal Instron 5982 testing machine was used for testing. The tests were conducted according to ASTM Standard

Chapter 3 Experimental Methods

E9 and the Young's modulus was calculated based on ASTM Standard E111. Each measurement was made from a preload of 30~50N, which was high enough to minimize potential problems with setting of the specimens in the machine. Hence, the initial straight-line portion of the stress-strain curve within the elastic limit could be measured with sufficient confidence. Moreover, to further eliminate possible errors associated with the compliance of the testing instrument, the latter was gauged by testing commercial pure metals which has known mechanical behaviours in compression. It was calculated using the equation given below

$$1/E^* = 1/E + A/K^*l \quad (3.2)$$

where K^* is the compliance of the testing machine, A is the cross-sectional area and l the length of the specimen; E is the true Young's modulus of the specimen material (bulk titanium) and E^* is the apparent Young's modulus, as determined from the slope of the elastic part of the stress-strain curve.

3.3.2 Functional properties characterisation

In addition to outstanding mechanical strength, unique functional properties are also expected from ECAP processed metals. In this project, investigations of two functional properties were involved in chapter 5 and 6, namely biocompatibility and electrical conductivity. They will be described in detail within each chapter.

3.4 Microstructure imaging and characterisation

Microstructure imaging is about contrast and characterisation is about interpretation of the contrast. A number of imaging techniques were employed to characterise the microstructural features of the multicomponent materials designed in this project. Contrast can be defined as “non-homogeneous intensity distribution” in the image. When it comes to the surface structure, topographic and morphological contrast is usually displayed by collecting light reflected or secondary electrons from the surface layer of the substrate. Regarding to the underlying microstructure, the mechanism of contrast is more complicated. Diffraction contrast based on Bragg's law (shown in equation 3.3, where d is lattice plane spacing, n is a positive integer, θ is the scattering angle and λ is wavelength of incident beam) is the main source of variation of a two dimensional intensity in this case.

$$2d_{hkl} \sin \theta = n\lambda \quad (3.3)$$

The principle of Bragg diffraction is presented in Fig. 3.5. The diffraction or constructive interference can only occur when the equation 3.3 is met. Both diffracted waves and other elastically scattered waves are collected by detector and they give different brightness or intensity. In this way, the contrast is correlated with crystal orientation. Therefore, features such as defects, different crystals (grains) and foreign phases can be visualised and statistics such as defect density and texture can be characterised.

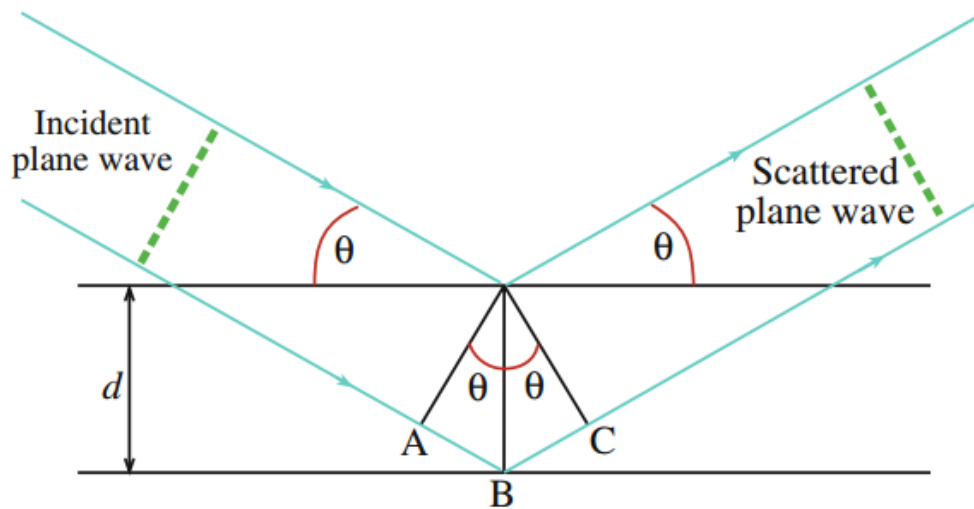


Figure. 3. 5 Schematic illustration of the Bragg diffraction at a set of two lattice planes [235]

3.4.1 Optical microscopy

Optical microscopy (OM) benefits from high depth of focus for uneven surfaces and imaging of large features at low magnification. OM images are formed by light reflected from the surface of the specimen. Due to the difference of removal rate during grinding, interfaces between two phase materials provide contrasts. Two microscopes were used through the project. One is a stereo microscope namely Olympus SZX16 equipped with digital camera. The other is an inverted metallurgical microscope called Olympus GX51 with digital camera.

3.4.2 X-ray diffraction

Comparing with light, x-rays give better spatial resolution. XRD pattern analysis is a powerful microstructure characterisation technique due to its capacity of phase identification, microstrain and dislocation density measurement, with simple sample preparation requirement. This information can be obtained from the spectrum by analysing Bragg

Chapter 3 Experimental Methods

reflection positions and width of peaks. In terms of position, peak shifting provides the information of the mean lattice parameters; whereas, peak broadening reveals the microstructural refinement and lattice strain which induced mainly by dislocations [236, 237]. In our case, it has been found that materials with ultrafine grain size exhibit considerable microstrain, which is usually related to strain fields from dislocations [238]. To deconvolute both crystalline size and microstrain induced broadening effects, the XRD patterns can be analysed using a simplified integral breadth method [239, 240]. The full width at half maximum (FWHM) of each peak is able to be measured using either Pearson VII or pseudo Voigt function depending on which fits better, and fitted according to a modified Williamson-Hall relationship. By measuring the peak broadening B and each Bragg angle θ_B , the lattice strain ε and crystallite size d can be calculated using equation given below [239, 240]

$$B \cos \theta_B = K\lambda/d + \varepsilon \sin \theta_B \quad (3.4)$$

where λ is the wavelength of the X-ray source, K is a constant ~ 0.9 . The dislocation density ρ can then be calculated from the following equation [239]

$$\rho = 2\sqrt{3}\langle\varepsilon^2\rangle^{1/2}/db \quad (3.5)$$

where b is the magnitude of the Burgers vector.

In this project, XRD was conducted using Cu K α radiation at 40 kV and 25 mA on a Philips X-ray diffractometer. Data was processed using the peak fitting program MDI Jade for accurate computation.

3.4.3 Electron microscopy

Comparing with X-rays, electrons have a smaller wavelength hence give higher resolution. Moreover, because electrons are negatively charged particles, they interact far more readily with matter than X-ray thus give much more information. As shown in Fig. 3.6, a wide range of signals can be generated from interaction between an incident electron beam and matter.

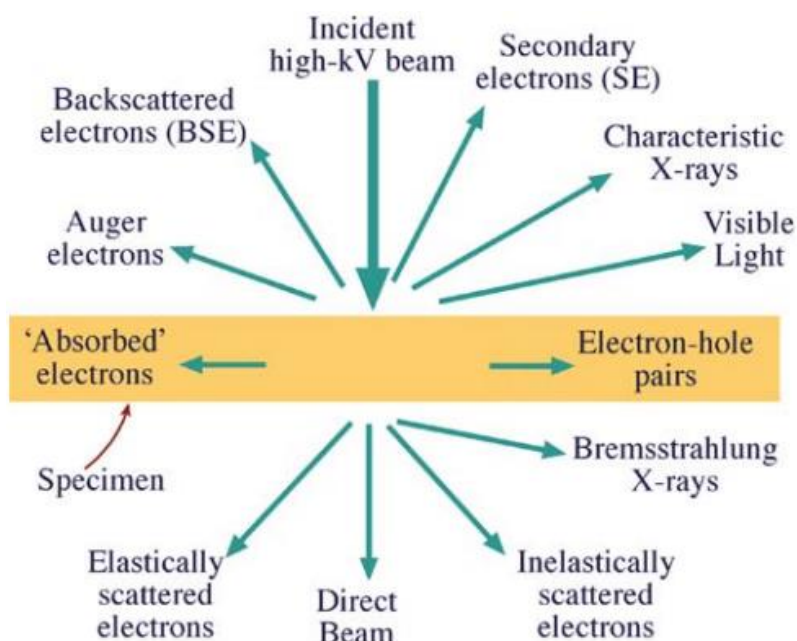


Figure. 3. 6 Illustration of signals generated from interaction between incident electron beam and a thin sample [241]

In scanning electron microscopy (SEM), a focused beam of electrons is used to scan over the surface of a sample to reconstruct a magnified image of the surface. Secondary electrons (SE) are collected to image topological and morphological features. Backscattered electrons (BSE) as a type of elastically scattered signal gives information of crystal structure and are used to distinguish different grains and phases. Furthermore, electron backscattered diffraction (EBSD) and transmission Kikuchi diffraction (TKD) are two powerful imaging techniques using backscattered and forward-scattered electrons to visualize grains and interfaces in polycrystalline materials, in which Bragg's law is used as the working principle.

Transmission electron microscopy (TEM) provides considerably higher resolution than SEM, owing to the smaller wavelength and less scattering of electrons. In TEM, transmitted electrons including direct or unscattered electrons and forward-scattered electrons (elastically or inelastically) are collected by the detector which is located underneath of the specimen. By manipulating the objective aperture to filter the selected area diffraction pattern (SADP) which are all located on the back focal plane, all electrons or only unscattered electrons or only diffracted electrons from specific crystal(s) can be collected and used to generate TEM images, bright field (BF) images or dark field (DF) images.

Scanning transmission electron microscopy (STEM) is a technique based on the setup of TEM. Different from the traditional TEM using parallel electron beams, in STEM a

convergent electron beam is used to scan over the sample. The working principle is similar to SEM, but the resolution is much higher in STEM. High-angle annular dark field (HAADF) detector is used to collect elastically scattered electrons and construct HAADF images having atomic number (Z) contrast at atomic-level resolution.

3.4.4 Energy dispersive X-ray spectroscopy

Energy dispersive X-ray spectroscopy (EDX) was extensively used as a tool to characterise the element constitutes and quantify the relative concentration of each element. The generation of characteristic X-rays is illustrated in Fig. 3.7. This process is initiated from the interaction between incident high-energy electron beam and inner-shell electrons. By “kicking out” an electron from the inner atomic orbitals, a hole is left on this orbital and an electron from higher orbitals drops into the vacated inner orbital to keep the atom to its ground state. This transition is accompanied by the generation of characteristic X-rays which can be collected by the detector and analysed by energy dispersive spectrometer system [242].

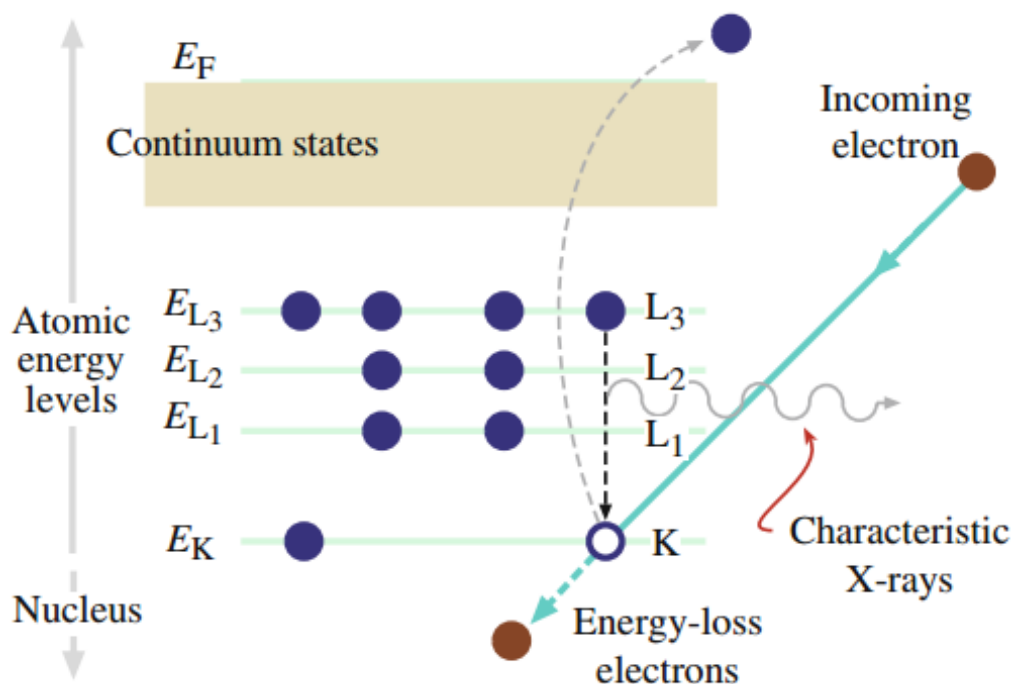


Figure. 3. 7 The schematic illustration of generation of characteristic X-rays [242]

In the project, two SEMs including Jeol 7001F FEG SEM equipped with EBSD detector and EDS detector and FEI Quanta 3D FEG FIB equipped with EBSD detector and two TEMs including FEI Tecnai G2 T20 TWIN LaB6 TEM and FEI Tecnai G2 F20 S-TWIN FEG STEM equipped with EDS detector were extensively used.

3.4.5 Sample preparation for electron microscopy

Sample preparation for imaging and characterisation is very important and takes not less time than data collection and interpretation. This is primarily due to the different milling rate and etching rate of constituents in multicomponent materials. A number of techniques were used for preparing EBSD and TEM samples. Because the sample preparation methods are different in three sub-projects, the specific procedures will be introduced separately in Chapter 4, 5 and 6. However, the principle is the same and briefly summarised here.

Mechanical grinding and polishing as fundamental procedure were used to create a highly reflective surface free of scratch. The specimen was usually ground with SiC paper up to 2400-grit using a Buehler Ecomet 3000 grinder, followed by mirror-polishing with a colloidal silica suspension (OP-S/OP-U). The mechanically prepared surface quality can be used for OM and SEM imaging.

Ion Beam milling and polishing were used to achieve higher surface quality that is free of residual strain and amorphous layer, for the applications such as EBSD and (S)TEM. Instead of scratching and rubbing, ion beam removes materials by a sputtering process, as shown in Fig. 3.8. When the accelerated ion beam strikes the sample surface, a series of elastic collisions occurs where momentum is transferred from ions to the atoms on the surface of the substrate. The atoms may be ejected as sputtered particles if they receive a component of kinetic energy that is sufficient to overcome the surface binding energy of the target material [243, 244].

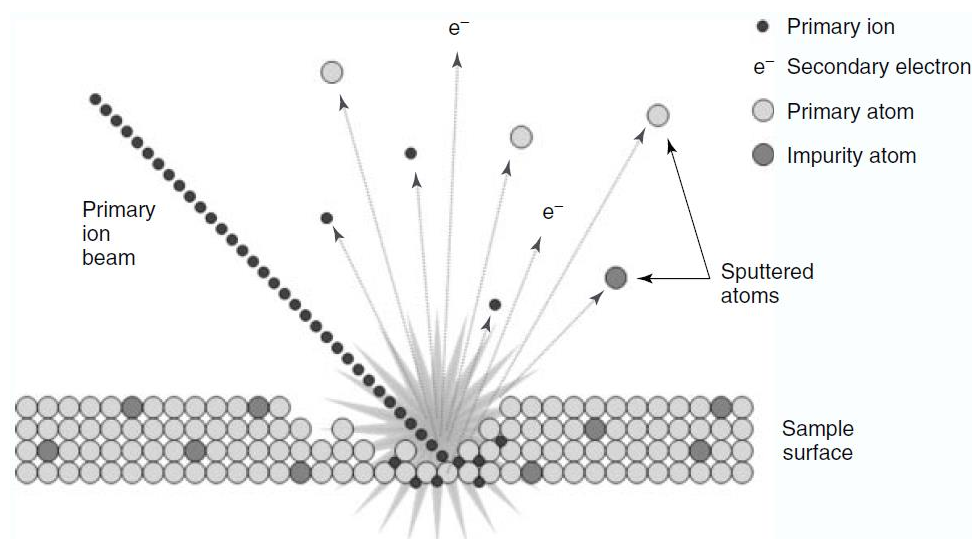


Figure. 3. 8 Schematic illustration of the ion beam sputtering process [243]

Chapter 3 Experimental Methods

This sputtering effect allows focus ion beam (FIB) to precisely mill and polish a piece of material in a controlled manner [243]. However, as we found in this study, the ion beam bombardment may also cause some secondary processes such as phase transformation and amorphization on the surface of the substrate.

In this project, ion beam milling and polishing were conducted on three systems including an FEI Quanta 3D FEG FIB, Gatan precision ion polishing system and Technoorg Gentle Mill 2.

Chapter 4 Multicomponent materials from aluminium and magnesium machining chips compacted by ECAP with back pressure

4.1. Outline of this chapter.....	51
4.2. Introduction	51
4.3 Experimental procedures and characterisation	54
4.3.1 Raw materials characterisation and ECAP compaction.....	54
4.3.2 Mechanical properties measurement.....	56
4.3.3 Microstructure characterisation.....	56
4.4 Results and Discussion	57
4.4.1 Density of Compacts	57
4.4.2 Grain size evolution	58
4.4.3 Mechanical properties	60
4.4.4 Phase identification	62
4.4.5 Electron microscopy characterisation	63
4.4.5 Nanoindentation characterisation.....	68
4.5 Summary of this chapter.....	70

4.1. Outline of this chapter

In the first sub-project, the pure-metal-metal-matrix composite and intermetallic/metal-matrix composite were studied. Multicomponent materials with outstanding and unique properties were manufactured from Al and Mg machining chips using ECAP compaction. The produced compact has a tangled architecture rather than a more common multifilament or multilayered arrangement, owing to the special morphology of machining chips. Moreover, by varying the weight fraction of the constituent materials, temperature and processing route, as well as employing subsequent heat treatment, the microstructure and the mechanical properties of the compact were varied. The width of the interdiffusion zone and the formation of intermetallic phases near the interfaces between the two metals were studied by energy-dispersive X-ray spectroscopy and nanoindentation. It was shown that substantial improvement of mechanical properties, such as an increase of strength, strain-hardening capability and ductility, can be obtained. This is achieved by changing the processing parameters of ECAP and the annealing temperature, as well as by optimising the weight fraction of the constituent metals.

4.2. Introduction

Machining chips are a form of material which is usually considered as wastes, however, in our opinion they are in great value. Statistics shows that in many case, up to 50% of the metal can end up as scrap and swarf, primarily due to the fact that manufacturing of metallic parts by casting or metal-forming processes commonly involves finishing machining to obtain the required surface quality of the part and dimensional precision [245]. The conventional way of recycling of machining chips is remelting and casting. As illustrated in Fig. 4.1, after melting the Mg scrap conventionally, the contaminated melt will go through refinement by distillation before cast into products [246]. Even though this route has been adopted by industry, there are a number of limitations, such as high energy consumption, inferior properties of cast ingots due to inevitable contamination and the material loss [247-250]. Besides, it is very difficult to apply this technique to recycle machining chips, owing to their elongated spiral shape and small size in comparison with other types of scrap with regular shape and big size [251].

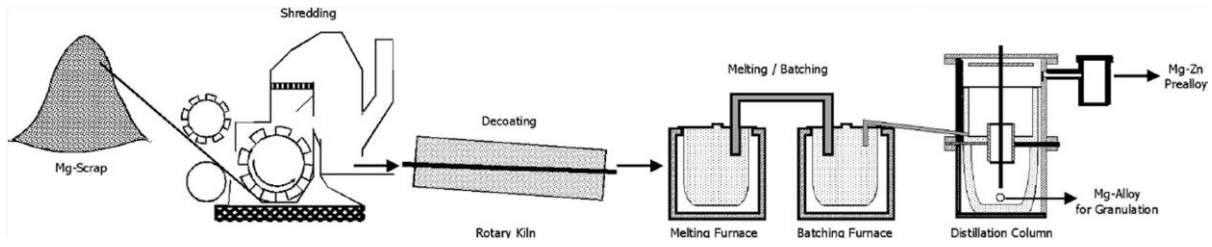


Figure. 4. 1 Recycling process of Mg scrap by remelting and subsequent refinement [246]

In recent years, solid state recycling as an alternative way to deal with waste machining chips has been gaining increasing attention in academic area. This is primary due to low processing temperature which results in significant energy and cost savings and high metal yield [252]. As shown from the pie charts in Fig. 4.2, comparing with conventional route with about 54% yield, direct solid state recycling such as extrusion and compression provides much higher yield of 95% [250].

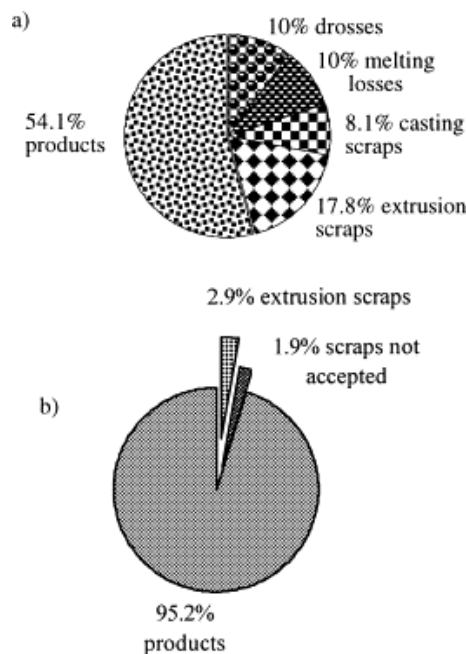


Figure. 4. 2 Comparison of recycling yield between (a) conventional melting route and (b) direct solid state route [250]

Although efforts have been put into developing more effective ways of recycling machining chips, they are still treated as a type of waste material. In our view, they can be regarded as a valuable source of ultra-fine grained (UFG) metals. Indeed, during machining they have undergone an intensive shear strain that commonly results in grain refinement [253, 254]. Furthermore, as compared to metal powders, a lower content of oxide contamination is present in machining chips owing to their smaller specific surface area. Therefore, machining

chips can be used as potential precursors to manufacture bulk UFG materials if sufficiently high density can be achieved by compaction.

As shown by a stream of publications, ECAP with back-pressure has several advantages in production of bulk high density billets from particulate metals over the conventional compaction processes [192, 193, 255-257]. These advantages include (i) extensive shear strain that breaks the oxide film to expose fresh metal at the surfaces of chips coming into contact, (ii) a change of the geometry of pores to orientations favourable for pore closure, (iii) high hydrostatic pressure promoting pore closure and (iv) creation of dislocation substructure, new grain boundaries and micro shear bands acting as fast diffusion paths that further enhance compaction [190, 256, 257]. Several groups have used ECAP for compacting machining chips for re-melting or - in combination with heat treatment - for production of solid rod from a single material [248, 258-262].

It seems very attractive to extend this method and also apply it to compact machining chips of *dissimilar materials*. In fact, the use of severe plastic deformation techniques to manufacture metallic multicomponent materials with combinations of properties inherited from their constituents have been increasingly investigated over the last decade, [1, 263]. However, to our knowledge, the possibility of creating such multicomponent materials by using compaction of swarf by ECAP has not been considered to date. As will be shown below, the weight ratio of the constituents and the ECAP parameters can be varied to obtain properties different from what can be achieved through the melting route. Subsequent heat treatment can also be employed to manipulate microstructure and the precipitation state, thus achieving properties superior to those of the individual constituents. If advanced properties are achieved, one can even speak of '*upcycling*', i.e. recycling that improves a material's value [264].

Magnesium and aluminium were chosen in this work because of a wide range of possible applications owing to their low density and relatively high strength. A number of studies were conducted to investigate conventional cast Al-Mg alloys processed by severe plastic deformation [265-268]. With the aim of widening the window of applications, this work explores compaction of Al/Mg machining chip blends by means of ECAP with back-pressure, in some cases followed by heat treatment.

The effect of the variation of the weight fraction of Al and Mg chips, the processing route and temperature, as well as the heat treatment, on the microstructure and the mechanical properties of the product was investigated. Special attention was paid to the formation of an

interdiffusion layer between Al and Mg, which defines the quality and strength of the multi-component material. To look into the effect of hydrostatic pressure, this parameter was varied. Although interdiffusion in Al/Mg in general has been studied extensively [269-272], its enhancement due to ECAP processing, especially under high hydrostatic pressure has not been considered. To our knowledge, the present work is a first study of this aspect of compaction of machining chips of Al and Mg.

4.3 Experimental procedures and characterisation

4.3.1 Raw materials characterisation and ECAP compaction

Commercially pure Al and Mg turning chips of helical shape with about 0.5 mm thickness were used. The average grain size of the Al and Mg chips was $0.71 \pm 0.22 \mu\text{m}$ and $6.11 \pm 2.59 \mu\text{m}$, respectively, cf. Fig. 4.3.

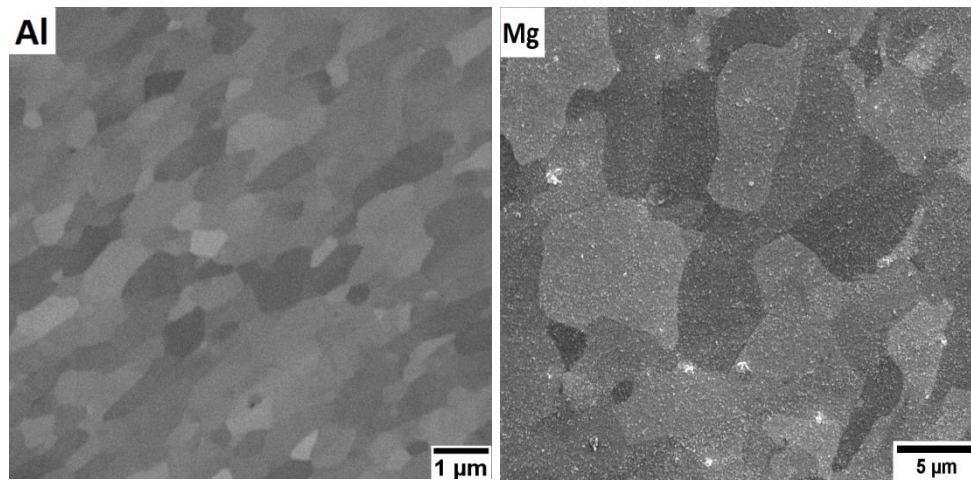


Figure. 4. 3 SEM images of the microstructure of as-received Al and Mg chips

Three compositions of Al/Mg chip blends by weight ratio were chosen, namely Al80Mg20, (80wt.%Al and 20wt.% Mg), Al50Mg50 (50wt.%Al and 50wt.% Mg) and Al20Mg80 (20wt.%Al and 80wt.% Mg). Al and Mg chips were first weighed and then mixed by SPEX in air without using any grinding media. The mixing time was three minutes. This regime ensured that the chips were mixed homogeneously without comminution and cold welding.

The ECAP process of swarf compaction is illustrated in Fig. 4.4. Machining chips are compressed in the entry channel, while the exit channel is blocked by a back-pressure punch. During this operation, the thrust of the forward punch creates a large hydrostatic pressure and pre-compacts chips in the entry channel. Plastic deformation by simple shear in the plane

where the entry and the exit channel intersect starts when the forward pressure exceeds the backward pressure and the pre-compact moves into the exit channel against the back-pressure punch, as seen in Fig. 4.4. Each blend was consolidated by two ECAP passes with back-pressure stepped up from 75MPa in the first pass to 125MPa in the second one. The second ECAP pass was conducted according to either Route A (RA), or Route B_C (RB_C). For comparison, some samples were compacted at a higher level of back-pressure of 150MPa in both passes. The equivalent true strain the material underwent after two passes was 2.3.

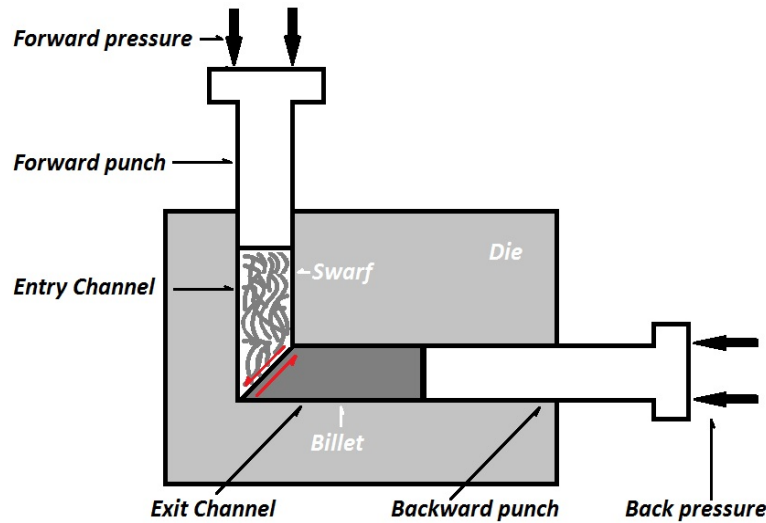


Figure. 4. 4 The schematic diagram of the processing chain to fabrication machining chips compacts

Two ECAP temperatures, viz. room temperature (RT) and 300°C, were chosen to investigate the effect of ECAP temperature on the compacts. Furthermore, heat treatment for 20 min at three different temperatures was carried out after room temperature ECAP in order to examine the effect of annealing on the microstructure and properties of the compacts. A summary of the processing routes used is given in Table 4.1.

Table. 4. 1 Compositions and Processing conditions

Compacts Designation	ECAP Route at RT	Annealing Temperatures after RT ECAP, °C			ECAP Route at 300°C
Al80Mg20	RA	100	200	300	RA
	RB _C	100	200	300	RB _C
Al50Mg50	RA	100	200	300	RA
	RB _C	100	200	300	RB _C
Al20Mg80	RA	100	200	300	RA
	RB _C	100	200	300	RB _C

4.3.2 Mechanical properties measurement

After compaction by ECAP, the density of the samples was determined by Archimedes' method (ASTM B311-93 (2002)). Tetrachlorethylene, with a density $\rho_{tetra} = 1.62 \text{ g/cm}^3$, was used as the immersion liquid.

Compacted billets were cut into cylindrical compression test specimens with a height of 7 mm and diameter of 4.5 mm. Compression tests were carried out using an Instron 5982 machine with a cross-head velocity of 0.007 mm/s corresponding to a nominal strain rate of 0.001 s^{-1} . The 0.2% offset method was used to determine the yield stress.

4.3.3 Microstructure characterisation

To check the possibility of formation of new intermetallic phases, the samples were characterised by X-ray diffraction using Cu K α radiation at 40kV and 25mA in a Philips X-ray diffractometer.

The presence of an interdiffusion zone was also investigated by nanoindentation of metallographically prepared cross-sections. Nanoindentation experiments were carried out using a Nanoindenter G200 (Agilent Technologies, Chandler, USA) equipped with a continuous stiffness measurement (CSM) unit and a three-sided Berkovich diamond pyramid. Machine stiffness and tip shape calibration was performed according to the Oliver-Pharr method [273]. The CSM frequency for all tests was set to 40 Hz, the harmonic amplitude of 3 nm was superimposed and a constant indentation strain rate of 0.05 s^{-1} was applied. The maximum indentation depth was set to 1000 nm for the determination of the bulk mechanical properties (the average depth being about 800 - 950 nm). The deformation behaviour of the interdiffusion zone formed was investigated by taking a series of nanoindentations across an Al/Mg interface with a preset indentation depth of 100 nm and 50 nm; the corresponding hardness and Young's modulus values were determined by averaging of the readings for the depths within the depth ranges of 80-90 nm and 40-45 nm.

Microstructure evolution was characterised by optical microscopy (Olympus GX51) and scanning electron microscopy (SEM, Jeol JSM-7001F operated at 15 kV). Energy dispersive X-ray spectroscopy (EDX) line scans across interfaces were carried out with an Oxford Instruments Si(Li) X-ray detector incorporated in the mentioned scanning microscope. The Al/Mg interfaces were also studied by TEM. Thin foils were prepared by ion-beam milling

using a Gatan PIPS system. Examination of the foils was carried out with a FEI Tecnai G2 T20 microscope operating at 200kV.

4.4 Results and Discussion

4.4.1 Density of compacts

The theoretical density of a compact for a given composition was calculated using the following equation:

$$\rho = (100\%) \times (\rho_{Al} \times \rho_{Mg}) / (\rho_{Al} \times (Mg)wt\% + \rho_{Mg} \times (Al)wt\%) \quad (4.1)$$

The relative density was defined as the actual density achieved for a particular composition normalised by the respective theoretical density. As shown in Fig. 4.5, after two ECAP passes, a reasonably high relative density above 96% was achieved for all conditions. A higher density was reached when the ECAP Route A, rather than Route B_C was used. This is attributed to continuous alignment of chips in shear direction and transformation of their shape to elliptical geometry, which is conducive for closure of voids between the chips under hydrostatic pressure [193]. After annealing treatment at 200° for 20 min, the density increased by about one percentage point, which can be explained by void shrinkage through enhanced thermally activated atom diffusion. ECAP at 300°C resulted in the density attaining nearly theoretical density levels, as at this temperature the atom transport was facilitated even more.

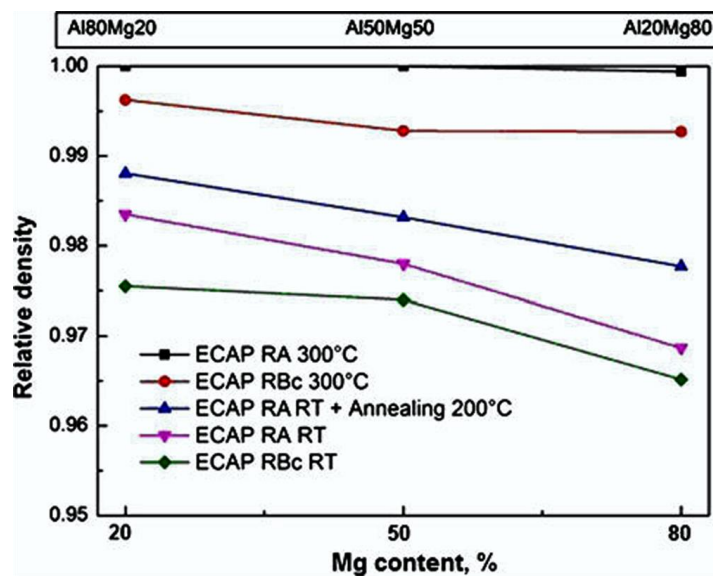


Figure. 4. 5 Relative densities for all compositions after two passes of ECAP

Additionally, our data provided a clear demonstration of a trend to density decrease with increasing Mg content. This can be rationalised as follows. As aluminium has high ductility, Al chips withstand the severe deformation introduced by two ECAP passes relatively easily, Fig. 4.6 (a). At room temperature aluminium flows into the spaces between serrations on magnesium chips. By contrast, owing to its hcp structure, magnesium has poor ductility at RT when only basal slip and twinning on pyramidal planes can be activated. As seen from Fig. 4.6 (b), cracks may form in magnesium chips during ECAP, which are not able to recover under hydrostatic pressure. At 300°C magnesium becomes ductile due to activation of non-basal slip systems [274], and fabrication of compacts with high relative density and no internal defects becomes possible, Fig. 4.6 (c).

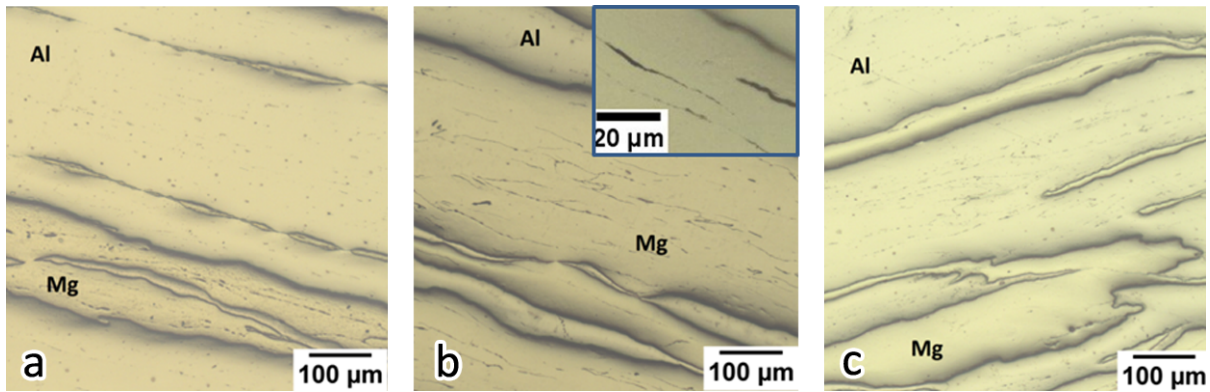


Figure. 4. 6 OM images of compacts processed by RA: (a) Al80Mg20 processed by two ECAP passes at RT; (b) Al20Mg80 processed by two ECAP passes at RT (inset shows cracks in Mg chip); and (c) Al80Mg20 processed by two ECAP passes at 300°C

4.4.2 Grain size evolution

The composition Al80Mg20 that provided the best results in terms of relative density was chosen for investigation of temperature regimes most suitable for ECAP compaction and annealing. Tuning of the annealing temperature was based on two considerations: stability of UFG microstructure and improvement of the bonding between the chips. The microstructure of the Al80Mg20 compact after annealing at 100°C, 200°C, and 300°C for 20 min was observed by SEM, as exemplified in Fig. 4.7. The microstructure was compared with that found after compaction by ECAP at 300°C. The data on the average grain size in the aluminium and magnesium components of the compact are presented in Fig. 4.8.

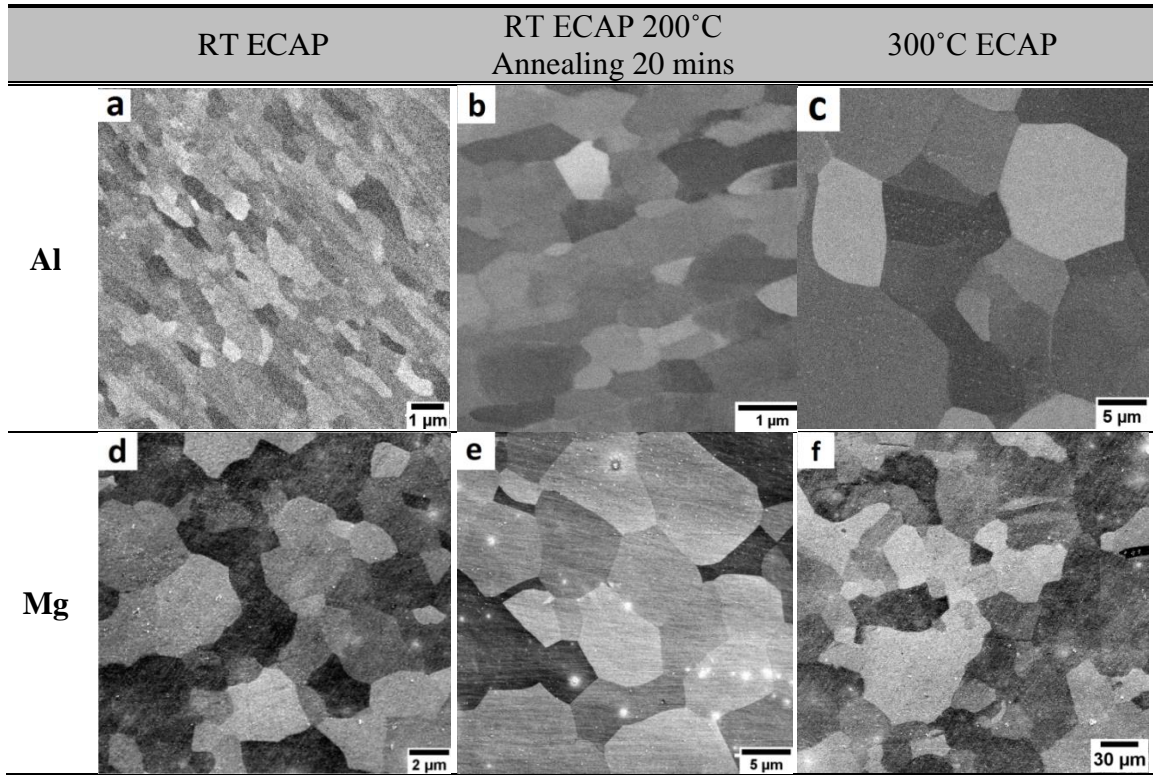


Figure. 4. 7 SEM images for Al and Mg grains in Al80Mg20 compact after different processing conditions

(a) – Al after ECAP at RT; (b) – Al after ECAP at RT and annealing at 200°C; (c) – Al after ECAP at 300°C; (d) – Mg after ECAP at RT; (e) – Mg after ECAP at RT and annealing at 200°C; (f) – Mg after ECAP at 300°C

Compaction by ECAP at room temperature reduced the grain size of as-received chips from 0.71 μm to 0.53 μm for Al and from 6.11 μm to 4.26 μm for Mg. Annealing at temperatures up to 200°C did not have any influence on the aluminium grain size but did raise the grain size of magnesium. After annealing at 300°C the grain size in both aluminium and magnesium parts of the compact increased significantly, while still remaining smaller than the grain sizes in compacts produced by ECAP at 300°C (5.33 μm and 34.62 μm for Al and Mg, respectively.) Although no annealing treatment at temperatures between 200°C and 300°C was conducted, it is sensible to recommend that, in order to reap the benefits of retained ultrafine grained structure, the annealing temperature should not exceed 200°C.

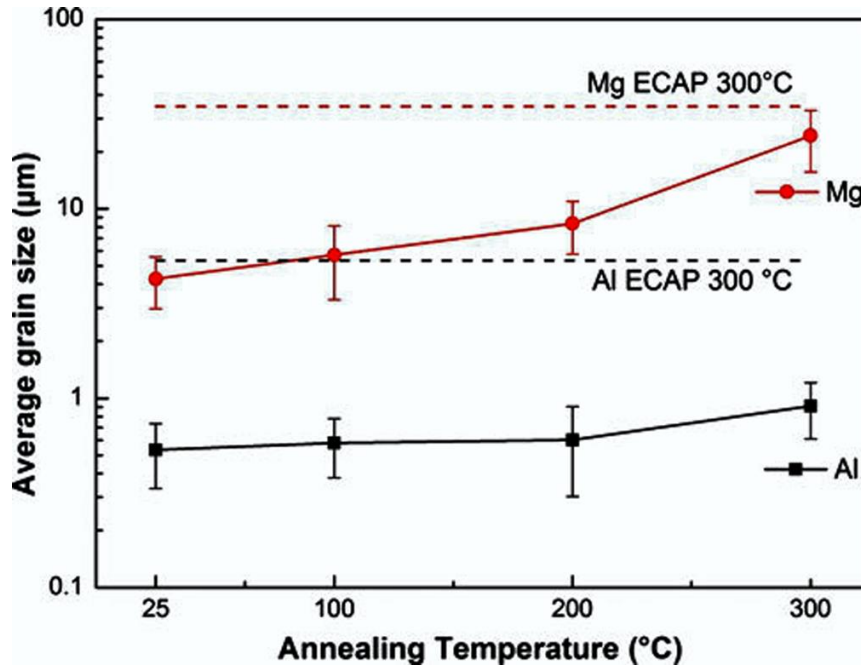


Figure. 4. 8 Average grain size vs. annealing temperature for Al and Mg in Al80Mg20 compacts produced by ECAP at RT using RA (compared to the grain size of compacts produced by ECAP at 300 °C, dashed line)

4.4.3 Mechanical properties

To evaluate the mechanical properties of the compacts obtained, compression tests were carried out. The results are presented in Table 4.2 and Fig. 4.9. It can be seen that ductility of compacts is inversely correlated with the weight fraction of Mg in the compact. After annealing at 200 °C, ductility of the compacts was improved over that of the compacts that were produced by RT ECAP and did not undergo annealing treatment. Still, the ductility of compacts produced by ECAP at 300 °C was much higher. Interestingly, opposite to a common tendency, both the ultimate strength and ductility were raised after ECAP at room temperature followed by annealing and after ECAP at 300 °C, while the yield stress was reduced. This means that the strain hardening capability of the material is substantially increased by this type of processing. The drop in the yield stress after annealing can be rationalised in terms of annihilation of dislocations, which are normally present in materials severely worked by both the initial machining and the subsequent ECAP.

Simultaneous increase of strength and ductility in ultrafine grained materials is still referred to in literature as a 'paradox'. This unusual phenomenon was investigated by Raabe et al. [1], who discussed possible mechanisms of interface strengthening combined with good ductility.

As will be shown below, the two of the mechanisms they proposed, which are most relevant to this study, are: (i) mechanical alloying at the interface due to plastically stimulated mixing beyond equilibrium solubility, and (ii) mechanical mixing based on plasticity driven short-range diffusion, resulting from deformation-induced non-equilibrium vacancies. To understand the ‘interface driven’ unusual properties of hybrid materials, the interface formation was investigated here in some detail.

Table. 4. 2 Mechanical properties of samples under various processing conditions

Material	Processing Conditions	σ_y (MPa)	σ_u (MPa)	δ_u (%)	δ (%)
Al80Mg20	ECAP RT	111.4	137.5	2.4	5.4
	ECAP RT + Annealing at 200°C	98.2	138.11	6.4	13.1
	ECAP 300°C	51.13	159.25	14.5	21.6
Al50Mg50	ECAP RT	79.38	119.94	2.2	5.2
	ECAP RT + Annealing at 200°C	64.17	125.8	7.9	11.3
	ECAP 300°C	46.28	132.08	12.3	17.8
Al20Mg80	ECAP RT	69.58	78.46	1.7	4.7
	ECAP RT + Annealing at 200°C	64.28	90.94	2.6	5.5
	ECAP 300°C	36.73	94.21	9.7	12.7

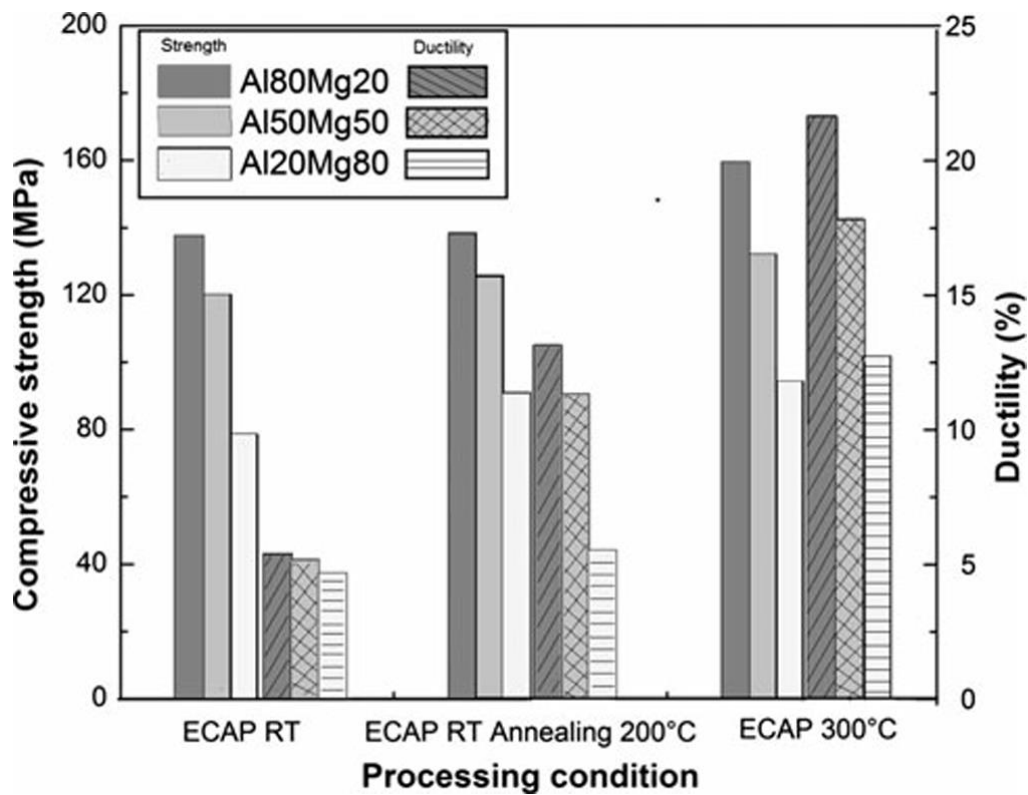


Figure. 4. 9 Compression strength (solid lines) and ductility (dashed lines) vs. processing conditions for three compact compositions

4.4.4 Phase identification

At least for some of processing conditions, the occurrence of diffusion bonding and formation of new intermetallic phases could be expected. XRD was used to identify the phases at Al-Mg interfaces. In the case of room temperature ECAP followed by annealing, no peaks except those associated with elemental Al and Mg were detected. Based on the XRD spectrum (Fig. 4.10), the formation of an intermetallic phase as a result of ECAP at 300°C was established. This phase was identified as Al_3Mg_2 . The observed broadening and reduced height of a diffraction peak associated with this phase can be explained by ultra-fine crystallite size, which, according to TEM data, was about 500 nm [275, 276]. Because of its small thickness (1 μm), another intermetallic phase, $\text{Al}_{12}\text{Mg}_{17}$, whose occurrence will be demonstrated by TEM analysis below, was not detected in the XRD spectrum – possibly due to insufficient precision of the XRD equipment used.

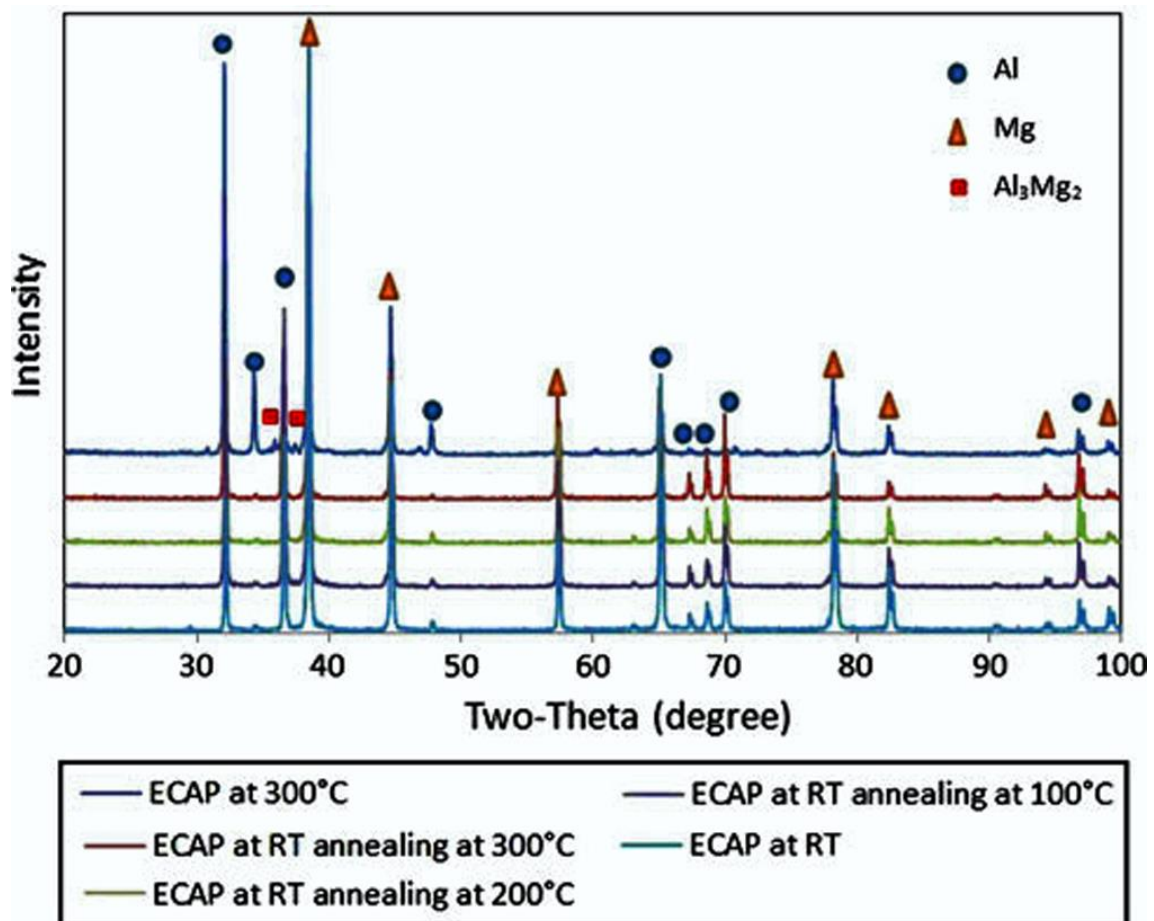


Figure. 4. 10 XRD spectrum of Al50Mg50 produced by ECAP (RA) under different conditions

4.4.5 Electron microscopy characterisation

To investigate the Al-Mg interfaces in greater detail, backscattered electron imaging using SEM and EDX line-scans, Fig. 4.11, were applied. Two interfaces were studied in Al80Mg20 compact after RT ECAP. Scans across an oxide-free and an oxide-containing interface are presented in Figs. 4.11 (a) and (b), respectively. The existence of oxide-free interfaces suggests that oxides at the chips surfaces were ruptured and dispersed by severe deformation. Apparently, oxides were not eliminated at all surfaces, possibly as the number of the ECAP passes used was not large enough. Below, the penetration depth of the atoms diffusing across an interface will be determined from the concentration profiles for the oxide-free interfaces.

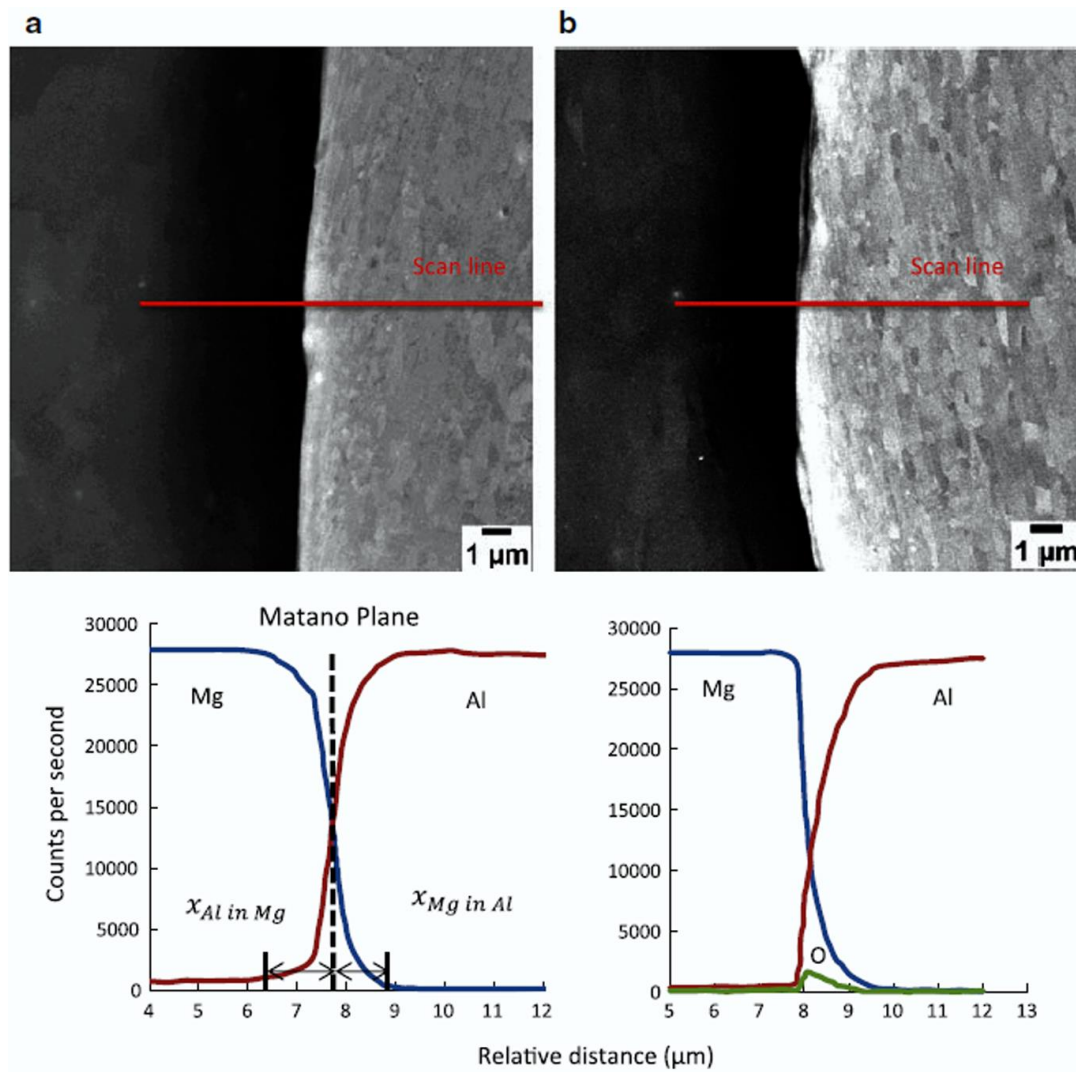


Figure. 4. 11 EDX line scan across an Al/Mg interface (counts per second) for a oxide-free interface and b oxide-containing interface

To identify an appropriate ECAP route for breaking the oxide layers on the chips, thus producing oxide-free interfaces, 100 line scans of the interfaces in compacts produced by Route A and Route B_C ECAP each were carried out. Through these scans it was shown that RA leads to a larger proportion of oxygen-free interfaces (about 83%) than RB_C (about 65%). For Route B_C ECAP the shearing direction in the second pass was within a plane inclined at about 120° to the shearing direction corresponding to the first pass [228]. Considering that chips were already aligned along the shearing direction after the first ECAP pass, the change of the shear plane was not beneficial for rupture of oxides, while for Route A, shearing was accumulated along the same shear plane. This explains why rupture of oxides was more efficient in RA than in RB_C ECAP.

To evaluate the interdiffusion, the penetration depth, x , was measured from graphs presented in Fig. 4.12, where x is defined as the distance between the position of the diffusion front and the Matano plane at a given time t . The diffusion front is defined by the distance where the concentration of the diffusing solute is fixed at 1%.

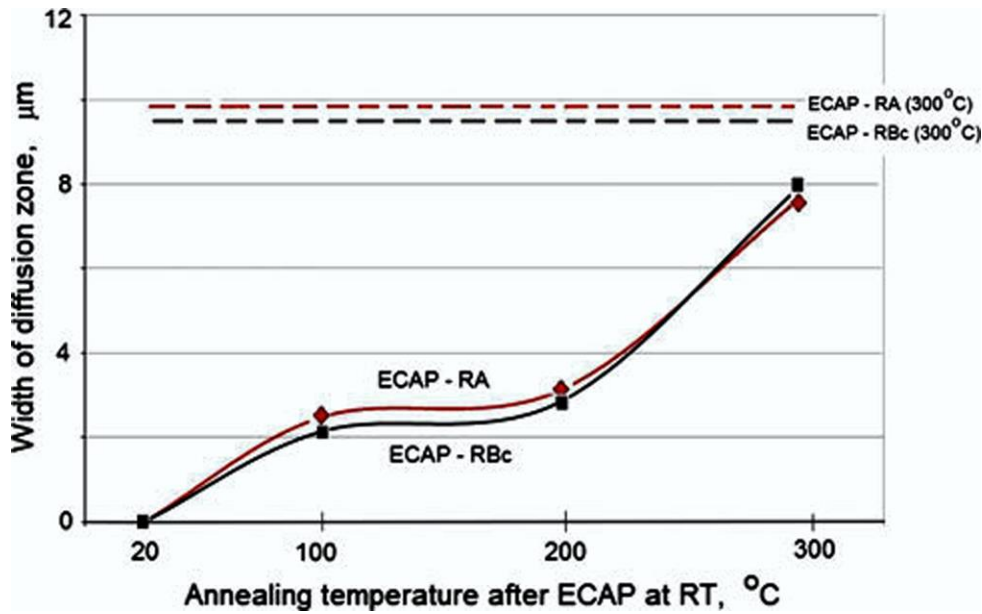


Figure. 4. 12 Interdiffusion zone width (from EDX line scan) vs. the annealing temperature after ECAP at RT (solid lines) compared to the width of interdiffusion zone in samples produced by ECAP at 300°C (dashed lines) for two different processing routes (RA and RBC)

The total interdiffusion length X is given by the sum of the penetration depths of Al in Mg, $x_{Al/Mg}$, and Mg in Al, $x_{Mg/Al}$, which was measured at oxide-free interfaces:

$$X = x_{Al/Mg} + x_{Mg/Al} \quad (4.2)$$

Chapter 4 1st sub-Project - Al/Mg Machining Chips Compacts

In Fig. 4.12, the width of interdiffusion zone is shown versus the annealing temperature after room temperature ECAP. It can be seen that an increase in annealing temperature improves the diffusivities of Al and Mg and Mg in Al resulting in widening of the penetration zone. The data for ECAP at 300°C, shown on Fig. 4.12 by dashed lines, indicate that for this case the interdiffusion layer is about half that for the RT ECAP with subsequent 20 min annealing at 300°C. This is explainable, as the time of exposure to the elevated temperature was shorter in the case of ECAP at 300°C. Furthermore, it can be seen that RA produces a slightly wider interdiffusion zone than RbC for almost all thermomechanical processing conditions considered. Formation of two layers adjacent to the interface with the presence of intermetallic phases, Al_3Mg_2 and $\text{Al}_{12}\text{Mg}_{17}$, is seen in Fig. 4.13. Interestingly, the interdiffusion zone obtained is wider than reported [271], which may be a result of the larger number of ECAP passes used in the present work.

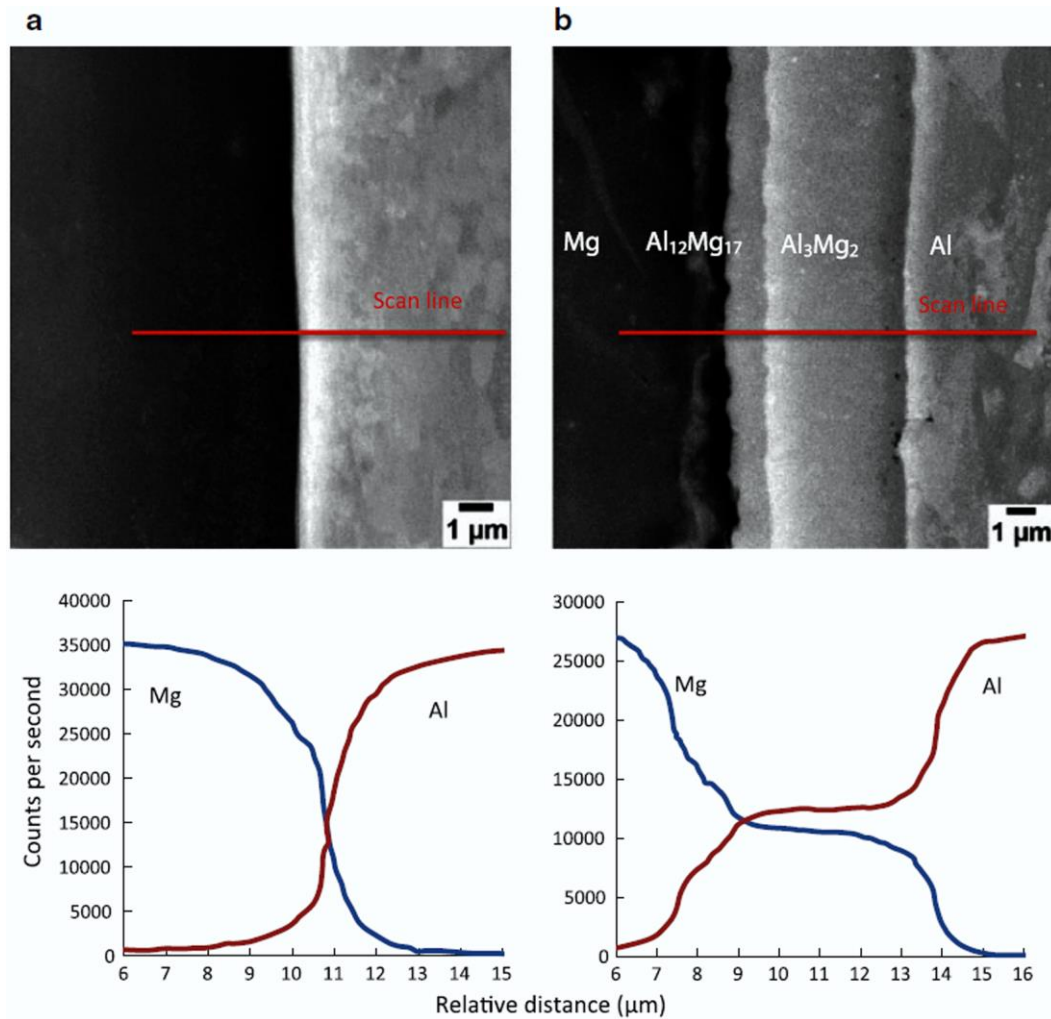


Figure. 4. 13 EDX line scan across an Al/Mg interface (counts per second) for samples produced by: a ECAP at RT (RA) followed by annealing at 200°C; b ECAP at 300°C

The presence of micro-cracks in magnesium at interfaces with Al in Al80Mg20 compact underwent RA at RT, Fig. 4.14, could also have contributed to enhanced diffusivity, since they may form a continuous network of ultrafast transport paths leading to a greater penetration depth, as shown in [100].

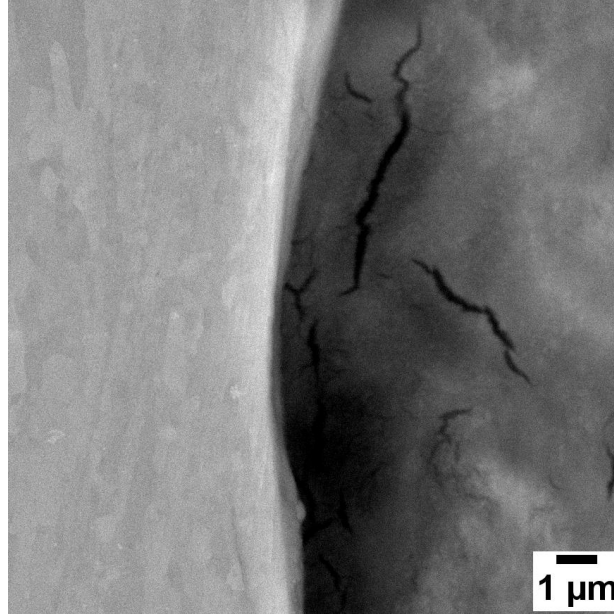


Figure. 4. 14 Microcracks in the Mg constituents of a compact after ECAP at RT

For more detailed identification of the intermetallic phases in the interdiffusion zone at Al/Mg interfaces after ECAP processing at 300 °C, these regions were further analysed by cross-sectional TEM. The bright-field (BF) image in Fig. 4.13a illustrates a multi-layer structure at the interface that comprises a thicker Al_3Mg_2 layer ($\sim 5.7 \mu\text{m}$) adjacent to Al and a thinner $\text{Al}_{12}\text{Mg}_{17}$ layer ($1.3 \mu\text{m}$) adjacent to Mg, in accord with the SEM observations. The selected area electron diffraction (SAED) patterns obtained for multiple grains from individual interdiffusion layers are shown in Fig. 4.13(b-e). These patterns are in excellent agreement with the theoretical patterns calculated for Al_3Mg_2 ($a = 28.24 \text{ \AA}$, space group $Fd\bar{3}m$) and for $\text{Al}_{12}\text{Mg}_{17}$ ($a = 10.54 \text{ \AA}$, space group $I\bar{4}3m$), respectively, thereby verifying the ordered intermetallic structure of the interfacial phases. The $\text{Al}_{12}\text{Mg}_{17}$ phase was found to contain just a monolayer of grains. By contrast, the grains in the Al_3Mg_2 layer show a greater variation. For instance, the grains near the $\text{Al}_3\text{Mg}_2/\text{Al}$ interface are predominantly ultra-fine ($\sim 500 \text{ nm}$), whereas those close to the $\text{Al}_{12}\text{Mg}_{17}/\text{Al}_3\text{Mg}_2$ interface are typically $1\sim 2 \mu\text{m}$ in size. The reasons for such grain size heterogeneity are not obvious. A possible explanation is that the Al_3Mg_2 layer was subjected to a non-uniform shear strain distribution across the layer

thickness causing variation in the extent of dynamic recrystallisation during the ECAP processing.

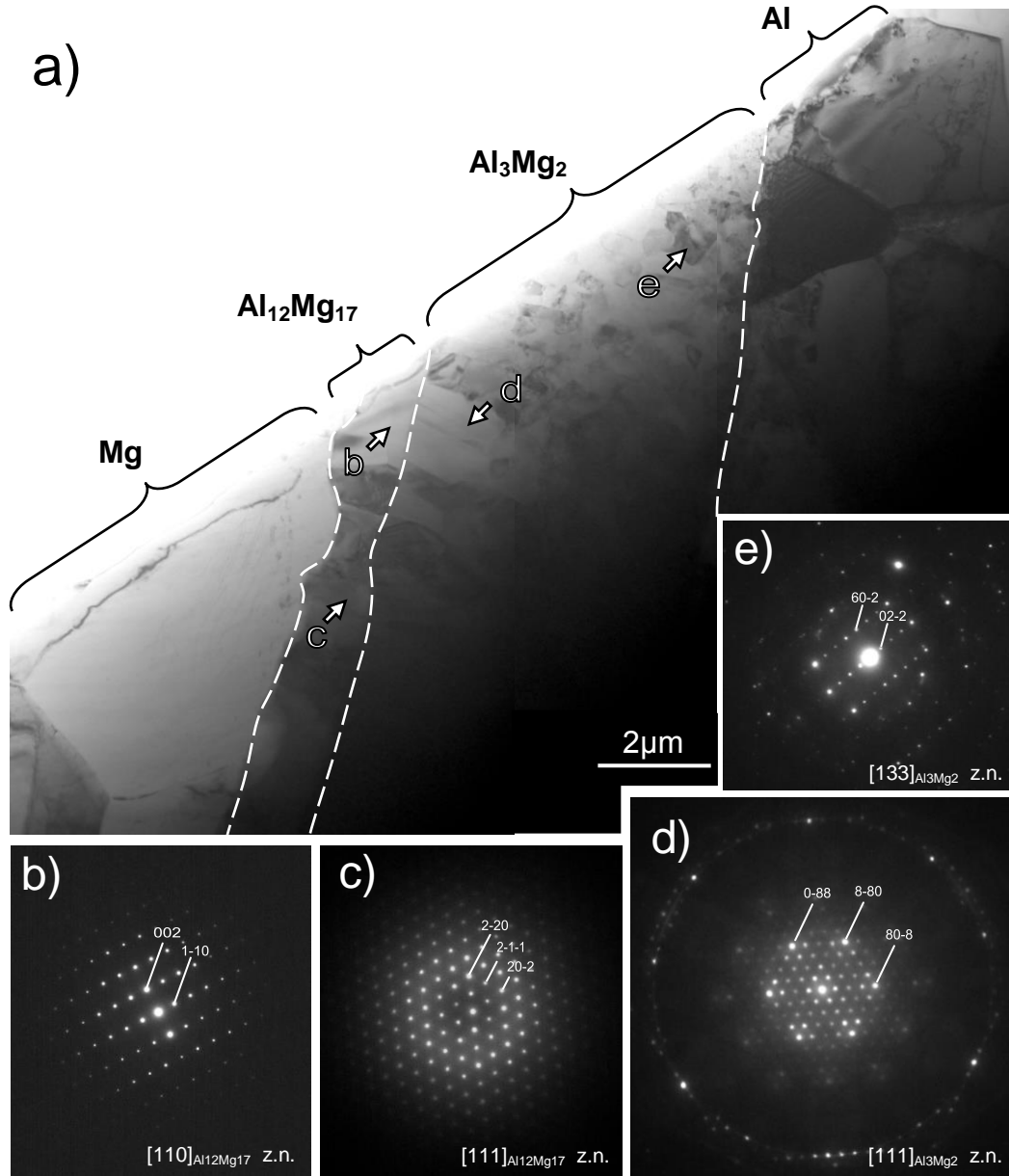


Figure. 4. 15 Al/Mg interdiffusion zone in Al80Mg20 sample processed by ECAP at 300°C. *a* BF-TEM image showing the overview of the interdiffusion zone; *b*, *c* zone-axis SAED patterns recorded for the grains labelled *b* and in the Al₁₂Mg₁₇ layer; and *d*, *e* zone-axis SAED patterns recorded for the grains labelled *s* and *e* in the Al₁₃Mg₂ layer. (All patterns correspond to the same scale)

4.4.5 Nanoindentation characterisation

Nanoindentation testing was performed on eleven samples, processed under different conditions, cf. Table 4.3. An example of the measured properties is shown in Fig. 4.16 for the case of ECAP RBc at 300 °C with 50 nm indentation size. The size of the interdiffusion zone, indicated by a distinct difference in the hardness values, was calculated as a normalised width of this zone perpendicular to the chip edge. As can be seen from the results presented in Table 4.3, the hardness of interdiffusion zone even in the absence of intermetallic components is much higher than the hardness of each constituent material, which explains the improved strength of the hybrid material. Simultaneous increase of ductility and strength with temperature of annealing is associated with an increase of grain size in Al and Mg with temperature. This leads to enhanced ductility and widening of multiple interdiffusion zones, which contributes to strength. A more significant improvement in strength and ductility was obtained with Al/Mg hybrids after ECAP at 300 °C is associated with dynamic recovery of microstructure during processing, with simultaneous formation of intermetallics within interdiffusion zone.

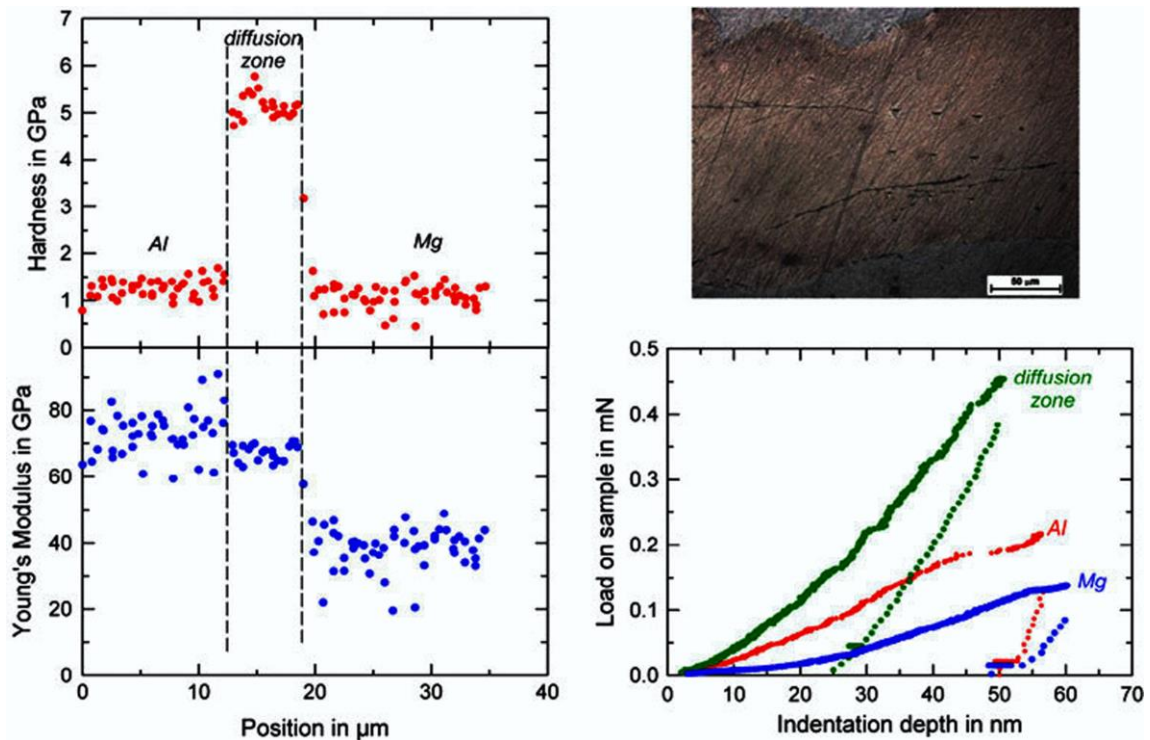


Figure. 4. 16 Results of nanoindentation testing in the case of ECAP RB_C at 300°C with 50nm indentation size

Chapter 4 1st sub-Project - Al/Mg Machining Chips Compacts

Table. 4. 3 Hardness, Young's modulus and width of the interdiffusion zone determined by nanoindentation

No	Processing Conditions	Indentation depth(nm)	Hardness (GPa)			Young's Modulus (GPa)			Interdiffusion zone (μm)
			Al	Mg	Al/Mg	Al	Mg	Al/Mg	
1	RA ECAP (RT)	100	1.23	1.12	2.45	75.6	38.4	55	2.3
		50	1.24	1.05	2.35	70.5	40.1	54	2.5
2	RA ECAP (RT) + Annealing at 100 °C	100	1.31	0.95	2.25	76.2	39.2	100	4.9
		50	1.25	0.95	2.95	75.0	38.0	110	6.1
3	RA ECAP (RT) + Annealing at 300 °C	100	1.05	0.95	4.80	71.9	30.7	95.0	5.5
		50							
4	RA ECAP (300 °C)	100	1.06	1.51	6.75	73.4	34.9	110	12.2
		50	1.51	0.92	8.00	70.0	33.0	120	12.6
5 ^a	RA ECAP (RT)	100	1.42	1.20	3.5	75.8	44.1	140	8.2
		50	1.70		3.8	72.6	40.6	100	7.2
6 ^a	RA ECAP (RT) + Annealing at 100 °C	100	1.19	0.99	3.42	76.9	36.1	130	10.2
		50	1.42	1.12	3.83	77.1	40	150	8.6
7 ^a	RA ECAP (RT) + Annealing at 300 °C	100	1.13	0.95	2.05	69.1	38.8	105	10.5
		50	1.57	1.25	2.82	74.8	40.2	110	10.1
8	RBc ECAP (RT)	100	1.28	0.91	-	73.7	36.9	-	0
		50							
9	RBc ECAP (RT) + Annealing at 100 °C	100	1.22	1.11	2.25	77.4	38.6	90	2.5
		50	1.52	1.30	3.29	70.8	43	90	2.8
10	RBc ECAP (RT) + Annealing at 300 °C	100							
		50	1.32	1.61	2.5	70.5	40.4	100	3.8
11	RBc ECAP (300 °C)	100	1.49	1.06	5.2	74.9	37.2	70	10.0
		50	1.50	1.10	5.2	74.5	40.2	66	7.2

As can be seen from Fig. 4.17, the width of the interdiffusion zone increases with the annealing temperature, but has a tendency to saturate. There is a dependence of this width on the processing route, Route A being more favourable for facilitating interdiffusion. In addition, if ECAP is performed at a higher back-pressure, the width of the interdiffusion zone is increased. (It was more than doubled when the back-pressure was increased from 75/125 MPa to 150/150 MPa.) However, ECAP at 300 °C results in a much broader interdiffusion

zone, with a width that seems not to be achievable by annealing of material processed by RT ECAP in the case when the back-pressure was at a lower level.

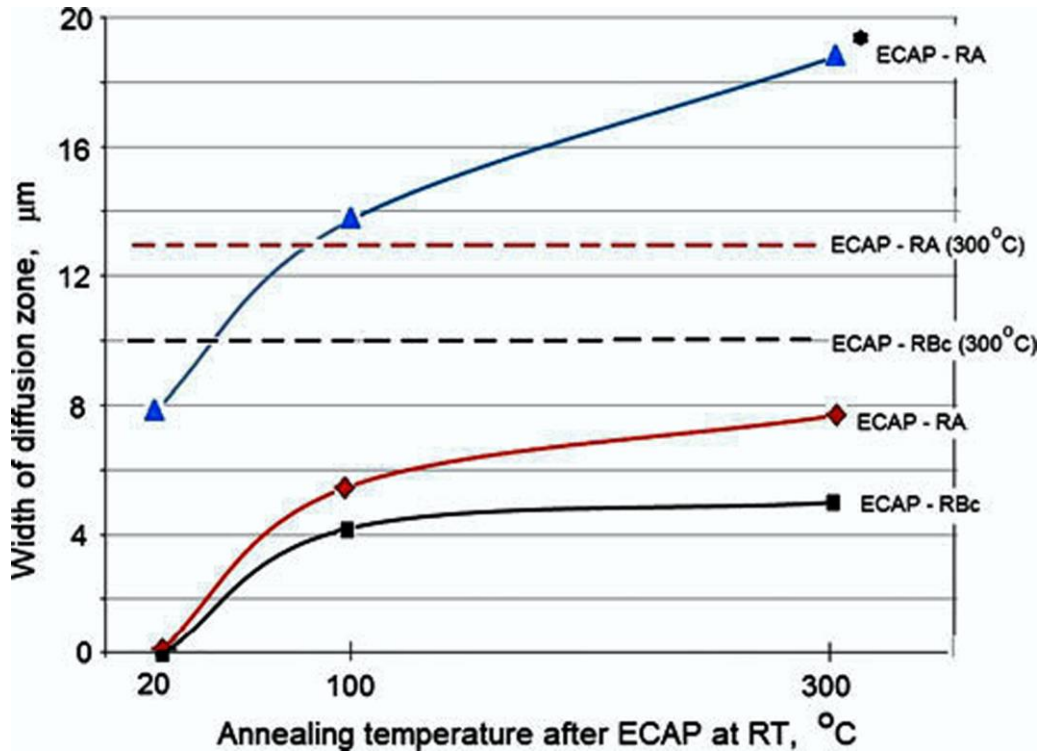


Figure. 4. 17 The width of the interdiffusion zone vs. annealing temperature after compaction by RT ECAP (solid lines) and compaction by ECAP at 300°C (dashed line). An asterisk indicates samples produced at a higher back pressure of 150MPa

4.5 Summary of this chapter

This work showed that multicomponent materials can be manufactured from machining chips by severe plastic deformation. Specifically, ECAP with back pressure was demonstrated to be an efficient consolidation technique for Al and Mg machining chips. The best properties of compacts were obtained for blends with the weight ratio of 80 % Al to 20 % Mg. It was further shown that the RA of ECAP provides more effective oxide breakage and interdiffusion bonding than RBC. Good bonding was achieved after ECAP at RT, which was further enhanced by annealing treatment. It is believed that the ultrafine grain structure resulting from machining and deformation induced vacancies introduced by ECAP is responsible for enhanced interdiffusion between Mg and Al during the annealing, thus promoting the formation of coherent bonding. The fine-grained microstructure was retained up to the annealing temperature of 200°C, providing a good balance of strength and ductility

Chapter 4 1st sub-Project - Al/Mg Machining Chips Compacts

of the compacts. Simultaneous increase in strength and ductility was obtained due to formation of interdiffusion zones and recovery of severely deformed microstructure of the constituent metals. The highest strength and ductility were obtained when ECAP consolidation was performed at the highest temperature used (300°C). This can be rationalised in terms of the formation of intermetallic phases at the interfaces between Al and Mg chips and an increased width of the interdiffusion zones at the interfaces.

Chapter 5 Ultrafine-grained porous titanium and porous titanium/magnesium composites fabricated by space holder-enabled Equal-Channel Angular Pressing

5.1 Outline of this chapter.....	75
5.2 Introduction	75
5.3 Specific experimental procedures and characterisation.....	80
5.3.1 Preparation of Ti/Mg/Si composites by ECAP compaction	80
5.3.2 Synthesis of porous Ti/Mg and porous Ti.....	81
5.3.3 Characterisation of porous Ti/Mg and porous Ti.....	82
5.3.4 Measurement of mechanical properties	83
5.3.5 Characterisation of microstructure of pore walls.....	84
5.3.6 Cell culture and cell viability	85
5.4 Results.....	85
5.4.1 Machinability	85
5.4.2 Porosity and Interconnectivity	86
5.4.3 Mechanical properties	88
5.4.4 Microstructure of the Ti struts in the porous structures	90
5.4.5 Characterisation of morphology of pore walls.....	91
5.4.6 Cell viability.....	93
5.5 Discussion	95
5.5.1 Redistribution of the constituents during ECAP.....	95
5.5.2 ECAP-assisted bonding between the constituents	96
5.6 Summary of this chapter.....	99

5.1 Outline of this chapter

In the second sub-project, an open porosity hybrid as a particular class of multicomponent materials was studied. Porous materials have a broad range of applications owing to their light weight and low stiffness [277]. In this project, the porous structure fabricated was aimed for biomedical applications. Compaction of powders by ECAP using a novel space holder method was employed to fabricate metallic scaffolds with tuneable porosity. Porous Ti and Ti/Mg composites with 60% and 50% percolating porosity were fabricated using powder blends with two kinds of sacrificial space holders. The high compressive strength and good ductility of porous Ti and porous Ti/Mg obtained in this way are believed to be associated with the ultrafine grain structure of the pore walls. To understand that, a detailed electron microscopy investigation was employed to analyse the interface between Ti/Ti and Ti/Mg particles, the grain structures in Ti particles and the topography of pore surfaces. It was found that using the proposed compaction method, high quality bonding between particles was obtained. Comparing with other powder metallurgy methods to fabricate Ti with an open pore structure, where thermal energy supplied by a laser beam or high temperature sintering is essential, the ECAP process conducted at a relatively low temperature of 400°C, was shown to produce unique properties.

5.2 Introduction

The concept of using porous structure to achieve adequate and permanent fixation of a bone implant to the skeletal system was first investigated in 1970s [278, 279]. At that time, instead of open porous structures, materials with a porous surface were extensively studied as a way to achieve implant fixation. Indeed, the solid inner core of an implant was considered to be necessary to provide the mechanical strength for load-bearing applications [279, 280]. As shown in Fig. 5.1, *plasma spraying* is a rapid and cost-efficient method to create a porous surface coating layer on a solid substrate [281]. The spray process is caused by the plasma gas with a typical core temperature that is up to ~20,000°C [149, 281]. The accelerated gas stream with a velocity up to ~ 2000 m s⁻¹ carries and melts the powder then impacts them on the substrate [149, 281]. By this way the porous surface is created.

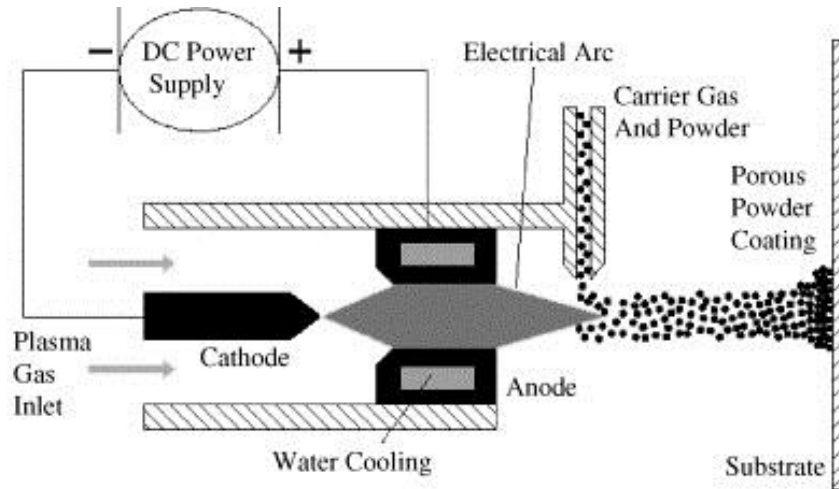


Figure. 5. 1 Schematic illustration of the plasma spraying process [149]

In vitro and in vivo tests were done for tailoring the pore size to achieve high rate of bone ingrowth [278, 282]. Clinical tests showed encouraging results indicating that biological fixation occurred through bone ingrowth. However, there was also a concerning aspect regarding the bone resorption and bone loss caused by stress shielding, owing to excessively high stiffness of the rigid implant. In a clinical trial, over 12% of patients suffered from moderate or severe bone resorption within two years after the implantation [283]. Due to this stress shielding, the use of large and rigid femoral implants was not recommended for patients whose bone mass was initially low [284]. To minimise the stiffness mismatch between the implant and the surrounding bone tissue and achieve optimum load transfer from the artificial implant to the adjacent bone, implants with low elastic modulus are being considered [285]. Based on this demand, new β -titanium alloy compositions with a low elastic modulus have been under development as an alternative to stainless steels, cobalt-based alloys, and α -titanium-based alloys [286, 287]. With porous surface of solid core β -Ti, good fixation of the implant is expected. However, there are still concerns related to this route because solid core material still has higher stiffness than bone. Besides, bone mass is lost and bone formation ability decreases as people age [288]. To further decrease the Young's modulus of the implant and achieve a higher degree of osseointegrated fixation, a highly open porous structure appears to be more attractive than a solid implant with porous surface [289]. Currently, highly porous Ti based materials are attracting a great deal of attention from the academic community and medical implant industry alike, as Ti and its alloys possess outstanding mechanical properties, corrosion resistance, and biocompatibility [287, 290-292].

The excessively high stiffness of an implant material and the associated stress shielding effect can readily be reduced by introducing porosity [149]. However, a downside of this approach is a significant loss of strength, which reduces the ability of the implant to withstand the mechanical loads placed upon it during service [149, 293]. Furthermore, with insufficient stiffness, interface de-bonding and implant loosening may occur [294]. Thus, the first and biggest problem porous Ti-based materials are facing today is inadequate strength. There are a number of factors that can affect the compressive strength of the porous structure, including the level of porosity, pore size, pore shape and interconnectivity of the structure [149, 150, 295]. To mimic the biomechanical properties of natural bone, these parameters need to be tailored to be close to those of the surrounding bone tissue. Ultimately, the strength of the structure depends on the properties of pore walls [277].

In the case of open porous Ti produced from Ti powders, bonding between the particles and their microstructure determine the properties of pore walls. In one of the current approaches, particles are bonded together by laser melting. *Selective laser melting* is a representative promising additive manufacturing technology that can be used to fabricate porous orthopedic implants [296-298]. As shown in Fig. 5.2, the porous structure architecture is built from Ti powders by using a laser to melt and solidify the required geometry layer-by-layer [299]. However, for the biomedical application, this technique is limited by the lack of control of the microstructure and the surface roughness due to thermal gradients that develop during rapid solidification [300].

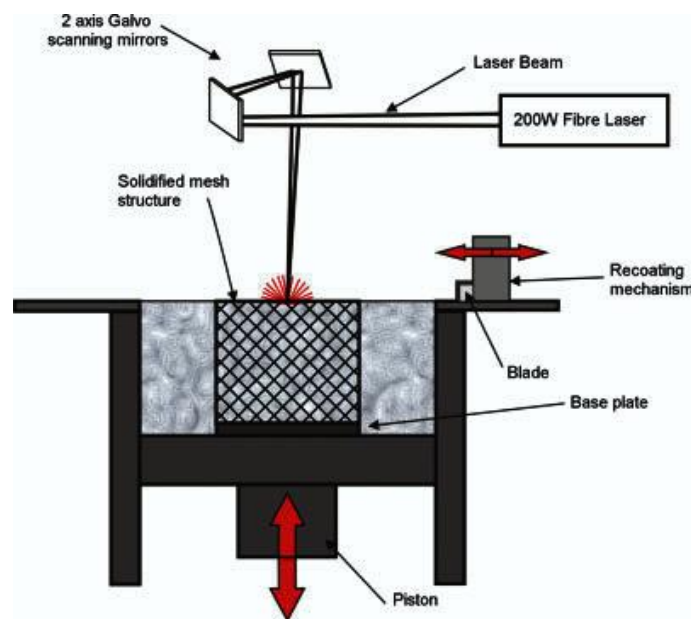


Figure. 5. 2 Schematic illustration of selective laser melting process [301]

Porous Ti can also be manufactured by *slurry foaming* [302] and *freeze casting* [303], whereby pores are formed by foaming agent and frozen solvent crystals, respectively, which do not have principle difference. To remove them from the green compacts and create interconnected pores, drying and freeze-drying processes are used [304]. Another extensively studied facile approach to fabricate porous Ti is the *space holder* method [305, 306]. As illustrated in Fig. 5.3, this process starts with mixing the sacrificial space holder powder – Mg with Ti powder and followed by hot pressing them to a green compact. After machining the compact to the desired shape, the sacrificial powders can be removed by dissolving or evaporating.

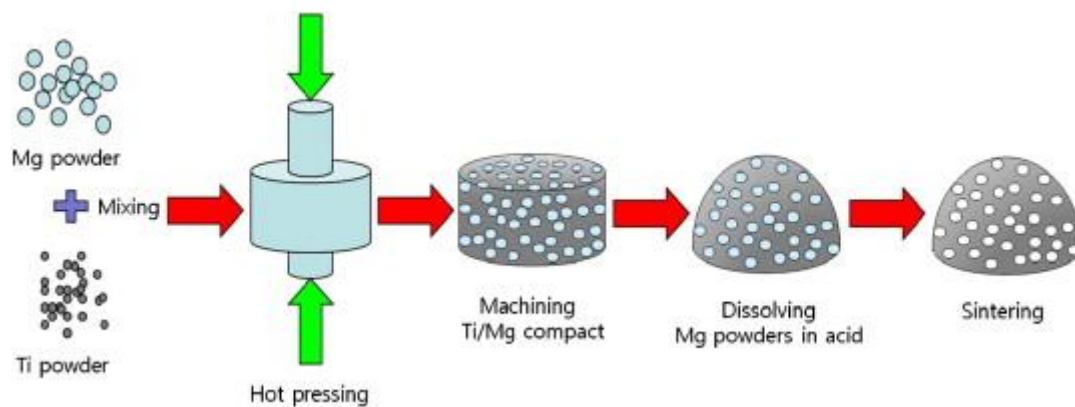


Figure. 5. 3 Schematic illustration of fabrication of porous Ti using space holder method [307]

Although the above mentioned three methods involve different routes, they can all be classified as powder metallurgy route and sintering in vacuum at around 1300°C invariably needs to be conducted as the last processing step to enhance inter-particle bonding and increase the strength of the struts [308]. In other words, a large thermal energy is needed to either melt or vacuum sinter Ti particles to enhance diffusivity of Ti and oxygen atoms in the oxide layer thus achieving sufficient bonding between Ti particles. Not only is this heat input costly [63], but it also causes undesirable grain coarsening. By contrast, the processing route proposed below does not involve the use of excessively high temperature and as such makes it possible to obtain a fine grain structure of the porous product.

Indeed, grain size is a key microstructural factor that has a significant effect on nearly all aspects of the physical and mechanical behaviour of polycrystalline metals. It also affects their chemical and biochemical response to the surrounding media, such as bodily fluids and tissues [12]. Recently, ultrafine-grained (UFG) and especially nano-grained (NG) metals

came to the fore in the context of implant applications as a promising alternative to alloys, which in many cases have adverse biological effects due to the release of alloying elements [309-312]. A particular avenue to obtaining bulk UFG/NG materials is severe plastic deformation (SPD) [12, 13]. Grain structure refinement and modification by SPD has been successfully used to obtain biomedical materials with improved biocompatibility and mechanical performance [313-318]. Comprehensive reviews of studies on cellular response to UFG/NG materials produced by SPD can be found in Refs. [319, 320]. The SPD techniques, such as equal channel angular pressing (ECAP), which were initially developed for processing bulk billets, can also be used for powder compaction [321]. An important benefit of ECAP with back-pressure as a means of powder compaction is that it can be carried out at lower temperatures than the conventional powder consolidation techniques. Owing to severe shear deformation combined with high hydrostatic pressure, this method offers higher density, finer microstructure, and possibly stronger bonding of the compact than traditional powder metallurgy techniques do [192, 193]. In this context, the experience of fabrication of multicomponent materials using ECAP compaction can be used in conjunction with the space holder method to replace the traditional powder consolidation techniques.

This approach, combining the mentioned benefits of compaction of powders by ECAP with the use of sacrificial space-holder powders, was consequently followed in the present study. The novelty was the use of two types of space-holder particles. Blends of commercial purity (CP) Ti powder as the base material and Mg and Si powders as the space-holders were used. CP Ti, rather than a commonly used alloy, such as Ti-6Al-4V, was chosen because it does not release toxic alloying elements in the body. Likewise, neither Mg nor Si causes cytotoxicity [322, 323]. Adding Mg had three objectives. The first one was to increase the processability of the mixture during deformation. The second one was to explore the potential of a porous Ti/Mg composite. The philosophy behind this concept is a recent proposal to add Mg as a biodegradable material to Ti strut, thus providing higher mechanical strength to the implant initially, while enabling its load bearing capacity and stiffness to decrease gradually as Mg dissolves away giving way to the ingrowing bone tissue [324, 325]. Finally, the use of Mg as space-holder in titanium makes it possible to provide the compact with machinability required for implant manufacturing. Porosity can be introduced after machining by leaching Mg particles from the manufactured implant.

In what follows, the procedures used to fabricate porous Ti and Ti/Mg composites with different levels of porosity using compaction of powders by ECAP, with subsequent removal

of sacrificial space-holder particles will be described. Then the results of mechanical testing and analysis of pore structure and the character of bonding between particles as a function of the processing conditions will be presented. Finally, cell response to the structures produced will be discussed.

5.3 Specific experimental procedures and characterisation

5.3.1 Preparation of Ti/Mg/Si composites by ECAP compaction

CP Ti powder (Grade 2, -325 mesh, Sumitomo, Japan), Mg granules (99.6% pure, -200 mesh, Materion, USA) and Si particles (99.9% pure, -40 mesh, Hokin, China) were used as the starting materials. Scanning electron microscopy (SEM) images of the powders are shown in Fig. 5.4, the average particle size being $49.5 \pm 9.5 \mu\text{m}$, $89.7 \pm 16.8 \mu\text{m}$, and $415.7 \pm 39.5 \mu\text{m}$, respectively. Since the level of porosity and pore size both play a critical role in bone ingrowth, the minimum requirement for pore size for cell migration and transport is considered to be $\sim 100 \mu\text{m}$; higher porosity and larger pore size result in greater bone ingrowth [150]. The composition of Ti/Mg/Si powder blend by volume ratio was chosen as Ti40Mg10Si50 (40 vol.% Ti, 10 vol.% Mg and 50 vol.% Si). 50 vol.% of Si is necessary here to ensure pore interconnectivity once this constituent is removed.

The powder blends were weighted in an argon-filled glove box, then mixed and stirred with 1 wt.% of isopropyl alcohol for 3 mins. Subsequently, this elemental mixture slurry was taken from glove box in a sealed container and poured into the entry channel of ECAP die, whilst the exit channel was blocked by a back-pressure punch. The mixture was cold compacted at 50 MPa and dried in at room temperature for 5 mins. Cold compaction as a pre-ECAP step was used to lock the position of each constituent because otherwise powder segregation occurred when the isopropyl alcohol evaporated and the adhesion force between particles disappeared. It is worth noting that good blending and avoiding segregation are essential to ensure a uniform distribution of all components in the composite and the desired interconnectivity of the porous structure. ECAP consolidation process was conducted at 400°C. One, two and four ECAP passes were used following Route Bc, which involves rotation of the sample by 90° about the long sample axis between the passes. The detailed operation of the ECAP apparatus was described in the chapter 4. The equivalent true strain (ϵ)

the material underwent in one pass was 1.15. With increasing number of ECAP passes a very large strain was accumulated. The cumulative equivalent strain was chosen as the main variable in this study to investigate the effect of plastic deformation of Ti/Mg/Si compacts on the mechanical properties and the biocompatibility of the porous structures produced.

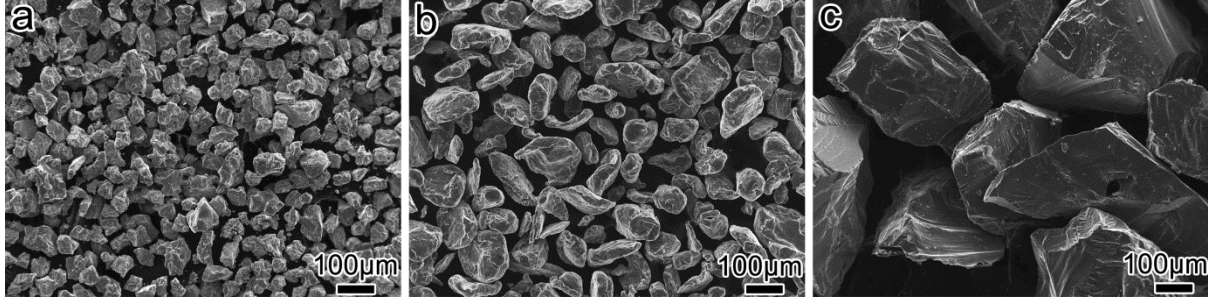
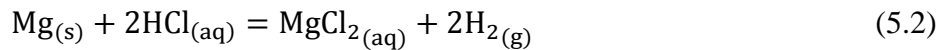
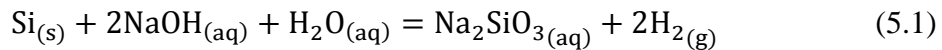


Figure. 5. 4 Scanning electron microscopy of the initial powder materials (a): titanium powder; (b) magnesium powder and (c) silicon powder

5.3.2 Synthesis of porous Ti/Mg and porous Ti

The compacts produced by ECAP were soaked in aqueous 5M sodium hydroxide (NaOH) solution at 60°C for 12 h to remove Si, washed and ultrasonically cleaned with distilled warm water. This recipe is similar to the one used as alkali treatment to make Ti surface bioactive for apatite precipitation by forming a thin sodium titanate layer [326]. To remove magnesium - the second sacrificial ingredient, porous Ti/Mg composites were immersed in 100 mM hydrochloric acid (HCl) at room temperature for 6 h followed by distilled warm water wash and air dry for 24 h. The reactions used to remove Si and Mg are given below:



The evolution of the material from Ti/Mg/Si compact to porous Ti/Mg composite with porosity of 50%, and then to porous Ti with 60% porosity can be followed in Fig. 5.5. The Ti/Mg composite seen in Fig. 5.5b was obtained by removing Si particles using reaction (5.1), while porous Ti depicted in Fig. 5.5c was fabricated as a next step, by leaching Mg out of the Ti/Mg composite according to reaction (5.2). Altogether, three types of materials (Ti/Mg/Si, Ti/Mg, and Ti) were considered - two of them (Ti/Mg and Ti) with porosity - using three ECAP histories: one, two, and four passes. Hence, six types of porous structures were investigated.

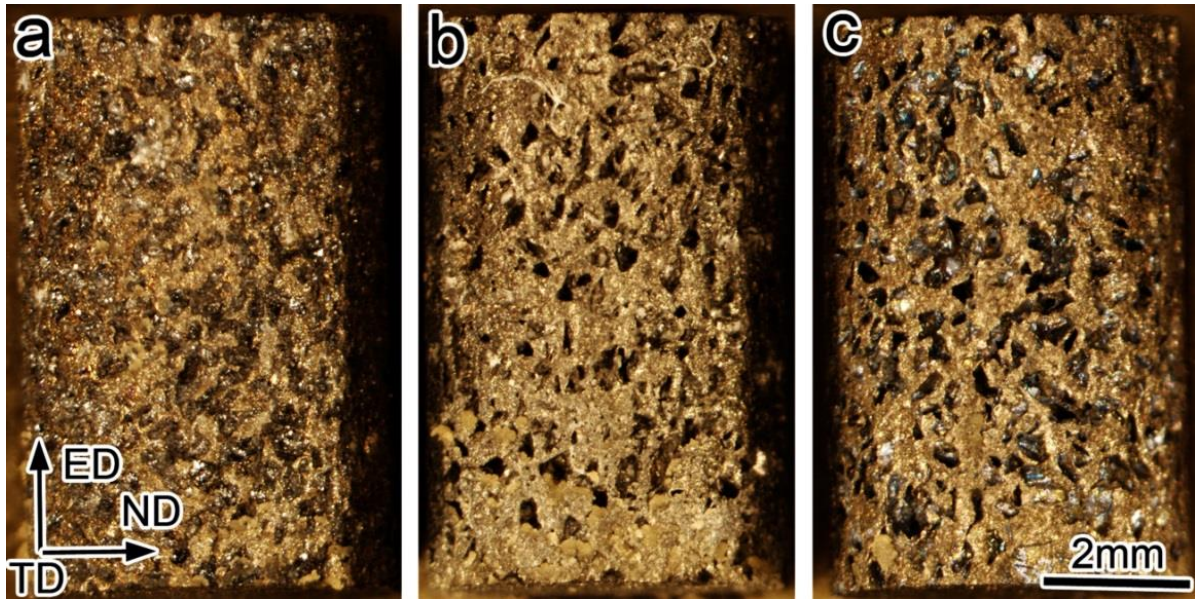


Figure. 5. 5 Optical micrographs of (a) the initial Ti/Mg/Si compact after compaction by a single ECAP pass, (b) porous Ti/Mg composite after Si particles were leached out, and (c) porous Ti after Mg granules were removed

5.3.3 Characterisation of porous Ti/Mg and porous Ti

A low-magnification overview of the porous structures was obtained using Olympus SZX-16 stereo optical microscope with digital camera. The morphology of the pores was examined using JEOL 7001 field emission gun (FEG) scanning electron microscope (SEM) and FEI Quanta FEG SEM. Porosity and pore interconnectivity were studied using SkyScan 1173 (Kontich, Belgium) micro computed tomography scanner (μ -CT). The basis of X-ray μ -CT is X-ray radiography, in which an X-ray beam is sent on a sample and the transmitted beam is recorded on a detector, as shown in Fig. 5.6 [327]. The contrast is caused by the difference in the photon absorbance of the components in the sample. In the case of porous structure, the pores do not absorb X-ray and generate high brightness. On the contrary, according to Beer-Lambert law, only a fraction of X-ray can be transmitted through pore wall material, which results in low brightness. By rotating the sample stage, the multiple angular views of the sample are able to be collected. With the aid of computation, they can be reconstructed to form a complete 3D representation of the internal microstructure over the sample [327].

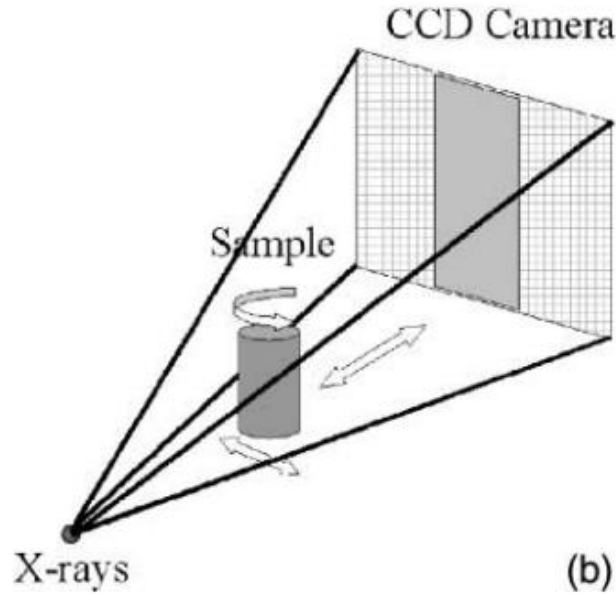


Figure. 5. 6 Schematic illustration of the working principle of micro-CT [327]

5.3.4 Measurement of mechanical properties

In order to evaluate the mechanical properties of porous Ti/Mg and porous Ti, uniaxial compression tests were conducted on cylindrical specimens with the height of 7 mm and diameter of 4.5 mm, which are shown in Figs. 5.5b and 5.5c. It should be noted that tensile tests were not carried out because compression tests are more widely accepted in this application and more available data can be used for comparison [328-331]. Besides, machining of tensile specimens from a porous material is challenging, and tensile tests on such specimens are prone to large scatter. However, the shortcoming of compression tests is also worth noting here. During the compressing test, alongside the deformation of the specimen, the testing setup (including the platens and the cross-head of the Instron machine) also deform slightly. Therefore, the apparent Young's modulus is lower than the true Young's modulus of the specimen material. To account for the compliance of the testing setup, the following equation was used:

$$\frac{1}{E^*} = \frac{1}{E} + \frac{A}{Kl} \quad (5.3)$$

where K is the compliance of the testing machine, A is the cross-sectional area and l the length of the specimen; E is the true Young's modulus of the specimen material (bulk titanium) and E^* is the apparent Young's modulus, as determined from the slope of the elastic part of the stress-strain curve.

To determine the elastic compliance of the Instron machine, testing of a pure bulk titanium specimen (with a known Young's modulus) was done on the basis of the above equation. The compliance of the machine was calculated to be 90.1 GPa mm.

Compression test samples were cut along the ECAP direction by wire cutting. Compression tests were carried out using an Instron 5982 machine with a cross-head velocity of 0.007 mm/s corresponding to a nominal strain rate of 10^{-3} s^{-1} .

5.3.5 Characterisation of microstructure of pore walls

With increasing number of ECAP passes, a higher degree of grain refinement and better bonding were expected in pore walls in Ti. To measure the grain size and interfacial microstructure, JEOL 7001 FEG SEM equipped with OI Aztec electron backscattered diffraction (EBSD) system and 200 kV FEI Tecnai F20 FEG scanning transmission electron microscope (STEM) equipped with Bruker Quantax 400 STEM X-ray analysis system were used. EBSD samples were prepared by hand grind/polishing followed by ion beam milling using precision ion polishing system (PIPS). Transmission electron microscopy (TEM) samples were prepared by wedge polishing using an Allied MultiPrep™ system and ion beam milling using PIPS.

The TEM sample prepared by wedge polishing is illustrated in Fig. 5.7. Comparing with traditional TEM preparation methods where parallel polishing with flat surface is used, here sample is polished using a wedge at an angle. Consequently, the electron transparent area is located at the tip of the sample. The procedure conducted in this sub-project was based the standard method stated in Ref. [332]. Followed by the mechanical polishing, ion beam milling was carried out to further thin the tip.

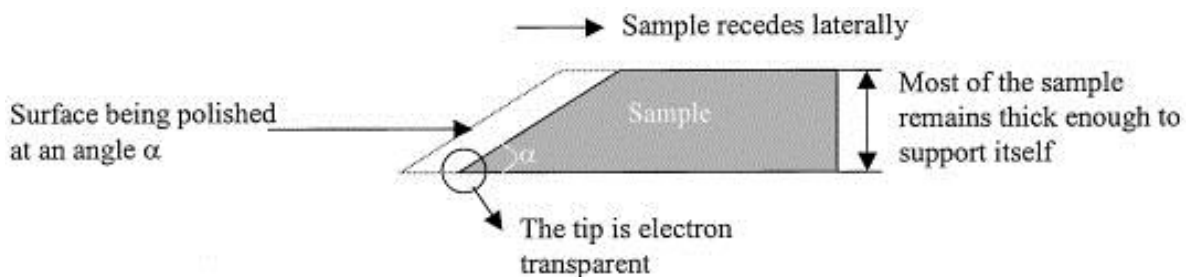


Figure. 5. 7 Schematic illustration of wedge polishing [333]

5.3.6 Cell culture and cell viability

Cell compatibility was investigated by in vitro test using preosteoblast cell line MC3T3-E1. Cells were cultured in α -Minimal Essential Media (Gibco, Life Technologies) supplemented with 10% Foetal Bovine Serum (Gibco, Life Technologies), 16.8mM HEPES buffer (Gibco, Life Technologies), 1% Penicillin/Streptomycin (Gibco, Life Technologies) and incubated at humidified incubator at 37°C, 5%CO₂. At 70% confluence, cells were harvested and plated at a density of 1×10^4 cells per well in a 96 multiwell plate. Porous Ti disc with 5 mm diameter and 1 mm thickness were placed in a 96 multi-well plate and seeded with 1×10^4 cells per well. Positive control wells containing dense Grade 2 Ti samples of the same size were set up in parallel. Experiment was set up in triplicate and plates were incubated at 37°C, 5% CO₂. Cell viability was determined by MTS assay (Cell Titer 96 Aqueous One Solution Cell Proliferation Assay, Promega) at day 3 and day 7 following manufacturer instructions. For SEM analysis, cells were fixed onto the porous Ti discs using 2.5% glutaraldehyde in 0.1M sodium cacodylate buffer for 4 hours and postfixes in 1% osmium tetroxide for 2 hours at room temperature. The fixed samples were then dehydrated in an ethanol series followed by a hexamethyldisilazane drying procedure. Finally, all samples were air dried for 30 mins, sputter-coated with gold, and characterised using an FEI Nova NanoSEM.

5.4 Results

5.4.1 Machinability

Machinability is usually an overlooked property, despite being a determining factor in fabrication of a desired shape of the implant. The importance of machinability of the compact, and the advantages of the space holder method in this regard were recently discussed by Kim et al. [307]. It was found that because Mg has higher strength and elastic modulus than NaCl as a space holder, the transverse rupture strength of Ti/Mg compact is higher than that of Ti/NaCl. This also leads to better machinability of Ti/Mg compacts. To verify the feasibility of machining the Ti₄₀Mg₁₀Si₅₀ composite fabricated by ECAP compaction, turning, drilling and wire cutting were performed on the compacts. Wire cut samples are shown in Fig. 5.5a and for turning and drilling, a hollow screw with the external thread M10 \times 1 \times 5 (shown in Fig. 5.8a) and inner diameter of 6 mm (shown in Fig. 5.8b) was fabricated. The hollow version mimics a cannulated screw. The figure demonstrates the integrity of the structure

after machining and subsequent leaching of the sacrificial material. Moreover, with a closer inspection of Fig. 5.8(c,d) it can be seen that no cracks initiated from the interfaces between pores and Ti struts, which indicates good bonding at interfaces between Si and Ti/Mg particles. With large volume fraction of Si particles this could be criticized by reduce of tool life especially for high-speed steel used in this study. However, cost-effective methodologies have been established for instance the use of fine reinforcements and polycrystalline diamond tooling [334].

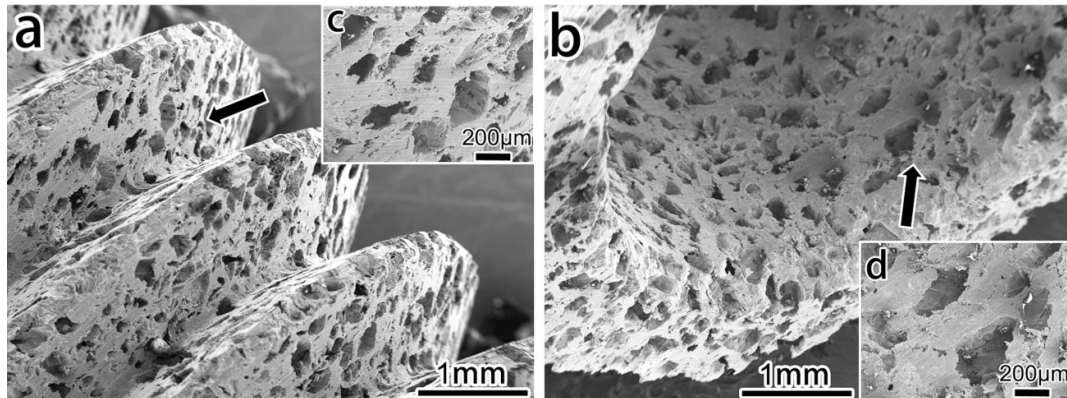


Figure. 5. 8 SEM images of (a) external thread fabricated by turning and (b) internal hollow core produced by drilling. Inserts (c) and (d) are the corresponding enlarged images

5.4.2 Porosity and interconnectivity

Pore morphology in the porous materials produced is presented in Fig. 5.9. Cylindrical samples 12 mm in diameter and 5 mm in height were cut into two halves. One half was made to porous Ti/Mg and the other one to porous Ti by the leaching techniques described above. They were characterised by μ -CT, and the corresponding images are presented in Fig. 5.9. It can be seen that pores are distributed uniformly, which indicates that the mixing of the three constituent powders was homogeneous. The μ -CT data confirm 100% interconnectivity in all six samples. This full interconnectivity is a result of the volume fraction of Si particles being sufficient high. The level of porosity in Ti/Mg and Ti were calculated to be 50% and 60%, respectively. It should be mentioned that during wet mixing Ti and Mg particles adhered to Si granules and after the latter were removed, Mg particles were exposed to open air. Percolating porosity in porous Ti/Mg enables the use of this material in partly bioresorbable implants. The Mg constituent will be dissolved in bodily fluids providing the surrounding bone tissue with the ability to grow into a porous Ti scaffold that is left. The average pore size and wall thickness calculated from the μ -CT results are presented in Fig. 5.10. It is seen

that the fourth ECAP pass gives rise to a slight increase in the average pore size and wall thickness of the porous Ti/Mg composite after two ECAP passes. In contrast, for porous Ti, an increase in the number of ECAP passes is accompanied with a substantial increase in both the pore size and the wall thickness. This may be associated with a redistribution of the constituents during ECAP. This observation will be explained in detail in section 5.5.1.

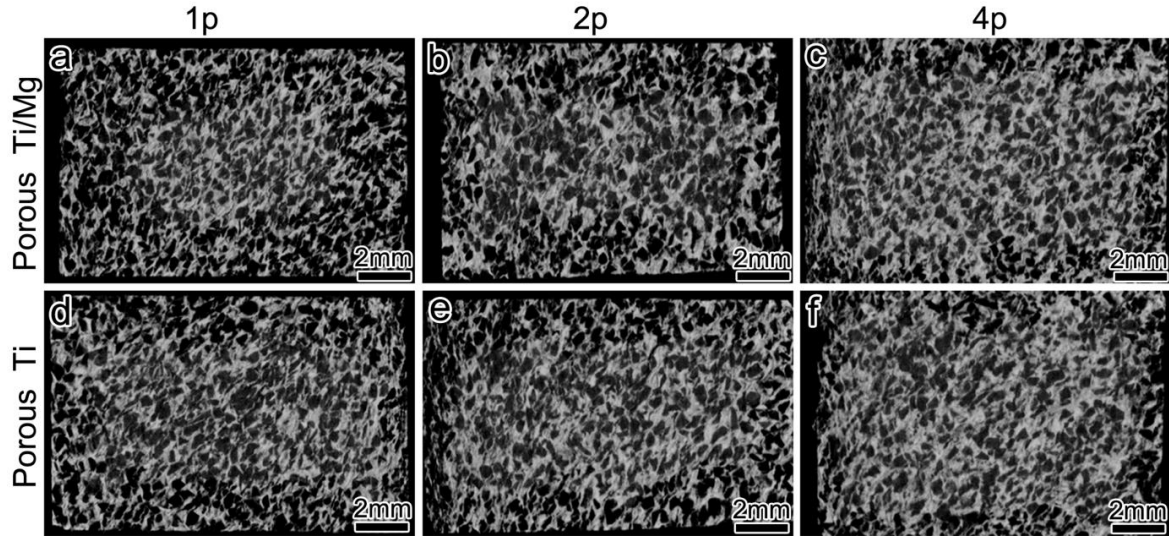


Figure. 5. 9 Micro-CT images for the porous Ti/Mg and porous Ti produced by ECAP compaction after (a,d) 1 pass, (b,e) 2 passes and (c,f) 4 passes

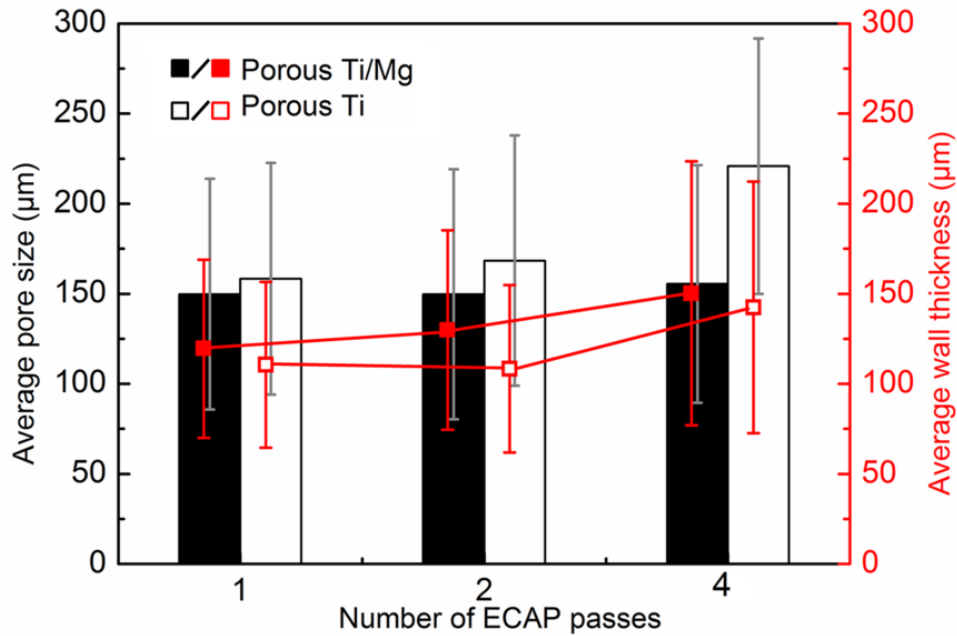


Figure. 5. 10 Average pore size and average wall thickness of porous Ti/Mg and porous Ti produced by ECAP compaction of Ti, Mg and Si particles with subsequent removal of sacrificial material

5.4.3 Mechanical properties

Fig. 5.11 shows representative stress-strain curves for the six kinds of porous materials investigated. Due to the elimination of sintering at 1300°C in the processing schedule used, the oxygen content of the materials produced is believed to be low and the curves do not show brittle behaviour [307, 335]. In the case of porous Ti and porous Ti/Mg whose processing history involved 4 ECAP passes, a strain hardening region is observed after plastic yielding. A reasonably good combination of compressive strength and ductility as reflected in the strain to failure was obtained, with the Ti/Mg composite that experienced 4 ECAP passes in its processing history showing the best results. The compressive strength and Young's modulus of the materials tested derived from the stress-strain curves are presented in Fig. 5.11. In determining the Young's modulus, the compliance of the testing machine, measured in separate compression tests on bulk pure Ti, was taken into account. The average values and the error bars in Fig. 5.12 were determined from three stress-strain curves measured for each material. Clearly with 10 vol.% of Mg efficiently bonded to Ti particles, porous Ti/Mg composites with 50% porosity have higher strength and elastic modulus than porous Ti with 60% of porosity. Also, a trend of increasing strength and elastic modulus with the number of ECAP passes is seen. After 4 ECAP passes, the compressive strength and Young's modulus of porous Ti/Mg composite are 168.2 ± 7.7 MPa and 5.7 ± 0.2 GPa, respectively. A drop in the magnitude of strength and elastic modulus to, respectively, 122.3 ± 9.4 MPa and 3.9 ± 0.5 GPa after removal of Mg was recorded. This result also indicates that with this amount of Mg particles, they did not hinder the bonding between Ti particles. Therefore once they were removed the Ti scaffold still retained a sufficiently high strength.

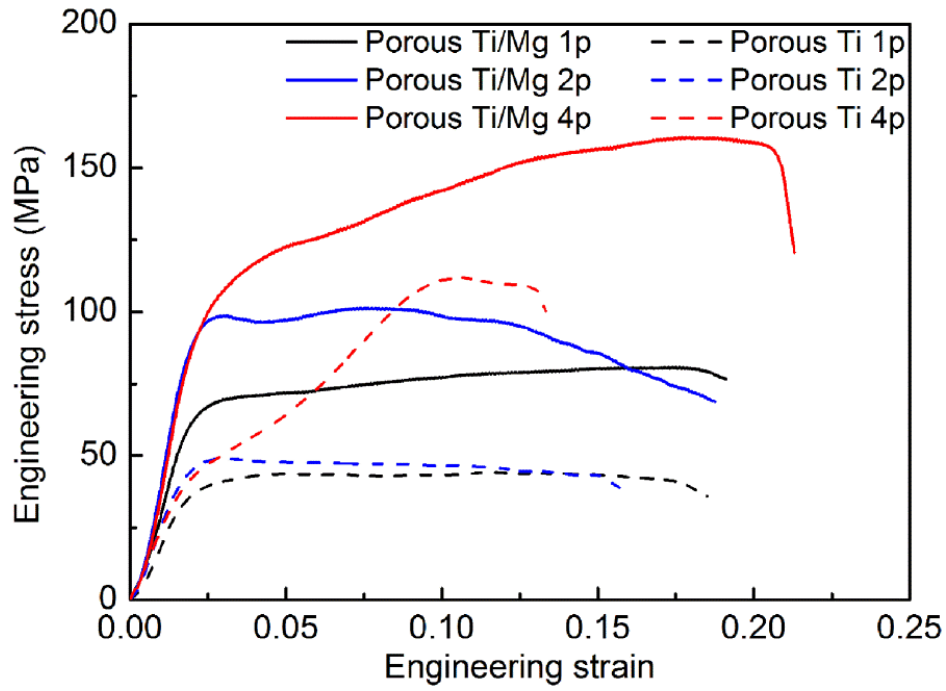


Figure. 5. 11 Engineering stress-strain curves for porous Ti/Mg and porous Ti for different numbers of ECAP passes

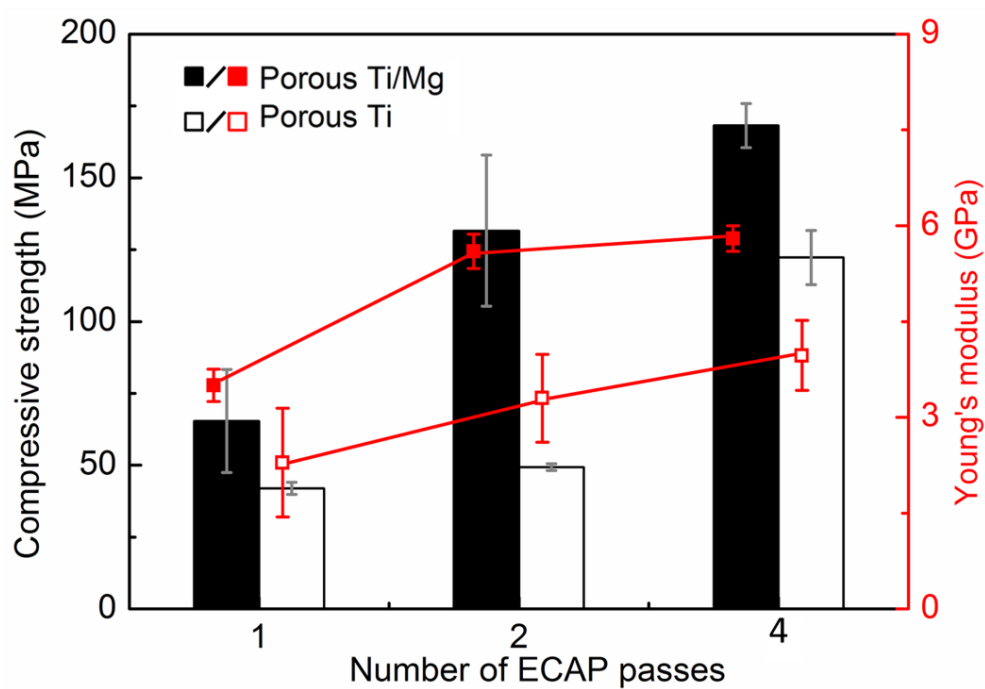


Figure. 5. 12 Compressive strength and Young's modulus of porous Ti/Mg and porous Ti produced by ECAP compaction of Ti, Mg and Si particles with subsequent removal of sacrificial material

5.4.4 Microstructure of the Ti struts in the porous structures

Grain refinement evolution with increasing number of ECAP passes is presented by coloured EBSD maps in Fig. 5.13. A misorientation of 15° was chosen to constitute a threshold value for high angle grain boundaries (HAGB); boundaries with misorientations below 15° are considered as low angle (or subgrain) boundaries. Measurements of grain size were made directly from the EBSD images using the linear intercept method. As shown in Fig. 5.14, an increase in the number of ECAP passes from 1 to 4 led to a grain refinement within the final Ti struts from $1.86 \pm 1.08 \mu\text{m}$ to $789 \pm 335 \text{ nm}$. With its average grain size in the sub-micron range, this material can be categorized as an UFG one [12].

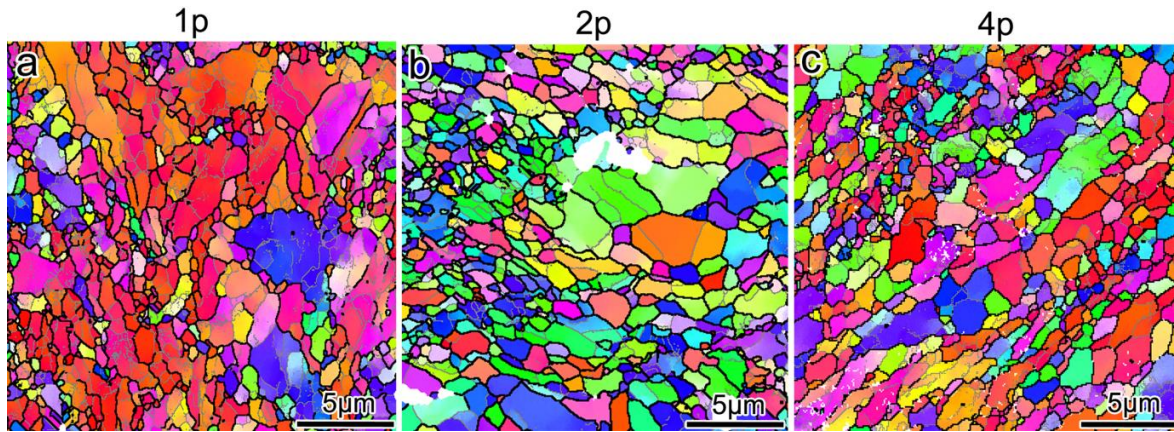


Figure. 5. 13 EBSD grain orientation maps for Ti struts after ECAP processing of (a) 1 pass, (b) 2 passes, and (c) 4 passes. The white area in Fig. 12 (b) corresponds to non-indexed pixels. Black lines denote high angle grain boundaries (HAGBs).

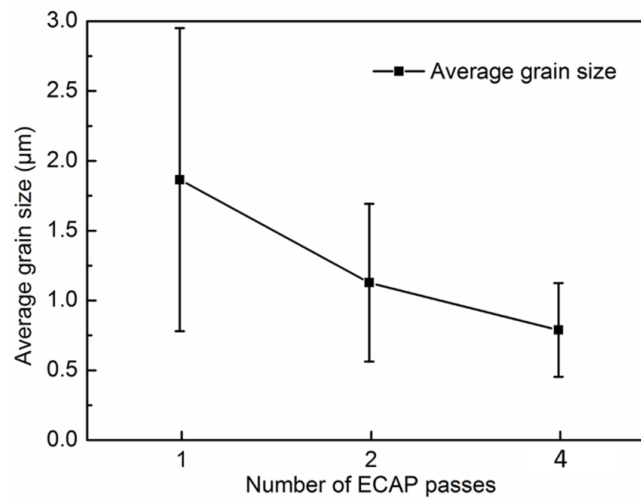


Figure. 5. 14 Evolution of average grain size in Ti struts with increasing number of ECAP passes.

To verify the grain size estimated from EBSD data, additional TEM measurements were carried out on specimens that underwent 4 ECAP passes; representative micrographs are shown in Fig. 5.15. From the bright field (BF) and dark field (DF) images, the occurrence of grains in the range from 50 to 200 nm is evident. This means at least part of the grain population can be classified as nano grains. The inset Fig. 5.15 (c) presents a continuous ring and suggests a random misorientation and high population of high angle grain boundaries.

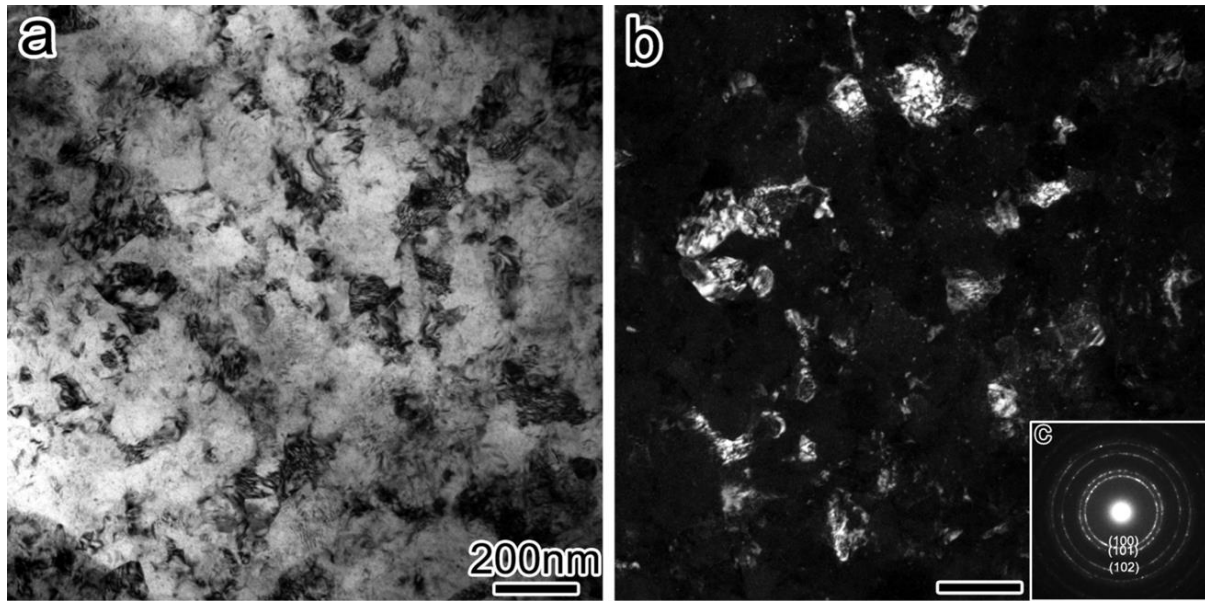
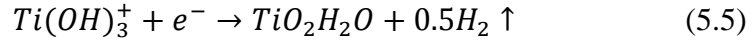
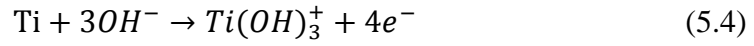


Figure. 5. 15 TEM images of cell wall Ti subjected to 4 ECAP passes with (a) bright field image, (b) tilted dark field image, and inset (c) showing the corresponding SAD pattern using the aperture diameter of 0.75 μm .

5.4.5 Characterisation of morphology of pore walls

The above results show that the porous structures produced by the methods described are tuneable and have adequate mechanical strength and ductility. However, to achieve rapid and stable osteogenesis, suitable pore surface morphology and chemistry are essential [336, 337]. The pore surface topography in porous Ti is presented in SEM pictures shown in Fig. 5.16. After removal of Si particles, two kinds of pore surface topography were observed. One - marked by black arrows in Fig. 5.16 (a, b) - is smooth and featureless. The other, indicated by red arrows, is rough. It is believed to be associated with the areas where the oxide layer on Ti particles was broken during deformation and after Si particles were removed, NaOH solvent reacted with fresh Ti to form titanate. The chemical reactions involved are shown below [338]:



Analysis was conducted based on more than 100 pores for each condition of porous Ti, i.e. those stemming from initial compacts processed by 1, 2, and 4 ECAP passes. Statistical analysis revealed that the proportion of pores possessing a rough surface increased from 18.7 % after 1 pass to 51.8 % after 2 passes and then further to 73.4 % after 4 passes. This trend can be explained by a higher incidence of oxide layer breakage with the increasing number of ECAP passes. The increase in the proportion of rough surfaces was accompanied with a decline in the surface roughness. A decrease of surface roughness with the number of ECAP passes is documented in Fig. 5.17. After Si particles were removed by NaOH 5M at 60°C, a porous titanate surface was formed, as shown in Figs. 5.17 (a-c). In the case of a four-pass sample, nearly globular particles with the average size of $320 \text{ nm} \pm 77 \text{ nm}$ and a smoother surface than that after one and two ECAP passes were observed. To remove Mg, 100 mM HCl was used and the surface morphology was changed. Topography features in Fig. 17 (f) have the smallest scale and correspond to the smoothest pore surface. Because these features were located on the pore surfaces, we could not conduct surface topography measurements by atomic force microscopy. Nevertheless, from SEM characterisation the trend of decreasing roughness with increasing number of ECAP passes is clear. It is also worth noting that this decreased pore surface roughness is believed to be an important factor in the enhanced strength and stiffness of the porous Ti [339].

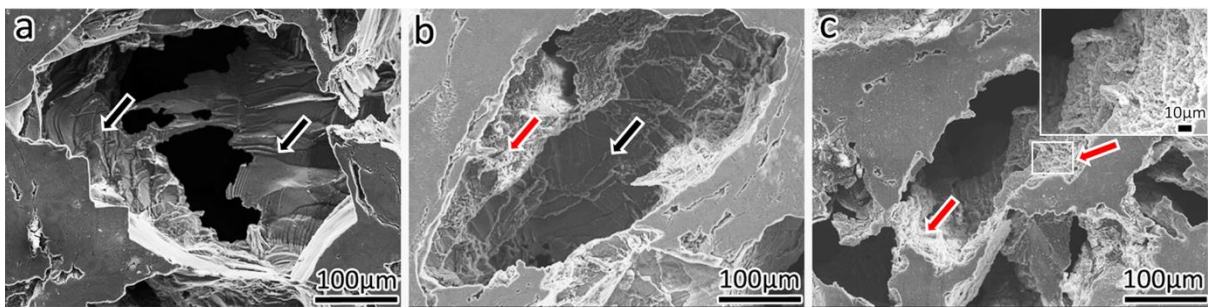


Figure. 5. 16 Three conditions of pore surfaces in porous Ti: (a) completely smooth surface, (b) partially smooth and partially rough surfaces, and (c) completely rough portions of a surface. The inset in (c) shows surface features at high magnification

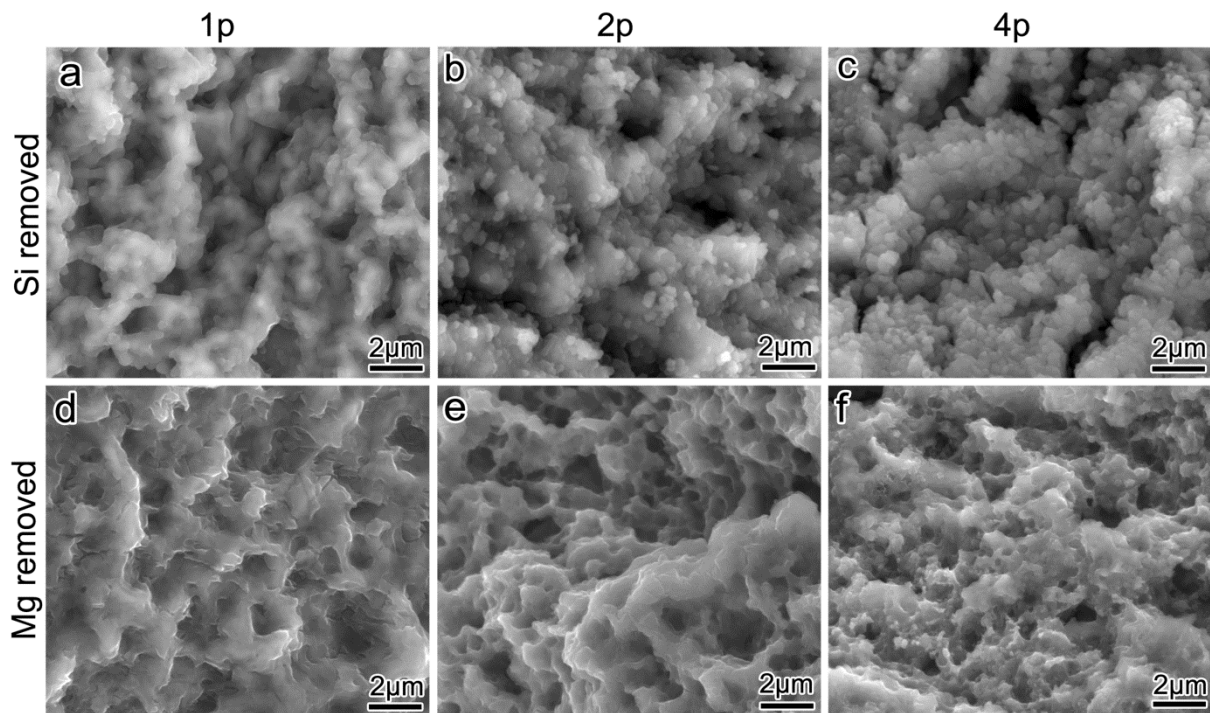


Figure. 5. 17 Representative SEM images of surfaces of pore walls in Ti (a-c) after removal of Si particles by 5M NaOH, (d-f) after subsequent removal of Mg particles by 100 mM HCl.

Note the evolution of the surface features with increasing number of ECAP passes

5.4.6 Cell viability

Since the fabrication route proposed is new, it is necessary to do a preliminary cell viability test to verify the biocompatibility of the porous Ti fabricated using this processing recipe. As shown in Fig. 5.18, based on the measurements of the metabolic activity, in short-term (3 days) there was no significant difference in terms of the MC3T3-E1 preosteoblast cell proliferation between porous and solid Ti, which indicates that viable cells and initial attachment did not depend much on the structure during three-day incubation. However, 4 days later the number of viable cells on porous four-pass Ti was increased substantially and was higher than for one- and two-pass porous Ti or bulk Ti. This result suggests that, based on 7 days incubation, the pore surface morphology of porous Ti that went through four ECAP passes at the compaction stage was most favourable for cell proliferation. Since it is generally accepted that micro/nanotopology influences the proliferation of MC3T3-E1 preosteoblast cells [340], this higher cell viability can be presumably explained by the largest surface area with micro/nanotopography features in the four-pass material. However, due to the difficulties of conducting the atomic force microscopy measurements on inclined pore walls, the surface roughness could not be quantitatively analysed here. Moreover, it is also generally

believed that the cell viability can be affected by the chemical compositions of the surface. The compositions of the culture media and the protein adsorption on the Ti surface can be altered by the ion release from the surface and the surface charge [341]. However, in this study, because all the porous Ti specimens prepared for cell viability tests were treated in a consistent way and also because we did not have access to X-ray photoelectron spectroscopy, the influence of the surface chemical composition of the surface on cell viability was not investigated in greater depth.

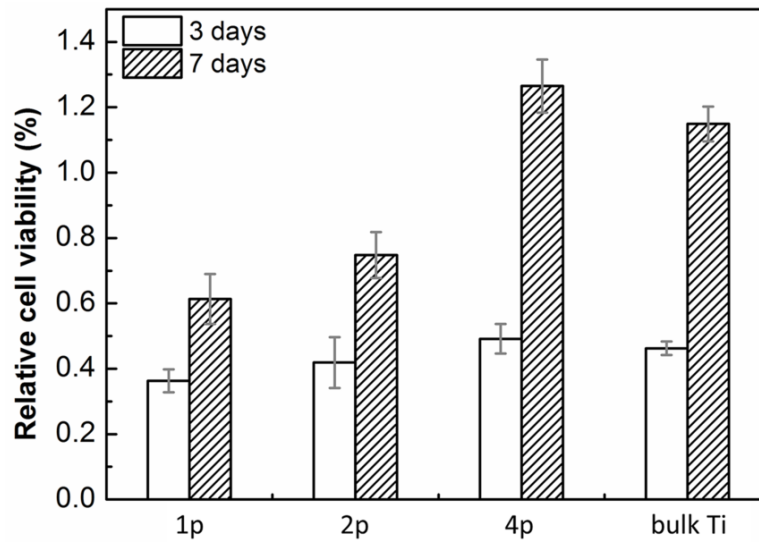


Figure. 5. 18 Cell viability measured by MTS assay after culturing for 3 and 7 days on the porous Ti scaffolds from 1, 2,4 ECAP processes.

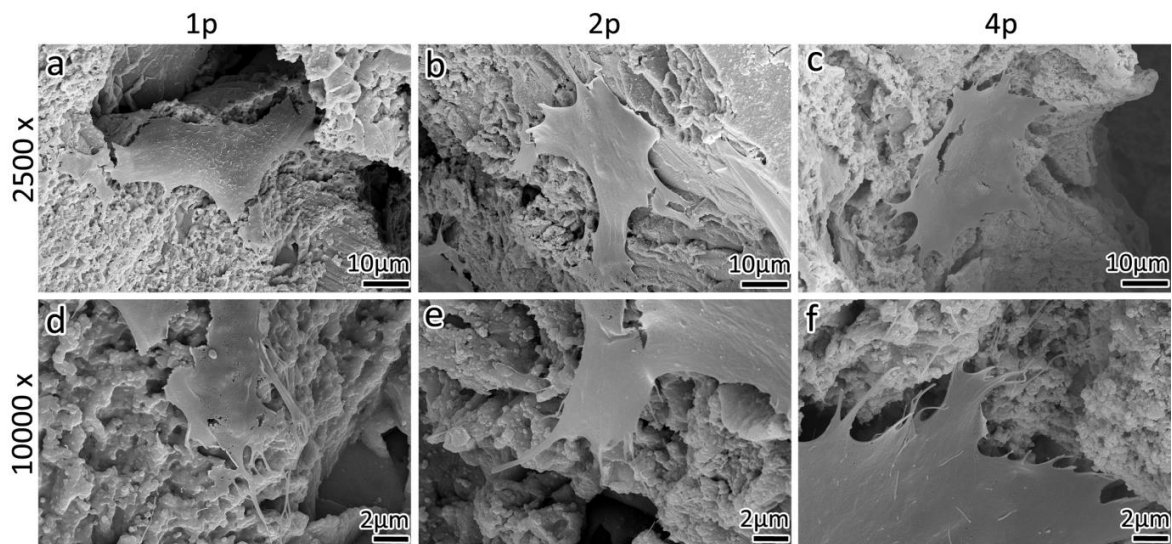


Figure. 5. 19 SEM images of preosteoblast MC3T3-E1 cells cultured for 3 days on porous Ti 1p, 2p and 4p at the magnification of 2500× (a-c) and the magnification of 10000× with details of filopodia (d-f).

Despite the difference of the roughness of the porous titanate surface in the materials experienced different numbers of ECAP passes, cells were flattened and attached to the inclined porous titanate surfaces, Fig. 5.19 (a-c). In addition, the spanning of pores by cells was not observed, which indicates that the average pore size achieved in this study (158.4 – 220.1 μm) is ideal for ingrowth of cells. With higher magnification shown in Fig. 5.19 (d-f), the lamellipodia and filopodia were developed and interacted with the porous titanate substrate manifested as membrane tethers. The cell-substrate interaction observed in SEM images suggests that the surfaces produced by the present processing sequence are beneficial for cell attachment.

5.5 Discussion

5.5.1 Redistribution of the constituents during ECAP

The observed increase of pore size and wall thickness with the increasing number of ECAP passes during the compaction of the elemental powder blends follows that redistribution of Ti, Mg and Si occurred during processing. The distribution of the different elements in the green compacts of Ti/Mg/Si powder consolidated by ECAP is illustrated by backscattered electron (BSE) images based on the atomic number (Z) contrast, cf. Fig. 5.20 (a-c). It is seen that Ti particles were heavily deformed and merged with neighbouring Ti, Mg, or Si particles after the first pass. No fragmentation of Si particles is seen in Fig. 5.20 (d, g). A fraction of Mg-rich regions (Mg particles) have an elongated shape, which indicates that they went through heavy shear deformation, Fig. 5.20 (j). However, the rest of Mg regions retained their original shapes, as one region is marked by arrow in Fig. 5.20 (j). When the composite underwent further ECAP passes, Si particles tended to fracture, whilst Mg and Ti particles as softer constituents were ‘extruded’ into the voids created by the fracturing. In the samples with four-pass history almost all Mg constituents were elongated and located predominantly around Si particles, Fig. 5.20 (l). Some Si particles are delineated by dashed lines in Fig. 5.20 (f, i, l). From these images it can also be surmised that clustering or agglomeration of Si took place. Si agglomeration can also be found in samples after two ECAP passes, yet to a lesser extent, Fig. (b, e, h). Almost no clustering was observed for the single ECAP-pass material, Fig. 5.20 (d, j).

Redistribution of particles in a composite during processing is not a new finding [342]. However, in this study, due to a mismatch of Young’s modulus and particle size of the

constituent particles, redistribution caused segregation of Ti and Si particles yet resulted in a more uniform distribution and size refinement of Mg particles. The level of Ti and Si particle agglomeration produced by ECAP processing is regarded as beneficial, since it promoted larger pore size and stronger struts without having a detrimental effect on porosity and pore interconnectivity.

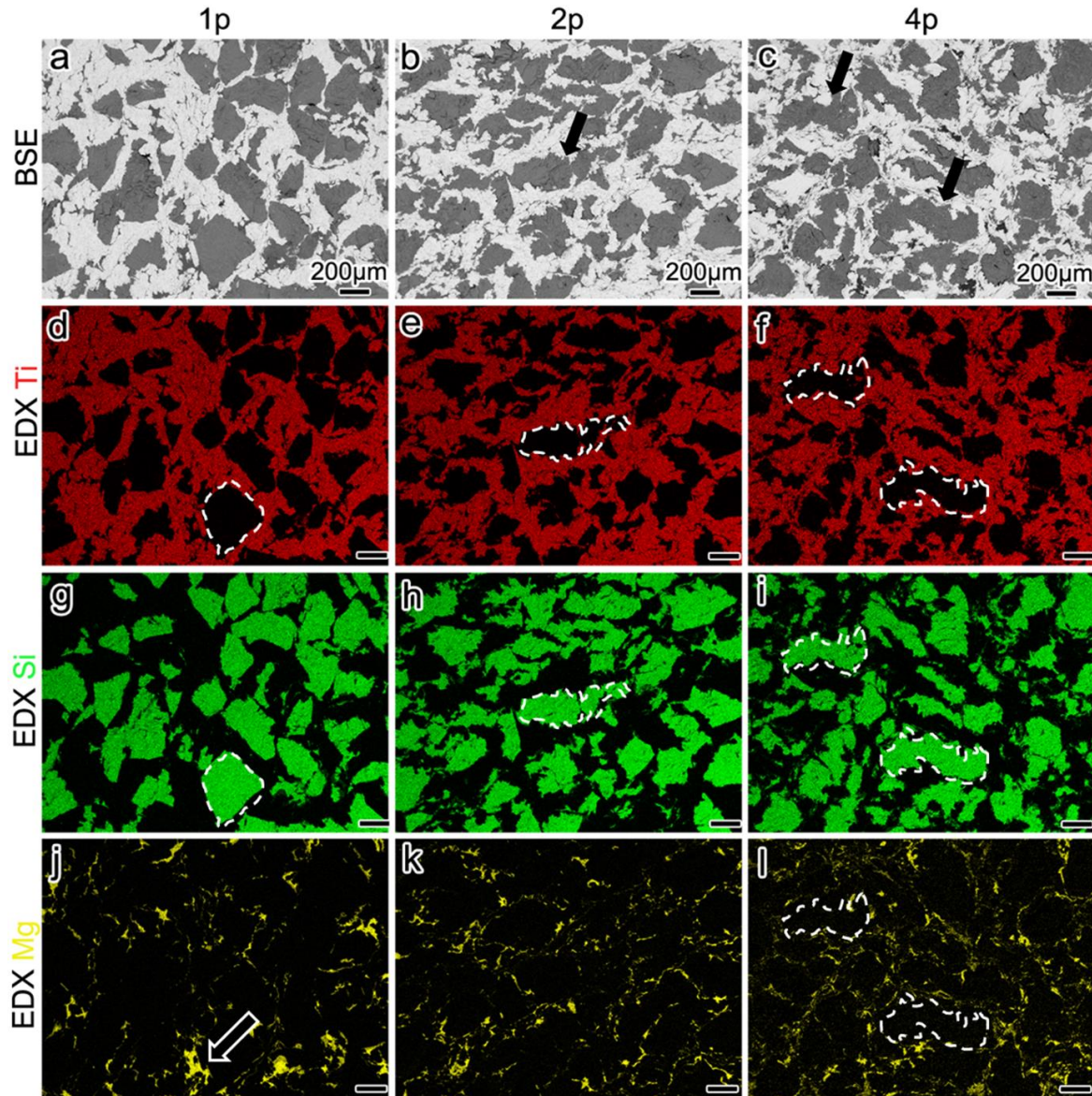


Figure. 5. 20 SEM-BSE images (a-c) and SEM-EDX mappings (d-l) of Ti/Mg/Si compacts after 1, 2 and 4 ECAP passes.

5.5.2 ECAP-assisted bonding between the constituents

One of the merits of ECAP-assisted compaction that makes it stand out from other powder consolidation techniques is its ability to achieve strong bonding at relatively low temperature

via fresh metal contact and solid state interdiffusion. Imposed severe plastic deformation of the particles, and especially severe shear promoting breakage of oxide layers, is essential for creating fresh metal surface contact. In Fig. 5.21, an interface between two Ti particles in a Ti/Mg/Si compact produced by 4 ECAP passes is presented in STEM-BF and high-angle annular dark field (HAADF) images. An object with a low atomic number perpendicular to the interface is seen in Fig. 5.21 (a, b). With higher magnification (c, d) and the corresponding EDX mappings (e, f), this object can be identified as a pair of Ti oxide particles with 10 nm thickness stacked or folded together. The rest of the interface is free of oxide layer. From our previous study [52] and the electron microscopy data obtained in the present work it can be conjectured that with the growing number of ECAP passes and the greater shear deformation imparted to powder particles, greater damage to the oxide layer is induced and fresh metal exposure is increased. High pressure involved in ECAP processing is also conducive for ‘fusion’ between the adjacent particles stripped bare of the oxide layers. The highest strength of porous Ti that went through 4 ECAP passes in its compaction history is believed to be caused by this mechanism.

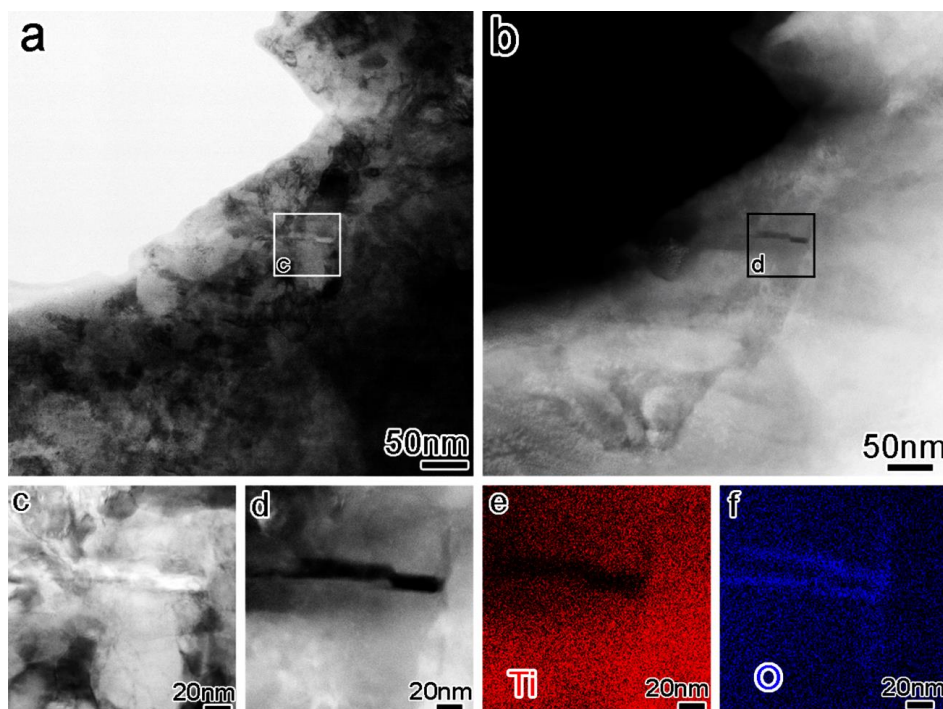


Figure. 5. 21 Interface between Ti particles in a compact obtained by 4 ECAP passes: (a) STEM-BF image and (b) STEM-HAADF image of interface between two Ti particles ‘fused’ together. Cross-sections (c) and (d) show an oxide fragment embedded in Ti; (e) and (f) are the corresponding STEM-EDX mappings showing the distribution of titanium and oxygen, respectively.

Strong bonding between Ti and Mg is also important, since without effective bonding Mg particles would not contribute much to the strength of porous Ti/Mg composites. Fig. 5.22 (a) and (b) present BF and HAADF images of interfaces between Ti and Mg particles. Diffuse boundaries between the constituent particles indicate that migration of Ti and Mg atoms across the interfaces occurred promoting bonding by interdiffusion. From Fig. 5.22 (d), it is clear that no oxygen-enriched region exists at the interface, which indicates that both Ti and Mg oxide layers were effectively broken during ECAP processing thus promoting bonding.

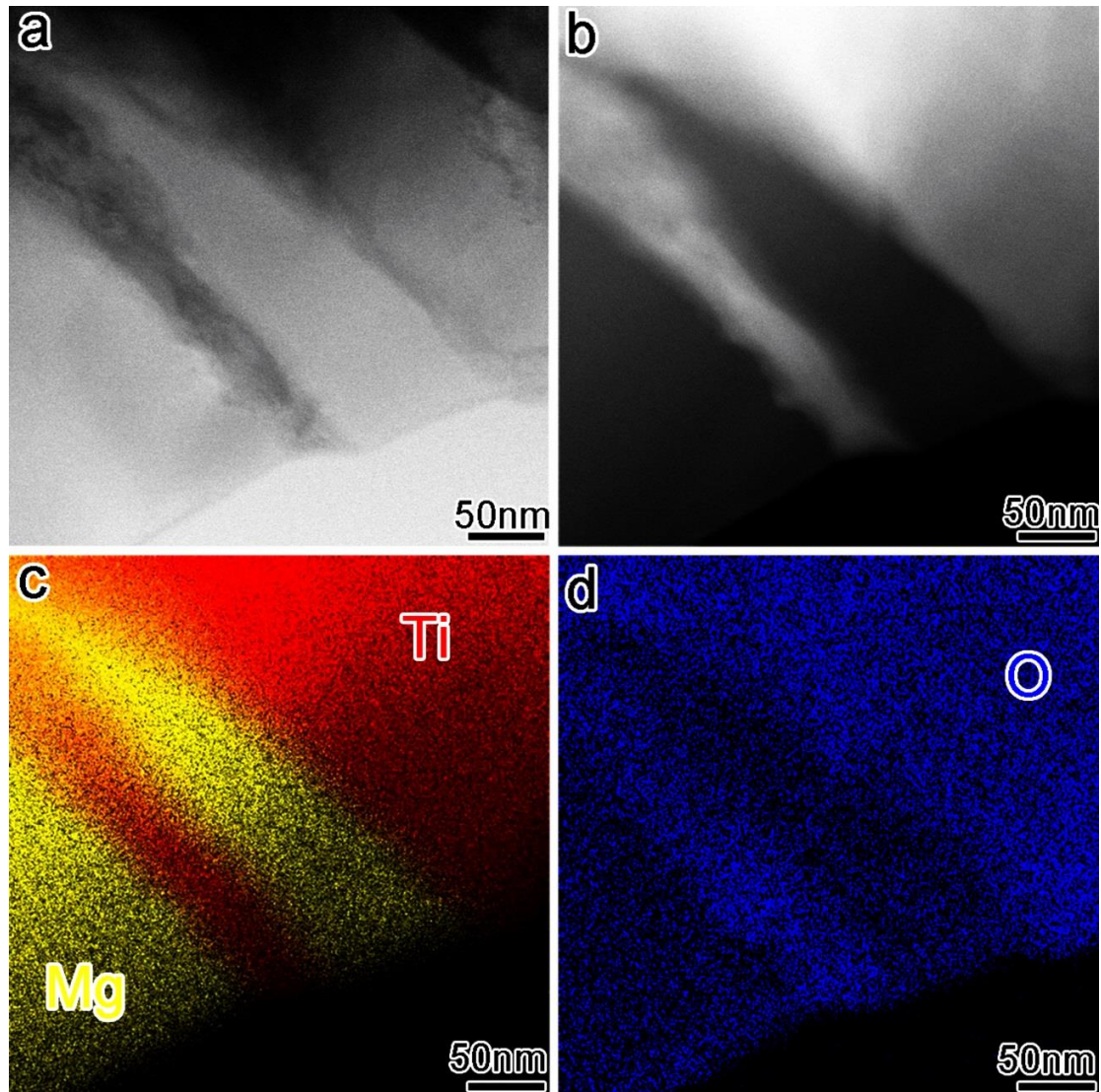


Figure. 5. 22 Interfaces between Ti and Mg particles in a compact after 4 ECAP passes: (a) STEM-BF and (b) STEM-HAADF image of interfaces between Ti and Mg; (c) and (d) present the corresponding STEM-EDX mappings

5.6 Summary of this chapter

Compaction by ECAP was utilised to consolidate an elemental powder blend, which comprised Ti, Mg and Si powders. Readily machinable compacts were produced in this way. By removing Si and the Mg constituents from the compact using chemical reactions, porous Ti and porous Ti/Mg composite were obtained. Due to the advantages provided by ECAP compaction, including the relatively low process temperature, the porous structures produced possessed unique properties. First, ECAP compaction resulted in exceptional grain refinement in Ti struts down to sub-micron range after four ECAP passes. This grain refinement gave rise to high compressive strength and acceptable ductility. Second, ECAP processing led to a redistribution of the constituents, leading to thicker struts and larger average pore size with increasing number of ECAP passes. With broader strut thickness their strength increased as well. Third, ECAP deformation led to breakage of the oxide layer of Ti and Mg particles thus promoting solid state interdiffusion between them. The quality of bonding between titanium particles as well as titanium and magnesium particles was improved in this way, as were strength and ductility of the struts. Also, a unique morphology of pore surfaces was obtained as a result of a chemical reaction between NaOH and fresh Ti. This pore surface morphology was found to be conducive for interaction of the porous scaffolds with preosteoblast cells.

Chapter 6 Bimetallic rod of aluminium alloy 6201 and austenitic steel 316L manufactured by Equal-Channel Angular Pressing

6.1 Outline of this chapter.....	103
6.2 Introduction	103
6.3 Experimental procedures and characterisation	107
6.3.1 Materials selection and ECAP processing	107
6.3.2 Electrical conductivity measurement	109
6.3.3 Measurement of mechanical properties	109
6.3.4 Microstructure characterisation.....	109
6.4 Results.....	111
6.4.1 Optical microscopic observation after ECAP	111
6.4.2 Mechanical properties measurements	111
6.4.3 Electrical conductivity measurement	112
6.4.4 XRD characterisation	115
6.4.5 TEM characterisation	118
6.5 Discussion	125
6.6 Summary of this chapter.....	125

6.1 Outline of this chapter

In the previous two sub-projects, ECAP was investigated as a potent compaction method and it did show its superior capacity over traditional powder metallurgy techniques. It has been proven that the severe plastic deformation and imposed hydrostatic pressure make ECAP an effective technique in fabrication of multicomponent materials for applications such as upcycling machining chips and fabrication of porous metallic structures.

In the third sub-project, the source of the constituents was scaled up from micron- to millimetre-size swarfs and powders to centimetre-size bulk metals. Correspondingly, the ability of ECAP investigated was switched from effective consolidation to co-deformation mechanism. In this chapter, ECAP was used to fabricate Al/steel bimetallic rod for application in overhead transmission conductors. Bimetallic rods consist of an Al alloy 6201 jacket layer and an austenitic stainless steel 316L core with three kinds of diameters. After processing at 175°C for 1 and 4 ECAP passes, simultaneous increase of both mechanical strength and electrical conductivity was achieved for one particular geometry out of three geometries tested. X-ray diffraction and transmission electron microscopy were conducted to analyse how the microstructure evolution was influenced by varying geometry and number of processing passes. Co-deformation mechanism of ECAP on bimetallic rod and dynamic ageing of Al alloy 6201 were discussed based on the microstructure characterisation results.

6.2 Introduction

This third sub-project includes a number of emerging and interesting topics. From the viewpoint of engineering opportunity, with the rapid increase in electricity demand high energy efficient conductor materials are needed. From the statistics provided by International Energy Agency (IEA), world electricity demand will increase by almost 80% over the period 2012-2040 [343]. Growing electricity demands increased load on existing transmission lines, many of which were built far before such magnitudes of load were considered. According to Joule's first law, when the amount of electrical current flowing is increased through the transmission lines, heat generation increases quadratic with the current and results in rising of nominal operating temperature. With rising temperatures, the conductors lose their mechanical strength leading to significant sag [344]. Therefore, high-capacity overhead

Chapter 6 3rd sub-Project Bimetallic Al/Steel Rods

transmission conductors which can carry high volume of powder without overheating or sagging are in highly demand.

Currently, the existing electric power transmission lines are mostly equipped with traditional Aluminium Conductor Steel Reinforced (ACSR) cables, which consist a bundle of galvanized high strength steel wires as core materials to provide mechanical strength and Al wires around them to carry most electrical current due to the skin effect. The popularity of this type of conductor is owing to its adequate mechanical strength, widespread manufacturing capacity and cost effectiveness [345]. Comparing with another widely used conductor – All Aluminium Alloy Conductor (AAAC) where only Al alloy 6xxx series wires are used, ACSR provides better performance regarding to long-term creep or relaxation and lower manufacturing cost [345]. To replace the traditional conductors for meet increasing electricity demand, efforts have been put into developing new Al alloys which combines high mechanical strength and high conductivity [346, 347] and better core materials that have higher strength to weight ratio, corrosion resistance, and conductivity than high strength steel.

In recent years a number of new products have been developed from industry. 3M invented Aluminium Conductor Composite Reinforced (ACCR) consisting of a core material of Al_2O_3 fibre-reinforced aluminium matrix composite and outer conductor of aluminium-zirconium wires. The outstanding feature in this product is the use of metal matrix composite (MMC) to achieve higher strength-to-weight ratio and lower thermal expansion than comparable size steel core conductor. So it is lighter and sag less, even at higher operating temperature [348, 349]. However, the main limitations of this product are its cost that is five times higher than conventional ACSR and the low conductivity of core materials since Al_2O_3 fibre is not conductive. Alternatively, a polymer matrix/carbon + glass fibre reinforced composite core was invented CTC Cable Corporation. The product - Aluminium Conductor Composite Core (ACCC) is designed to fulfil high tensile strength, low coefficient of thermal expansion and high temperature sag resistance [350]. However, the drawbacks of this product are the large difference of the thermal expansion coefficient and elastic modulus between outer aluminium and composite core [351].

Apart from using fibre-reinforced composite as core material, progress has also been achieved on improving the traditional steel core. Alumoweld Aluminium-Clad Steel overhead ground wire is invented by AFL. With a high-purity aluminium powder compacted around a high-strength steel rod and subsequent applications of heat and pressure, a bimetallic rod with

a dense welded Al jacket layer is obtain. By combining aluminium cladding with steel, this bimetallic rod possesses higher strength to weight ratio, higher corrosion resistance and better conductivity [352]. The method of cladding Al powder on steel rod is not stated; however from perspective of powder metallurgy this cladding route is not efficient and with inevitable aluminium oxide on the powder the electrical conductivity is decreased by the scattering effect. Most importantly, with inevitable residual porosity left after powder compaction, galvanic corrosion between steel and Al could occur and accelerate corrosion of Al. To improve this route, using plastic deformation to bond bulk Al jacket to steel core can be potentially used if good interfacial bonding is achieved between them, as stated in Chapter 2.2.

In fact, using deformation techniques to manufacture bimetallic rod with core-jacket or core-sleeve architecture have been investigated by several groups in past decade. One of the most investigated methods is co-extrusion, as schematically shown in Fig. 6.1. Researchers have tried to bond Al jacket to Cu core for electrical conductor application [353]. Moreover, using similar route, efforts have been made to bond Al/Mg [272] and Al/Ti [354] for lightweight applications. Experiment and simulation results showed that, large thickness of the sleeve layer, optimum die angle and small extrusion ration have positive influences on metal flow during deformation process and good interfacial bonding [353, 355-357]. Moreover, to further investigate the effect of geometrical features of the core materials on the mechanical properties, three different architectures of Al alloy cores were embedded to Mg ally by extrusion [358]. The results showed that the core architectures can affect the microstructure and texture evolution of sleeve component in co-extrusion process [358].

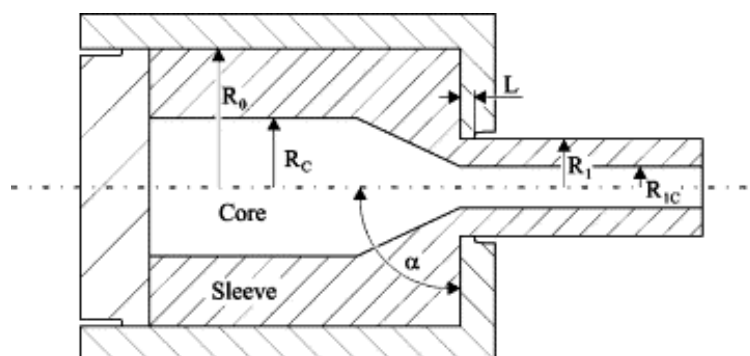


Figure. 6. 1 Schematic illustration of bimetal rod co-extrusion [359]

Alternatively, rotary swaging was also investigated for fabrication of bimetallic rod with core-jacket architecture. As the process illustrated in Fig. 6.2, by using continuous forging

motion, components are expected to be bonded together with metallurgical bonds. Three-layered Al-Cu clad composites with different stacking sequences were fabricated using cold rotary swaging to investigate the effect of geometry on the mechanical behaviour [360].

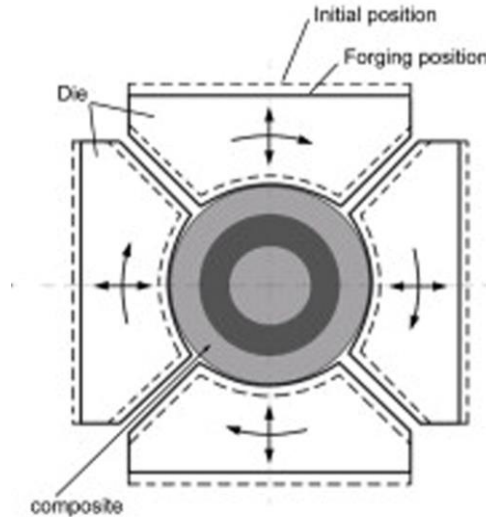


Figure. 6. 2 Schematic illustration rotary swaging of bimetallic rod [360]

In the above mentioned two methods, only moderate plastic deformation is involved for achieving good bonding properties between jacket layer and core. As it has been stated in the chapter of literature review, for metallic hybrid, high amount of plastic deformation is beneficial for the establishment of high strength bonds and severe plastic deformation techniques enjoy their strength in this aspect.

Based on this principle, the first try of using ECAP to manufacture bimetallic Al/Cu rod was conducted by A.R. Eivani et al. [361]. Their study showed that the shear strength between two materials was reasonably high after one pass ECAP and can be increased with a second pass. After this research, attempts have been made to achieve diffusion bonding with higher interfacial strength between the mating surfaces by modifying thermal mechanical processing parameters [362]. Also, it was found that the decrease in die angle leads to a higher bonding strength between the jacket layer and core [363]. It is worth noting here that due to the capacity of ECAP for continuous industry-scale application [364-366], this design has the potential for producing bimetallic wires for transmission lines. As shown in Fig. 6.3, ECAP-conform process as one derivative ECAP technique provides the possibility of upscaling the ECAP processed rods to wires.

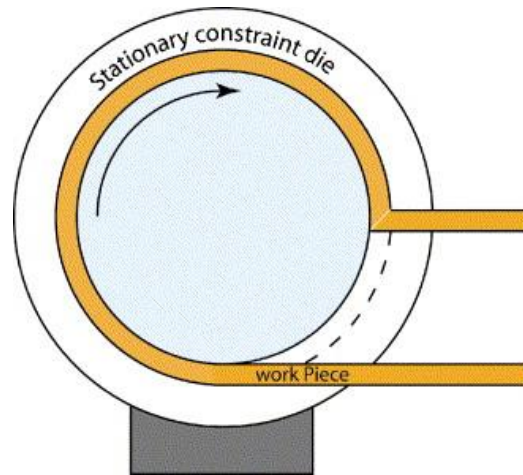


Figure. 6. 3 Schematic illustration of ECAP-Conform process [366]

Although these previous studies showed ECAP is a promising technique in fabrication of bimetallic rod or wires with core-jacket architecture, there are several aspects of this route needed to be further investigated. This sub-project aims at investigating the influences of geometrical factors on co-deformation mechanism of bimetallic rods using ECAP and the possibility of tailoring this aspect of design to achieve simultaneous increase of mechanical strength and electrical conductivity.

6.3 Experimental procedures and characterisation

6.3.1 Materials selection and ECAP processing

To meet the requirements for the potential engineering application, careful materials selection was carried out first. Rather than using some of the available high strength steels, a conventional austenitic stainless steel 316L was selected due to its following attributes: high corrosion resistance, good formability and, most importantly, its being non-ferromagnetic. In the conventional overhead electrical conductors, a magnetic field originates from the high carbon steel wire, which is a ferromagnetic material. The magnetic field interferes with the flow of the electrical current and causes extra power losses due to an increase in the effective electrical resistance of the aluminium conductor. Furthermore, the dissipated power also leads to an increase in the temperature of the electrical conductor and may cause fatal problems with its stability [367]. In contrast, the non-ferromagnetic properties of austenitic steels eliminate the magnetic loss and enhance the stability and reliability of the conductor [367, 368].

Chapter 6 3rd sub-Project Bimetallic Al/Steel Rods

For the outer jacket Al, aluminium alloy AA6201 is chosen. This alloy is widely used owing to its good combination of enhanced strength and relatively high conductivity, with the ultimate tensile strength (UTS) in the range 255-330MPa and electrical conductivity of 57.5-52.5% International Annealed Copper Standard (IACS) comparing to the UTS of about 160MPa and conductivity of 62% provided by pure Al [369-371]. Moreover, severe plastic deformation has been tried to further simultaneously enhance its strength and electrical conductivity [371-373]. By imposing extreme deformation at elevated temperature, decomposition of solid solution and formation of nanosized second-phase precipitates at the expense of solute atoms occurs. This dynamic aging provided by SPD processing results in a microstructure possessing ultrafine grains, nanosized precipitates, very low content of solute atoms and absence of GP zones, which leads to significant enhancement of electrical conductivity and strength [371]. At this stage, it is also worthwhile to point out that, based on the same principle that using pure matrix for carrying current and fine particles for strengthening, a number of other processing routes have also been investigated for this application in recent years. Al/Ca composite conductor was produced via powder consolidation, hot extrusion and room temperature swaging [351]. Calcium is added as the form of particles and bonded to matrix Al powders to provide strengthening. Moreover, Al_3BC is another promising secondary phase to enhance the performance of 1070 EC-grade Al, which can be introduced by Al-8B-2C master alloy [374].

The chemical compositions of austenitic stainless steel 316L and Al alloy 6201 used in this study are shown in Table. 6.1. Steel bars with three diameters as 3, 4 and 5mm were produced. Correspondingly, Al tube with internal diameter of 3, 4 and 5mm and outer diameter of 10mm were made, respectively. The height of bars and tubes was 40mm. Steel bars were inserted to their corresponding Al tubes with shrink fit. Therefore, three geometries of bimetallic rods were prepared as as-received materials. They were bimetallic rod with steel core Ø3, Ø4 and Ø5, or in another word, bimetallic rod with Al jacket layer having thickness of 3.5, 3 and 2.5mm, respectively.

Bimetallic rods underwent ECAP processing at 175°C for 1 pass or 4 passes following route B_C. A very low back pressure of 15MPa was used to prevent sliding between two components, which has a similar function to welding layers together at the edges to prevent slippage in ARB process [375]. Processing temperature of 175°C was chosen to avoid the strain induced martensite formation [376].

Chapter 6 3rd sub-Project Bimetallic Al/Steel Rods

With increasing number of ECAP passes, strain was accumulated and greater grain refinement was expected. Therefore, two main variables as diameter of the steel core (thickness of the jacket Al layer) and number of ECAP processing pass were chosen in this study. Altogether, six types of bimetallic structures having three kinds of geometries and two kinds of processing histories were manufactured. The properties and microstructure evolution in the single phase Al rod in isolation, not within a bimetallic rod, was also considered to compare and evaluate the effect of co-deformation.

Table. 6. 1 Chemical compositions of stainless steel 316L and AA6201 in wt. %

Steel	Fe	C	Mn	Ni	Cr	Mo	Si	Cu	S	P	V
316L	Bal	0.02	1.51	10.0	16.6	2.09	0.38	0.43	0.02	0.04	0.05

AA6201	Al	Si	Mg	Cu	Fe	Mg	Zn	Cr	Ni	Mn	Ti
	Bal	0.56	0.73	0.13	0.31	0.73	0.13	0.01	0.01	0.14	0.01

6.3.2 Electrical conductivity measurement

The SIGMATEST Ec device (Foerster Instruments Inc., Pittsburgh, USA) was used to determine the electrical conductivity of the samples. This equipment operates on the basis of the eddy-current method. Since the size and shape of the tested samples can affect the measurement, all tested samples had the same cylinder geometry with 10 mm height and 10 mm diameter. Each sample was tested 10 times to calculate the average value of the electrical conductivity.

6.3.3 Measurement of mechanical properties

Tensile test was not conducted for evaluation of the mechanical properties because the diameter of the cross-section cannot be reduced for gauge section and the lack of gripping technique to insure tensile deformation of both core and sheath at same time. Instead, compression tests were carried out, which is a common practice in testing of bimetallic rods [377-380]. However, besides the shortcoming mentioned in Section 5.3.4, viz. the effect of compliance of the testing machine, another limitation of compression tests in this application is the inability to obtain the ultimate strength of the ductile bimetallic rods. The phenomenon of the decrease in force prior to fracture in tensile tests does not occur in compression tests due to the increasing cross-sectional area in the latter one [381]. Therefore, there is no force maximum prior to fracture when testing a ductile material using compression tests. The tests were conducted using an Instron 5982 machine. The compression samples had 10 mm height

and 10 mm diameter. The cross-head velocity was set to 0.01 mm/s to provide a nominal strain rate of 10^{-3} s^{-1} .

6.3.4 Microstructure characterisation

Low-magnification overviews of the cross sections were obtained using Olympus SZX-16 stereo optical microscope with digital camera. X-ray diffraction (XRD) using Cu $K\alpha$ radiation at 40 kV and 25 mA in a Philips X-ray diffractometer was performed. As in the previous chapter, data was processed using the peak fitting program MDI Jade for accurate computation. TEM characterisation was performed using an FEI Tecnai F20 FEG TEM operating at an acceleration voltage of 200 kV. TEM lamella was prepared by focused ion beam (FIB) technique on FEI Quanta 3D FEG microscope. The process chain of FIB lift-out technique is presented in Fig. 6.4. In Fig. 6.4 (a), a protective Pt layer is deposited across the interested interface between Al and steel. It also worth noting in this figure that, the milling rate of Al is about 2.5 times faster than steel. Fig. 6.4 (b,c) show that the lamella is cut and lifted out by a Kleindiek probe. Then the lamella is mounted on a Cu grid and thinned and polished by ion beam, as shown in Fig. 6.4 (d-f).

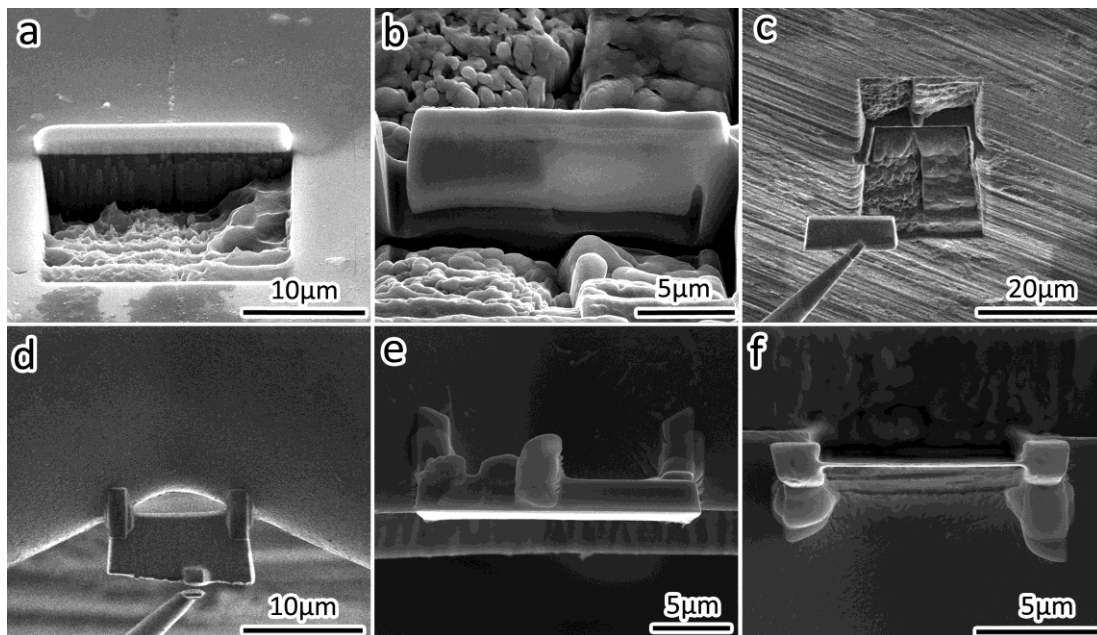


Figure. 6. 4 Secondary electron images showing the process chain for fabrication of TEM lamella using FIB: (a) deposited Pt layer and a milled surface; (b) a j-cut is used to allow an easy lift-out; (c) lamella is attached to Kleindiek probe and lifted out; (d) lamella is mounted on a V-shaped Cu grid and Kleindiek is cut and detached from lamella; (e) lamella is ready to be thinned and polished; (f) lamella with thickness less than 100nm

6.4 Results

6.4.1 Optical microscopic observation after ECAP

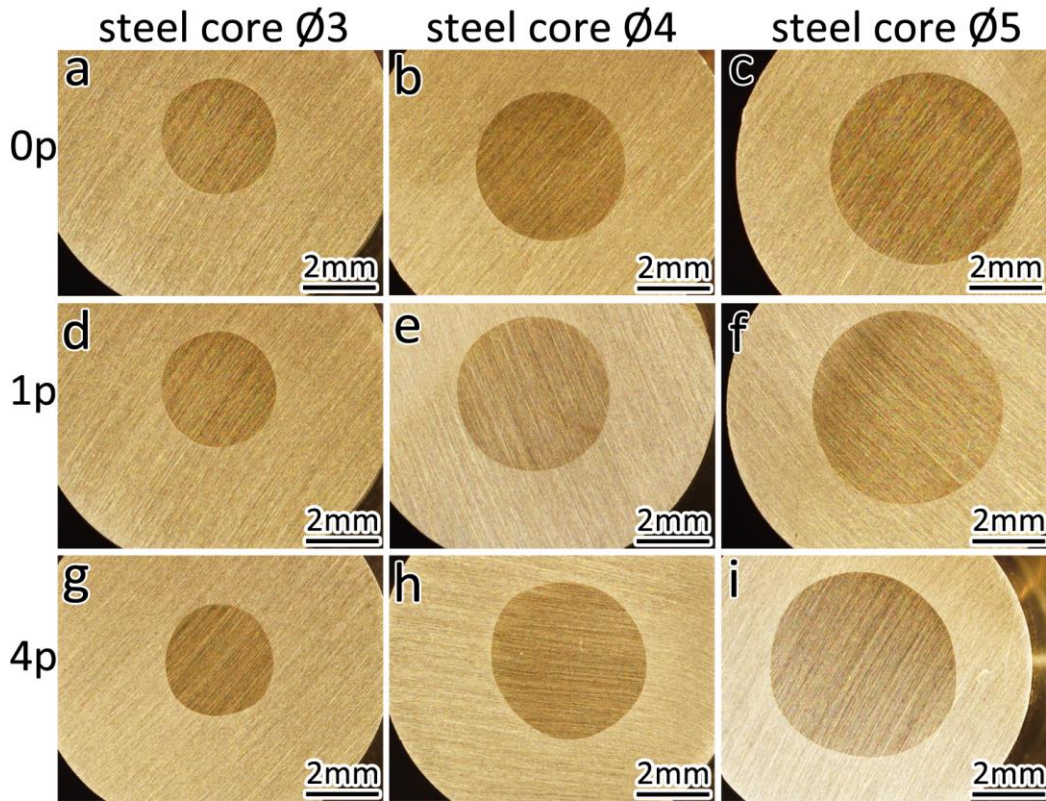


Figure. 6. 5 Optical microscopy images of the cross-sections showing the shape transformation of the steel cores after one and four ECAP passes: (a-c) initial shapes of samples with three different core diameters (before ECAP, denoted 0p), (d-e) after one ECAP pass (denoted 1p), (g-i) after four ECAP passes (denoted 4p).

From the optical micrographs shown in Fig. 6.5, it is clearly seen that, after 1 ECAP pass the shapes of steel cores changed from perfect circle to irregularity and after 4 passes they became even far from circle shape. This observation indicates that co-deformation of steel core exists and the amount of deformation increases with higher ECAP passes. Meanwhile, no delamination at the interfaces between these two components was observed after ECAP processing.

6.4.2 Mechanical properties measurements

To evaluate the impact of the co-deformation induced by ECAP on the mechanical strength of bimetallic rods, compression test was carried out. The compressive yield strengths at 0.2%

offset of tested materials are listed in Table. 6.2. It can be seen that, in as-received condition, bimetallic rods possess slightly higher strength than Al rod, which is in a range from 25 to 50MPa depending on the diameter of the steel core. In another word, the steel core did not bring much strengthening effect to the bimetallic rod. However, after 4 ECAP processes, the difference increases and varies from 50MPa to 100MPa. For bimetallic rod with steel core Ø3 and Ø4, the increment mostly occurred after 1 pass, from 300MPa and 306MPa to 390MPa and 418MPa, respectively. The following 3 passes did not contribute much to strengthening the theses two bimetallic rods.

Table. 6. 2 *Compressive yield strength at 0.2% offset of AA6201 rod and bimetallic rods with three geometries after 0, 1, and 4 ECAP passes (in MPa)*

Number of ECAP passes	Al rod Ø10	Bimetallic rod with steel core Ø3	Bimetallic rod with steel core Ø4	Bimetallic rod with steel core Ø5
0	274	300	306	325
1	323	390	418	492
4	380	424	449	590

6.4.3 Electrical conductivity measurement

The electrical conductivity results are shown in Table. 6.3. It is seen that with increasing number of ECAP passes, the electrical conductivity of stand-alone AA6201 and steel 316L decreases slightly due to the deformation-induced crystal lattice defects that scatter electrons [371]. This is at variance with the results of the work conducted by Valiev et al. [371], who demonstrated simultaneous enhancement of strength and conductivity in AA6201 after about 20 revolutions under high-pressure torsion. We note that this deformation corresponded to an equivalent strain of 483. In contrast, in this study, 4 ECAP passes imposed a much lower equivalent strain of 4.6, which was apparently not high enough for improving electrical conductivity to the same extent. Similarly, in the case of bimetallic rods with Ø4 and Ø5 steel core, samples in the initial condition exhibited a higher electrical conductivity than those with an ECAP processing history.

However, for the bimetallic rod with Ø3 steel core, ECAP brought about a slightly increase of the average conductivity from 42.37% IACS to 42.79% IACS and 43.19% IACS after one and four ECAP passes, respectively. Combining the results from the compression test, this suggests that for the bimetallic rod with Ø3 steel core, ECAP processing gave rise to a higher

yield strength and, at the same time, a greater electrical conductivity over the characteristics of the initial rod. In other words, it can be concluded that the usual trend of an inverse relation between electrical conductivity and strength was confirmed for AA6201 rod. However for bimetallic rod, it was possible to reverse this trend: conductivity and strength were enhanced simultaneously as a result of ECAP processing.

Table. 6. 3 *Electrical conductivity of AA6201 rod, steel rod and bimetallic rod with three geometries after 0, 1, and 4 ECAP passes (in IACS %)*

Number of ECAP passes	Conductivity of AA6201 rod Ø10	Conductivity of bimetallic rod with Ø3 steel core	Conductivity of bimetallic rod with Ø4 steel core	Conductivity of bimetallic rod with Ø5 steel core	Conductivity of steel rod Ø10
0	47.23±0.13	42.37±0.98	37.40±0.85	25.51±0.48	2.26±0.01
1	46.59±0.26	42.79±0.34	34.49±1.05	21.83±0.53	2.25±0.01
4	46.36±0.13	43.19±0.43	34.69±0.36	23.78±0.35	2.19±0.02

Because the lengths of steel core and AA6201 sheath were equal, the overall electrical resistivity of the bimetallic rod ρ could be modelled as in a parallel circuit [382], which can be written as:

$$\frac{1}{\rho} = \frac{1}{\rho_{steel}} f_{steel} + \frac{1}{\rho_{AA6201}} f_{AA6201} \quad (6.1)$$

where f_{steel} and f_{AA6201} are the volume fractions of steel core and AA6201 sheath, and ρ_{steel} and ρ_{AA6201} denote the electrical resistivity of the steel and AA6201 components, respectively. For the bimetallic rods with Ø3, Ø4, and Ø5 steel core, the volume fractions are, respectively, 9%, 16%, and 25%. Resistivity values in microohm × metres units can be converted to % IACS conductivity values using the following formula:

$$1.724/resistivity = \% IACS \times 10^{-2} \quad (6.2)$$

Using equations (6.1) and (6.2), the magnitudes of the electrical conductivity of bimetallic rods in the initial condition can be predicted as 42.71 % IACS, 40.03 % IACS, and 35.99 % IACS. Except for the bimetallic rod with Ø3 steel core, the calculated conductivity values are significantly higher than the measured ones. This could be due to the use of the formula for direct-current contact voltage, while experimentally, the eddy current method was used to determine the conductivity. Besides, possible changes of resistivity of the individual phases as a result of microstructure by ECAP deformation could not be considered in Eq. (6.1).

Chapter 6 3rd sub-Project Bimetallic Al/Steel Rods

Therefore, this simplistic model is not suitable for this application and further studies would be needed to account for the mentioned resistivity changes.

To get a better insight into the influence of the ECAP processing history and the geometry factor on the overall performance of the bimetallic rod, the electrical conductivity and yield strength results are plotted together in Fig. 6.6. Three hybrid geometries are represented in terms of the volume fraction of the steel core in the bimetallic structure. The dashed black line in the figure corresponds to the yield strength of bimetallic rods (calculated on the basis of a linear rule-of-mixture) in the initial non-ECAP condition. The solid black line represents a decrease of the electrical conductivity with increasing volume fraction of steel core. We can employ the steel volume fraction dependence of yield strength of non-processed bimetallic rods as represented by the mentioned dashed line to assess the benefits of ECAP processing. Indeed, making use of that curve, one can see that after one ECAP pass the yield strength of bimetallic rods with 9%, 16%, and 25% volume fraction of steel is equivalent to the yield strength of unprocessed bimetallic rods with approximately 40%, 52%, and 78% volume fraction of steel, respectively, cf. the blue dashed lines. Similarly, after four passes, the yield strength of the bimetallic rods is equivalent to that of unprocessed bimetallic rods with approximately 54%, 60%, and 100% volume fraction of steel, respectively, cf. the red dashed lines. That is to say, through processing by ECAP, a bimetallic rod with a thinner steel core can maintain the same level of yield strength as an unprocessed bimetallic rod with a thicker one, while the electrical conductivity of the former will be greater due to the larger volume fraction of aluminium it has. Comparing bimetallic rods that are equivalent in terms of yield strength - 390, 418, and 492 MPa, it can be seen that the electrical conductivity of 17, 13, and 4 % IACS (indicated by the blue points on the solid black line) rises to 43, 34, and 22 % IACS after one ECAP pass, respectively, due to the increased volume fractions of AA6201 component. In the same way, for bimetallic rods with the yield strength of 424, 449, and 590 MPa, the electrical conductivity of unprocessed rods rises from 12, 8, and 2 % IACS (see the red points on the solid black line) to 43, 35, and 24 % IACS after four ECAP passes, respectively.

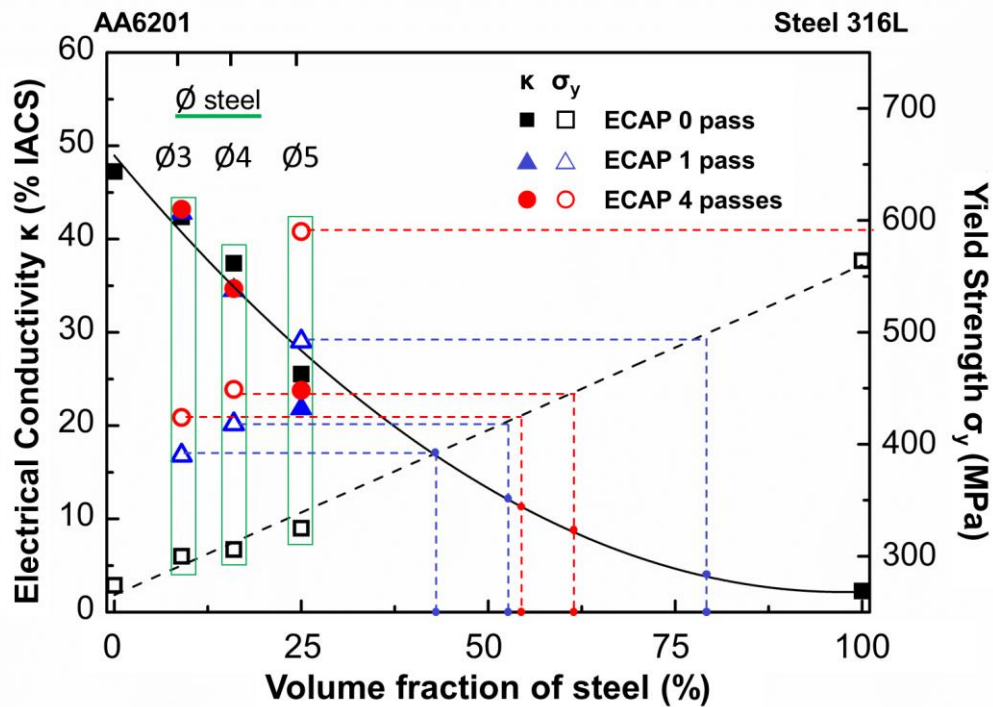


Figure. 6. 6 Electrical conductivity and yield strength of as-received Ø10 AA6201 and steel rods and bimetallic rods with three different geometries (Ø3, Ø4, and Ø5 steel core) after 0, 1, and 4 ECAP passes

The result can be interpreted as follows. Through ECAP processing, one can attain a certain level of strength of Al clad steel rod or wire with a thinner steel core. This means a lighter product with a higher specific strength and, for certain core/rod diameter ratios, a higher electrical conductivity.

6.4.4 XRD characterisation

XRD analysis was conducted on all 12 samples prepared. The XRD spectra of bimetallic rod with Ø5 steel core after 0, 1, and 4 ECAP passes are presented in Fig. 6.7. Phase identification failed to detect any martensite after 4 ECAP passes, which means that either martensitic transformation did not occur in the first place or the amount of martensite formed was below the detection limit of XRD. At any rate, it can be stated safely that ECAP processing did not introduce a significant amount of martensite. From XRD data, the lattice parameter of AA6201 constituent was calculated by determining the positions of diffraction peaks. In this study, peaks for (220), (311) and (222) reflections were chosen as shown in Fig. 6.8. Since the calculated lattice parameter is significantly affected by the diffraction angle θ ,

the error in the calculated magnitude $\sin\theta$ being smaller for larger θ values, the (111) and (200) diffraction peaks were not included. The lattice microstrain, the crystalline size, and the dislocation density were determined by measuring peak broadening, as detailed in Refs. [383-385]. XRD peak profiles were fitted using the Pearson VII function with K-alpha2 present and the full-width at half-maximum (FWHM) of peaks was obtained as a measure of peak broadening. The instrumental broadening was determined using a well annealed (400 °C for 4 hours) commercially pure Al sample. The true peak broadening B was calculated using $B = \sqrt{B_{obs}^2 - B_{inst}^2}$, where B_{obs} is the observed peak broadening and B_{inst} is the instrumental broadening one [386].

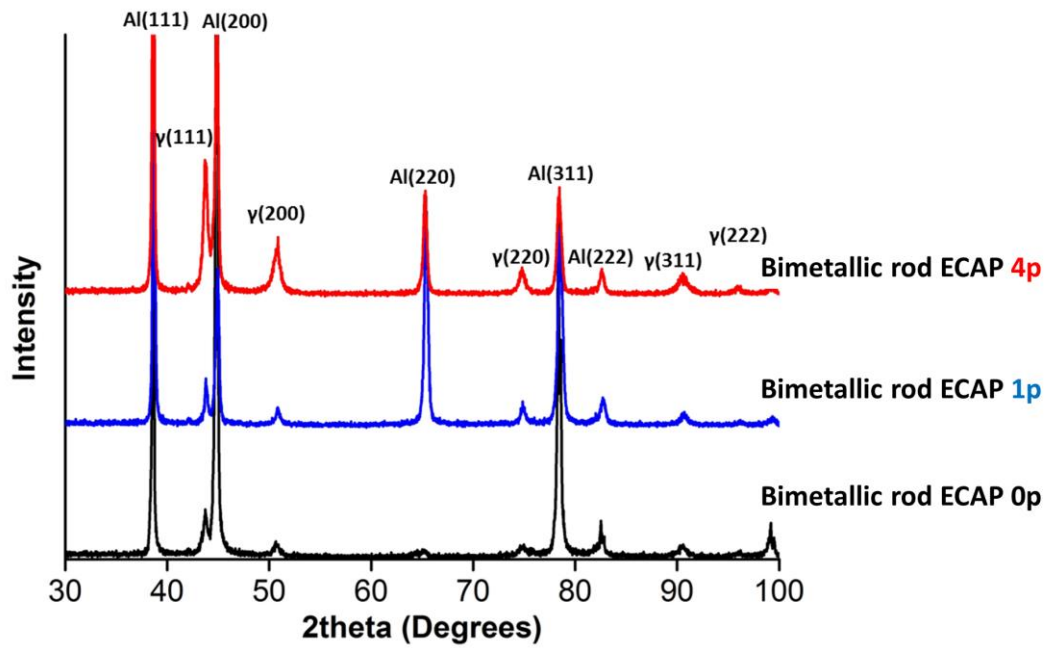


Figure. 6. 7 X-ray diffraction patterns of bimetallic rods with Ø5 steel core after 0, 1, and 4 ECAP passes

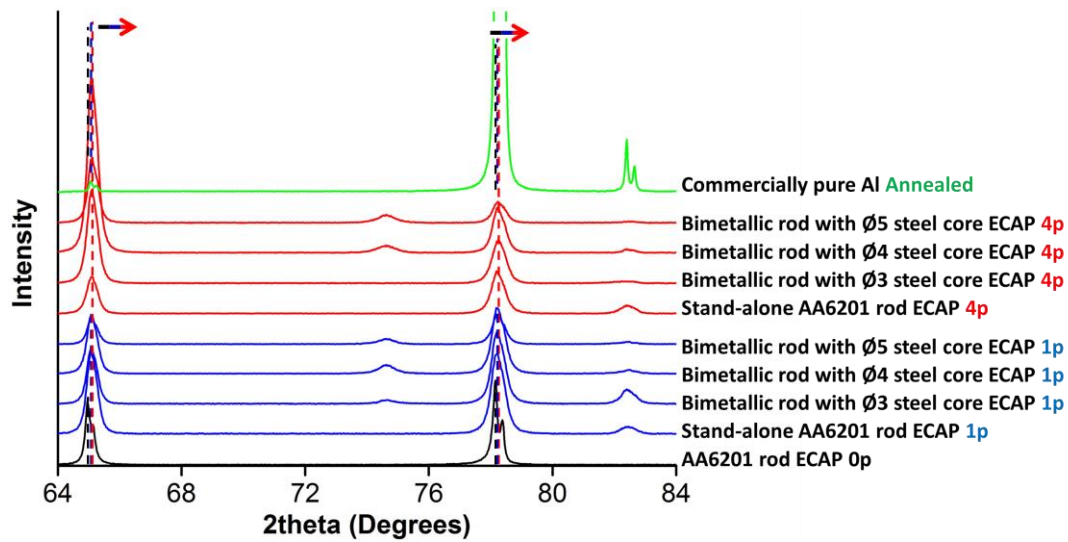


Figure. 6. 8 X-ray diffraction patterns of stand-alone AA6201 and bimetallic rods with three different geometries ($\varnothing 3$, $\varnothing 4$, and $\varnothing 5$ steel core) after 0, 1, and 4 ECAP passes. Note the well annealed commercially pure Al was used as a reference material.

As seen from Fig. 6.8, in which the diffraction patterns for the AA6201 constituent after 0, 1, and 4 ECAP passes are juxtaposed, there is a clear shift of (220) and (311) peaks for Al phase to greater diffraction angles, which reveals a decrease of the lattice parameter [387]. The characteristics of stand-alone AA6201 and the AA6201 constituents of the bimetallic rods determined from the peak shift and peak broadening are presented in Table 4. It is seen that AA6201 has the largest lattice parameter of 4.0550 Å. With severe plastic deformation imposed on the stand-alone AA6201 at 175 °C, this value dropped to 4.0524 Å and 4.0517 Å, indicating a purification of AA6201 matrix by dynamic ageing. However, apparently the extent of depletion of solid solution was not large enough to compensate for the contribution of deformation-induced lattice defects to electron scattering. Therefore, the electrical conductivity still decreased even with less solute atoms in solid solution. The AA6201 component in bimetallic rods exhibits the same trend of decreasing lattice parameter with the increasing amount of plastic strain imparted to the rod. However, by comparing the magnitudes of the lattice parameter in a stand-alone AA6201 rod and AA6201/steel bimetallic rod, it can be found that with the steel core embedded, the extent of purification of the AA6201 bulk is even higher. After one and four EACP passes, the magnitudes of the lattice parameter of AA6201 component in bimetallic rods were, 4.0515~4.0520 Å and 4.0505~4.0513 Å. These values are smaller than the above figures for the stand-alone AA6201. This indicates that having steel core co-deformed with the AA6201 sheath can promote the dynamic ageing thus leading to the formation of secondary precipitate phases

and the concomitant depletion of solid solution. This is obviously a desired scenario, as the precipitates formed do not contribute to electron scattering significantly, while the reduction of the concentration of alloying atoms in solid solution decreases the density of scattering centres and promotes better electrical conductivity. A decrease of the lattice parameter signifies a drop in the solute concentration.

Table. 6. 4 *Microstructural characteristics of AA6201 rod and the AA6201 constituents of bimetallic rods after one and four ECAP passes*

Al in	ECAP passes	Lattice parameter (Å)	Crystallite size (nm)	Microlattice strain	Dislocation density (m ⁻²)
Al annealed	0p	4.0502	—	—	—
Al rod Ø10	0p	4.0550	—	—	—
	1p	4.0524	462	0.0025	6.5×10 ¹³
	4p	4.0517	231	0.0029	1.5×10 ¹⁴
Bimetallic rod with Ø3 steel core	1p	4.0520	231	0.0031	1.6×10 ¹⁴
	4p	4.0505	198	0.0029	1.8×10 ¹⁴
Bimetallic rod with Ø4 steel core	1p	4.0515	198	0.0033	2.0×10 ¹⁴
	4p	4.0513	115	0.0027	2.8×10 ¹⁴
Bimetallic rod with Ø5 steel core	1p	4.0516	115	0.0033	3.4×10 ¹⁴
	4p	4.0505	126	0.0031	3.0×10 ¹⁴

The dislocation density in the AA6201 rod showed an almost two-fold increase, from 6.5×10¹³ m⁻² after the first ECAP pass to 1.5×10¹⁴ m⁻² after the fourth one. However, in the AA6201 component in bimetallic rods the dislocation density jumped to 1.6×10¹⁴ to 3.4×10¹⁴ m⁻², after just one pass of ECAP. It remained pretty steady, and was in the range of 1.8×10¹⁴ to 3.0×10¹⁴ m⁻² after the fourth ECAP pass. The crystallite size also evolved as a result of ECAP processing: after four passes, the average crystallite size of stand-alone AA6201 rod decreased to 231 nm, which is comparable with the values reported in [388, 389]. The AA6201 component in bimetallic configuration exhibited an average crystallite size that approached saturation after just one ECAP pass, with characteristic values down to 115 nm.

6.4.5 TEM characterisation

Based on the results presented above, three bimetallic rods were chosen for further characterization by TEM. FIB lift-out was employed to cut TEM lamellas from the interface

regions between the AA6201 cladding layer and the steel core. Figs. 6.10 – 6.13 show that the microstructure varied significantly with increasing imposed strain and different core/rod diameter ratios. The influence of the number of ECAP passes can be seen from Figs. 6.10 and 6.12 that refer to samples with the same core diameter of Ø3 but different amount of imposed equivalent strain, 1.15 or 4.6 (one or four passes, respectively). Figs. 6.12 and 6.13 provide a comparison between the microstructures for the same processing history (four ECAP passes), but different core diameters (Ø3 and Ø5 steel core).

An overview of an interface between AA6201 and steel components of a bimetallic rod with Ø3 steel core after one ECAP pass is shown in a bright-field (BF) TEM image in Fig. 6.10 (a). It can be seen that these two components were tightly joined without obvious gap between them. However, a closer inspection of Fig. 6.10 (c) reveals an elongated void along the interface 40 nm in width. To the left side of the interface, an interfacial Al layer that underwent profuse plastic flow is observed; it is highlighted by a red dashed circle. Because AA6201 is softer than austenitic steel 316L, it is believed to accommodate a larger amount of plastic strain by the intensive plastic flow at the interface. Obviously, the material on the steel side accumulated a large strain, as well. As seen in Fig. 6.10 (d), next to the interface there is an area with subgrain structures having the size smaller than 50 nm. Farther away from the interface, grain structures change to micro size, with extended boundaries inclined to the pressing direction (henceforth referred to as extrusion direction, ED), as indicated by the yellow dashed lines in Fig. 6.10 (a, d). In the AA6201 component, grains are equiaxed, as shown in Fig. 6.10 (a, b). The average grain size was calculated by averaging over 100 grains to be 224 ± 103 nm, which is close to the value of 231 nm obtained by XRD analysis.

A higher magnification micrograph, Fig. 6.11 (a), shows the nanostructured steel grains in the vicinity of the interface. By obtaining the selected area diffraction pattern (SADP) of this region, the presence of a martensite in this region was detected. It cannot be ruled out that the martensitic phase transformation is an artefact of ion beam milling during sample preparation, as it may have been dislocations generated in the sputtering process that have facilitated the transformation in the severe plastically deformed sample. But the occurrence of martensite could also be a genuine effect of severe plastic deformation by ECAP producing a strain-induced phase transformation near the interface. Indeed, the discontinuous ring pattern in Fig. 6.11 (b) speaks in favour of this explanation, as it indicates that the misorientations between the nano-grains formed are low and they are not fully dynamically recrystallized to form high-angle grain boundaries.

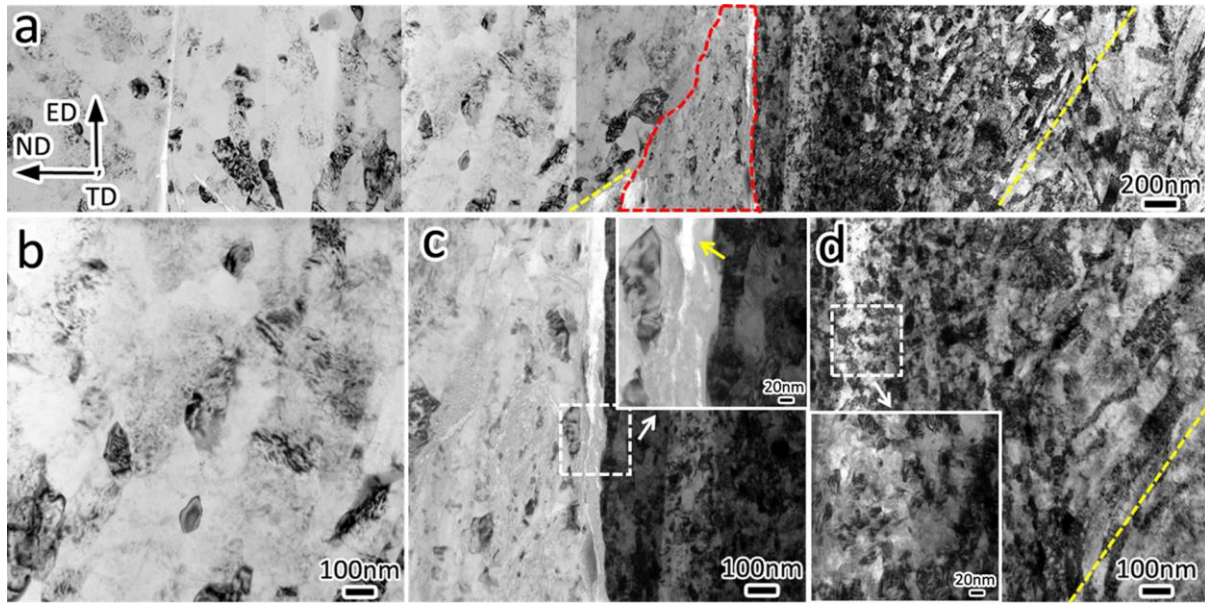


Figure. 6. 9 TEM-BF images of (a) the interface between AA6201 (left) and steel (right) from bimetallic rod with Ø3 steel core after one ECAP pass, (b) AA6201, (c) interface, and (d) steel with high magnification. Insets are enlarged views of the areas indicated by arrows.

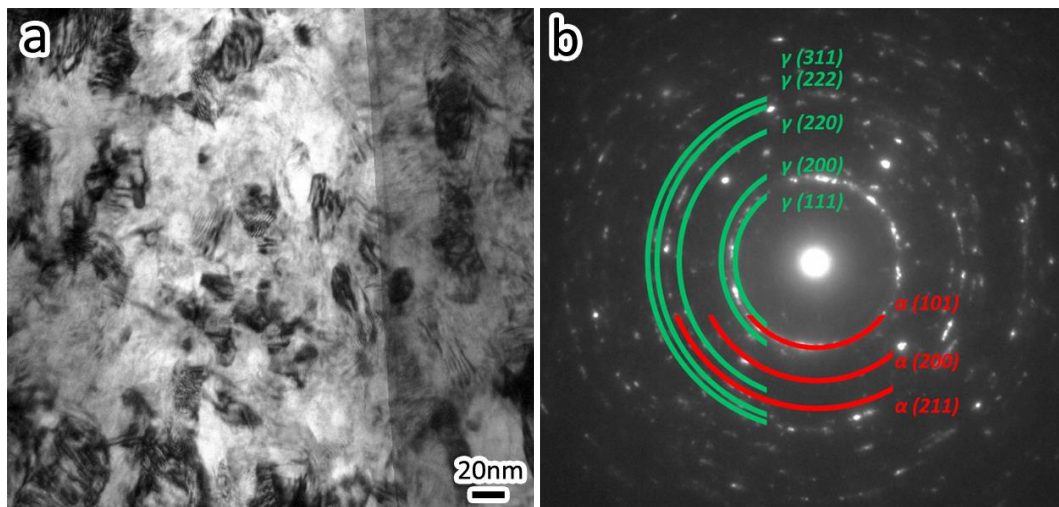


Figure. 6. 10 TEM-BF images of the steel component at the interface with nanostructured grains and (b) the corresponding SADP shows the present of austenite - γ and martensite - α phases. SADP was taken using aperture diameter of 180nm

TEM-BF images in Fig. 6.12 demonstrate that a larger amount of imposed strain after four ECAP passes altered the interface microstructures in a number of ways. First, comparing with a lesser strain after the first pass, the extremely deformed zone got larger with three more passes, cf. Fig 6.12 (a). It can be seen from the inset that the scale of the subgrain structure is around 50 nm. Second, the interface between AA6201 and steel in Fig. 6.12 (c) shows that

both components are tightly bonded. An amorphous layer, about 60 nm thick, was detected. Third, in the case of steel component, the extra three ECAP passes did not bring about any further grain refinement. On the contrary, the grains were coarsened and got elongated in the extrusion direction as shown in Figs. 6.12 (a, d). In essence, the microstructure of the steel core evolved from a nano/submicron sized subgrain pattern inclined to the extrusion direction to an ultrafine grain structure, with grains aligned in the extrusion direction, as seen in Fig. 6.12 (d). This is believed to be a consequence of dynamic recrystallization, the recrystallized grain structure consuming the subgrain structure developed after the first pass. Finally, in Fig. 6.12 (b), equiaxed grains without any preferred orientation were predominant in the AA6201 component of the bimetallic rod. The grain size determined by averaging over 100 grains was 200 ± 85 nm, a figure that is very close to that obtained by XRD analysis (198 nm).

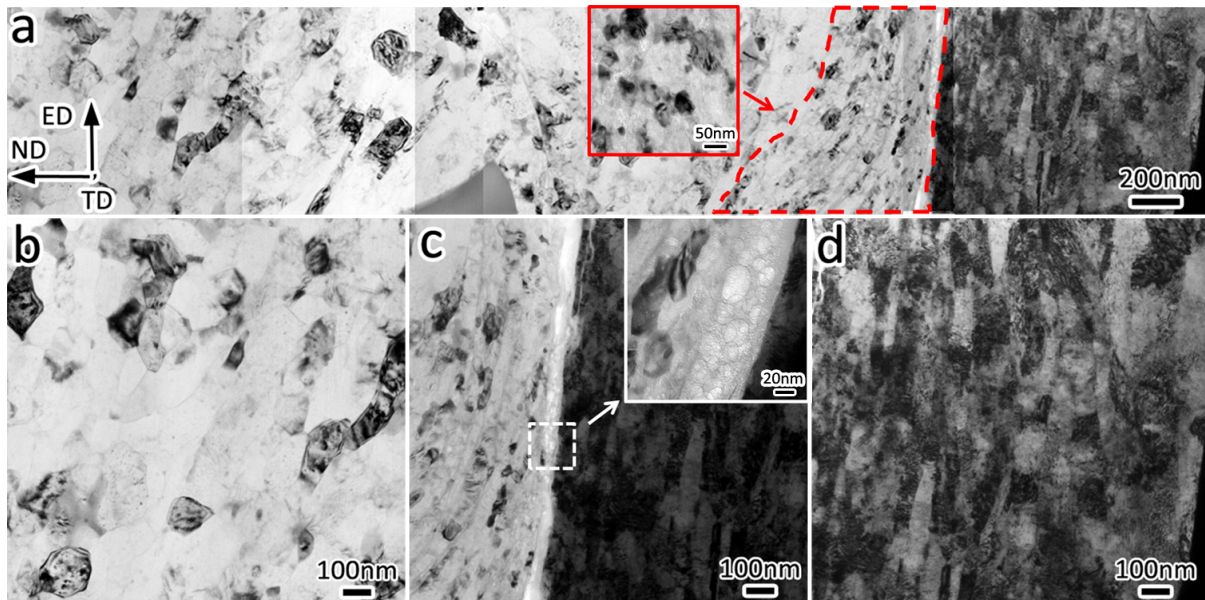


Figure. 6. 11 TEM-BF images of (a) the interface between Al(left)/steel(right) from bimetallic rod with steel core Ø3 after 4 ECAP passes, (b) Al, (c) interface and (d) steel with high magnification. Insets are enlarged view of the areas pointed by arrows

TEM images of bimetallic rod with Ø5 steel core (the largest diameter of steel core and the thinnest AA6201 cladding layer) after 4 ECAP passes, i.e. for the same amount of imposed strain as in Fig. 6, is shown in Fig. 6.13. The most prominent features in Fig. 6.13 (a) are fragments of the amorphous layer at the interface indicated by arrows. In an enlarged view in Fig. 6.13 (c), they appear to be caused by a shear instability and a displacement of the two components at the interface relative to each other. Plastic instability at the interface is documented by the occurrence of shear banding in the steel phase shown in Fig. 6.13 (a, d).

The inset in Fig. 6.13 (c) shows that AA6201 and steel interpenetrated each other at the interface and formed a mechanical interlocking between the mating surfaces. Shear banding in the steel component is likely to be related to this process as a way to accommodate the severe plastic strain in bimetallic co-deformation. In addition, it can be seen that steel grains have well-defined grain boundaries in contrast to the subgrain structures in the lower strain case (one ECAP pass) case in Fig. 6.12 (d). Alignment of the grains in the extrusion direction is also visible, although they are less elongated than in bimetallic rod with a smaller steel core presented in Fig. 6.12 (d). Finally, back to the AA6201 component in Fig. 6.13 (b), it can be seen that grains are equiaxed, with the average grain size of 130 ± 49 nm, in accord with the value obtained by XRD (126nm).

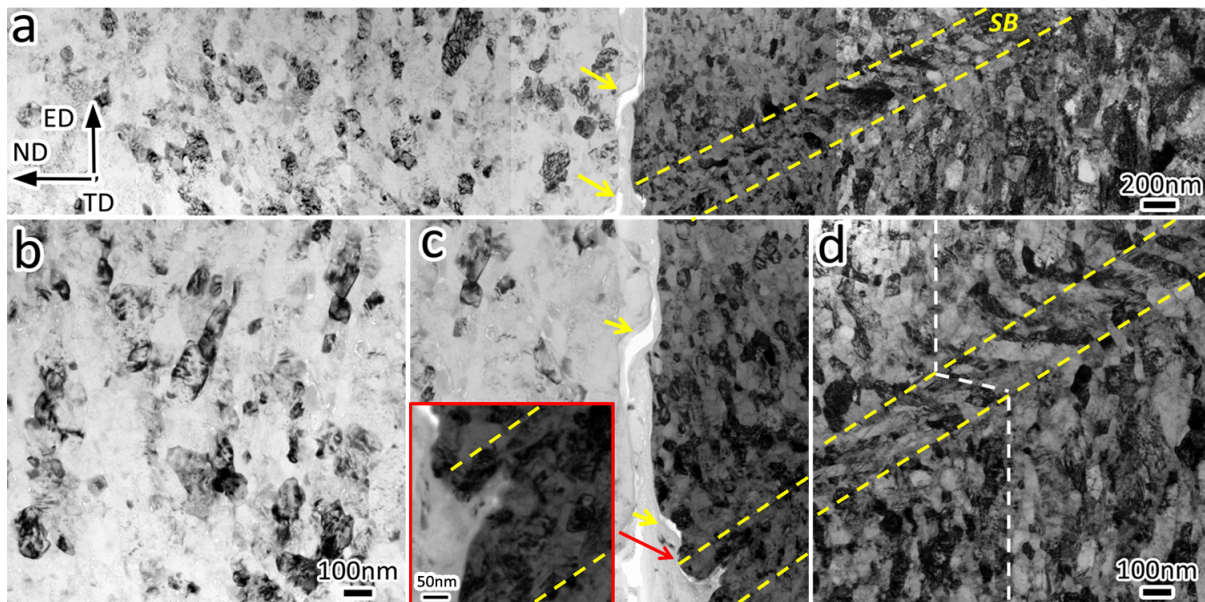


Figure. 6. 12 TEM-BF images of (a) the interface between AA6201 (left) and steel (right) from bimetallic rod with $\varnothing 5$ steel core after four ECAP passes, (b) AA6201, (c) interface, and (d) steel with high magnification. A pair of dashed lines delineate a shear band (SB).

A close-up picture of the grain structure in steel after ECAP processing is presented in Fig. 6.15. With an average grain size of 65 ± 20 nm, the material can be classified as nanostructured. No martensite was detected by selected area diffraction pattern (SADP). A continuous ring pattern suggests a random grain orientation and the occurrence of a large fraction of high-angle grain boundaries (HAGBs) in this region. This again confirms the XRD phase identification results showing that no phase transformation occurred during ECAP processing.

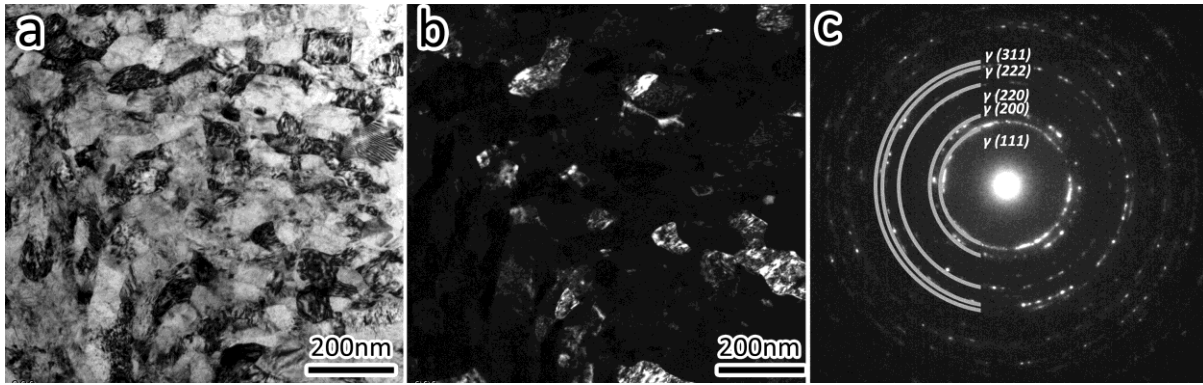


Figure. 6. 13 TEM images of steel core Ø5 subjected to 4 ECAP passes with (a) BF image, (b) DF images and (c) the corresponding SADP using aperture diameter of 0.75 μm

TEM characterisation was used to image precipitates in AA6201 grains. As shown in Fig. 6.15 (a), the as-received AA6201 contained needle-shaped metastable β'' precipitates on [001] planes. After one ECAP pass at 175 °C, the precipitates disappeared and dislocation cells were present, as seen in one grain in Fig. 6.15 (b). This suggests that solute atoms in solid solution and dislocations contributed to a decrease of conductivity. After three more ECAP passes dislocation cell boundaries were transferred to grain boundaries and few nanosized second-phase precipitates were developed, cf. Fig. 6.15 (c). By contrast, Fig. 6.15 (d) shows that the AA6201 component that went through just one ECAP pass, but with a Ø3 steel core embedded, had a developed fine grain structure with well-defined grain boundaries. Solute aggregate nanostructures are also observed here. In this case, the combination of these microstructural features led to an increase of conductivity. With higher imposed strain, a large number of spherical-shaped solute aggregate nanostructures are observed, cf. Fig. 6.15 (e, f), which have similar morphology to those in Refs. [371, 390, 391]. All these features contribute to raising the electrical conductivity.

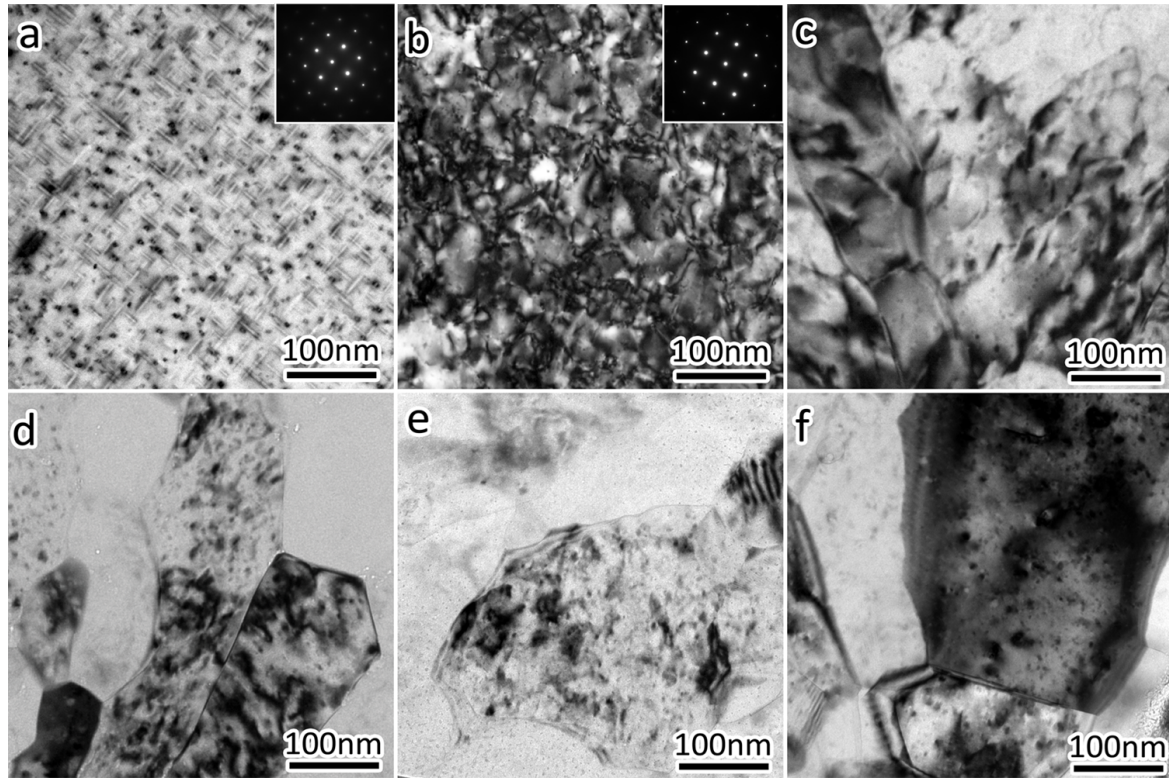


Figure. 6. 14 TEM-BF images showing AA6201 grain(s) from (a) as-received Al alloy with needle-shaped β'' precipitates clearly visible on (001) plane, (b, c) stand-alone Al after one and four ECAP passes, (d, e) AA6201 component in bimetallic rod with $\varnothing 3$ steel core after one and four ECAP passes, (f) AA6201 component in bimetallic rod with $\varnothing 5$ steel core after four ECAP passes. Note that (a, b) were taken normally to $\langle 001 \rangle$ zone axis, whereas, due to the strong diffraction contrast, (c-f) were not taken on zone axis. The occurrence of strain contours in some of the images should be noted.

The dynamic ageing of 6xxx series Al alloys under severe plastic deformation has been studied by a number of groups. The main finding is that the severe plastic deformation can cause fragmentation of metastable β' phase into several parts with spherical shape [392]. With increasing amount of plastic deformation, they grow to nano sized solute aggregates, which process is accompanied with a depletion of solid solution [371]. The high density of ECAP-induced crystal lattice defects such as vacancies and dislocations can increase the diffusivity of solutes in a very significant way, thus accelerating dynamic ageing [389, 391-393]. Based on this knowledge, it can be summarised that, due to load sharing between the steel core and the AA6201 cladding, ECAP processing can provide a strain on the cladding layer sufficient to achieve effective dynamic ageing, therefore ‘purify’ the bulk through formation of nano scale solute clusters analogous to what was found for HPT processing [371]. This is at

variance with the case of stand-alone AA6201. It can be conjectured that the strain provided by ECAP was insufficient to induce simultaneous increase of strength and conductivity was not achieved in this case.

6.5 Discussion

From the quantitative analysis by XRD and TEM conducted in this study, it can be seen that, under the same processing conditions, the AA6201 component of the hybrid material with an embedded steel core went through more efficient dynamic recrystallisation (as revealed by the smaller average grain size and the morphology of the grains) and dynamic ageing (as reflected in the magnitude of the lattice parameter) than stand-alone AA6201. In addition, by comparing different hybrid materials, it was found that the geometry of the rod, i.e. the core/rod diameter ratio, has a strong influence on the interface bonding. These phenomena lead us to discuss the size effect on co-deformation mechanism. By analogy with the co-deformation mechanism that has been considered for extrusion [353], spiral extrusion [394], and accumulative roll bonding [395], the microstructure evolution in the current system can be associated with friction between the AA6201 cladding layer and the die wall on its outer surface and the steel core on its inner surface.

During ECAP deformation, the die wall causes a frictional shear stress in the AA6201 layer acting in the direction opposite to the extrusion direction. With the steel core having a different flow velocity, there is also a friction shear stress acting in the extrusion direction at the interface between AA6201 and steel. The flow velocity difference between the regions near the outer surface of the rod and the interface decreases with increasing cladding layer thickness. This phenomenon was also found in extrusion process [353]. Due to a smaller distance between the two friction surfaces, a thinner cladding layer would be experiencing a higher level of shear stress, which is consistent with a more pronounced grain refinement in this case, as observed experimentally, cf. Fig. 6.12 (b) and Fig. 6.13 (b).

Obviously, the load sharing between the steel core and the AA6201 according to the area ratio between them determines the level of stresses acting in both constituents. In addition, plastic deformation near the interface depends on the inherent mechanical properties of the two materials involved. Aluminium as the softer component accommodates more plastic strain than steel. That is why for a thicker AA6201 cladding layer, the grain refinement within the steel core is limited (as seen in Fig. 6.12 (d)), as compared to the very fine grain

structure observed in Fig. 6.13 (d) for a thin AA6201 layer. Also, the occurrence of a shear band in the steel core of 5 mm diameter is a sign that strain accommodation therein was reaching its limits, plastic instability setting in.

6.6 Summary of this chapter

AA6201/316L steel bimetallic rods were successfully produced using ECAP. This technique has the potential to be scaled up for the application in overhead transmission lines. Bimetallic rods with different geometry factors of the steel core and Al cladding produced in this way were investigated. It was found that, beside the sound interface after processing, ECAP can significantly increase the mechanical performance of the hybrid rods. Moreover, among the three variants considered, one kind of geometry, viz. a bimetallic rod with a steel core of 3 mm in diameter and Al sheath 3.5 mm in thickness exhibited an outstanding performance in terms of simultaneous increase of mechanical strength and electrical conductivity after ECAP processing.

It was found that an embedded steel core can promote the dynamic recrystallization and dynamic ageing processes in AA6201 cladding components. The working hypothesis is that under co-deformation by ECAP, the Al sheath accommodates a greater plastic strain than a mono-material rod under the same processing condition. In addition, the friction shear stress provided by the steel core also contributes to development of favourable microstructure. Thus, on top of simple shear and hydrostatic pressure imparted to the material in the ECAP process, friction shear stress between the cladding layer and the core also influences the interface properties and the local microstructure evolution near the interface. More specifically, having larger hard core material and a thinner cladding layer, while keeping the outer diameter of the bimetallic rod unchanged, leads to a more pronounced grain refinement in both constituents of the hybrid structure. A thinner core and a thicker cladding layer contribute to better interface bonding. An optimum should be sought on the basis of these findings, depending on the targeted levels of strength, electrical conductivity, durability of the rods, and cost of production.

Chapter 7 Conclusion and Recommendations for Future Work

7.1 Outline of this chapter.....	129
7.2 Al/Mg machining chips compacts	129
7.2.1 Maximising interface density and minimizing interface space.....	131
7.2.2 Using different kinds of materials.....	131
7.3 Porous Ti and porous Ti/Mg	132
7.3.1 Biological test of porous Ti/Mg composite.....	133
7.3.2 Fabrication of ultrafine-grained porous Mg	133
7.4 Al/Steel bimetallic rod	134
7.4.1 Test of more geometries.....	135
7.4.2 Development of finite elements tool	135

Chapter 7 Conclusion and Recommendations for Future Work

7.1 Outline of this chapter

In this PhD work, the hypothesis that ECAP can be employed as an effective and special technique for designing and manufacturing architected multicomponent materials was validated for three case studies. Whilst being different with regard to the object of processing, the three sub-projects demonstrated that not only can ECAP produce a macro-scale architecture, but it can also refine the microstructure in each constituent of the hybrid material fabricated. In addition, these three sub-projects extended the potentialities of ECAP in the area of architected multicomponent materials. The main contribution and the major findings of these three studies to the field of multicomponent materials and SPD techniques are reviewed and summarised. They laid the groundwork for further studies that should help closing the gaps between the process designs explored in the thesis at laboratory scale and real engineering products.

7.2 Al/Mg machining chips compacts

In the first sub-project, machining chips were used for the first time as the raw materials to produce multicomponent material. The processing chain of this route is shown in Fig. 7.1.

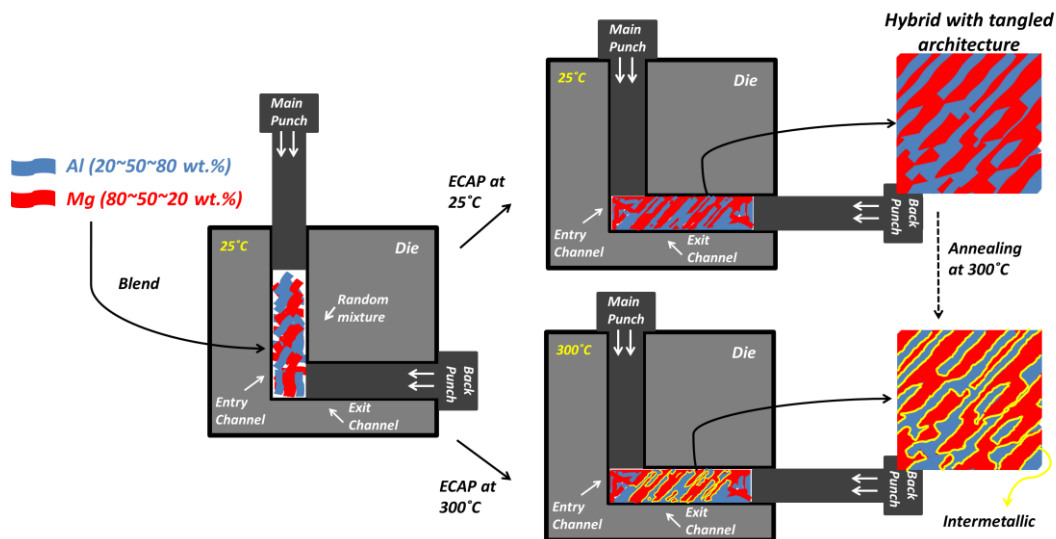


Figure. 7. 1 Schematic illustration of the processing chain of the first sub-project – using ECAP to fabricate metal-metal composites and intermetallic-metal composites from machining chips

Chapter 7 Conclusion and Recommendations for Future Work

In this study, we found that by employing ECAP and careful design, machining chips could be used as valuable raw materials to fabricate multicomponent materials with a high strength to weight ratio and high ductility. This favourable combination of properties was achieved thanks to the the high bonding strength between the constituents and the tangled as-deformed architecture. The formation of high strength bonds is caused by the efficient consolidation and ultrafast interdiffusion between chips. The tangled architecture is derived from the unique morphology and length scale of machining chips. As shown in Fig. 7.2, machining chips, with their helical shape and millimetre to centimetre size, fill the hole in the length sales of conventional components of hybrid materials, such as powders and 2D layers.

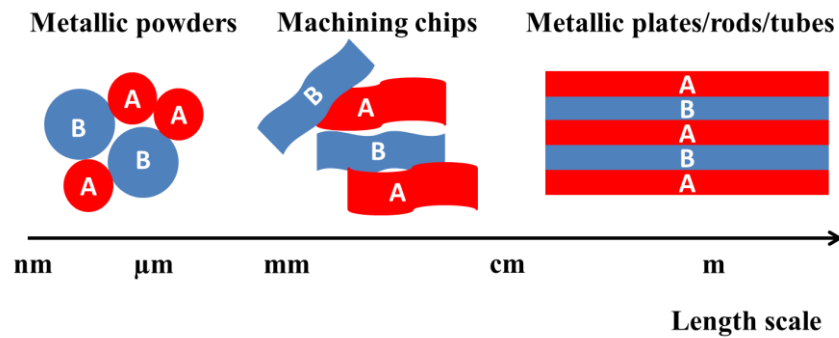


Figure. 7. 2 *The unique morphology and length scale of machining chips among other raw materials for fabricating multicomponent materials*

Furthermore, the role of the parameters of ECAP processing in this application was also investigated. First, with regard to strain path, in comparison with route B_C, route A imparts a larger plastic strain to machining chips thus enabling better densification and higher strength. Second, increasing back pressure can facilitate interdiffusion between chips due to higher imposed hydrostatic pressure on mating surfaces. Third, by conducting annealing treatment at elevated temperature, the diffusion bonding can be enhanced and lead to better mechanical performance. Finally, perhaps the most significant finding was the simultaneous increase of strength and ductility of the billet after ECAP at 300°C with respect to the results of ECAP at room temperature. This effect can be associated with the formation of intermetallic phases at interfaces that enhanced the bonding strength and the (quasi)-static recovery of the severely deformed microstructure of the constituent metals during ECAP processing.

Even though the findings point to a new route of manufacturing multicomponent materials, the mechanical properties of the materials fabricated in this study are inferior to those of the

Chapter 7 Conclusion and Recommendations for Future Work

massive Al and Mg alloys [396, 397]. Nevertheless, it is believed that there still are lots of opportunities for improving the processing performance.

7.2.1 Maximising interface density and minimising interface space

Due to the importance of the heterophase interfaces with respect to both mechanical and functional properties as stated in Chapter 2, it would be worthwhile trying out 50 vol.% composition of both kinds of machining chips to achieve the maximum interface density. Furthermore, by increasing the number of ECAP passes, fragmentation of chips and decrease of interface space is expected. It will be interesting to know what the most efficient strain path for reducing the interface excess volume would be and how much space reduction can be achieved for various numbers of passes. By conducting such further studies, more value may be added to tangled architected multicomponent materials produced from machining chips.

7.2.2 Using different kinds of materials

In addition to the combination of Al and Mg, further possibilities and applications can be obtained by using different kinds of machining chips. For example, Al and Ti machining chips can be used for lightweight applications. Considerable amount of machining chips of both materials are produced annually [250, 398]. Besides, combinations of them have been studied in several architectures such as multilayers and multifilaments, using a number of techniques. These include accumulative roll bonding (ARB) [399] and accumulative drawing [155]. In addition, it will also be promising to try compacting Cu and Nb machining chips together using ECAP. By imposing a large number of passes, the phase fragmentation is expected to occur, which would lead to an increase of interface density and a decrease of interface spacing. Compared with a continuous nanolayered Cu/Nb fabricated by ARB [162], as shown in Fig. 7.3, this proposed route may provide a discontinuous and tangled nanolayered architecture which also has potential applications in the area of radiation tolerant and shock resistant materials.

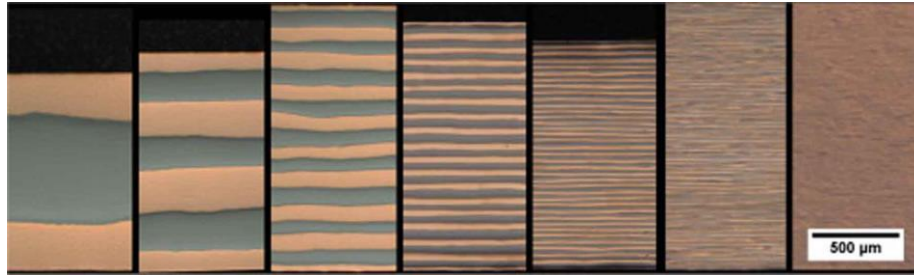


Figure. 7. 3 Optical micrographs showing the evolution of multi-layered Cu/Nb with increasing number of ARB processes [400]

7.3 Porous Ti and porous Ti/Mg

In the second sub-project, by incorporating the space holder method, ECAP compaction was first used for fabrication of porous structure. The processing chain is shown in Fig. 7.4.

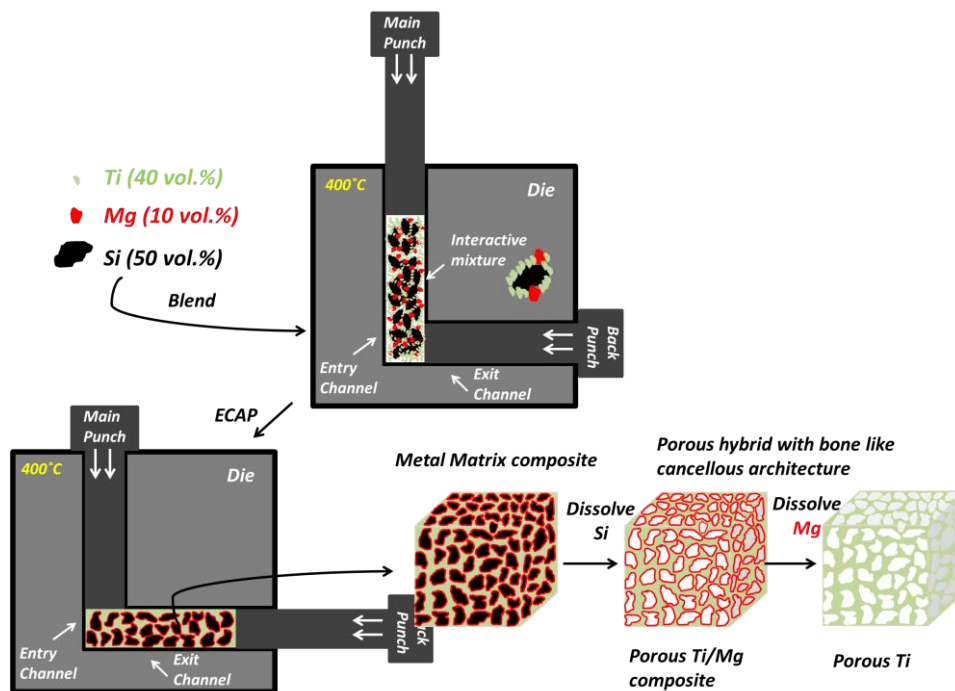


Figure. 7. 4 Schematic illustration of the processing chain of the second sub-project – using space holder enabled ECAP to fabricate a porous scaffold

Compared with traditional powder compaction methods, the strength of ECAP compaction is quite conspicuous in this application. The first and most significant outcome is the successful synthesis of porous Ti/Mg composite with ultrafine-grained Ti pore walls. This was achieved owing to the low processing temperature and the elimination of high temperature post annealing. Again, this demonstrated the usefulness of severe plastic deformation in terms of

Chapter 7 Conclusion and Recommendations for Future Work

interfacial bonding and microstructure refinement it enables. Second, the method also stands out from the viewpoint of the strain hardening behaviour and ductile failure of this material it produced. Third, quite fortunately, it was found that during processing, the inevitable redistribution of particles due to the mismatch of Young's modulus and particle sizes is beneficial for stronger and thicker pore walls. Finally, it was also interesting to observe that, due to Ti oxide layer breakage during processing, a unique morphology of pore surfaces was obtained as a result of a chemical reaction between NaOH and fresh Ti. This pore surface morphology was found to be conducive for interaction of the porous scaffolds with preosteoblast cells.

Based on these promising results, further work directed at perfecting the proposed fabrication route appears worthwhile.

7.3.1 Biological test of porous Ti/Mg composite

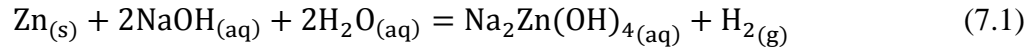
For intended medical applications, porous Ti/Mg composite maybe a more attractive product than porous Ti. The higher strength of the composite ensures a higher load bearing capability in the beginning and continual reduction of stiffness through dissolving of Mg during the healing process. Therefore, it will be necessary to predict how long it will take to completely dissolve the Mg component from the porous Ti/Mg composite. This can be done by mass loss measurement, in which the samples is be immersed in a simulated body fluid for various times and the weight loss percentage is determined as $(W_{\text{Before immersion}} - W_{\text{After immersion}}) / W_{\text{Before immersion}}$, where W denotes the weight of the sample [401, 402]. Since Mg phase takes 20 vol.% of the porous Ti/Mg composite, its weight can be calculated. Therefore, its degradation rate can be predicted based on such measurements.

7.3.2 Fabrication of ultrafine-grained porous Mg

Porous Mg scaffolds is a promising biodegradable product that is receiving increasing attentions in recent years [403-405]. Compared with full dense, bulk Mg medical devices, the interconnected porous structure allows tissue ingrowth into the pores, prevents implant loosening, permits the transport of body fluid and provides possible pathways for drug delivery [403, 406]. However, due to the higher surface area, porous Mg is more prone to be corroded [404]. Besides, its strength is lower than that of its bulk counterpart. Here, using similar route, ultrafine-grained porous Mg is expected to be fabricated. Zn as a biocompatible

Chapter 7 Conclusion and Recommendations for Future Work

and bioresorbable metal can be used as the space holder material and leached out in body fluid or aqueous solution of sodium hydroxide by the reaction given below [407]:



Because of the expected ultrafine-grained microstructure, the corrosion resistance and strength of the Mg struts are believed to be higher than those produced by traditional methods [408, 409]. Moreover, by imposing high back pressure, it is possible to add drug powders to the mixture of Mg and Zn and conduct the consolidation at room temperature. Anti-inflammatory or other drugs can be gradually realised when Mg is dissolving in the body [406, 410].

7.4 Al/Steel bimetallic rod

In the third sub-project, ECAP was adapted to processing of bimetallic rod with concentric jacket/core architecture. The targeted application is in wires for advanced overhead transmission lines. The processing chain is illustrated in Fig. 7.5. It can be upscaled for continuous manufacturing of the composite wire.

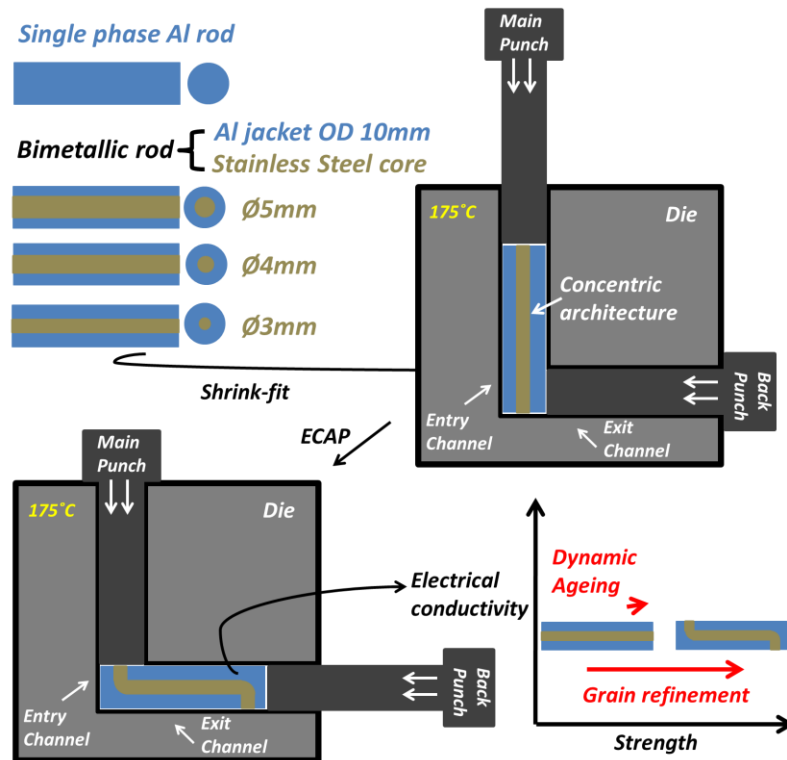


Figure. 7. 5 Schematic illustration of the processing chain of the third sub-project – using ECAP to fabricate bimetallic rod with concentric jacket/core architecture

Chapter 7 Conclusion and Recommendations for Future Work

In this study, a new design strategy for attaining high strength and high electrical conductivity in the bimetallic rod architecture was achieved. This is due to grain refinement in both components and enhancement of solid solution decomposition in the Al alloy component. Perhaps the most significant finding in this work is about the co-deformation mechanism. Comparing between a single phase Al rod and a hybrid of steel with an Al jacket layer in a bimetallic architecture, one can recognise that the latter went through considerably higher rate of dynamic recrystallisation and dynamic ageing. Within the jacket/core concentric architecture, the microstructure evolution in both constituents can also be altered by varying the volume fraction of jacket and core components. Specifically, a larger core and thinner jacket would lead to a more efficient grain refinement in both constituents. A slimmer core and thicker jacket layer would contribute to better interface bonding. This is an interesting example of how the properties of the composite can be controlled by varying its architecture.

We note that after ECAP processing of a bimetallic composite with a particular geometry, the mechanical strength was significantly improved while electrical conductivity was maintained. These results can thus be considered as a successful proof of concept. However, there is still a long way for this design to be taken up by industry. More systematic experiments and simulation studies are necessary to have a convincing case for pushing this approach towards real engineering applications.

7.4.1 Test of more geometries

Even though it was found that the co-deformation caused by embedment of hard core can accelerate microstructure refinement of jacket material, it would be interesting to further reduce the diameter of the steel core below 3mm and investigate when it will no longer contribute to microstructure variation of the jacket layer. Obtaining this value can help the design reduce the use of steel and achieve higher electrical conductivity and specific strength of the hybrid wire.

7.4.2 Development of finite elements tool

During the ECAP deformation, the initial concentric architecture was inevitably changed by metal flowing between the constituents. Thus, the core was inclined to the axis in the jacket layer. Because the targeted architecture is set as a concentric pattern, it will be very useful to

Chapter 7 Conclusion and Recommendations for Future Work

develop a finite element tool for optimisation of initial geometrical pattern by back simulation for a certain ECAP processing route.

References:

- [1] Raabe D, Choi PP, Li Y, Kostka A, Sauvage X, Lecouturier F, et al. Metallic composites processed via extreme deformation: Torward the limits of strength in bulk materials. *MRS Bulletin* 2010;35:982-91
- [2] Bachmaier A, Pippin R. Generation of metallic nanocomposites by severe plastic deformation. *International Materials Reviews* 2013;58:41-62.
- [3] Ashby MF, Cebon D. Materials selection in mechanical design. *Le Journal de Physique IV* 1993;3:C7-1-C7-9.
- [4] Ashby M. Multi-objective optimization in material design and selection. *Acta materialia* 2000;48:359-69.
- [5] Ashby M, Brechet Y. Designing hybrid materials. *Acta materialia* 2003;51:5801-21.
- [6] Ashby M. Designing architected materials. *Scripta Materialia* 2013;68:4-7.
- [7] Ashby M. Hybrid Materials to Expand the Boundaries of Material-Property Space. *Journal of the American Ceramic Society* 2011;94:s3-s14.
- [8] Bouaziz O, Brechet Y, Embury J. Heterogeneous and architected materials: a possible strategy for design of structural materials. *Advanced Engineering Materials* 2008;10:24-36.
- [9] Brechet Y, Embury JD. Architected materials: Expanding materials space. *Scripta Materialia* 2013;68:1-3.
- [10] Valiev RZ, Krasilnikov NA, Tsenev NK. Plastic deformation of alloys with submicron-grained structure. *Materials Science and Engineering: A* 1991;137:35-40.
- [11] Valiev RZ, Estrin Y, Horita Z, Langdon TG, Zehetbauer MJ, Zhu YT. Producing bulk ultrafine-grained materials by severe plastic deformation. *JOM* 2006;58:33-9.
- [12] Estrin Y, Vinogradov A. Extreme grain refinement by severe plastic deformation: A wealth of challenging science. *Acta Materialia* 2013;61:782-817.
- [13] Langdon TG. Twenty-five years of ultrafine-grained materials: Achieving exceptional properties through grain refinement. *Acta Materialia* 2013;61:7035-59.
- [14] Lapovok R, Qi Y, Ng H, Maier V, Estrin Y. Multicomponent materials from machining chips compacted by equal-channel angular pressing. *Journal of Materials Science* 2014;49:1193-204.
- [15] Ohsaki S, Kato S, Tsuji N, Ohkubo T, Hono K. Bulk mechanical alloying of Cu–Ag and Cu/Zr two-phase microstructures by accumulative roll-bonding process. *Acta Materialia* 2007;55:2885-95.
- [16] Sauvage X, Wetscher F, Pareige P. Mechanical alloying of Cu and Fe induced by severe plastic deformation of a Cu–Fe composite. *Acta Materialia* 2005;53:2127-35.
- [17] Lapovok R, Ng HP, Tomus D, Estrin Y. Bimetallic copper–aluminium tube by severe plastic deformation. *Scripta Materialia* 2012;66:1081-4.
- [18] Latypov MI, Beygelzimer Y, Kulagin R, Varyukhin V, Kim HS. Toward architecturing of metal composites by twist extrusion. *Materials Research Letters* 2015:1-8.
- [19] Bouaziz O, Kim HS, Estrin Y. Architecturing of Metal - Based Composites with Concurrent Nanostructuring: A New Paradigm of Materials Design. *Advanced Engineering Materials* 2013;15:336-40.
- [20] Beygelzimer Y, Estrin Y, Kulagin R. Synthesis of Hybrid Materials by Severe Plastic Deformation: A New Paradigm of SPD Processing. *Advanced Engineering Materials* 2015:n/a-n/a.

References

- [21] Voestalpine. Clad linepipe plates - Linepipe - Engery - voestalpine steel division <http://www.voestalpine.com/stahl/en/Energy/Linepipe/Clad-linepipe-plates>. 2015.
- [22] Jinglei-Technology. Explosion clad steel plate <http://www.jinglei-china.com/en/pdulist.php>. 2015.
- [23] Nanjing Runbang Metal Clad Material Co. L. Composite plates <http://en.runbang.com.cn/yingyong.html>. 2015.
- [24] Materials XaTCM. Clad metal plates http://www.c-tlc.com.cn/English_new/index.asp. 2015.
- [25] Li L, Nagai K, Yin F. Progress in cold roll bonding of metals. *Science and Technology of Advanced Materials* 2008;9:023001.
- [26] Mori K-i, Bay N, Fratini L, Micari F, Tekkaya AE. Joining by plastic deformation. *CIRP Annals - Manufacturing Technology* 2013;62:673-94.
- [27] Vodenitcharova T, Kabir K, Hoffman M. Indentation of metallic foam core sandwich panels with soft aluminium face sheets. *Materials Science and Engineering: A* 2012;558:175-85.
- [28] McCormack TM, Miller R, Kesler O, Gibson LJ. Failure of sandwich beams with metallic foam cores. *International Journal of Solids and Structures* 2001;38:4901-20.
- [29] Bart-Smith H, Hutchinson JW, Evans AG. Measurement and analysis of the structural performance of cellular metal sandwich construction. *International Journal of Mechanical Sciences* 2001;43:1945-63.
- [30] Smith BH, Szyniszewski S, Hajjar JF, Schafer BW, Arwade SR. Steel foam for structures: A review of applications, manufacturing and material properties. *Journal of Constructional Steel Research* 2012;71:1-10.
- [31] Kabir K, Vodenitcharova T, Hoffman M. Response of aluminium foam-cored sandwich panels to bending load. *Composites Part B: Engineering* 2014;64:24-32.
- [32] Xu A, Vodenitcharova T, Kabir K, Flores-Johnson EA, Hoffman M. Finite element analysis of indentation of aluminium foam and sandwich panels with aluminium foam core. *Materials Science and Engineering: A* 2014;599:125-33.
- [33] Kabir KR, Vodenitcharova T, Hoffman M. Structural response of aluminium foam hybrid sandwich panels under three-point bending loading. *International Journal of Modern Physics B* 2009;23:1733-8.
- [34] Nee AY. *Handbook of Manufacturing Engineering and Technology*: Springer; 2015.
- [35] Sun Z. Joining dissimilar material combinations: materials and processes. *International Journal of Materials and Product Technology* 1995;10:16-26.
- [36] Messler Jr RW. Chapter 11 - Joining of Metals, Alloys, and Intermetallics. In: Messler RW, editor. *Joining of Materials and Structures*. Burlington: Butterworth-Heinemann; 2004. p. 535-82.
- [37] Findik F. Recent developments in explosive welding. *Mater Des* 2011;32:1081-93.
- [38] Murr LE. Explosive Welding, Forming, and Powder Consolidation. *Handbook of Materials Structures, Properties, Processing and Performance*: Springer; 2015. p. 863-89.
- [39] Acarer M, Demir B. An investigation of mechanical and metallurgical properties of explosive welded aluminum–dual phase steel. *Materials letters* 2008;62:4158-60.
- [40] Durgutlu A, Gülenç B, Findik F. Examination of copper/stainless steel joints formed by explosive welding. *Mater Des* 2005;26:497-507.
- [41] Kahraman N, Gülenç B, Findik F. Joining of titanium/stainless steel by explosive welding and effect on interface. *Journal of Materials Processing Technology* 2005;169:127-33.
- [42] Ashani J, Bagheri S. Explosive scarf welding of aluminum to copper plates and their interface properties. *Materialwissenschaft und Werkstofftechnik* 2009;40:690-8.

References

- [43] Yan Y, Zhang Z, Shen W, Wang J, Zhang L, Chin B. Microstructure and properties of magnesium AZ31B–aluminum 7075 explosively welded composite plate. *Materials Science and Engineering: A* 2010;527:2241-5.
- [44] Kahraman N, Gülenç B. Microstructural and mechanical properties of Cu–Ti plates bonded through explosive welding process. *Journal of Materials Processing Technology* 2005;169:67-71.
- [45] Topolski K, Wieciński P, Szulc Z, Gałka A, Garbacz H. Progress in the characterization of explosively joined Ti/Ni bimetals. *Mater Des* 2014;63:479-87.
- [46] Paul H, Lityńska-Dobrzyńska L, Prażmowski M. Microstructure and phase constitution near the interface of explosively welded aluminum/copper plates. *Metallurgical and Materials Transactions A* 2013;44:3836-51.
- [47] Wang B, Luo X, Wang B, Zhao S, Xie F. Microstructure and Its Formation Mechanism in the Interface of Ti/NiCr Explosive Cladding Bar. *J Mater Eng Perform* 2015;24:1050-8.
- [48] Haitao J, Xiaoqian Y, Jixiong L, Xiaoge D, Shangwu Z. Influence of Asymmetric Rolling Parameters on the Microstructure and Mechanical Properties of Titanium Explosive Clad Plate. *Rare Metal Mat Eng* 2014;43:2631-6.
- [49] Kim I-K, Hong SI. Effect of heat treatment on the bending behavior of tri-layered Cu/Al/Cu composite plates. *Mater Des* 2013;47:590-8.
- [50] Guo X, Tao J, Wang W, Li H, Wang C. Effects of the inner mould material on the aluminium–316L stainless steel explosive clad pipe. *Mater Des* 2013;49:116-22.
- [51] Mendes R, Ribeiro J, Loureiro A. Effect of explosive characteristics on the explosive welding of stainless steel to carbon steel in cylindrical configuration. *Mater Des* 2013;51:182-92.
- [52] Gulenc B. Investigation of interface properties and weldability of aluminum and copper plates by explosive welding method. *Mater Des* 2008;29:275-8.
- [53] Zhang XP, Yang TH, Castagne S, Gu CF, Wang JT. Proposal of bond criterion for hot roll bonding and its application. *Mater Des* 2011;32:2239-45.
- [54] Soltan Ali Nezhad M, Haerian Ardakani A. A study of joint quality of aluminum and low carbon steel strips by warm rolling. *Mater Des* 2009;30:1103-9.
- [55] Zhao DS, Yan JC, Wang Y, Yang SQ. Relative slipping of interface of titanium alloy to stainless steel during vacuum hot roll bonding. *Materials Science and Engineering: A* 2009;499:282-6.
- [56] Chaudhari GP, Acoff VL. Titanium aluminide sheets made using roll bonding and reaction annealing. *Intermetallics* 2010;18:472-8.
- [57] Movahedi M, Madaah-Hosseini H, Kokabi A. The influence of roll bonding parameters on the bond strength of Al-3003/Zn soldering sheets. *Materials Science and Engineering: A* 2008;487:417-23.
- [58] Zhang X, Yang T, Castagne S, Wang J. Microstructure; bonding strength and thickness ratio of Al/Mg/Al alloy laminated composites prepared by hot rolling. *Materials Science and Engineering: A* 2011;528:1954-60.
- [59] Chen C-Y, Chen H-L, Hwang W-S. Influence of interfacial structure development on the fracture mechanism and bond strength of aluminum/copper bimetal plate. *Mater Trans* 2006;47:1232-9.
- [60] Manesh D, Taheri K. An investigation of deformation behavior and bonding strength of bimetal strip during rolling. *Mechanics of Materials* 2005;37:531-42.
- [61] Chen S, Ke F, Zhou M, Bai Y. Atomistic investigation of the effects of temperature and surface roughness on diffusion bonding between Cu and Al. *Acta Materialia* 2007;55:3169-75.
- [62] engineering Vp. Diffusion bonding 2015.

References

- [63] M. Qian GBS, C.J. Bettles. . Sintering of titanium and its alloys In: Fang ZZ, editor. Sintering of advanced materials: Woodhead Publishing 2010. p. 336-8.
- [64] Sabetghadam H, Hanzaki AZ, Araee A. Diffusion bonding of 410 stainless steel to copper using a nickel interlayer. *Materials Characterization* 2010;61:626-34.
- [65] Zhang J, Shen Q, Luo G, Li M, Zhang L. Microstructure and bonding strength of diffusion welding of Mo/Cu joints with Ni interlayer. *Mater Des* 2012;39:81-6.
- [66] Ghosh M, Bhanumurthy K, Kale G, Krishnan J, Chatterjee S. Diffusion bonding of titanium to 304 stainless steel. *Journal of Nuclear Materials* 2003;322:235-41.
- [67] Elrefaey A, Tillmann W. Solid state diffusion bonding of titanium to steel using a copper base alloy as interlayer. *Journal of materials processing technology* 2009;209:2746-52.
- [68] Li Y, Liu P, Wang J, Ma H. XRD and SEM analysis near the diffusion bonding interface of Mg/Al dissimilar materials. *Vacuum* 2007;82:15-9.
- [69] Luo G, Zhang J, Li M, Wei Q, Shen Q, Zhang L. Interfacial Microstructure and Mechanical Strength of 93W/Ta Diffusion-Bonded Joints with Ni Interlayer. *Metallurgical and Materials Transactions A* 2013;44:602-5.
- [70] Sabetghadam H, Hanzaki AZ, Araee A, Hadian A. Microstructural evaluation of 410 SS/Cu diffusion-bonded joint. *Journal of Materials Science & Technology* 2010;26:163-9.
- [71] Li B, Zhang Z, Shen Y, Hu W, Luo L. Dissimilar friction stir welding of Ti–6Al–4V alloy and aluminum alloy employing a modified butt joint configuration: Influences of process variables on the weld interfaces and tensile properties. *Mater Des* 2014;53:838-48.
- [72] Groche P, Wohletz S, Brenneis M, Pabst C, Resch F. Joining by forming—a review on joint mechanisms, applications and future trends. *Journal of Materials Processing Technology* 2014;214:1972-94.
- [73] Kwon Y, Shigematsu I, Saito N. Dissimilar friction stir welding between magnesium and aluminum alloys. *Materials Letters* 2008;62:3827-9.
- [74] Nandan R, DebRoy T, Bhadeshia HKDH. Recent advances in friction-stir welding – Process, weldment structure and properties. *Progress in Materials Science* 2008;53:980-1023.
- [75] Kasai H, Morisada Y, Fujii H. Dissimilar FSW of immiscible materials: Steel/magnesium. *Materials Science and Engineering: A* 2015;624:250-5.
- [76] Sato YS, Park SHC, Michiuchi M, Kokawa H. Constitutional liquation during dissimilar friction stir welding of Al and Mg alloys. *Scripta Materialia* 2004;50:1233-6.
- [77] Venkateswaran P, Reynolds AP. Factors affecting the properties of Friction Stir Welds between aluminum and magnesium alloys. *Materials Science and Engineering: A* 2012;545:26-37.
- [78] Tanaka T, Morishige T, Hirata T. Comprehensive analysis of joint strength for dissimilar friction stir welds of mild steel to aluminum alloys. *Scripta Materialia* 2009;61:756-9.
- [79] van der Rest C, Jacques PJ, Simar A. On the joining of steel and aluminium by means of a new friction melt bonding process. *Scripta Materialia* 2014;77:25-8.
- [80] Chen Y, Nakata K. Microstructural characterization and mechanical properties in friction stir welding of aluminum and titanium dissimilar alloys. *Mater Des* 2009;30:469-74.
- [81] Fazel-Najafabadi M, Kashani-Bozorg S, Zarei-Hanzaki A. Joining of CP-Ti to 304 stainless steel using friction stir welding technique. *Mater Des* 2010;31:4800-7.
- [82] Akbari M, Behnagh RA. Dissimilar friction-stir lap joining of 5083 aluminum alloy to CuZn34 brass. *Metallurgical and Materials Transactions B* 2012;43:1177-86.

References

- [83] Xue P, Ni DR, Wang D, Xiao BL, Ma ZY. Effect of friction stir welding parameters on the microstructure and mechanical properties of the dissimilar Al–Cu joints. *Materials Science and Engineering: A* 2011;528:4683-9.
- [84] Coelho RS, Kostka A, dos Santos JF, Kaysser-Pyzalla A. Friction-stir dissimilar welding of aluminium alloy to high strength steels: Mechanical properties and their relation to microstructure. *Materials Science and Engineering: A* 2012;556:175-83.
- [85] Kicukov E, Gursel A. Ultrasonic welding of dissimilar materials: A review. *Periodicals of Engineering and Natural Sciences (PEN)* 2015;3.
- [86] Kim TH, Yum J, Hu SJ, Spicer JP, Abell JA. Process robustness of single lap ultrasonic welding of thin, dissimilar materials. *CIRP Annals - Manufacturing Technology* 2011;60:17-20.
- [87] Annoni M, Carboni M. Ultrasonic metal welding of AA  6022-T4 lap joints: Part I-Technological characterisation and static mechanical behaviour. *Science and Technology of Welding and Joining* 2011;16:107-15.
- [88] Yang J, Cao B. Investigation of resistance heat assisted ultrasonic welding of 6061 aluminum alloys to pure copper. *Mater Des* 2015;74:19-24.
- [89] Yang J, Cao B, He X, Luo H. Microstructure evolution and mechanical properties of Cu-Al joints by ultrasonic welding. *Science and Technology of Welding and Joining* 2014;19:500-4.
- [90] Tsujino J, Hidai K, Hasegawa A, Kanai R, Matsuura H, Matsushima K, et al. Ultrasonic butt welding of aluminum, aluminum alloy and stainless steel plate specimens. *Ultrasonics* 2002;40:371-4.
- [91] Zhu Z, Lee KY, Wang X. Ultrasonic welding of dissimilar metals, AA6061 and Ti6Al4V. *The International Journal of Advanced Manufacturing Technology* 2012;59:569-74.
- [92] Panteli A, Robson JD, Brough I, Prangnell PB. The effect of high strain rate deformation on intermetallic reaction during ultrasonic welding aluminium to magnesium. *Materials Science and Engineering: A* 2012;556:31-42.
- [93] Janaki Ram G, Yang Y, Nylander C, Aydelotte B, Stucker B, Adams B. Interface microstructures and bond formation in ultrasonic consolidation. *Proceedings of the 18th Solid Freeform Fabrication Symposium, Austin, TX* 2007.
- [94] Ng M-K, Li L, Fan Z, Gao RX, Smith Iii EF, Ehmann KF, et al. Joining sheet metals by electrically-assisted roll bonding. *CIRP Annals - Manufacturing Technology* 2015;64:273-6.
- [95] Lee KS, Lee YS, Kwon YN. Influence of secondary warm rolling on the interface microstructure and mechanical properties of a roll-bonded three-ply Al/Mg/Al sheet. *Materials Science and Engineering: A* 2014;606:205-13.
- [96] Messler Jr RW. Chapter 4 - Adhesive Bonding and Cementing. In: Messler RW, editor. *Joining of Materials and Structures*. Burlington: Butterworth-Heinemann; 2004. p. 177-226.
- [97] Shewmon P. Diffusion in solids. The Minerals, Metals & Materials Society, *Diffusion in Solids Second Edition(Retroactive Coverage)(United States)*, 1989 1989:246.
- [98] Mehrer H. *Diffusion in solids: fundamentals, methods, materials, diffusion-controlled processes*: Springer Science & Business Media; 2007.
- [99] Kaur I, Mishin Y, Gust W. *Fundamentals of Grain and Interphase Boundary Diffusion*. Stuttgart; 1995.
- [100] Ribbe J, Baither D, Schmitz G, Divinski SV. Network of Porosity Formed in Ultrafine-Grained Copper Produced by Equal Channel Angular Pressing. *Physical Review Letters* 2009;102:165501-4.

References

- [101] Ribbe J, Baither D, Schmitz G, Divinski SV. Ultrafast diffusion and internal porosity in ultrafine-grained copper–lead alloy prepared by equal channel angular pressing. *Scripta Materialia* 2009;61:129-32.
- [102] 16 - Metal matrix, fibre–metal and ceramic matrix composites for aerospace applications. In: Mouritz AP, editor. *Introduction to Aerospace Materials*: Woodhead Publishing; 2012. p. 394-410.
- [103] ZHANG D, ZHANG G, LI Z. The Current State and Trend of Metal Matrix Composites [J]. *Materials China* 2010;4:004.
- [104] Macke A, Schultz BF, Rohatgi PK, Gupta N. Metal matrix composites for automotive applications. *Advanced Composite Materials for Automotive Applications: Structural Integrity and Crashworthiness* 2013:311-44.
- [105] Subramanian J, Seetharaman S, Gupta M. Processing and Properties of Aluminum and Magnesium Based Composites Containing Amorphous Reinforcement: A Review. *Metals* 2015;5:743-62.
- [106] Walker JC, Rainforth WM, Jones H. Lubricated sliding wear behaviour of aluminium alloy composites. *Wear* 2005;259:577-89.
- [107] Corrochano J, Walker JC, Lieblisch M, Ibáñez J, Rainforth WM. Dry sliding wear behaviour of powder metallurgy Al–Mg–Si alloy–MoSi₂ composites and the relationship with the microstructure. *Wear* 2011;270:658-65.
- [108] Tjong SC. Novel Nanoparticle - Reinforced Metal Matrix Composites with Enhanced Mechanical Properties. *Advanced engineering materials* 2007;9:639-52.
- [109] Mortensen A, Llorca J. Metal matrix composites. *Annual review of materials research* 2010;40:243-70.
- [110] Suresh S. *Fundamentals of metal-matrix composites*: Elsevier; 2013.
- [111] *Titanium Matrix Composites*. Titanium: Springer Berlin Heidelberg; 2007. p. 367-82.
- [112] Yang Y, Lan J, Li X. Study on bulk aluminum matrix nano-composite fabricated by ultrasonic dispersion of nano-sized SiC particles in molten aluminum alloy. *Materials Science and Engineering: A* 2004;380:378-83.
- [113] Mula S, Padhi P, Panigrahi S, Pabi S, Ghosh S. On structure and mechanical properties of ultrasonically cast Al–2% Al₂O₃ nanocomposite. *Materials Research Bulletin* 2009;44:1154-60.
- [114] Cao G, Konishi H, Li X. Mechanical properties and microstructure of SiC-reinforced Mg-(2, 4) Al-1Si nanocomposites fabricated by ultrasonic cavitation based solidification processing. *Materials Science and Engineering: A* 2008;486:357-62.
- [115] Llorca-Isern N, Artieda-Guzmán C. 9 - Metal-based composite powders. In: Chang I, Zhao Y, editors. *Advances in Powder Metallurgy*: Woodhead Publishing; 2013. p. 241-72.
- [116] Vintila R, Charest A, Drew RAL, Brochu M. Synthesis and consolidation via spark plasma sintering of nanostructured Al-5356/B4C composite. *Materials Science and Engineering: A* 2011;528:4395-407.
- [117] Ye J, Ajdelsztajn L, Schoenung JM. Bulk nanocrystalline aluminum 5083 alloy fabricated by a novel technique: Cryomilling and spark plasma sintering. *Metallurgical and Materials Transactions A* 2006;37:2569-79.
- [118] Tamari N, Tanaka T, Tanaka K, Kondoh I, Kawahara M, Tokita M. Effect of spark plasma sintering on densification and mechanical properties of silicon carbide. *Nippon seramikku kyokai gakujutsu ronbunshi* 1995;103:740-2.
- [119] Chawla N, Krishan K. *Metal matrix composites*: Wiley Online Library; 2006.
- [120] Deng KK, Wu K, Wang XJ, Wu YW, Hu XS, Zheng MY, et al. Microstructure evolution and mechanical properties of a particulate reinforced magnesium matrix

References

- composites forged at elevated temperatures. *Materials Science and Engineering: A* 2010;527:1630-5.
- [121] Shang S-j, Deng K-k, Nie K-b, Li J-c, Zhou S-s, Xu F-j, et al. Microstructure and mechanical properties of SiCp/Mg–Al–Zn composites containing Mg₁₇Al₁₂ phases processed by low-speed extrusion. *Materials Science and Engineering: A* 2014;610:243-9.
- [122] Deng KK, Wang XJ, Wu YW, Hu XS, Wu K, Gan WM. Effect of particle size on microstructure and mechanical properties of SiCp/AZ91 magnesium matrix composite. *Materials Science and Engineering: A* 2012;543:158-63.
- [123] Nie KB, Wang XJ, Xu L, Wu K, Hu XS, Zheng MY. Effect of hot extrusion on microstructures and mechanical properties of SiC nanoparticles reinforced magnesium matrix composite. *J Alloy Compd* 2012;512:355-60.
- [124] Ghosh AK. Chapter 2 - Solid-State Processing. In: Needleman SSM, editor. *Fundamentals of Metal-Matrix Composites*. Boston: Butterworth-Heinemann; 1993. p. 23-41.
- [125] Lim SCV, Rollett AD. Length scale effects on recrystallization and texture evolution in Cu layers of a roll-bonded Cu–Nb composite. *Materials Science and Engineering: A* 2009;520:189-96.
- [126] Bevk J, Harbison JP, Bell JL. Anomalous increase in strength of insitu formed Cu - Nb multifilamentary composites. *Journal of Applied Physics* 1978;49:6031-8.
- [127] Frommeyer G, Wassermann G. Microstructure and anomalous mechanical properties of in situ-produced silver-copper composite wires. *Acta Metallurgica* 1975;23:1353-60.
- [128] Misra A, Hirth JP, Hoagland RG. Length-scale-dependent deformation mechanisms in incoherent metallic multilayered composites. *Acta Materialia* 2005;53:4817-24.
- [129] Funkenbusch PD, Courtney TH. On the strength of heavily cold worked in situ composites. *Acta Metallurgica* 1985;33:913-22.
- [130] Demkowicz MJ, Wang J, Hoagland RG. Chapter 83 - Interfaces Between Dissimilar Crystalline Solids. In: Hirth JP, editor. *Dislocations in Solids*: Elsevier; 2008. p. 141-205.
- [131] Dupouy F, Snoeck E, Casanove M, Roucau C, Peyrade J, Askenazy S. Microstructural characterization of high strength and high conductivity nanocomposite wires. *Scripta materialia* 1996;34:1067-73.
- [132] Thilly L, Veron M, Ludwig O, Lecouturier F, Peyrade J, Askenazy S. High-strength materials: in-situ investigations of dislocation behaviour in Cu-Nb multifilamentary nanostructured composites. *Philosophical Magazine A* 2002;82:925-42.
- [133] Spencer K, Lecouturier F, Thilly L, Embury JD. Established and Emerging Materials for use as High - Field Magnet Conductors. *Advanced Engineering Materials* 2004;6:290-7.
- [134] Demkowicz MJ, Thilly L. Structure, shear resistance and interaction with point defects of interfaces in Cu–Nb nanocomposites synthesized by severe plastic deformation. *Acta Materialia* 2011;59:7744-56.
- [135] Russell AM, Chumbley LS, Tian Y. Deformation processed metal–metal composites. *Advanced Engineering Materials* 2000;2:11-22.
- [136] Rdzawski Z, Gluchowski W, Stobrawa J, Kempinski W, Andrzejewski B. Microstructure and properties of nanofilament Cu-Nb and Cu-Ag composites. *Materials* 2014.
- [137] Beyerlein IJ, Mara NA, Bhattacharyya D, Alexander DJ, Necker CT. Texture evolution via combined slip and deformation twinning in rolled silver–copper cast eutectic nanocomposite. *International Journal of Plasticity* 2011;27:121-46.

References

- [138] Tian YZ, Wu SD, Zhang ZF, Figueiredo RB, Gao N, Langdon TG. Microstructural evolution and mechanical properties of a two-phase Cu–Ag alloy processed by high-pressure torsion to ultrahigh strains. *Acta Materialia* 2011;59:2783-96.
- [139] Zhang RF, Germann TC, Wang J, Liu XY, Beyerlein IJ. Role of interface structure on the plastic response of Cu/Nb nanolaminates under shock compression: Non-equilibrium molecular dynamics simulations. *Scripta Materialia* 2013;68:114-7.
- [140] Han W, Demkowicz MJ, Mara NA, Fu E, Sinha S, Rollett AD, et al. Design of radiation tolerant materials via interface engineering. *Advanced materials* 2013;25:6975-9.
- [141] Delincé M, Bréchet Y, Embury JD, Geers MGD, Jacques PJ, Pardoen T. Structure–property optimization of ultrafine-grained dual-phase steels using a microstructure-based strain hardening model. *Acta Materialia* 2007;55:2337-50.
- [142] Edalati K, Toh S, Watanabe M, Horita Z. In situ production of bulk intermetallic-based nanocomposites and nanostructured intermetallics by high-pressure torsion. *Scripta Materialia* 2012;66:386-9.
- [143] Ankem S, Margolin H, Greene CA, Neuberger BW, Oberson PG. Mechanical properties of alloys consisting of two ductile phases. *Progress in Materials Science* 2006;51:632-709.
- [144] Banhart J. Manufacturing routes for metallic foams. *Jom* 2000;52:22-7.
- [145] Lefebvre L-P, Banhart J, Dunand D. Porous metals and metallic foams: current status and recent developments. *Advanced Engineering Materials* 2008;10:775-87.
- [146] Idris MI, Vodenitcharova T, Hoffman M. Mechanical behaviour and energy absorption of closed-cell aluminium foam panels in uniaxial compression. *Materials Science and Engineering: A* 2009;517:37-45.
- [147] Banhart J. Manufacture, characterisation and application of cellular metals and metal foams. *Progress in Materials Science* 2001;46:559-632.
- [148] Singh R, Lee P, Dashwood R, Lindley T. Titanium foams for biomedical applications: a review. *Materials Science and Technology* 2010;25:127-36.
- [149] Ryan G, Pandit A, Apatsidis DP. Fabrication methods of porous metals for use in orthopaedic applications. *Biomaterials* 2006;27:2651-70.
- [150] Karageorgiou V, Kaplan D. Porosity of 3D biomaterial scaffolds and osteogenesis. *Biomaterials* 2005;26:5474-91.
- [151] Han Y-q, Ben L-h, Yao J-j, Wu C-j. Microstructural characterization of Cu/Al composites and effect of cooling rate at the Cu/Al interfacial region. *International Journal of Minerals, Metallurgy, and Materials* 2015;22:94-101.
- [152] Barg S, Soltmann C, Schwab A, Koch D, Schwieger W, Grathwohl G. Novel open cell aluminum foams and their use as reactive support for zeolite crystallization. *Journal of Porous Materials* 2011;18:89-98.
- [153] González C, Llorca J. Micromechanical modelling of deformation and failure in Ti–6Al–4V/SiC composites. *Acta Materialia* 2001;49:3505-19.
- [154] Ramanujam R, Muthukrishnan N, Raju R. Optimization of cutting parameters for turning Al–SiC(10p) MMC using ANOVA and grey relational analysis. *Int J Precis Eng Manuf* 2011;12:651-6.
- [155] Marr T, Freudenberger J, Seifert D, Klauß H, Romberg J, Okulov I, et al. Ti–Al composite wires with high specific strength. *Metals* 2011;1:79-97.
- [156] Gleiter H. Nanostructured materials: basic concepts and microstructure. *Acta Materialia* 2000;48:1-29.
- [157] Valiev R, Alexandrov I, Enikeev N, Murashkin MY, Semenova I. Towards enhancement of properties of UFG metals and alloys by grain boundary engineering using SPD processing. *Rev Adv Mater Sci* 2010;25:1-10.

References

- [158] Sauvage X, Wilde G, Divinski SV, Horita Z, Valiev RZ. Grain boundaries in ultrafine grained materials processed by severe plastic deformation and related phenomena. *Materials Science and Engineering: A* 2012;540:1-12.
- [159] Ekiz EH, Lach TG, Averbach RS, Mara NA, Beyerlein IJ, Pouryazdan M, et al. Microstructural evolution of nanolayered Cu–Nb composites subjected to high-pressure torsion. *Acta Materialia* 2014;72:178-91.
- [160] Demkowicz M, Bellon P, Wirth B. Atomic-scale design of radiation-tolerant nanocomposites. *MRS bulletin* 2010;35:992-8.
- [161] Dunlop JW, Fratzl P. Multilevel architectures in natural materials. *Scripta Materialia* 2013;68:8-12.
- [162] Carpenter JS, Vogel SC, LeDonne JE, Hammon DL, Beyerlein IJ, Mara NA. Bulk texture evolution of Cu–Nb nanolamellar composites during accumulative roll bonding. *Acta Materialia* 2012;60:1576-86.
- [163] Chang H, Zheng M, Gan W, Wu K, Maawad E, Brokmeier H. Texture evolution of the Mg/Al laminated composite fabricated by the accumulative roll bonding. *Scripta Materialia* 2009;61:717-20.
- [164] Han W, Carpenter J, Wang J, Beyerlein I, Mara N. Atomic-level study of twin nucleation from face-centered-cubic/body-centered-cubic interfaces in nanolamellar composites. *Appl Phys Lett* 2012;100:011911.
- [165] Beyerlein IJ, Mayeur JR, Zheng S, Mara NA, Wang J, Misra A. Emergence of stable interfaces under extreme plastic deformation. *Proceedings of the national academy of sciences* 2014;111:4386-90.
- [166] Kulagin R, Latypov MI, Kim HS, Varyukhin V, Beygelzimer Y. Cross flow during twist extrusion: theory, experiment, and application. *Metallurgical and Materials Transactions A* 2013;44:3211-20.
- [167] Bouaziz O. Geometrically induced strain hardening. *Scripta Materialia* 2013;68:28-30.
- [168] Hall EO. The Deformation and Ageing of Mild Steel: II Characteristics of the Lüders Deformation. *Proceedings of the Physical Society Section B* 1951;64:742.
- [169] Petch NJ. The cleavage strength of polycrystals. *J Iron Steel Inst Lond* 1953;173:25-8.
- [170] Shen Z, Wagoner RH, Clark WAT. Dislocation and grain boundary interactions in metals. *Acta Metallurgica* 1988;36:3231-42.
- [171] Zhu YT, Liao XZ, Wu XL. Deformation twinning in nanocrystalline materials. *Progress in Materials Science* 2012;57:1-62.
- [172] Shan Z, Stach E, Wierzorek J, Knapp J, Follstaedt D, Mao S. Grain boundary-mediated plasticity in nanocrystalline nickel. *Science* 2004;305:654-7.
- [173] Schiøtz J, Di Tolla FD, Jacobsen KW. Softening of nanocrystalline metals at very small grain sizes. *Nature* 1998;391:561-3.
- [174] Kocks UF, Mecking H. Physics and phenomenology of strain hardening: the FCC case. *Progress in Materials Science* 2003;48:171-273.
- [175] Estrin Y, Toth L, Molinari A, Bréchet Y. A dislocation-based model for all hardening stages in large strain deformation. *Acta materialia* 1998;46:5509-22.
- [176] Tóth LsS, Molinari A, Estrin Y. Strain hardening at large strains as predicted by dislocation based polycrystal plasticity model. *Journal of engineering materials and technology* 2002;124:71-7.
- [177] Sakai T, Belyakov A, Kaibyshev R, Miura H, Jonas JJ. Dynamic and post-dynamic recrystallization under hot, cold and severe plastic deformation conditions. *Progress in materials science* 2014;60:130-207.

References

- [178] Valiev RZ, Islamgaliev RK, Alexandrov IV. Bulk nanostructured materials from severe plastic deformation *Progress in Materials Science* 2000;45:87.
- [179] Shrivastava S, Jonas J, Canova G. Equivalent strain in large deformation torsion testing: theoretical and practical considerations. *Journal of the Mechanics and Physics of Solids* 1982;30:75-90.
- [180] Valiev R, Ivanisenko YV, Rauch E, Baudalet B. Structure and deformation behaviour of Armco iron subjected to severe plastic deformation. *Acta Materialia* 1996;44:4705-12.
- [181] Hirth JP. The influence of grain boundaries on mechanical properties. *Metallurgical Transactions* 1972;3:3047-67.
- [182] Wang J, Kang K, Zhang RF, Zheng SJ, Beyerlein IJ, Mara NA. Structure and Property of Interfaces in ARB Cu/Nb Laminated Composites. *JOM* 2012;64:1208-17.
- [183] Segal VM, Hartwig KT, Goforth RE. In situ composites processed by simple shear. *Mater Sci Eng A-Struct Mater Prop Microstruct Process* 1997;224:107-15.
- [184] Segal VM. Materials processing by simple shear. *Materials Science and Engineering: A* 1995;197:157-64.
- [185] Segal VM, Reznikov VI, Drobyshvskiy AE, Kopylov VI. Plastic working of metals by simple shear. *Russian Metallurgy* 1981;1:99-105.
- [186] Zhu YT, Lowe TC, Langdon TG. Performance and applications of nanostructured materials produced by severe plastic deformation. *Scripta Materialia* 2004;51:825-30.
- [187] Valiev RZ, Langdon TG. Principles of equal channel angular pressing as a processing tool for grain refinement. *Progress in Materials Science* 2006;51:881-981.
- [188] Iwahashi Y, Wang J, Horita Z, Nemoto M, Langdon TG. Principle of equal-channel angular pressing for the processing of ultra-fine grained materials. *Scripta Materialia* 1996;35:143-6.
- [189] Lapovok RY. The role of back-pressure in equal channel angular extrusion. *Journal of materials science* 2005;40:341-6.
- [190] Haase C, Lapovok R, Ng HP, Estrin Y. Production of Ti-6Al-4V billet through compaction of blended elemental powders by equal channel angular pressing *Materials Science and Engineering A* 2012;550:263-73.
- [191] Lapovok R, Tomus D, Muddle BC. Compaction of Ti-6Al-4V powder by ECAE with back-pressure. In: Zhang D, Pickering K, Gabbitas B, Cao P, Langdon A, Torrens R, et al., editors. *Advanced Materials and Processing Iv*. Stafa-Zurich: Trans Tech Publications Ltd; 2007. p. 33-6.
- [192] Lapovok R, Tomus D, Bettles C. Shear deformation with imposed hydrostatic pressure for enhanced compaction of powder. *Scripta Materialia* 2008;58:898-901.
- [193] Lapovok R, Tomus D, Muddle BC. Low-temperature compaction of Ti-6Al-4V powder using equal channel angular extrusion with back pressure. *Mater Sci Eng A-Struct Mater Prop Microstruct Process* 2008;490:171-80.
- [194] Ng HP, Haase C, Lapovok R, Estrin Y. Improving sinterability of Ti-6Al-4V from blended elemental powders through equal channel angular pressing. *Materials Science and Engineering: A* 2013;565:396-404.
- [195] Xia KN. Consolidation of Particles by Severe Plastic Deformation: Mechanism and Applications in Processing Bulk Ultrafine and Nanostructured Alloys and Composites. *Advanced Engineering Materials* 2009;12:724-9.
- [196] Xia K, Wu X, Honma T, Ringer SP. Ultrafine pure aluminium through back pressure equal channel angular consolidation (BP-ECAC) of particles. *Journal of materials science* 2007;42:1551-60.

References

- [197] Kubota M, Wu XL, Xu W, Xia KN. Mechanical properties of bulk aluminium consolidated from mechanically milled particles by back pressure equal channel angular pressing. *Mater Sci Eng A-Struct Mater Prop Microstruct Process* 2010;527:6533-6.
- [198] Xu W, Wu X, Honma T, Ringer SP, Xia K. Nanostructured Al-Al₂O₃ composite formed in situ during consolidation of ultrafine Al particles by back pressure equal channel angular pressing. *Acta Materialia* 2009;57:4321-30.
- [199] Bachmaier A, Hohenwarter A, Pippan R. New procedure to generate stable nanocrystallites by severe plastic deformation. *Scripta Materialia* 2009;61:1016-9.
- [200] Casati R, Vedani M, Dellasega D, Bassani P, Tuissi A. Consolidated Al/Al₂O₃ Nanocomposites by Equal Channel Angular Pressing and Hot Extrusion. *Materials and Manufacturing Processes* 2014:1-5.
- [201] Derakhshandeh R, Jahromi AJ. An investigation on the capability of equal channel angular pressing for consolidation of aluminum and aluminum composite powder. *Mater Des* 2011;32:3377-88.
- [202] Sabirov I, Kolednik O, Valiev RZ, Pippan R. Equal channel angular pressing of metal matrix composites: Effect on particle distribution and fracture toughness. *Acta Materialia* 2005;53:4919-30.
- [203] Quang P, Jeong YG, Yoon SC, Hong SH, Kim HS. Consolidation of 1 vol. % carbon nanotube reinforced metal matrix nanocomposites via equal channel angular pressing. *Journal of Materials Processing Technology* 2007;187:318-20.
- [204] Zhang Z, Topping T, Li Y, Vogt R, Zhou Y, Haines C, et al. Mechanical behavior of ultrafine-grained Al composites reinforced with B₄C nanoparticles. *Scripta Materialia* 2011;65:652-5.
- [205] Gan WM, Wu K, Zheng MY, Wang XJ, Chang H, Brokmeier HG. Microstructure and mechanical property of the ECAPed Mg₂Si/Mg composite. *Materials Science and Engineering: A* 2009;516:283-9.
- [206] Wang GS, Fan GH, Geng L, Hu W, Huang YD. Microstructure evolution and mechanical properties of TiB₂/Cu composites processed by equal channel angular pressing at elevated temperature. *Materials Science and Engineering: A* 2013;571:144-9.
- [207] Zhilyaev AP, Langdon TG. Using high-pressure torsion for metal processing: Fundamentals and applications. *Progress in Materials Science* 2008;53:893-979.
- [208] Sun YF, Fujii H, Nakamura T, Tsuji N, Todaka D, Umemoto M. Critical strain for mechanical alloying of Cu–Ag, Cu–Ni and Cu–Zr by high-pressure torsion. *Scripta Materialia* 2011;65:489-92.
- [209] Oh-ishi K, Edalati K, Kim HS, Hono K, Horita Z. High-pressure torsion for enhanced atomic diffusion and promoting solid-state reactions in the aluminum–copper system. *Acta Materialia* 2013;61:3482-9.
- [210] Huang J, Zhu Y, Liao X, Valiev R. Amorphization of TiNi induced by high-pressure torsion. *Philosophical magazine letters* 2004;84:183-90.
- [211] Quelennec X, Menand A, Le Breton JM, Pippan R, Sauvage X. Homogeneous Cu–Fe supersaturated solid solutions prepared by severe plastic deformation. *Philos Mag* 2010;90:1179-95.
- [212] Edalati K, Toh S, Iwaoka H, Watanabe M, Horita Z, Kashioka D, et al. Ultrahigh strength and high plasticity in TiAl intermetallics with bimodal grain structure and nanotwins. *Scripta Materialia* 2012;67:814-7.
- [213] Raabe D, Ohsaki S, Hono K. Mechanical alloying and amorphization in Cu–Nb–Ag in situ composite wires studied by transmission electron microscopy and atom probe tomography. *Acta Materialia* 2009;57:5254-63.

References

- [214] Romankov S, Park YC, Shchetinin IV, Yoon JM. Atomic-scale intermixing, amorphization and microstructural development in a multicomponent system subjected to surface severe plastic deformation. *Acta Materialia* 2013;61:1254-65.
- [215] Saito Y, Utsunomiya H, Tsuji N, Sakai T. Novel ultra-high straining process for bulk materials—development of the accumulative roll-bonding (ARB) process. *Acta materialia* 1999;47:579-83.
- [216] Tsuji N, Saito Y, Lee S-H, Minamino Y. ARB (accumulative roll-bonding) and other new techniques to produce bulk ultrafine grained materials. *Advanced Engineering Materials* 2003;5:338-44.
- [217] Han WZ, Misra A, Mara NA, Germann TC, Baldwin JK, Shimada T, et al. Role of interfaces in shock-induced plasticity in Cu/Nb nanolaminates. *Philos Mag* 2011;91:4172-85.
- [218] Toroghinejad MR, Jamaati R, Dutkiewicz J, Szpunar JA. Investigation of nanostructured aluminum/copper composite produced by accumulative roll bonding and folding process. *Mater Des* 2013;51:274-9.
- [219] Dehsorkhi RN, Qods F, Tajally M. Investigation on microstructure and mechanical properties of Al–Zn composite during accumulative roll bonding (ARB) process. *Materials Science and Engineering: A* 2011;530:63-72.
- [220] Knezevic M, Nizolek T, Ardeljan M, Beyerlein IJ, Mara NA, Pollock TM. Texture evolution in two-phase Zr/Nb lamellar composites during accumulative roll bonding. *International Journal of Plasticity* 2014;57:16-28.
- [221] Tohidi A, Ketabchi M, Hasannia A. Nanograined Ti–Nb microalloy steel achieved by Accumulative Roll Bonding (ARB) process. *Materials Science and Engineering: A* 2013;577:43-7.
- [222] Tayyebi M, Eghbali B. Processing of Al/304 stainless steel composite by roll bonding. *Materials Science and Technology* 2012;28:1414-9.
- [223] Eslami A, Zebarjad SM, Moshksar M. Study on mechanical and magnetic properties of Cu/Ni multilayer composite fabricated by accumulative roll bonding process. *Materials Science and Technology* 2013;29:1000-5.
- [224] Stover A, Krywopusk N, Fritz G, Barron S, Gibbins J, Weihs T. An analysis of the microstructure and properties of cold-rolled Ni: Al laminate foils. *Journal of Materials Science* 2013;48:5917-29.
- [225] Segal VM. Equal channel angular extrusion: from macromechanics to structure formation. *Materials Science and Engineering: A* 1999;271:322-33.
- [226] Stolyarov VV, Zhu YT, Alexandrov IV, Lowe TC, Valiev RZ. Influence of ECAP routes on the microstructure and properties of pure Ti. *Materials Science and Engineering: A* 2001;299:59-67.
- [227] Furukawa M, Horita Z, Langdon TG. Factors influencing the shearing patterns in equal-channel angular pressing. *Materials Science and Engineering: A* 2002;332:97-109.
- [228] Iwahashi Y, Horita Z, Nemoto M, Langdon TG. The process of grain refinement in equal-channel angular pressing. *Acta Materialia* 1998;46:3317-31.
- [229] Mishin OV, Bowen JR, Lathabai S. Quantification of microstructure refinement in aluminium deformed by equal channel angular extrusion: Route A vs. route Bc in a 90 ° die. *Scripta Materialia* 2010;63:20-3.
- [230] Li S, Li X, Yang L. Role of strain path change in grain refinement by severe plastic deformation: A case study of equal channel angular extrusion. *Acta Materialia* 2013;61:4398-413.
- [231] Ban CY, Yao Z, Gao HT, Zhu SX, Guo YP, Cui JZ. Study on New Extrusion Route of Equal Channel Angular Processing in High Purity Aluminium. *Advanced Materials Research: Trans Tech Publ*; 2015. p. 343-7.

References

- [232] Salimyanfard F, Toroghinejad MR, Ashrafizadeh F, Hoseini M, Szpunar JA. Investigation of texture and mechanical properties of copper processed by new route of equal channel angular pressing. *Mater Des* 2013;44:374-81.
- [233] Furukawa M, Horita Z, Nemoto M, Langdon TG. Review: Processing of metals by equal-channel angular pressing. *JOURNAL OF MATERIALS SCIENCE* 2001;36:2835-43.
- [234] Li Y, Zhang Y, Tao N, Lu K. Effect of the Zener–Hollomon parameter on the microstructures and mechanical properties of Cu subjected to plastic deformation. *Acta Materialia* 2009;57:761-72.
- [235] Williams D, Carter CB. Elastic Scattering. *Transmission Electron Microscopy*: Springer US; 2009. p. 39-51.
- [236] Ungár T. The Meaning of Size Obtained from Broadened X-ray Diffraction Peaks. *Advanced Engineering Materials* 2003;5:323-9.
- [237] Ungár T. Microstructural parameters from X-ray diffraction peak broadening. *Scripta Materialia* 2004;51:777-81.
- [238] Ungar T, Revesz A, Borbely A. Dislocations and Grain Size in Electrodeposited Nanocrystalline Ni Determined by the Modified Williamson-Hall and Warren-Averbach Procedures. *Journal of Applied Crystallography* 1998;31:554-8.
- [239] Williamson GK, Smallman RE. III. Dislocation densities in some annealed and cold-worked metals from measurements on the X-ray debye-scherrer spectrum. *Philos Mag* 1956;1:34-46.
- [240] Williamson GK, Hall WH. X-ray line broadening from filed aluminium and wolfram. *Acta Metallurgica* 1953;1:22-31.
- [241] Williams D, Carter CB. The Transmission Electron Microscope. *Transmission Electron Microscopy*: Springer US; 2009. p. 3-22.
- [242] Williams D, Carter CB. Inelastic Scattering and Beam Damage. *Transmission Electron Microscopy*: Springer US; 2009. p. 53-71.
- [243] Yao N. Focused ion beam systems: basics and applications: Cambridge University Press; 2007.
- [244] Giannuzzi L, Prenitzer B, Kempshall B. Ion - Solid Interactions. In: Giannuzzi L, Stevie F, editors. *Introduction to Focused Ion Beams*: Springer US; 2005. p. 13-52.
- [245] Antrekowisch H, Hanko G, Ebner P. Recycling of different types of magnesium scrap. In: Kaplan HI, editor. *Magnesium Technology: TMS*; 2002. p. 43-8.
- [246] Hanko G, Antrekowitsch H, Ebner P. Recycling automotive magnesium scrap. *JOM* 2002;54:51-4.
- [247] Van Geertruyden WH, Prescott CA, Misiolek WZ, Peterson R. Evaluation of light gauge Al scrap remelting after consolidation via the extrusion process. *Light Metal Age* 2005;63:14-8.
- [248] Lapovok RY, Thomson PF. Production of dense rod from magnesium swarf for re-melting. Warrendale: Minerals, Metals & Materials Soc; 2004.
- [249] Gronostajski J, Marciniak H, Matuszak A. New methods of aluminium and aluminium-alloy chips recycling. *Journal of Materials Processing Technology* 2000;106 34-9.
- [250] Matuszak A, Gronostajski J. The recycling of metals by plastic deformation: an example of recycling of aluminium and its alloys chips. *Journal of Materials Processing Technology* 1999;92-93:35-42.
- [251] Sharma C, Nakagawa T, Takenaka N. Recent development in the recycling of machining swarfs by sintering and powder forging. *Ann Cirp* 1977;25:121-5.
- [252] Cui J, Roven HJ. Recycling of automotive aluminum. *Transactions of Nonferrous Metals Society of China* 2010;20:2057-63.

References

- [253] Abolghasem S, Basu S, Shekhar S, Cai J, Shankar MR. Mapping subgrain sizes resulting from severe simple shear deformation. *Acta Materialia* 2012;60:376-86.
- [254] Shankar MR, Rao BC, Lee S, Chandrasekar S, King AH, Compton WD. Severe plastic deformation (SPD) of titanium at near-ambient temperature. *Acta Materialia* 2006;54:3691-700.
- [255] Moss M, Lapovok R, Bettles CJ. The equal channel angular pressing of magnesium and magnesium alloy powders. *JOM* 2007;59:54-7.
- [256] Lapovok R, Tomus D, Skripnyuk VM, Barnett MR, Gibson MA. The effect of hydrogenation on the ECAP compaction of Ti-6Al-4V powder and the mechanical properties of compacts. *Mater Sci Eng A-Struct Mater Prop Microstruct Process* 2009;513-14:97-108.
- [257] Xia. K. Consolidation of particles by severe plastic deformation: mechanism and application in processing bulk ultrafine and nanostructured alloys and composites. *Advanced Engineering Materials* 2010;12:724-9.
- [258] Luo P, McDonald DT, Xu W, Palanisamy S, Dargusch MS, Xia K. A modified Hall-Petch relationship in ultrafine-grained titanium recycled from chips by equal channel angular pressing. *Scripta Materialia* 2012;66:785-8.
- [259] Luo P, McDonald DT, Zhu SM, Palanisamy S, Dargusch MS, Xia K. Analysis of microstructure and strengthening in pure titanium recycled from machining chips by equal channel angular pressing using electron backscatter diffraction. *Mater Sci Eng A-Struct Mater Prop Microstruct Process* 2012;538:252-8.
- [260] Haase M, Khalifa NB, Tekkaya AE, Misiolek WZ. Improving mechanical properties of chip-based aluminium extrudates by integrated extrusion and equal channel angular pressing (iECAP). *Materials Science and Engineering A* 2012;539:194-204.
- [261] Ying T, Zheng M, Hu X, Wu K. Recycling of AZ91 Mg alloy through consolidation of machined chips by extrusion and ECAP. *Transactions of Nonferrous Metals Society of China* 2010;20:604-7.
- [262] Peng T, Wang QD, Han YK, Zheng J, Guo W. Consolidation behavior of Mg-10Gd-2Y-0.5Zr chips during solid state recycling *Journal of Alloy and Compounds* 2010;503:253-9.
- [263] Bachmaier A, Pippan R. Generation of metallic nanocomposites by severe plastic deformation. *International Materials Reviews* 2013;58:41-62.
- [264] Braungart M. Eco-engineering: Living in a materials world: Upcycle to eliminate waste. *Nature* 2013;494:174-5.
- [265] Chen YJ, Chai YC, Roven HJ, Gireesh SS, Yu YD, Hjelen J. Microstructure and mechanical properties of Al-xMg alloys processed by room temperature ECAP. *Materials Science and Engineering: A* 2012;545:139-47.
- [266] Kapoor R, Chakravarty JK. Deformation behavior of an ultrafine-grained Al-Mg alloy produced by equal-channel angular pressing. *Acta Materialia* 2007;55:5408-18.
- [267] Liu M, Roven HJ, Murashkin M, Valiev RZ. Structural characterization by high-resolution electron microscopy of an Al-Mg alloy processed by high-pressure torsion. *Materials Science and Engineering: A* 2009;503:122-5.
- [268] Liu M-p, Roven HJ, Liu X-t, Murashkin M, Valiev RZ, Ungár T, et al. Special nanostructures in Al-Mg alloys subjected to high pressure torsion. *Transactions of Nonferrous Metals Society of China* 2010;20:2051-6.
- [269] Zhang DL, Massalski TB, Paruchuri MR. Formation of metastable and equilibrium phases during mechanical alloying of Al and Mg powders. *Metallurgical and Materials Transactions A* 1994;25:73-9.
- [270] Scudino S, Sakaliyska M, Surreddi KB, Eckert J. Mechanical alloying and milling of Al-Mg alloys. *J Alloy Compd* 2009;483:2-7.

References

- [271] Liu XB, Chen RS, Han EH. Preliminary investigations on the Mg–Al–Zn/Al laminated composite fabricated by equal channel angular extrusion. *Journal of Materials Processing Technology* 2009;209:4675-81.
- [272] Sankaran A, Vadakke Madam S, Nouri A, Barnett MR. Attaining high compressive strains in pure Mg at room temperature by encasing with pure Al. *Scripta Materialia* 2012;66:725-8.
- [273] Oliver WC, Pharr GM. An improved technique for determining hardness and elastic modulus using load and displacement sensing indentation experiments. *Journal of Materials Research* 1992;7:564-1583.
- [274] Honeycombe R. The plastic deformation of metals. 2nd ed. London: Edward Arnold 1984.
- [275] Cullity BD, Stock SR. Structure of polycrystalline aggregates. *Elements of x-ray diffraction*. Upper Saddle River, New Jwese: Pretice Hall; 2001. p. 386-9.
- [276] Ungár T. Microstructural parameters from X-ray diffraction peak broadening. *Scripta Materialia* 2004;51:777-81.
- [277] Gibson LJ, Ashby MF, Harley BA. Cellular materials in nature and medicine: Cambridge University Press; 2010.
- [278] Klawitter JJ, Bagwell JG, Weinstein AM, Sauer BW, Pruitt JR. An evaluation of bone growth into porous high density polyethylene. *Journal of Biomedical Materials Research* 1976;10:311-23.
- [279] Pilliar R, Cameron H, Macnab I. Porous surface layered prosthetic devices. *Biomedical engineering* 1975;10:126-31.
- [280] Ducheyne P, De Meester P, Aernoudt E, Martens M, Mulier JC. Influence of a functional dynamic loading on bone ingrowth into surface pores of orthopedic implants. *Journal of Biomedical Materials Research* 1977;11:811-38.
- [281] Jaeggi C, Frauchiger V, Eitel F, Stiefel M, Schmotzer H, Siegmann S. The effect of surface alloying of Ti powder for vacuum plasma spraying of open porous titanium coatings. *Acta Materialia* 2011;59:717-25.
- [282] Bobyn J, Pilliar R, Cameron H, Weatherly G. The optimum pore size for the fixation of porous-surfaced metal implants by the ingrowth of bone. *Clinical Orthopaedics and Related Research* 1980;150:263-70.
- [283] Engh C, Bobyn J, Glassman A. Porous-coated hip replacement. The factors governing bone ingrowth, stress shielding, and clinical results. *Journal of Bone & Joint Surgery, British Volume* 1987;69:45-55.
- [284] Kröger H, Venesmaa P, Jurvelin J, Miettinen H, Suomalainen O, Alhava E. Bone density at the proximal femur after total hip arthroplasty. *Clinical Orthopaedics and Related Research* 1998;352:66-74.
- [285] Huiskes R, Weinans H, van Rietbergen B. The relationship between stress shielding and bone resorption around total hip stems and the effects of flexible materials. *Clinical orthopaedics and related research* 1992;274:124-34.
- [286] Kuroda D, Niinomi M, Morinaga M, Kato Y, Yashiro T. Design and mechanical properties of new β type titanium alloys for implant materials. *Materials Science and Engineering: A* 1998;243:244-9.
- [287] Geetha M, Singh A, Asokamani R, Gogia A. Ti based biomaterials, the ultimate choice for orthopaedic implants—a review. *Progress in Materials Science* 2009;54:397-425.
- [288] Kanis JA, Melton LJ, Christiansen C, Johnston CC, Khaltsev N. The diagnosis of osteoporosis. *Journal of Bone and Mineral Research* 1994;9:1137-41.
- [289] Wu S, Liu X, Yeung KWK, Liu C, Yang X. Biomimetic porous scaffolds for bone tissue engineering. *Materials Science and Engineering: R: Reports* 2014;80:1-36.

References

- [290] Long M, Rack H. Titanium alloys in total joint replacement—a materials science perspective. *Biomaterials* 1998;19:1621-39.
- [291] Rack H, Qazi J. Titanium alloys for biomedical applications. *Materials Science and Engineering: C* 2006;26:1269-77.
- [292] Li Y, Yang C, Zhao H, Qu S, Li X, Li Y. New Developments of Ti-Based Alloys for Biomedical Applications. *Materials* 2014;7:1709-800.
- [293] Hollister SJ. Scaffold design and manufacturing: from concept to clinic. *Advanced Materials* 2009;21:3330-42.
- [294] Huiskes R. The various stress patterns of press-fit, ingrown, and cemented femoral stems. *Clinical orthopaedics and related research* 1990;261:27-38.
- [295] Van Bael S, Chai YC, Truscetto S, Moesen M, Kerckhofs G, Van Oosterwyck H, et al. The effect of pore geometry on the in vitro biological behavior of human periosteum-derived cells seeded on selective laser-melted Ti6Al4V bone scaffolds. *Acta Biomater* 2012;8:2824-34.
- [296] Lin CY, Wirtz T, LaMarca F, Hollister SJ. Structural and mechanical evaluations of a topology optimized titanium interbody fusion cage fabricated by selective laser melting process. *Journal of Biomedical Materials Research Part A* 2007;83:272-9.
- [297] Pattanayak DK, Fukuda A, Matsushita T, Takemoto M, Fujibayashi S, Sasaki K, et al. Bioactive Ti metal analogous to human cancellous bone: Fabrication by selective laser melting and chemical treatments. *Acta Biomater* 2011;7:1398-406.
- [298] Fukuda A, Takemoto M, Saito T, Fujibayashi S, Neo M, Pattanayak DK, et al. Osteoinduction of porous Ti implants with a channel structure fabricated by selective laser melting. *Acta Biomater* 2011;7:2327-36.
- [299] Dadbakhsh S, Speirs M, Kruth J-P, Van Humbeeck J. Influence of SLM on shape memory and compression behaviour of NiTi scaffolds. *CIRP Annals - Manufacturing Technology* 2015;64:209-12.
- [300] Vrancken B, Thijs L, Kruth J-P, Van Humbeeck J. Heat treatment of Ti6Al4V produced by Selective Laser Melting: Microstructure and mechanical properties. *J Alloy Compd* 2012;541:177-85.
- [301] Mullen L, Stamp RC, Brooks WK, Jones E, Sutcliffe CJ. Selective Laser Melting: A regular unit cell approach for the manufacture of porous, titanium, bone in - growth constructs, suitable for orthopedic applications. *Journal of Biomedical Materials Research Part B: Applied Biomaterials* 2009;89:325-34.
- [302] Kato K, Ochiai S, Yamamoto A, Daigo Y, Honma K, Matano S, et al. Novel multilayer Ti foam with cortical bone strength and cytocompatibility. *Acta Biomater* 2013;9:5802-9.
- [303] Yook S-W, Jung H-D, Park C-H, Shin K-H, Koh Y-H, Estrin Y, et al. Reverse freeze casting: A new method for fabricating highly porous titanium scaffolds with aligned large pores. *Acta Biomater* 2012;8:2401-10.
- [304] Yook S-W, Kim H-E, Koh Y-H. Fabrication of porous titanium scaffolds with high compressive strength using camphene-based freeze casting. *Materials Letters* 2009;63:1502-4.
- [305] Wen CE, Mabuchi M, Yamada Y, Shimojima K, Chino Y, Asahina T. Processing of biocompatible porous Ti and Mg. *Scripta Materialia* 2001;45:1147-53.
- [306] Arifvianto B, Zhou J. Fabrication of Metallic Biomedical Scaffolds with the Space Holder Method: A Review. *Materials* 2014;7:3588-622.
- [307] Kim SW, Jung H-D, Kang M-H, Kim H-E, Koh Y-H, Estrin Y. Fabrication of porous titanium scaffold with controlled porous structure and net-shape using magnesium as spacer. *Materials Science and Engineering: C* 2013;33:2808-15.

References

- [308] Watanabe T, Horikoshi Y. The sintering phenomenon of titanium powders- A discussion. *International Journal of Powder Metallurgy and Powder Technology* 1976;12:209-14.
- [309] Vinogradov AY, Stolyarov VV, Hashimoto S, Valiev RZ. Cyclic behavior of ultrafine-grain titanium produced by severe plastic deformation. *Materials Science and Engineering: A* 2001;318:163-73.
- [310] Zhao X, Yang X, Liu X, Wang X, Langdon TG. The processing of pure titanium through multiple passes of ECAP at room temperature. *Materials Science and Engineering: A* 2010;527:6335-9.
- [311] Okazaki Y, Rao S, Tateishi T, Ito Y. Cytocompatibility of various metal and development of new titanium alloys for medical implants. *Materials Science and Engineering: A* 1998;243:250-6.
- [312] Medvedev A, Ng H, Lapovok R, Estrin Y, Lowe T, Anumalasetty V. Comparison of laboratory-scale and industrial-scale Equal Channel Angular Pressing of commercial purity titanium. *Materials Letters* 2015.
- [313] Mishnaevsky Jr L, Levashov E, Valiev RZ, Segurado J, Sabirov I, Enikeev N, et al. Nanostructured titanium-based materials for medical implants: Modeling and development. *Materials Science and Engineering: R: Reports* 2014;81:1-19.
- [314] Estrin Y, Ivanova EP, Michalska A, Truong VK, Lapovok R, Boyd R. Accelerated stem cell attachment to ultrafine grained titanium. *Acta Biomater* 2011;7:900-6.
- [315] Estrin Y, Kasper C, Diederichs S, Lapovok R. Accelerated growth of preosteoblastic cells on ultrafine grained titanium. *Journal of Biomedical Materials Research Part A* 2009;90:1239-42.
- [316] Park J-W, Kim Y-J, Park CH, Lee D-H, Ko YG, Jang J-H, et al. Enhanced osteoblast response to an equal channel angular pressing-processed pure titanium substrate with microrough surface topography. *Acta Biomater* 2009;5:3272-80.
- [317] Kim TN, Balakrishnan A, Lee B, Kim W, Dvorankova B, Smetana K, et al. In vitro fibroblast response to ultra fine grained titanium produced by a severe plastic deformation process. *Journal of Materials Science: Materials in Medicine* 2008;19:553-7.
- [318] Nie F, Zheng Y, Wei S, Wang D, Yu Z, Salimgareeva G, et al. In vitro and in vivo studies on nanocrystalline Ti fabricated by equal channel angular pressing with microcrystalline CP Ti as control. *Journal of Biomedical Materials Research Part A* 2013;101:1694-707.
- [319] Bagherifard S, Ghelichi R, Khademhosseini A, Guagliano M. Cell response to nanocrystallized metallic substrates obtained through severe plastic deformation. *ACS applied materials & interfaces* 2014.
- [320] Lowe TC, Reiss RA. Understanding the biological responses of nanostructured metals and surfaces. *IOP Conference Series: Materials Science and Engineering: IOP Publishing*; 2014. p. 012172.
- [321] Valiev RZ, Langdon TG. Principles of equal-channel angular pressing as a processing tool for grain refinement. *Progress in Materials Science* 2006;51:881-981.
- [322] Henstock JR, Canham LT, Anderson SI. Silicon: The evolution of its use in biomaterials. *Acta Biomater* 2015;11:17-26.
- [323] Witte F. The history of biodegradable magnesium implants: A review. *Acta Biomater* 2010;6:1680-92.
- [324] Esen Z, Dikici B, Duygulu O, Dericioglu AF. Titanium–magnesium based composites: Mechanical properties and in vitro corrosion response in Ringer's solution. *Materials Science and Engineering: A* 2013;573:119-26.

References

- [325] Jiang G, Wang C, Li Q, Dong J, He G. Porous titanium with entangled structure filled with biodegradable magnesium for potential biomedical applications. *Materials Science and Engineering: C* 2015;47:142-9.
- [326] Pattanayak DK, Yamaguchi S, Matsushita T, Nakamura T, Kokubo T. Apatite-forming ability of titanium in terms of pH of the exposed solution. *Journal of The Royal Society Interface* 2012;9:2145-55.
- [327] Salvo L, Cloetens P, Maire E, Zabler S, Blandin J, Buffière J-Y, et al. X-ray microtomography an attractive characterisation technique in materials science. *Nuclear instruments and methods in physics research section B: Beam interactions with materials and atoms* 2003;200:273-86.
- [328] Lewis G. Properties of open-cell porous metals and alloys for orthopaedic applications. *Journal of Materials Science: Materials in Medicine* 2013;24:2293-325.
- [329] Kalantari SM, Arabi H, Mirdamadi S, Mirsalehi SA. Biocompatibility and compressive properties of Ti-6Al-4V scaffolds having Mg element. *Journal of the mechanical behavior of biomedical materials* 2015;48:183-91.
- [330] Li FP, Li JS, Liu GJ, Kou HC, Xu GS, Zhou L. Fabrication and Compressive Properties of Porous Ti6Al4V Alloy with Elongated Pores for Biomedical Application. *Materials Science Forum: Trans Tech Publ*; 2015. p. 354-8.
- [331] Li F, Li J, Xu G, Liu G, Kou H, Zhou L. Fabrication, pore structure and compressive behavior of anisotropic porous titanium for human trabecular bone implant applications. *Journal of the mechanical behavior of biomedical materials* 2015;46:104-14.
- [332] Robertson M, Burns M, Morrison T. The preparation of semiconductor TEM specimens by low-angle polishing. *Microsc Soc Can Bull* 2006;34:19.
- [333] Li H, Salamanca-Riba L. The concept of high angle wedge polishing and thickness monitoring in TEM sample preparation. *Ultramicroscopy* 2001;88:171-8.
- [334] Miracle DB. Metal matrix composites – From science to technological significance. *Compos Sci Technol* 2005;65:2526-40.
- [335] Li JC, Dunand DC. Mechanical properties of directionally freeze-cast titanium foams. *Acta Materialia* 2011;59:146-58.
- [336] Amin Yavari S, van der Stok J, Chai YC, Wauthle R, Tahmasebi Birgani Z, Habibovic P, et al. Bone regeneration performance of surface-treated porous titanium. *Biomaterials* 2014;35:6172-81.
- [337] Amin Yavari S, Chai YC, Böttger AJ, Wauthle R, Schrooten J, Weinans H, et al. Effects of anodizing parameters and heat treatment on nanotopographical features, bioactivity, and cell culture response of additively manufactured porous titanium. *Materials Science and Engineering: C* 2015;51:132-8.
- [338] Kim HM, Miyaji F, Kokubo T, Nakamura T. Preparation of bioactive Ti and its alloys via simple chemical surface treatment. *Journal of biomedical materials research* 1996;32:409-17.
- [339] Tuncer N, Arslan G, Maire E, Salvo L. Investigation of spacer size effect on architecture and mechanical properties of porous titanium. *Materials Science and Engineering: A* 2011;530:633-42.
- [340] Zhuang X, Zhou B, Ouyang J, Sun H, Wu Y, Liu Q, et al. Enhanced MC3T3-E1 preosteoblast response and bone formation on the addition of nano-needle and nanoporous features to microtopographical titanium surfaces. *Biomedical Materials* 2014;9:045001-12.
- [341] Le Guehennec L, Lopez-Heredia M-A, Enkel B, Weiss P, Amouriq Y, Layrolle P. Osteoblastic cell behaviour on different titanium implant surfaces. *Acta Biomater* 2008;4:535-43.

References

- [342] Park J, Lenshek DX, Povirk GL. Reinforcement redistribution in Al SiC composites under cyclic deformations. *Acta Materialia* 1997;45:1351-64.
- [343] World energy outlook 2014 factsheet - How will global energy markets evolve to 2040? . 75739 Paris Cedex 15, France International Energy Agency www.worldenergyoutlook.org; 2014.
- [344] Amils X. Steel core for an electric transmission cable and method of fabricating it. Google Patents; 2014.
- [345] Bayliss CR, Hardy BJ. 18. Overhead Line Conductor and Technical Specifications. *Transmission and Distribution Electrical Engineering* (4th Edition): Elsevier.
- [346] Knych T, Piwowarska M, Uliasz P. Studies on the process of heat treatment of conductive AlZr alloys obtained in various productive processes. *Archives of metallurgy and materials* 2011;56:685-92.
- [347] Mamala A, Scieżor W. Evaluation of the effect of selected alloying elements on the mechanical and electrical aluminium properties. *Archives of Metallurgy and Materials* 2014;59:413-7.
- [348] 3M. 3M™ ACCR's low weight and thermal expansion result in low sag at high ampacities. 2015. p. 3M™ ACCR's low weight and thermal expansion result in low sag at high ampacities.
- [349] McCullough C, Mortensen A, Werner PS, Dève HE, Anderson TL. Fiber reinforced aluminum matrix composite wire. Google Patents; 2001.
- [350] Bryant D, Hiel C, Ferguson WC. Aluminum conductor composite core reinforced cable and method of manufacture. Google Patents; 2008.
- [351] Tian L, Anderson I, Riedemann T, Russell A, Kim H. Prospects for novel deformation processed Al/Ca composite conductors for overhead high voltage direct current (HVDC) power transmission. *Electric Power Systems Research* 2013;105:105-14.
- [352] AFL. Aluminum Clad Steel - High strength and lightweight for superior quality. 2015. p. Aluminum Clad Steel - High strength and lightweight for superior quality.
- [353] Khosravifard A, Ebrahimi R. Investigation of parameters affecting interface strength in Al/Cu clad bimetal rod extrusion process. *Mater Des* 2010;31:493-9.
- [354] Dietrich D, Grittner N, Mehner T, Nickel D, Schaper M, Maier H, et al. Microstructural evolution in the bonding zones of co-extruded aluminium/titanium. *Journal of Materials Science* 2014;49:2442-55.
- [355] Kang CG, Jung YJ, Kwon HC. Finite element simulation of die design for hot extrusion process of Al/Cu clad composite and its experimental investigation. *Journal of Materials Processing Technology* 2002;124:49-56.
- [356] Luo JT, Xu Y, Zhao SJ. Cold extrusion forming of copper/aluminum clad composite. *Applied Mechanics and Materials: Trans Tech Publ*; 2009. p. 441-4.
- [357] Kittner K, Awiszus B. The Process of Co-Extrusion—An Analysis. *Key Engineering Materials: Trans Tech Publ*; 2012. p. 81-8.
- [358] Feng B, Xin Y, Hong R, Yu H, Wu Y, Liu Q. The effect of architecture on the mechanical properties of Mg–3Al–1Zn Rods Containing Hard Al Alloy Cores. *Scripta Materialia* 2015;98:56-9.
- [359] Kazanowski P, Epler ME, Misiolek WZ. Bi-metal rod extrusion—process and product optimization. *Materials Science and Engineering: A* 2004;369:170-80.
- [360] Kocich R, Macháčková A, Kunčická L, Fojtík F. Fabrication and characterization of cold-swaged multilayered Al–Cu clad composites. *Mater Des* 2015;71:36-47.
- [361] Eivani AR, Taheri AK. A new method for producing bimetallic rods. *Materials Letters* 2007;61:4110-3.
- [362] Eslami P, Taheri AK. An investigation on diffusion bonding of aluminum to copper using equal channel angular extrusion process. *Materials letters* 2011;65:1862-4.

References

- [363] Zebardast M, Taheri AK. The cold welding of copper to aluminum using equal channel angular extrusion (ECAE) process. *Journal of Materials Processing Technology* 2011;211:1034-43.
- [364] Lapovok R, McKenzie PWJ, Thomson PF, Semiatin SL. Processing and properties of ultrafine-grain aluminum alloy 5005 sheet. *Journal of Materials Science* 2007;42:1649-59.
- [365] Lapovok R, Tóth L, Winkler M, Semiatin S. A comparison of continuous SPD processes for improving the mechanical properties of aluminum alloy 6111. *Journal of materials research* 2009;24:459-69.
- [366] Raab GJ, Valiev RZ, Lowe TC, Zhu YT. Continuous processing of ultrafine grained Al by ECAP–Conform. *Materials Science and Engineering: A* 2004;382:30-4.
- [367] Kim B, Kim S, Woo B, Lee H, Park J, Jeong Y, et al. High tensile nonmagnetic stainless steel wire for overhead electric conductor, low loss overhead electric conductor using the wire, and method of manufacturing the wire and overhead electric conductor. Google Patents; 2005.
- [368] Verhoeven F, Hejzman D, Lagae G, Gogola P. Non-magnetic stainless steel wire as an armouring wire for power cables. Google Patents; 2015.
- [369] Nefzger P, Kaintzyk U, Nolasco JF. Overhead power lines: planning, design, construction: Springer Science & Business Media; 2003.
- [370] Short TA. Electric power distribution handbook: CRC press; 2014.
- [371] Valiev RZ, Murashkin MY, Sabirov I. A nanostructural design to produce high-strength Al alloys with enhanced electrical conductivity. *Scripta Materialia* 2014;76:13-6.
- [372] Murashkin MY, Sabirov I, Kazykhanov V, Bobruk E, Dubravina A, Valiev R. Enhanced mechanical properties and electrical conductivity in ultrafine-grained Al alloy processed via ECAP-PC. *Journal of Materials Science* 2013;48:4501-9.
- [373] Cubero-Sesin JM, In H, Arita M, Iwaoka H, Horita Z. High-pressure torsion for fabrication of high-strength and high-electrical conductivity Al micro-wires. *Journal of Materials Science* 2014;49:6550-7.
- [374] Zhao Q, Cui X, Qian Z, Liu X. The synergistic effect of Al–B–C master alloy to improve conductivity and strength of 1070 alloy. *J Alloy Compd* 2015;639:478-82.
- [375] Hailiang Y, Tieu AK, Cheng L, Xiong L, Godbole A, Huijun L, et al. A deformation mechanism of hard metal surrounded by soft metal during roll forming. *Scientific reports* 2014;4.
- [376] Ueno H, Kakihata K, Kaneko Y, Hashimoto S, Vinogradov A. Enhanced fatigue properties of nanostructured austenitic SUS 316L stainless steel. *Acta Materialia* 2011;59:7060-9.
- [377] Mamalis AG, Szalay A, Vaxevanidis NM, Manolakos DE. Fabrication of bimetallic rods by explosive cladding and warm extrusion. *Journal of Materials Processing Technology* 1998;83:48-53.
- [378] Lee KS, Kang S-H, Lee Y-S. Synthesis of Zr-based bulk metallic glass–crystalline aluminum alloy composite by co-extrusion. *Materials Letters* 2010;64:129-32.
- [379] Lee KS, Jun H-J, Lee Y-S. Fabrication of bimetallic rods consist of a Zr-based bulk metallic glass and a crystalline copper by co-extrusion. *Intermetallics* 2010;18:1958-63.
- [380] Liu Y, Blandin JJ, Kapelski G, Su áy M, Yang XJ. Interface characterization and mechanical properties of BMG/Cu composites prepared by coextrusion. *Intermetallics* 2012;30:57-64.
- [381] Dowling NE. Mechanical behavior of materials: engineering methods for deformation, fracture, and fatigue: Prentice hall; 1993.

References

- [382] Verhoeven JD, Downing HL, Chumbley LS, Gibson ED. The resistivity and microstructure of heavily drawn Cu - Nb alloys. *Journal of Applied Physics* 1989;65:1293-301.
- [383] Williamson G, Smallman R. III. Dislocation densities in some annealed and cold-worked metals from measurements on the X-ray debye-scherrer spectrum. *Philos Mag* 1956;1:34-46.
- [384] Smallman R, Westmacott K. Stacking faults in face-centred cubic metals and alloys. *Philos Mag* 1957;2:669-83.
- [385] Zhao YH, Liao XZ, Jin Z, Valiev RZ, Zhu YT. Microstructures and mechanical properties of ultrafine grained 7075 Al alloy processed by ECAP and their evolutions during annealing. *Acta Materialia* 2004;52:4589-99.
- [386] Wen H, Topping TD, Isheim D, Seidman DN, Lavernia EJ. Strengthening mechanisms in a high-strength bulk nanostructured Cu-Zn-Al alloy processed via cryomilling and spark plasma sintering. *Acta Materialia* 2013;61:2769-82.
- [387] Lubarda V. On the effective lattice parameter of binary alloys. *Mechanics of materials* 2003;35:53-68.
- [388] Veveřka A, Cabibbo M, Langdon TG. A characterization of microstructure and microhardness on longitudinal planes of an Al-Mg-Si alloy processed by ECAP. *Materials Characterization* 2013;84:126-33.
- [389] Vaseghi M, Taheri AK, Hong SI, Kim HS. Dynamic ageing and the mechanical response of Al-Mg-Si alloy through equal channel angular pressing. *Mater Des* 2010;31:4076-82.
- [390] Roven HJ, Liu M, Werenskiold JC. Dynamic precipitation during severe plastic deformation of an Al-Mg-Si aluminium alloy. *Materials Science and Engineering: A* 2008;483-484:54-8.
- [391] Sha G, Tugcu K, Liao XZ, Trimby PW, Murashkin MY, Valiev RZ, et al. Strength, grain refinement and solute nanostructures of an Al-Mg-Si alloy (AA6060) processed by high-pressure torsion. *Acta Materialia* 2014;63:169-79.
- [392] Oh-ishi K, Hashi Y, Sadakata A, Kaneko K, Horita Z, Langdon TG. Microstructural control of an Al-Mg-Si alloy using equal-channel angular pressing. *Materials Science Forum: Trans Tech Publ*; 2002. p. 333-8.
- [393] Tugcu K, Sha G, Liao XZ, Trimby P, Xia JH, Murashkin MY, et al. Enhanced grain refinement of an Al-Mg-Si alloy by high-pressure torsion processing at 100 °C. *Materials Science and Engineering: A* 2012;552:415-8.
- [394] Sapanathan T, Khoddam S, Zahiri SH. Spiral extrusion of aluminum/copper composite for future manufacturing of hybrid rods: A study of bond strength and interfacial characteristics. *J Alloy Compd* 2013;571:85-92.
- [395] Mozaffari A, Manesh HD, Janghorban K. Evaluation of mechanical properties and structure of multilayered Al/Ni composites produced by accumulative roll bonding (ARB) process. *J Alloy Compd* 2010;489:103-9.
- [396] Nie J-F. Precipitation and hardening in magnesium alloys. *Metallurgical and Materials Transactions A* 2012;43:3891-939.
- [397] Lumley R. *Fundamentals of aluminium metallurgy: Production, processing and applications*: Elsevier; 2010.
- [398] McDonald D, Lui E, Palanisamy S, Dargusch M, Xia K. Achieving Superior Strength and Ductility in Ti-6Al-4V Recycled from Machining Chips by Equal Channel Angular Pressing. *Metallurgical and Materials Transactions A* 2014;45:4089-102.
- [399] Ng HP, Przybilla T, Schmidt C, Lapovok R, Orlov D, Höppel H-W, et al. Asymmetric accumulative roll bonding of aluminium-titanium composite sheets. *Materials Science and Engineering: A* 2013;576:306-15.

References

- [400] Nizolek T, Mara NA, Beyerlein IJ, Avallone JT, Scott JE, Pollock TM. Processing and Deformation Behavior of Bulk Cu–Nb Nanolaminates. *Metallogr Microstruct Anal* 2014;3:470-6.
- [401] Kirkland NT, Birbilis N. *Magnesium Biomaterials: Design, Testing, and Best Practice*: Springer; 2014.
- [402] Chen X-B, Li Y-C, Hodgson PD, Wen C. The importance of particle size in porous titanium and nonporous counterparts for surface energy and its impact on apatite formation. *Acta Biomater* 2009;5:2290-302.
- [403] Zheng YF, Gu XN, Witte F. Biodegradable metals. *Materials Science and Engineering: R: Reports* 2014;77:1-34.
- [404] Yazdimamaghani M, Razavi M, Vashae D, Tayebi L. Surface modification of biodegradable porous Mg bone scaffold using polycaprolactone/bioactive glass composite. *Materials Science and Engineering: C* 2015;49:436-44.
- [405] Purnama A, Hermawan H, Mantovani D. Biodegradable Metal Stents: A Focused Review on Materials and Clinical Studies. *Journal of Biomaterials and Tissue Engineering* 2014;4:868-74.
- [406] Aghion E, Yered T, Perez Y, Gueta Y. The prospects of carrying and releasing drugs via biodegradable magnesium foam. *Advanced Engineering Materials* 2010;12:B374-B9.
- [407] Bowen PK, Drelich J, Goldman J. Zinc exhibits ideal physiological corrosion behavior for bioabsorbable stents. *Advanced Materials* 2013;25:2577-82.
- [408] Orlov D, Ralston KD, Birbilis N, Estrin Y. Enhanced corrosion resistance of Mg alloy ZK60 after processing by integrated extrusion and equal channel angular pressing. *Acta Materialia* 2011;59:6176-86.
- [409] Zhang F, Ma A, Jiang J, Xu H, Song D, Lu F, et al. Enhanced biodegradation behavior of ultrafine-grained ZE41A magnesium alloy in Hank's solution. *Progress in Natural Science: Materials International* 2013;23:420-4.
- [410] Lyndon JA, Boyd BJ, Birbilis N. Metallic implant drug/device combinations for controlled drug release in orthopaedic applications. *Journal of Controlled Release* 2014;179:63-75.